NASA CONTRACTOR
REPORT

NASA CR-184044

RESEARCH REPORTS - 1990 NASA/ASEE SUMMER FACULTY
FELLOWSHIP PROGRAM

The University of Alabama
Tuscaloosa, Alabama
and
The University of Alabama in Huntsville
Huntsville, Alabama

October 1990

Final Report

RESEARCH REPORTS

1990 NASA/ASEE SUMMER FACULTY FELLOWSHIP PROGRAM

George C. Marshall Space Flight Center

The University of Alabama

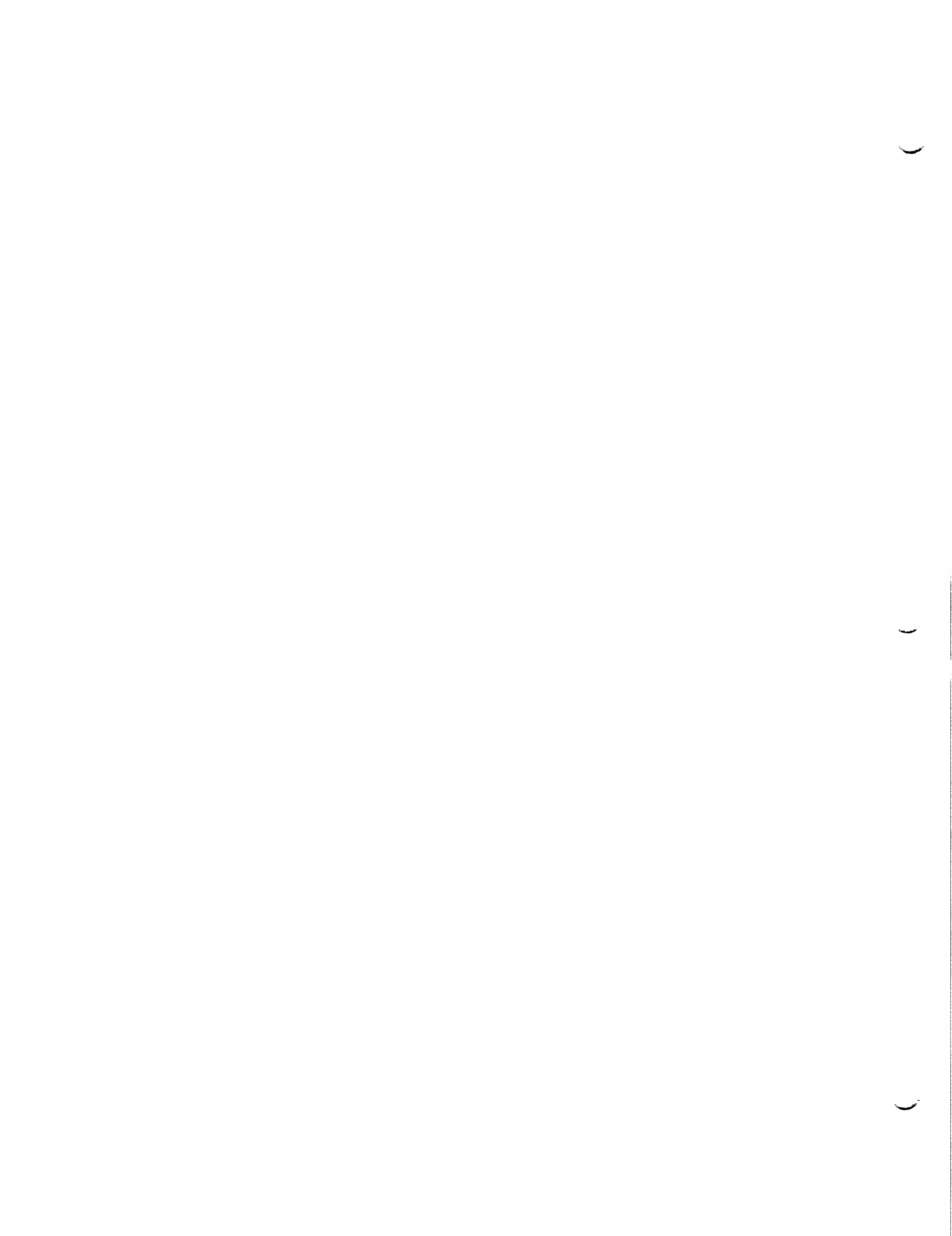and

The University of Alabama in Huntsville

EDITORS:

Dr. L. Michael Freeman
Associate Professor of Aerospace Engineering
The University of Alabama

Dr. Charles R. Chappell
Associate Director for Science
Marshall Space Flight Center

Dr. Frank Six
University Affairs Officer
Marshall Space Flight Center

Dr. Gerald R. Karr
Chairman of Mechanical Engineering
The University of Alabama in Huntsville

1. REPORT NO. NASA CR-184044	2. GOVERNMENT ACCESSION NO.	3. RECIPIENT'S CATALOG NO.
4. TITLE AND SUBTITLE Research Reports - 1990 NASA/ASEE Summer Faculty Fellowship Program		5. REPORT DATE October 1990
		6. PERFORMING ORGANIZATION CODE
7. AUTHOR(S) M. Freeman, R. Chappell, F. Six, G. Karr, Editors		8. PERFORMING ORGANIZATION REPORT #
9. PERFORMING ORGANIZATION NAME AND ADDRESS The University of Alabama Tuscaloosa, Alabama, and The University of Alabama in Huntsville		10. WORK UNIT NO.
		11. CONTRACT OR GRANT NO. NGT-01-002-099
12. SPONSORING AGENCY NAME AND ADDRESS National Aeronautics and Space Administration Washington, DC 20546		13. TYPE OF REPORT & PERIOD COVERED Contractor Report
		14. SPONSORING AGENCY CODE

15. SUPPLEMENTARY NOTES

16. ABSTRACT

For the 26th consecutive year, a NASA/ASEE Summer Faculty Fellowship Program was conducted at the Marshall Space Flight Center (MSFC). The program was conducted by The University of Alabama and MSFC during the period June 4, 1990 through August 10, 1990. Operated under the auspices of the American Society for Engineering Education, the MSFC program, as well as those at other NASA centers, was sponsored by the Office of Educational Affairs, NASA Headquarters, Washington, D.C. The basic objectives of the programs, which are in the 27th year of operation nationally, are (1) to further the professional knowledge of qualified engineering and science faculty members; (2) to stimulate an exchange of ideas between participants and NASA; (3) to enrich and refresh the research and teaching activities of the participants' institutions; and (4) to contribute to the research objectives of the NASA centers.

The Faculty Fellows spent 10 weeks at MSFC engaged in a research project compatible with their interests and background and worked in collaboration with a NASA/MSFC colleague. This document is a compilation of Fellows' reports on their research during the summer of 1990. The University of Alabama Report No. BER-509-94 presents the Co-Directors' report on the administrative operations of the program. Further information can be obtained by contacting any of the editors.

17. KEY WORDS Advanced projects; information and electronic systems; materials and processes; propulsion; space science; structures and dynamics; mission operations; systems analysis and integration; public affairs; safety, reliability, maintainability, and quality assurance.	18. DISTRIBUTION STATEMENT Unclassified - Unlimited Dr. Frank Six 11/8/90 Date University Affairs Officer	
19. SECURITY CLASSIF. (of this report) Unclassified	20. SECURITY CLASSIF. (of this page) Unclassified	21. NO. OF PAGES 22. PRICE 310 NTIS

TABLE OF CONTENTS

1990

NASA/ASEE SUMMER FACULTY FELLOWSHIP PROGRAM

MARSHALL SPACE FLIGHT CENTER
THE UNIVERSITY OF ALABAMA

EFFECTS OF ANTIMONY SUBSTITUTION ON BISMUTH

BASED SUPERCONDUCTORS

Prepared by: Alfonso Barrientos.

Academic Rank: Assistant Professor.

University and   University of Puerto Rico.
Department: Physics R.U.M.

NASA/MSFC:

    Laboratory: Space Science Laboratory.
    Division: Microgravity Science and and
                            Applications Division.
    Branch: Chemistry and Polymeric
                            Materials.

MSFC Colleague: Dr. Marcus Vlasse

Contract No: NGT-01-002-099
                                The University of Alabama

I

Introduction

The discovery of high temperature superconductors of the LaBaCuO(1) and YBaCuO(2) families and the homologous series BiSrCaCuO(3-6) and TlBaCaCuO(7) has produced an explosion of interest, stimulating a great activity in the investigation of these new materials.

BiSrCuO was the first superconducting material that did not contain rare earth elements and has a critical temperature of about 20 K. The compound $Bi_2Sr_2CuO_6$ (2:2:0:1) in the standard notation was the first member of the family where double BiO rock salt-like layers alternate with CuO_2 sheets.

The other compounds of the bismuth family , with Ca addition, $Bi_2Sr_2CaCu_2O_8$ (2:2:1:2) and $Bi_2Sr_2Ca_2Cu_3O_{10}$ (2:2:2:3) are also built from double Bi-O layers with transition temperatures over 80 K for the low phase (L) and 110 K for the high phase (H). However, zero-resistance temperatures greater than 100 K are difficult to obtain in the 2:2:2:3 unless Pb(8) is added to the system.

Many attempts to enhance the transition temperature and improve the stability of the lattice have been made. Total and partial substitution, doping, and new compounds are constantly being reported.

A few papers have reported the existence of critical temperatures as high as 132 K(9) in the Bi based compound doped with Sb, and 140 K(10) by simultaneous chemical substitution of Sb and Pb. They claim that lead leads to a more stable and reproducible system. On the other hand other researchers(11,12) have found that Sb doping proved to be detrimental for the superconducting properties.

The work reported here was undertaken to investigate the effect of Sb substitution and simultaneous substitution of Pb and Sb on the superconducting transition temperatures in the BiSrCaCuO system; particularly in the 2:2:2:3 phase since any small increase in the transition temperature could be of great interest.

Experimental

More than 90 different samples were prepared based on 2:2:2:3 stoichiometry in the BiSrCaCuO system. After this preliminary attempt, four different families of samples have been investigated in the present study. In the first family of samples we substituted Bi by Sb to form $Bi_{1.9}Sb_{0.1}Sr_2Ca_2Cu_3O_y$. The second group of samples were prepared by simultaneous addition of Pb and

Sb with nominal composition $Bi_{1.8}Pb_{0.1}Sb_{0.1}Sr_2Ca_2Cu_3O_y$. The third and fourth groups were prepared to determine the effect when the Pb concentration is increased; having nominal composition $Bi_{1.7}Pb_{0.2}Sb_{0.1}Sr_2Ca_2Cu_3O_y$ and $Bi_{1.6}Pb_{0.3}Sb_{0.1}Sr_2Ca_2Cu_3Oy$

High purity (99.99% - 99.999%) Bi_2O_3, PbO, Sb_2O_3, $SrCO_3$, CaO and CuO powders were weighed in different molar ratios. The weighed powders were dispersed in isopropyl alcohol, ball milled, dried and ground. The powder mixtures were calcined in air at 810°C for 20 hours, then reground and cold pressed into pellets (2 mm thick, 12 mm diameter), using 3000 psi pressure. The pellet samples were subsequently sintered in air with varying processing temperatures and times. The samples were not very sensitive to the cooling rate, so they were furnace cooled.

Samples were prepared in a Fisher furnace. The furnace had three ramp rates and their corresponding holding times, for both, heating and cooling. The temperature can be controlled up to 0.01 degree. The XRD scans were recorded using a Rigaku diffractometer with graphite monochomated $CuK\alpha$ radiation and Bragg-Brentano geometry.

DC temperature dependence resistivity measurements were carried out by the four probe standard technique using a closed cycle refrigerator system, with excitation current of 1 mA. The sample dimension was 0.21 cm(W), 0.15 cm(H) and 1.00 cm(L) Inductance measurement also were carried out, having the superconducting sample as a core in a small coil using a 4275A Hewlett Packard inductance meter.

Results and Discussion

Peaks for XRD at 5.72° and 4.78° (2θ values) corresponding to (200) reflections identify the low and high temperature phases, respectively. Unfortunately, those peaks are not very well defined in our spectra, therefore we concentrated our attention on the 2θ values of 23° (L) and 24° (H) which correspond to (008) and (0010) reflections respectively.

The first family of samples with stoichiometry $Bi_{1.9}Sb_{0.1}Sr_2Ca_2Cu_3O_y$ was heat treated in the temperature range from 810 °C to 900 °C. The most significant ones were sintered for 12 h at 873 °C and 878 °C after a previous calcination and additional sintering at 850 °C for 12 h. At 873 °C a small shoulder in the right side of the low temperature phase (23°) indicates the presence of a small amount of the high temperature phase. When the heat treatment temperature was increased to 878 °C, it produced signicant increases in the amount of the high temperature phase. However, when the processing temperature is increased further, the sample decomposes and the XRD pattern becomes very complicated. The 2:2:1:2 phase can still be identified.

The second set of samples were prepared in parallel conditions as the previous set. Figure 2, shows XRD data for the Sb/Pb compound with nominal composition $Bi_{1.8}Pb_{0.1}Sr_{0.1}Sr_2Ca_2Cu_3O_y$. They were sintered for 12 h at 868 °C, 873 °C, 878 °C, and 883 °C. As the sintering temperature increases from 868 °C to 878 °C the concentration of the low temperature phase seems to decrease in favor of the high temperature phase. Again increasing the processing temperature leads to the degradation of the high temperature phase and the system reenters to the 80 K phase. This behavior has been reported by many researchers in Bi based compounds containing Pb.

It must be mentioned that the x-ray diffraction peak corresponding to the high temperature phase starts to form at 850 °C but it has a very low intensity (I_H/I_L is aproximately 1/10). The temperature is higher for the samples with pure Sb.

The other two groups with 10% and 15% Pb substitution and 5% Sb present esentially the same behavior as the one described above. However, the Pb content tends to decrease the sintering temperature for the formation of the high temperature phase. Illustration of such behavior for our best samples of each group is given in figure 3.

Samples of the third and fourth families were treated for a very short time, 1 to 5 minutes, at temperatures between 880 °C to 930 C. The XRD patterns for this samples are depicted in figure 4. Samples with 10% Pb and 5% Sb, after the calcination process, were heated at 880 °C for 5 minutes and quenched in air. The result is a 2:2:1:2 phase highly oriented. When the sample is heated at 930 °C for 3 minutes the result is also a very highly oriented sample but the low temperature phase decomposes giving rise to the formation of 2:2:0:1 phase. This phase has a critical temperature at 20 K corresponding to the 2θ value of 7.18°. The low temperature phase peak is not present any more.

Similar resuls were observed for samples with 15% lead concentration but the orientation effect seems to appear at slightly lower temperatures.

The electrical superconducting properties of the sample with 5% lead and 5% antimony are shown in figure 5. The resistivity of this sample exhibits metallic behavior in the normal state and starts to decrease sharply at about 115 K, with a second transition at 85 K and zero resistance at 40 K which is indication of a highly inhomogeneous superconductor.

Inductance measurements were taken showing clearly the presence of 2:2:1:2 and 2:2:2:3 phases.

Conclusions

According to our study we have found:

1) There is no evidence of temperature onset at 140 K or 132 K in samples with antimony and lead-antimony additions. On the contrary these substitutions leads invariably to a mixture of two superconducting phases, with the 85 K phase representing the major constituent.

2) Increase in lead doping promotes the formation of the 110 K phase at lower temperatures.

3) Increasing in sintering temperatures, after the formation of the high temperature phase, forces the system to reenter the low temperature phase.

4) Sintering temperatures very close to the melting point for a short periods of time produce very highly oriented samples in the 85 K phase. However, for temperatures much higher than the melting point, the orientation persist but the low temperature phase degrades, forming the very low temperature phase (20 K). As the lead concentration increases the orientation effect starts at lower temperatures.

5) The fact that small changes in sintering temperatures have a great impact on the phase transformation, maybe an indication that these transformations are characterized by very short diffusion path lenghts.

Acknowledgements

Figure Captions

Fig 1. X-ray diffraction scan for $Bi_{1.9}Sb_{0.1}Sr_2Ca_2Cu_3O_y$ samples sintered for 12 h at (a) 873 °C and (b) 878 °C.

Fig 2. X-ray diffraction scan for $Bi_{1.8}Pb_{0.1}Sb_{0.1}Sr_2Ca_2Cu_3O_y$ samples sintered for 12 h at (a) 868 °C, (b) 873 °C, (c) 878 °C, and (d) 883 °C.

Fig 3. X-ray diffraction data for (a) $Bi_{1.7}Pb_{0.2}Sb_{0.1}Sr_2Ca_2Cu_3O_y$ sintered at 870 °C for 24 h, and (b) $Bi_{1.6}Pb_{0.3}Sb_{0.1}Sr_2Ca_2Cu_3O_y$ sintered at 860 for 60 h.

Fig 4. X-ray diffraction data for $Bi_{1.7}Pb_{0.2}Sb_{0.1}Sr_2Ca_2Cu_3O_y$ sintered at (a) 880 °C for 5 minutes, and (b) 930 °C for 3 minutes.

Fig 5. Resistance temperature dependence curve for $Bi_{1.8}Pb_{0.1}Sb_{0.1}Sr_2Ca_2Cu_3O_y$.

References

(1) J. G. Bednorz, and K. A. Muller, Z. Phys. B **64**, 189 (1986)

(2) M. K. Wu, J. R. Ashburn, C. J. Tong, P. H. Hor, R. L. Meng, L. Gao, Z. J. Huang, Y. Q. Wang, and C. W. Chu, Phys. Rev. Lett. **58**, 908 (1987).

(3) C. Michel, M. Herview, M. M. Borel, A. Grandin, F. Deslandes, J. Provost, and B. Raveau, Z. Phys. B **68**, 421 (1987).

(4) H. Maeda, Y. Tanaka, M. Fukutomi, and T. Asano, Japan. J. Appl. Phys. Lett. **27**, 2 (1988)

(5) P. Border, J. J. Capponi, C. Chaillout, J. Chenavas, A. W. Hewat, E. A. Hewat, J. L. Hodeau, M. Marezio, J. L. Tolence, and D. Tranqui, Physica C. **153-155**, 623 (1988).

(6) J. M. Tarascon, Y. Le Page, P. Barboux, B. G. Bagley, L. H. Greene, W. R. McKinnon, G. W. Hull, M. Giroud, and D. M. Huang, Phys. Rev. B **37**, 9382 (1988).

(7) Z. Z. Sheng, and A. M. Herman, Nature. **332**, 138 (1988).

(8) M. Takano, J. Takada, K. Oda, H. Kitaguchi, Y. Miura, Y. Ikeda, Y. Tommi, and H. Mazaki, Jpn. J. Appl. **27**, L996 (1988).

(9) L. Hongbao, C. Liezhao, Z. Ling, M. Zhiqiang, L. Xiaoxian, Y. Zhidong, X. Bai, M. Xianglei, Z. Guien, R. Yaozhong, C. Zhaojia, and Z. Yuheng, Solid State Commun. **69**, 867 (1989).

(10) C. Tingzhu, L. Jiang. F. Chengao, Y. Li, L. Yuntao, Z. Guien, M. Zhiqiang, W. Haiqian, C. Zhaojia, and Z. Yuheng, Supercond. Sci. Technol. **3**, 87 (1990).

(11) P. K. Ummat, W. R. Datars, V. V. Gridin, and C. V. Stagar, Solid State Commun. **74**, 983 (1990).

(12) C. V. Tomy, R. Prasad, N. C. Soni, K. Adhikary, A. Guinar, and S. K. Malik, Solid State Commun. **74**, 493 (1990).
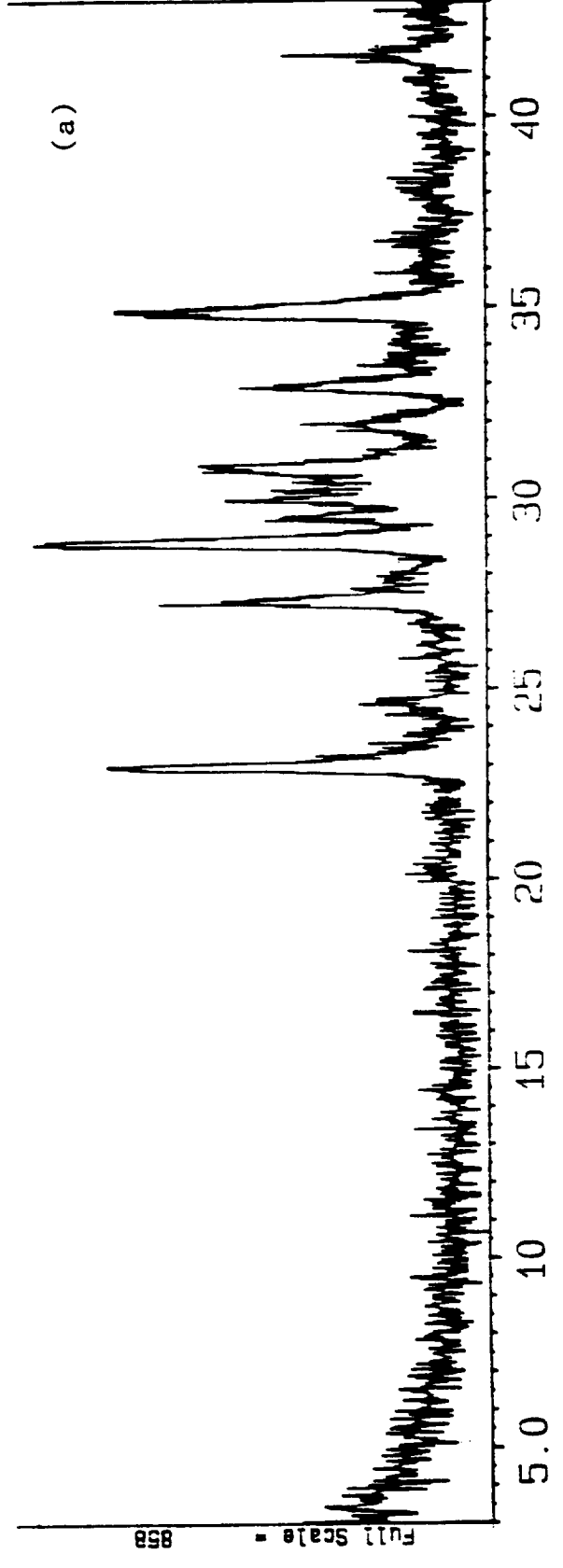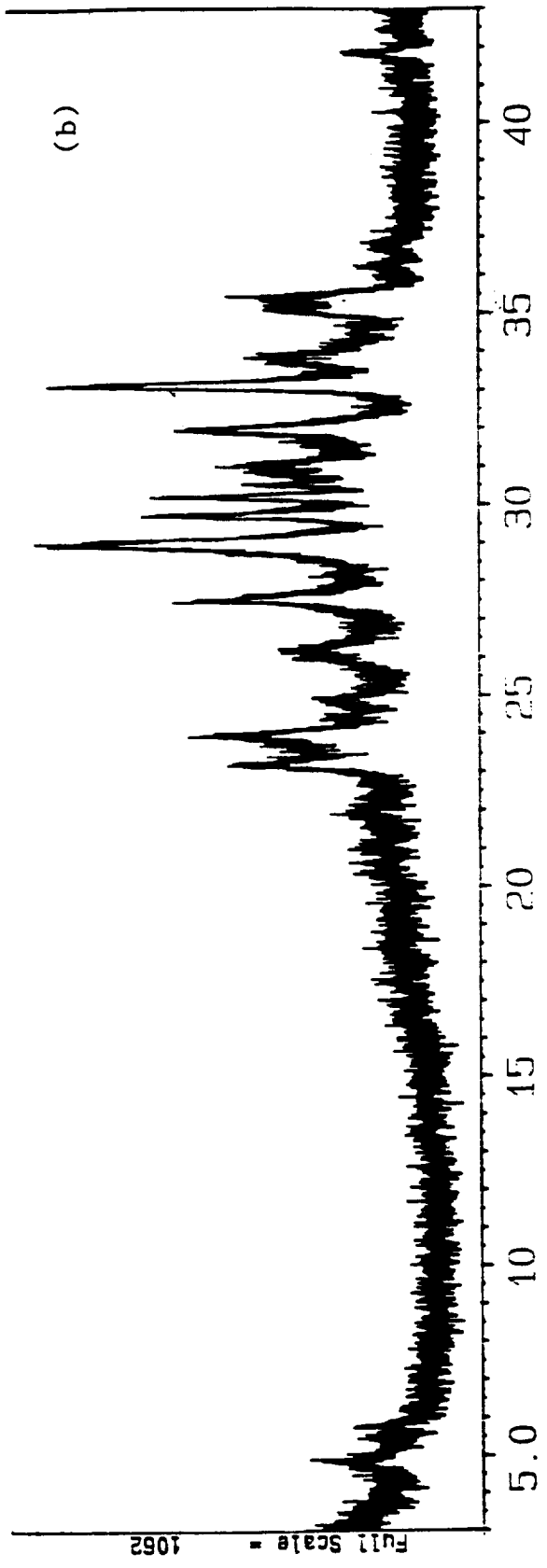
Figure 1.
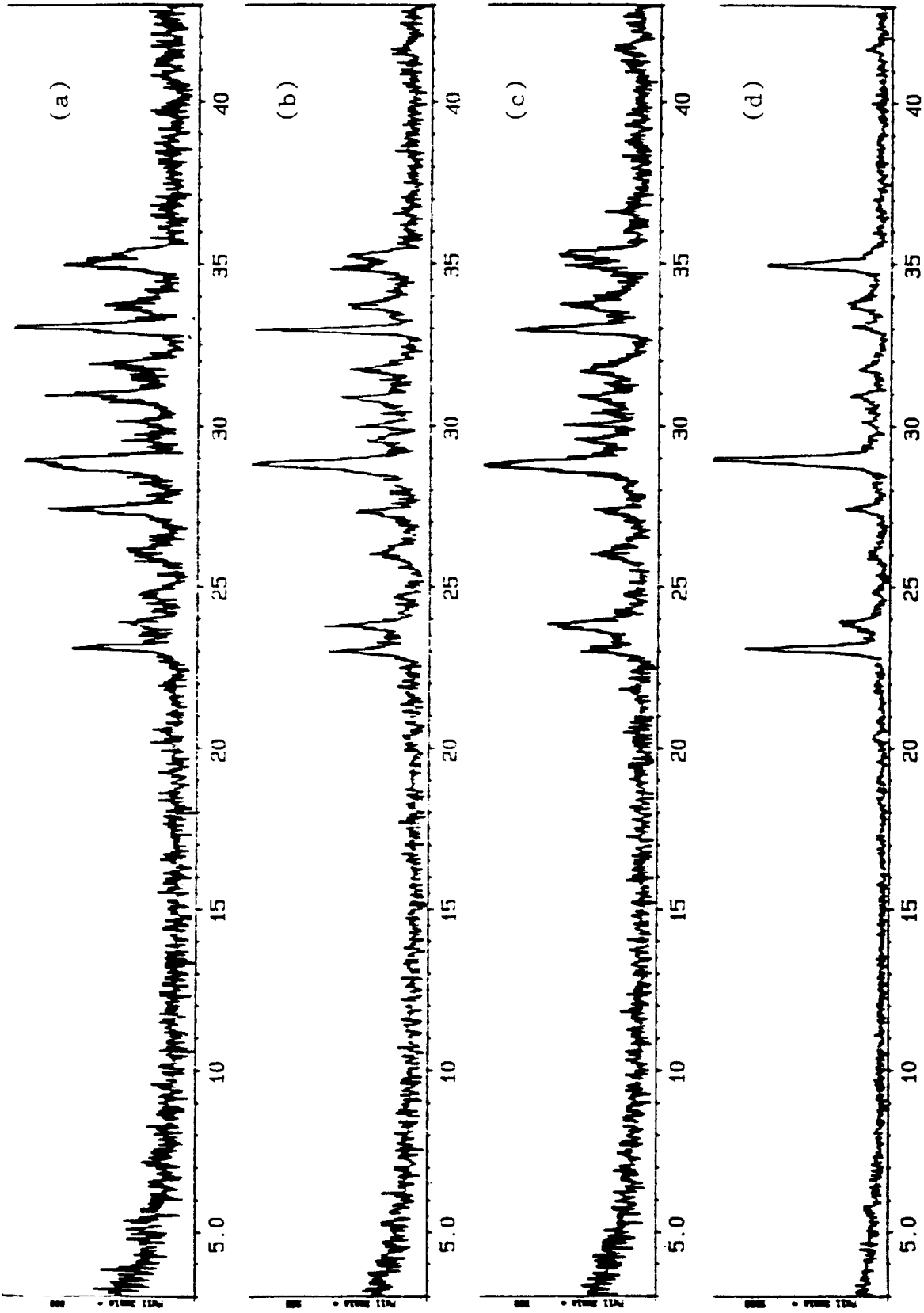
Figure 2.
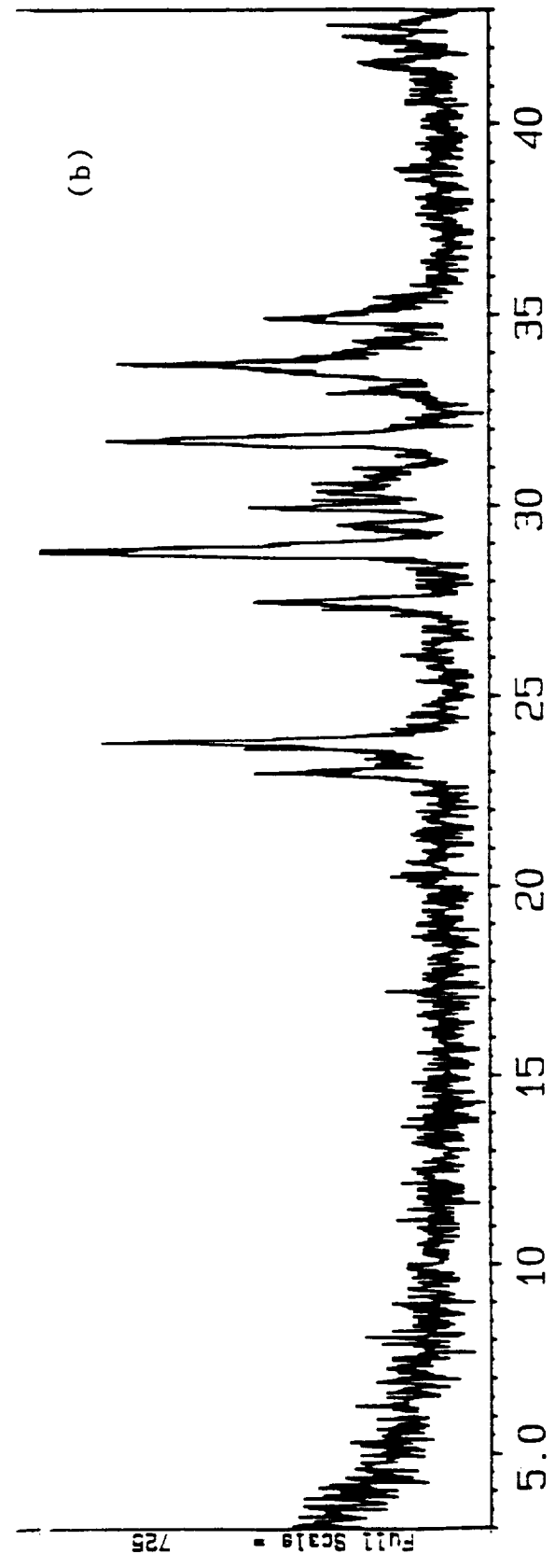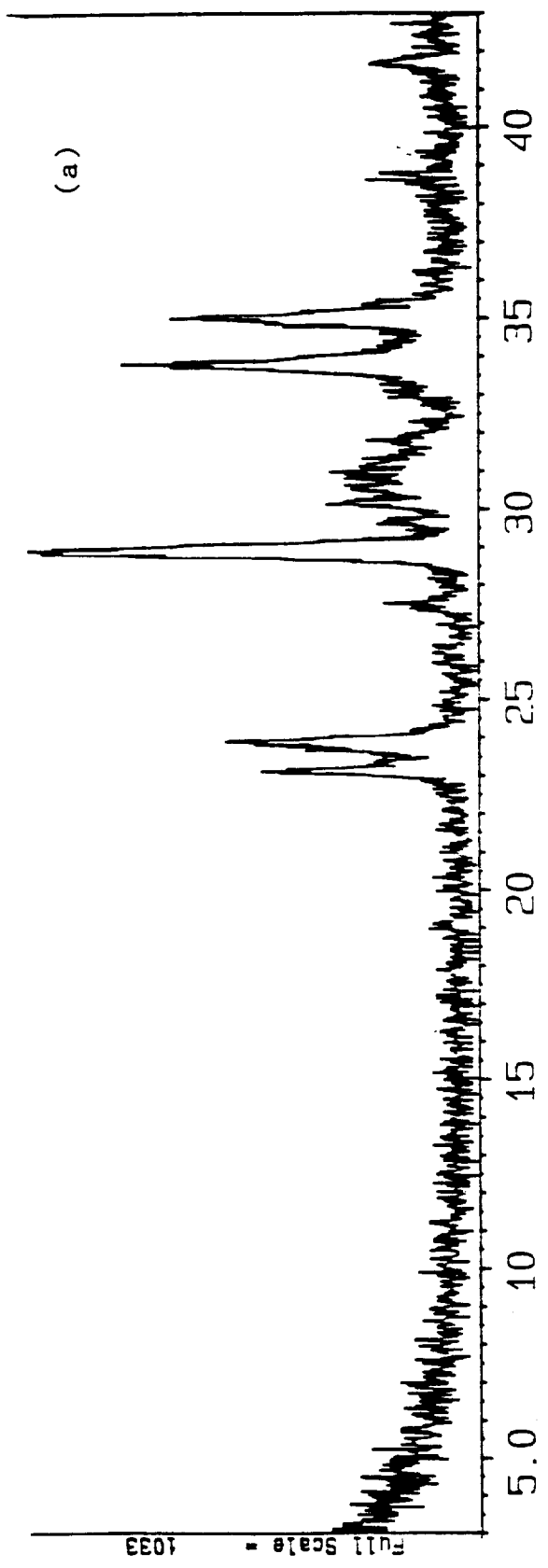
Figure 3.

Figure 4.

Figure 5.

(a)

Temperature (K)

Resistance (ohms)
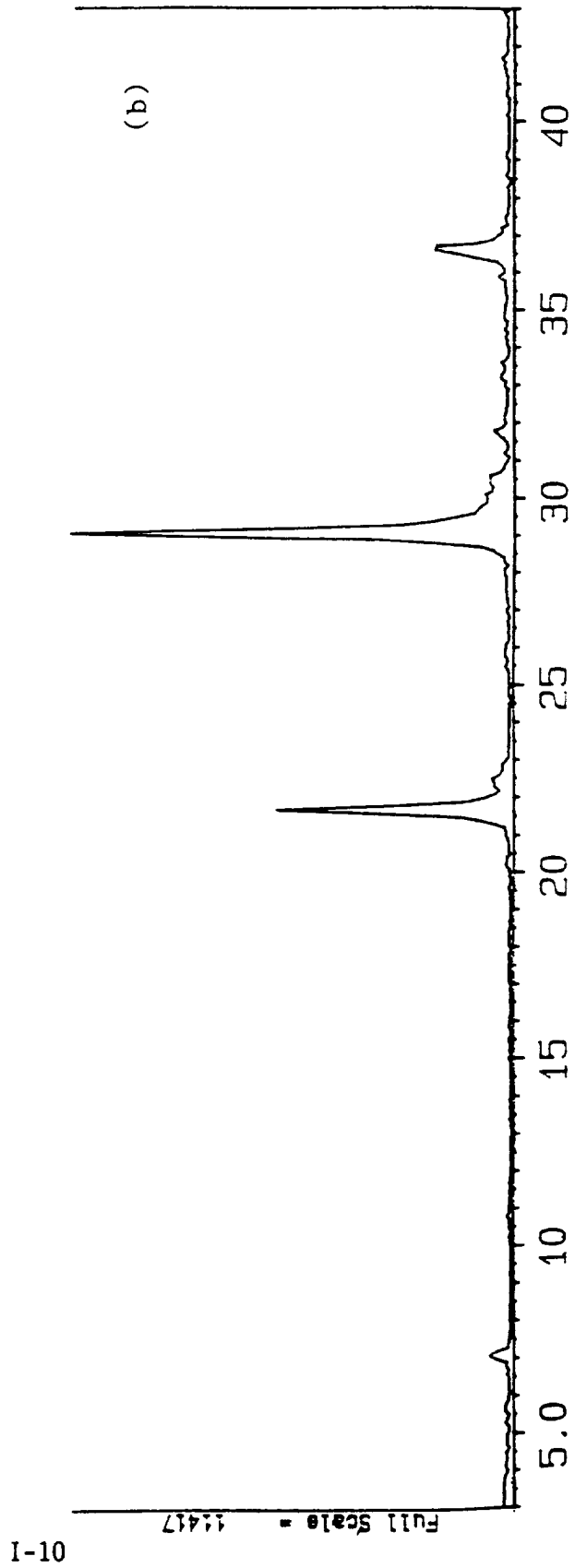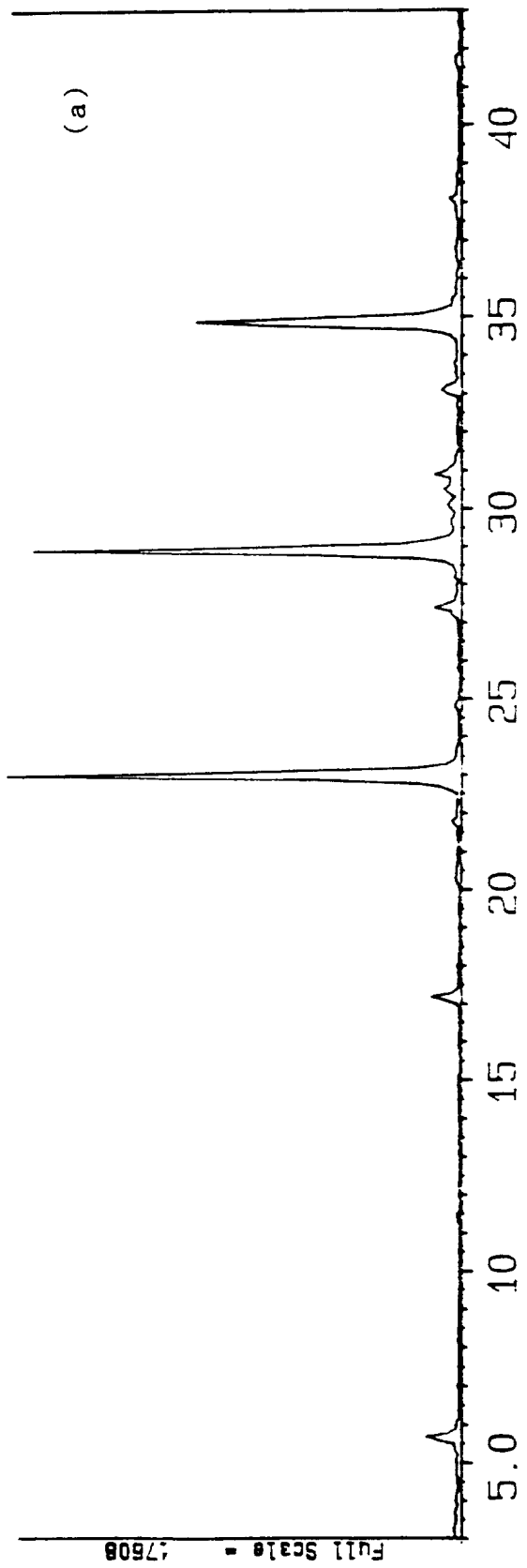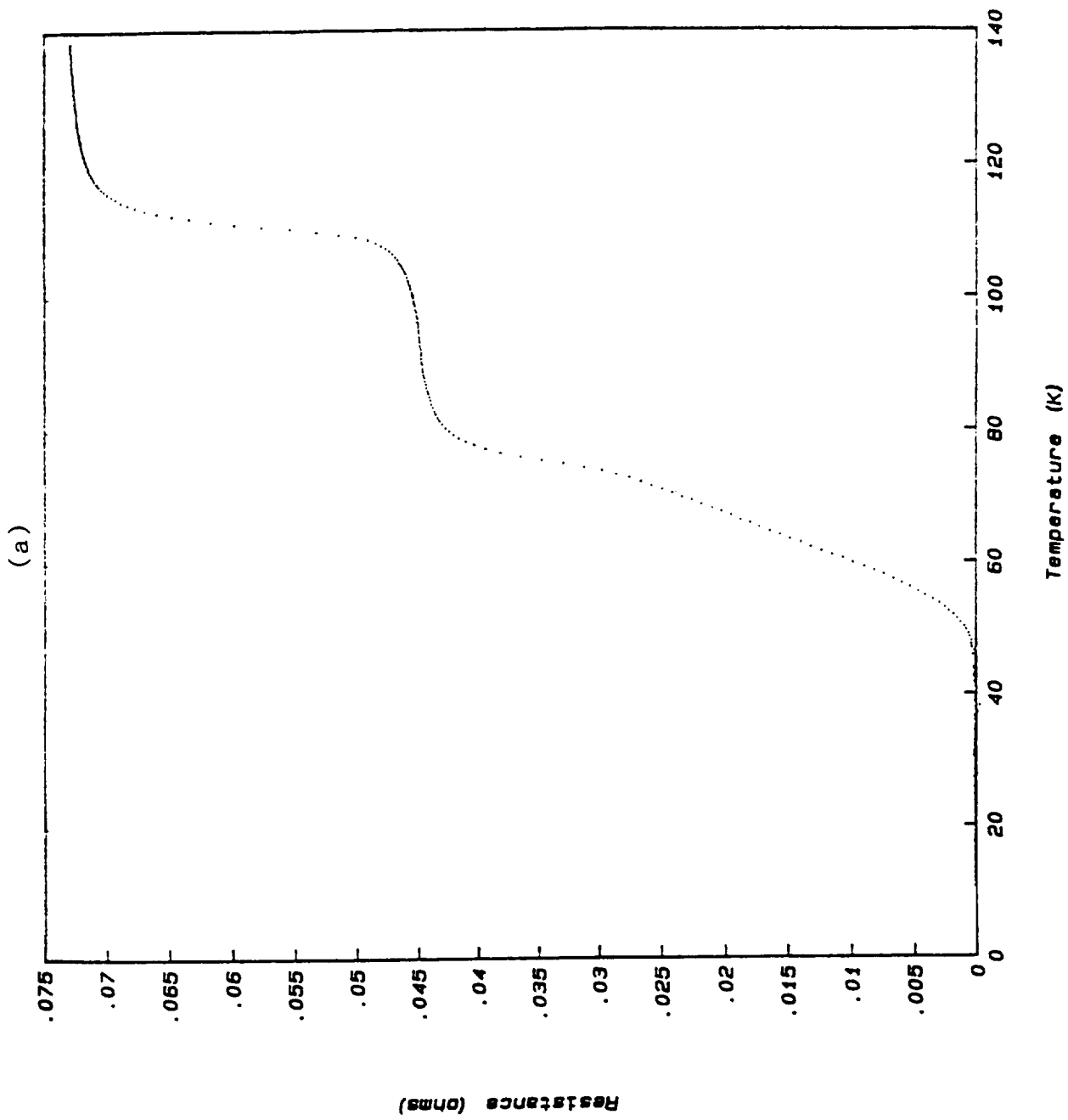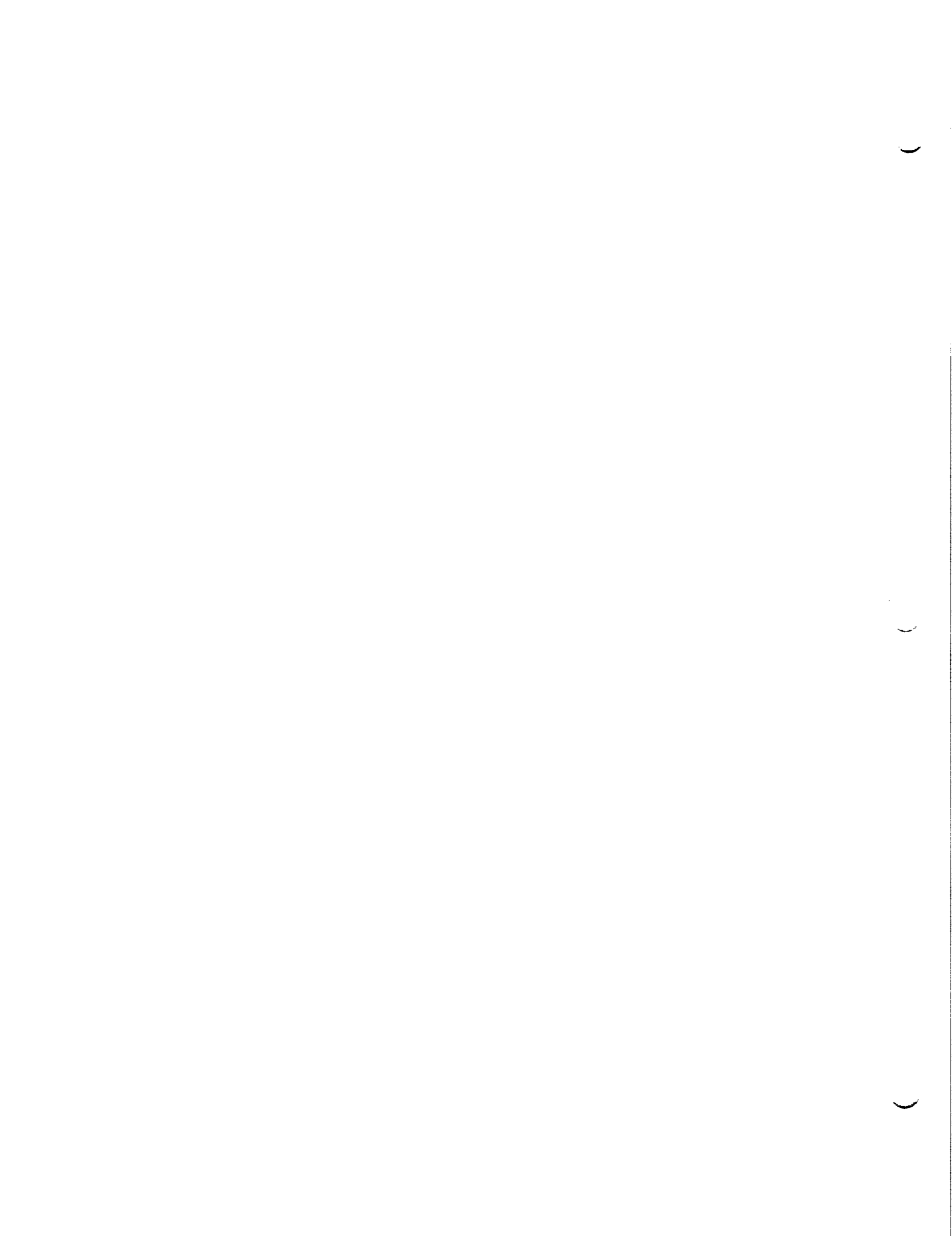
N91-18969

NASA/ASEE SUMMER FACULTY FELLOWSHIP PROGRAM

MARSHALL SPACE FLIGHT CENTER
THE UNIVERSITY OF ALABAMA

BIAS AND UNCERTAINTY IN THE ABSORPTION EMISSION

MEASUREMENT OF ATOMIC SODIUM DENSITY IN THE SSME EXIT PLANE

Prepared By: Leslie E. Bauman

Academic Rank: Associate Professor and
                                Senior Research Scientist

University and   Mississippi State University
Departments: Physics & Astronomy and
                                Diagnostic Instrumentation
                                   and Analysis Laboratory

NASA/MSFC:
        Laboratory: Propulsion
        Division: Propulsion Systems
        Branch: Performance Analysis

MSFC Colleague: Dr. Charles F. Schafer

Contract No: NGT-01-002-099
                                The University of Alabama
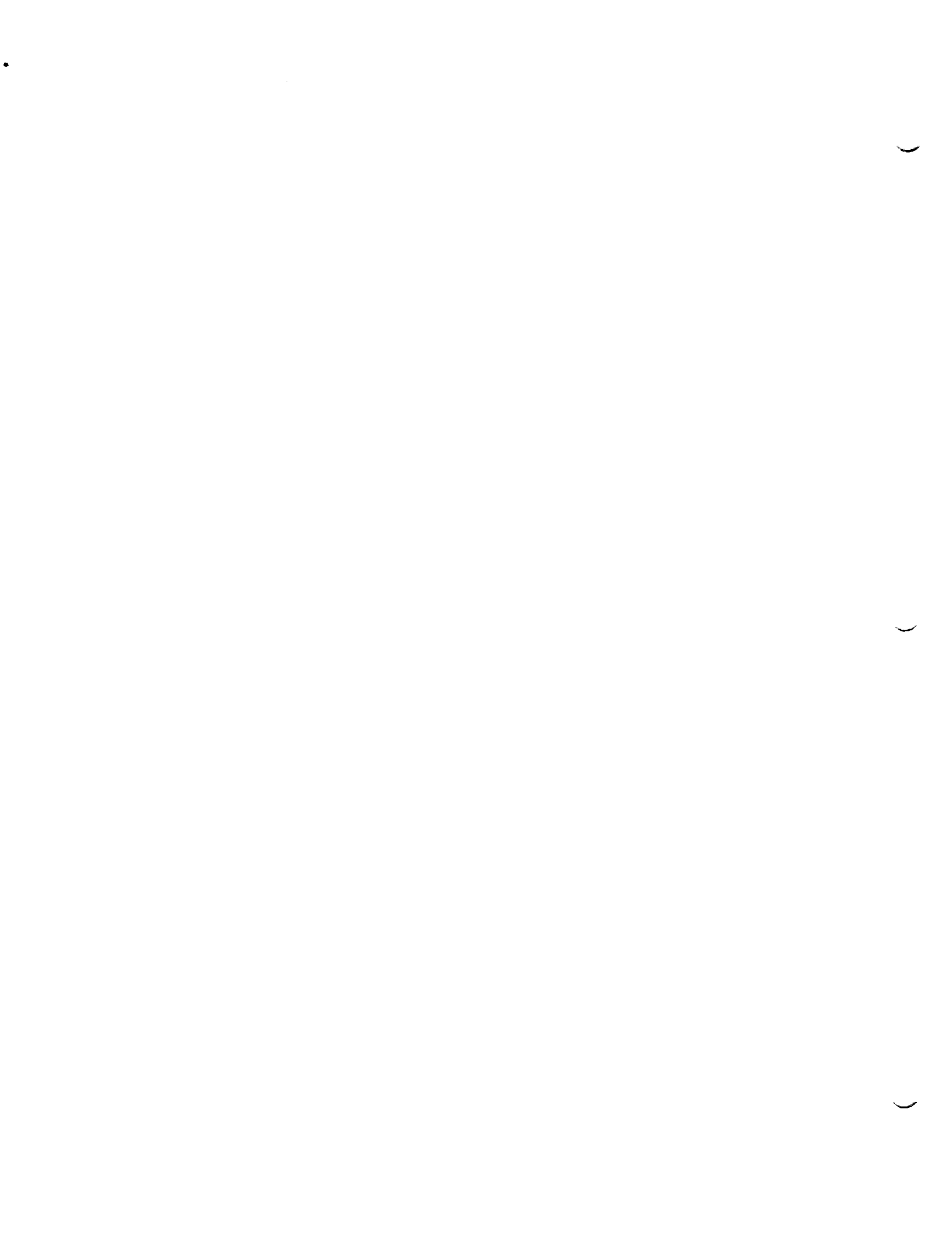
BIAS AND UNCERTAINTY IN THE ABSORPTION EMISSION MEASUREMENT OF ATOMIC SODIUM DENSITY IN THE SSME EXIT PLANE

Leslie E. Bauman*

INTRODUCTION

The measurement of atomic sodium concentration in the TTB 019 firing of April 1990 is significant in that it represents the first measurement of density at the exit plane of the space shuttle main engine (SSME).[1] The knowledge of the sodium density, combined with the certainty that the exit plane of the plume is optically thin at the sodium D-line wavelengths, provides essential information for evaluation of diagnostic techniques using sodium atoms, such as resonant Doppler velocimetry[2] for temperature, pressure, and velocity through high resolution fluorescent lineshape analysis.

The technique used for the sodium atom line transmission (SALT) measurements is that of resonant absorption emission using a hollow cathode lamp as the reference source. The lamp provides narrow band sodium D-line emission as well as nearby neon lines for reference measurements. The reference is essential to account for such effects as fluctuations in the source emission, transmission losses through beamsteering or fog in the path, etc. The detection system is a polychromator, which separates the neon and sodium lines but spectrally integrates the lines.

The SALT measurements were reported at the 1990 Advanced Earth to Orbit Propulsion Conference and are summarized here for clarity. Pre- and post-firing of the engine the reference intensities of the sodium and neon lines were measured; these signals (corrected for background), $I_{Na,0}$ and $I_{Ne,0}$, were stable with a signal-to-noise (S/N) ratio of 600 to 1. During the test, measures were made of the transmitted signals, $I_{Na,t}$ and $I_{Ne,t}$, as well as the lamp-off emission/background signals, $B_{Na,t}$ and $B_{Ne,t}$ with an effective time resolution of 1 second. The transmission, T, is found then as

$$T = \frac{I_{Ne,0}}{I_{Na,0}} \frac{I_{Na,t} - B_{Na,t}}{I_{Ne,t} - B_{Ne,t}} \ . \tag{1}$$

Through the use of TDK predictions of temperature and density for the flight engine case and radiative transfer calculations, this line-of-sight, spectrally integrated transmission indicates a sodium atom concentration, i.e. mole fraction, of 0.91e-10. The calculation does assume a sodium constant mole fraction across the plume and since the sodium is present in the cryogenic fuel, the assumption of uniform distribution across the plume seems well founded.

But tied into the calculation are also assumptions and measurement uncertainties that are the subject of this paper. Because of the narrow shape of the source emission, the uncertainties in the absorption profile could introduce considerable bias in the measurement. The following were investigated as part of this work: (1) the inclusion of hyperfine splitting[3] of the D-lines in the calculation, (2) the use of the flight engine predictions of plume temperature and density versus those for the large throat engine (The engine for the TTB 019 firing was actually the large throat engine but the large throat TDK data was not available and the flight engine data was used.), (3) the assumption of a

---

*Mailing Address: P.O. Box 5167, Mississippi State, MS 39762.
Phone: (601) 325-2806. Fax: (601) 325-8465.

Gaussian, i.e. Doppler, distribution for the source radiance with a temperature of 400 K, (4) the use atomic collisional shift and width values from the work by Jongerius,[4] and (5) a Doppler shift from a 7Å outward velocity vector at the plume edge.

Also included in the study was the bias introduced by an uncertainty in the measurement of the D1/D2 line ratio in the source. When this ratio was observed to deviate from that predicted by equilibrium statistics, additional complexity was added to the system in the form of an optical multi-channel analyzer in order to track the ratio between the source sodium D1 and D2 line emissions.

CALCULATIONS

Numeric Calculations. A computer program was written to perform the numerical integration of the radiative transfer equation to solve for the spectral plume radiance, B_ν, plume optical depth, τ_ν, and source radiance, I_ν, given inputs of the plume temperature, water and hydrogen densities, and velocity as functions of the beam path across the plume. The absorption line was modeled as a Voigt function[5] using the calculations of Humlicek.[6] This function which arises from a classical impact theory of line broadening has its limitations but is an accurate model for the regime of these measurements. The assumption used by Dobson and Eskridge (DE) to model the source radiance as a Gaussian function, i.e. including Doppler broadening only, was retained. This is valid only since the plume is optically thin; if the absorption were stronger the wings of the source function would become important and a Voigt model including the natural width of the line should be used. (Ideally, when appropriate equipment is available, the spectrum of the source should be measured.) The calculation includes overlap of the D1 and D2 lines as well as the hyperfine lines. The transmission is then found from spectral integrations over the D1 and D2 line regions where the source function is significant,

$$
T = \frac{\int_{D1} I_\nu \exp(-\tau_\nu)d\nu + F \int_{D2} I_\nu \exp(-\tau_\nu)d\nu}{\int_{D1} I_\nu \, d\nu + F \int_{D2} I_\nu \, d\nu} \quad , \tag{2}
$$

where F is the measured deviation from equilibrium for the D1 to D2 lamp emission ratio. The negative natural logarithm of the transmission is an effective optical depth for the combined lines, τ_{Na}, and is linear with the sodium mole fraction at the low densities of the SSME plume, so that the desired sodium mole fraction, [Na], can be found from the measured transmission through the constant C found from numerical calculations as [Na] = C τ_{Na}. The biases and uncertainties in the measurement were studied by solving for the constant C for a range of sodium concentrations.

Approximate Calculation. In the limit that the lamp lineshape is infinitely narrow and collisional or Doppler induced lineshifts are negligible, one can calculate the effective optical depth as

$$
\tau_{D1\ or\ D2} \approx 3.28e\text{-}10\ [Na]\ f_{D1\ or\ D2} \int_{plume} N\ T^{-\frac{1}{2}}\,dx\ , \tag{4}
$$

where f is the dimensionless oscillator strength, N is the plume density in molecules/cm^3, and T is the plume temperature in Kelvin. While this approximation may not provide an accurate absolute measure of the sodium concentration, it allows inspection of the bias from the use of TDK predictions in the calculations.

RESULTS

As a test case, numerical calculations were performed on the flight engine data with the same assumptions as used by DE, i.e. no hyperfine splitting, no Doppler shift and the same Jongerius shift and width values. A sodium concentration of 0.88e-10 was determined (C = 1.45e-9). This compares to the results of DE of [Na] = 0.91e-10. As the calculations were performed with different Voigt schemes and different numerical integration schemes, the agreement seemed acceptable.

Hyperfine Splitting. There is a significant error from neglecting hyperfine splitting. For the flight engine data, the addition of hyperfine splitting to the model gives C = 1.75e-9, an increase of 20%.

Large Throat. The integral of the plume density divided by the square root of temperature is 18% higher for the large throat predictions compared to those for the flight engine and a consequent decrease in the calculated sodium concentration was expected. A value of 0.88e-10 was determined (C = 1.44e-9), serendipitously canceling the effect of inclusion of hyperfine splitting -- the bias from using the TDK predictions for the flight engine rather than the large throat engine is about 20%.

Source Line Width. Varying the source temperature by æ100K changes the Doppler width of the sodium lines by approximately æ12%. The bias in the calculated sodium concentration was only 5% for the entire range.

Doppler Shift. With only the suggestion that the plume velocity vector is 7° outward at the plume edge, it was necessary to construct a model for the outward velocity component. I chose a model that tapered this outward component down to zero at the position of the shock through a square root relationship to the proportional distance out from the shock. The central region of the plume shows a negligible line shift, the far region has a small red shift and the near region has a small blue shift. The net effect is to slightly lower the absorption at line center leading to an increased value for the sodium concentration. For the chosen model the sodium concentration was found to be 0.90e-10, a 2% bias. If an outward velocity is present at the measurement position, ignoring the Doppler shift will bias the measurements to a lower concentration than actual.

Collisional Shift and Width. Using the error limits given by Jongerius[4] variations in the width gave a 5% variation in the calculated sodium concentration. Variations in the line shifts did not measurably affect the calculations.

Lamp D1 to D2 Ratio. Varying this measurement parameter over 10% leads to a variation in sodium concentration of 3%.

Combining these last four uncertainties in a square root of the sum of the squares fashion gives a combined uncertainty of less than 10% for the sodium concentration. The hyperfine splitting can easily be kept in the model at the expense of computing time so this bias should not be included in the combination and hopefully the TDK calculations are accurate enough to not add appreciable error. This ±10% uncertainty is small compared to the measurement uncertainty of nearly ±40%.

CONCLUSIONS AND SUGGESTIONS

One question that I had about the SALT measurements was that since the integrated line strengths are well known, why not use a broadband source where there would be no bias due to lack of information about lineshapes or shifts? The answer is that compared to the

precision of the SALT measurements, the biases introduced by uncertainties in lineshapes and shifts are not important. And, the wavelength regions would need to be narrowly set on the sodium lines or small uncertainties in the measured intensities would amplifying the uncertainty in the measured sodium concentration. In my estimation, the SALT technique as applied to the TTB is a good one.

I do however have two suggestions for improving the measurement precision. The first involves the data collection scheme and in particular time averaging. A useful rule of thumb for experimentalists is to average the most fundamental property. In the case of the SALT measurements, the fundamental property is the optical depth, directly proportional to the sodium concentration, and because of the optical thinness of the plume very nearly one minus the transmission. So ideally, one should time-average the transmission measurement, i.e. the sodium to neon intensity ratio, rather than time averaging the intensities as is done with the SALT data collection.

In a simple look at the fluctuations, if the important fluctuations are those of the sodium optical depth and broadband transmission and source effects, lumped together as A, then

$$\langle I_{Ne,t}\rangle_t = (\bar{A} \pm \delta A)\, I_{Ne,0} \tag{5}$$

and

$$\langle I_{Na,t}\rangle_t = (\bar{A} \pm \delta A) I_{Na,0} \exp[-(\bar{\tau} \pm \delta\tau)] . \tag{6}$$

Then ratioing the time-averaged signals will give

$$T_{avg} \approx (1 \pm 2\,\delta A/\bar{A}) \exp[-(\bar{\tau} \pm \delta\tau)] , \tag{7}$$

essentially doubling the uncertainty due to the time varying broadband transmission factor. On the other hand, if the instrument time response is fast enough to resolve the fluctuations, then averaging the ratio of the sodium and neon signals will remove this uncertainty.

My other suggestion is to double pass the SALT beam, doubling the measured optical depth. If this can be done without a concommitent increase in the measured transmission uncertainty, then the uncertainty in the sodium concentration will be halved. The uncertainty would be expected to increase because of beam transmission effects, but I would not expect it to double and the uncertainty would need to double in order to cancel the benefits of the double pass operation. The adoption of both of these suggestions will, I believe, lead to a better measurement of the SSME plume atomic sodium density.

REFERENCES
1. Dobson, C.C., Eskridge, R.H., "Resonant Absorption and Emission Measurements of Atomic Sodium in the SSME Exit Plane," Advanced Earth to Orbit Propulsion Conference, Huntsville, AL, 1990.
2. Zimmermann, M., and Miles, R.B., Appl. Phys. Lett., 37, 885, 1981.
3. Fairbank Jr., W.M., H nsch, T.W., and Schawlow, A.L., J. Opt. Soc. Amer., 65, 199, 1975.
4. Jongerius, M.J., Van Bergen, A.R.D., Hollander, Tj., and Alkemade, C. Th. J., J. Quant. Spectrosc. Radiat. Transfer, 25, 1, 1981.
5. Mitchell, A.C.G., Zemansky, M.W., Resonance Radiation and Excited Atoms, Cambridge Press, London, 1971.
6. Humlicek, J., J. Quant. Spectrosc. Radiat. Transfer, 27, 437, 1982.

1990

NASA/ASEE SUMMER FACULTY FELLOWSHIP PROGRAM

MARSHALL SPACE FLIGHT CENTER
THE UNIVERSITY OF ALABAMA

UPDATING AND AUGMENTING
NASA SPACELINK ELECTRONIC INFORMATION SYSTEM

Prepared By: Jean A. Blake

Academic Rank: Professor

University and Department   Alabama A & M University
                                      Mathematics

NASA/MSFC

        Division: Public Affairs Office

        Branch: Public Services & Education

NASA Colleague: Jeffrey S. Ehmen

Date: August 1, 1990

Contract No: NGT-01-002-099
                                      The University of Alabama

ACKNOWLEDGEMENT

My deepest gratitude is hereby extended to the NASA/ASEE
Summer Faculty Fellowship Program and its directors for the
very rewarding experience afforded me this summer. I pay
special tribute to Dr. Frank Six, and Dr. Mike Freeman, the
directors of this program. I especially thank my NASA
colleagues, Jeff Ehmen, Bill Anderson, and Alan Cunningham
who facilitated my summer's experience updating and
augmenting the information in the Spacelink Electronic
Information System.

INFORMATION SUMMARY

NASA Spacelink is a collection of NASA information and
educational materials stored on a computer at the Marshall
Space Flight Center in Huntsville, Alabama. It is provided
by the NASA Educational Affairs Division and is operated by
the Public Services and Education Branch of the Marshall
Center Public Affairs Office.

It is designed to communicate with a wide variety of
computers and modems, especially those most commonly found
in classrooms and homes. It was made available to the
public in February, 1988. The system may be accessed by
educators and the public over regular telephone lines.
NASA Spacelink is free except for the cost of long distance
calls.

The material prepared for Spacelink has found widespread
use by teachers and others across the nation, and is being
used to stimulate students in their quest for excellence.
The following is a partial summary of Spacelink's usage.

In February, 1990 Spacelink had almost 10,000 registered
callers. (Inactive callers drop out after 90 days.) Table
1 shows a positive growth of about 325 callers per month
(school months are higher, summer months are lower).

1990	Growth in Callers
March	442
April	375
May	202
June	282
July	170

Table 1

Table 2 gives a summary of the registered callers.

NASA/SPACELINK REGISTERED CALLER SUMMARY
30-Jul-90   07:52:47

Active Callers	05253
Teachers	00824
Students	01206
Journalists	00147
Other	02751
No category	00325

Table 2

The accompanying four charts -- Calls per Hour, Calls per
Month, Files Accessed per Month, and NASA/Spacelink Usage
Statistics -- give a partial summary of Spacelink's usage,
testifying to the fact that Spacelink is a very worthwhile
NASA investment.

NASA/SPACELINK

Calls per Hour (last 33,926 calls)
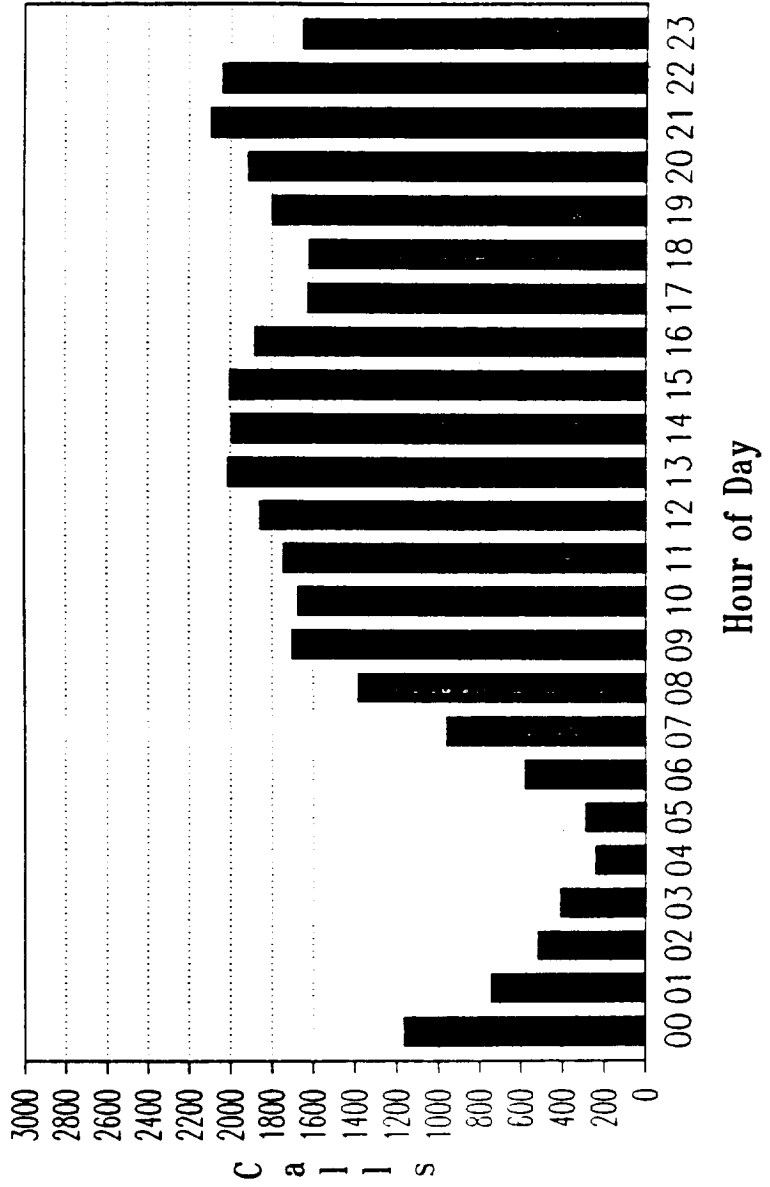
NASA/SPACELINK
Calls per Month
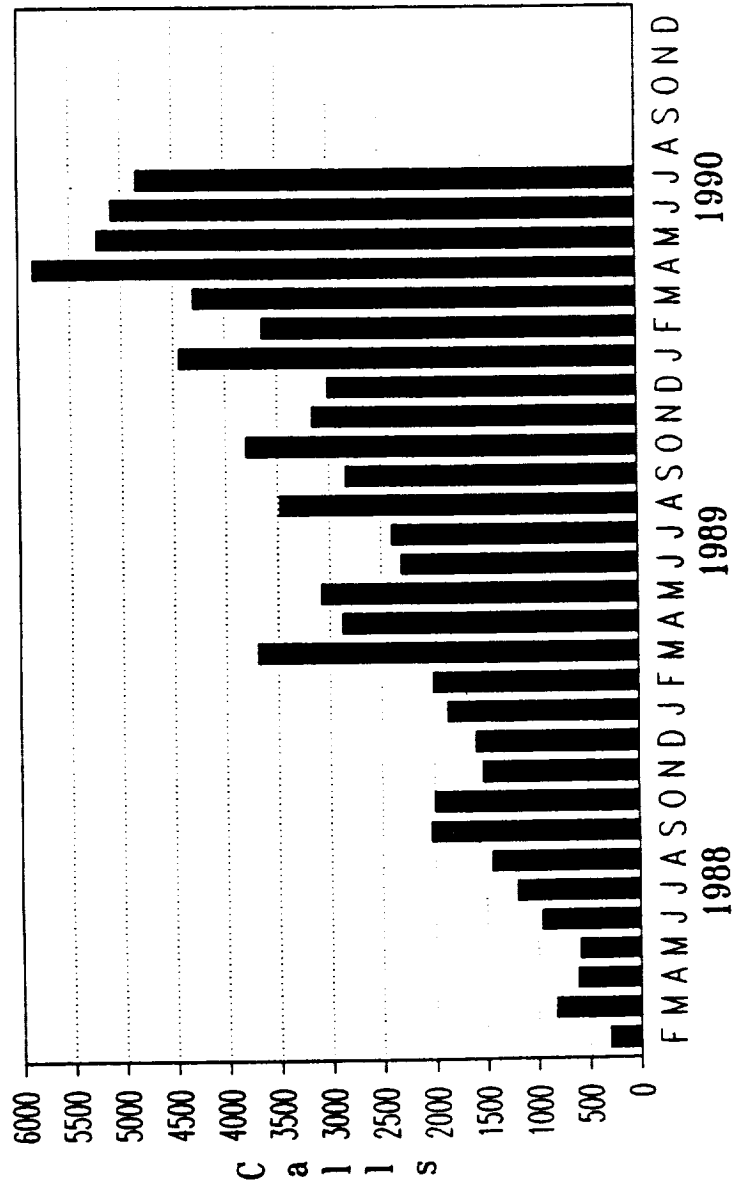
NASA/SPACELINK

Files Accessed per Month
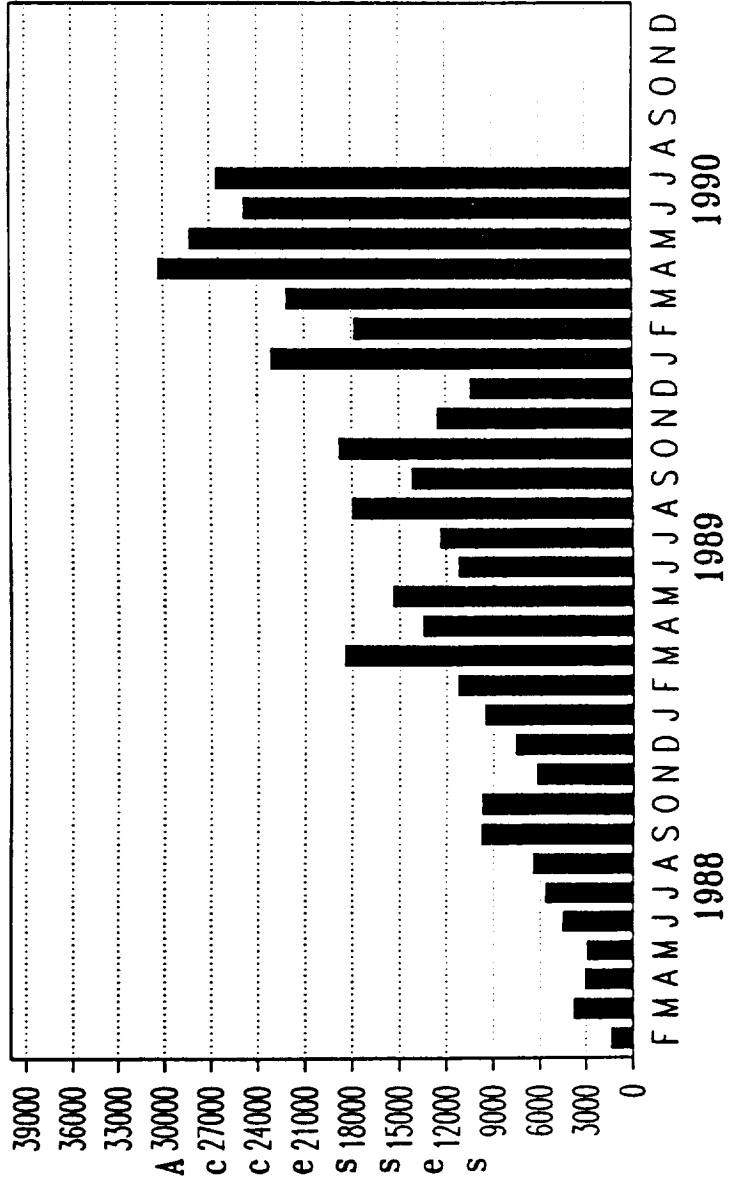
NASA/Spacelink Usage Statistics

During an average school year month (April, 1990)

- 2301 callers made a total of 5929 connections totalling 1088 hours
- Calls from teachers were 17% of connection hours for the month
- Callers made an average of 2 calls per month
- Each connection averaged 12.27 minutes
- Each caller averaged 28 minutes per month
- 2301 callers made a total of 26,399 document accesses
- Each caller accessed an average of 11 documents each month or five documents per call

Caller population (April, 1990)

Total of 4805 registered callers

- 961 Teachers
- 861 Students
- 134 Journalists
- 2552 'Other'
- 297 Gave no information

1990

NASA/ASEE SUMMER FACULTY FELLOWSHIP PROGRAM

MARSHALL SPACE FLIGHT CENTER
THE UNIVERSITY OF ALABAMA

LIGHTNING OBSERVATIONS FROM SPACE SHUTTLE

Prepared By: William L. Boeck

Academic Rank: Professor

University and   Niagara University
Department: Computer   and   Information
                                  Sciences

NASA/MSFC:
     Laboratory: Space Science
     Division: Earth Science and Application
     Branch: Remote Sensing

MSFC Colleague: Dr. Richard Blakeslee

Contract No: NGT-01-002-099
                                  The University of Alabama
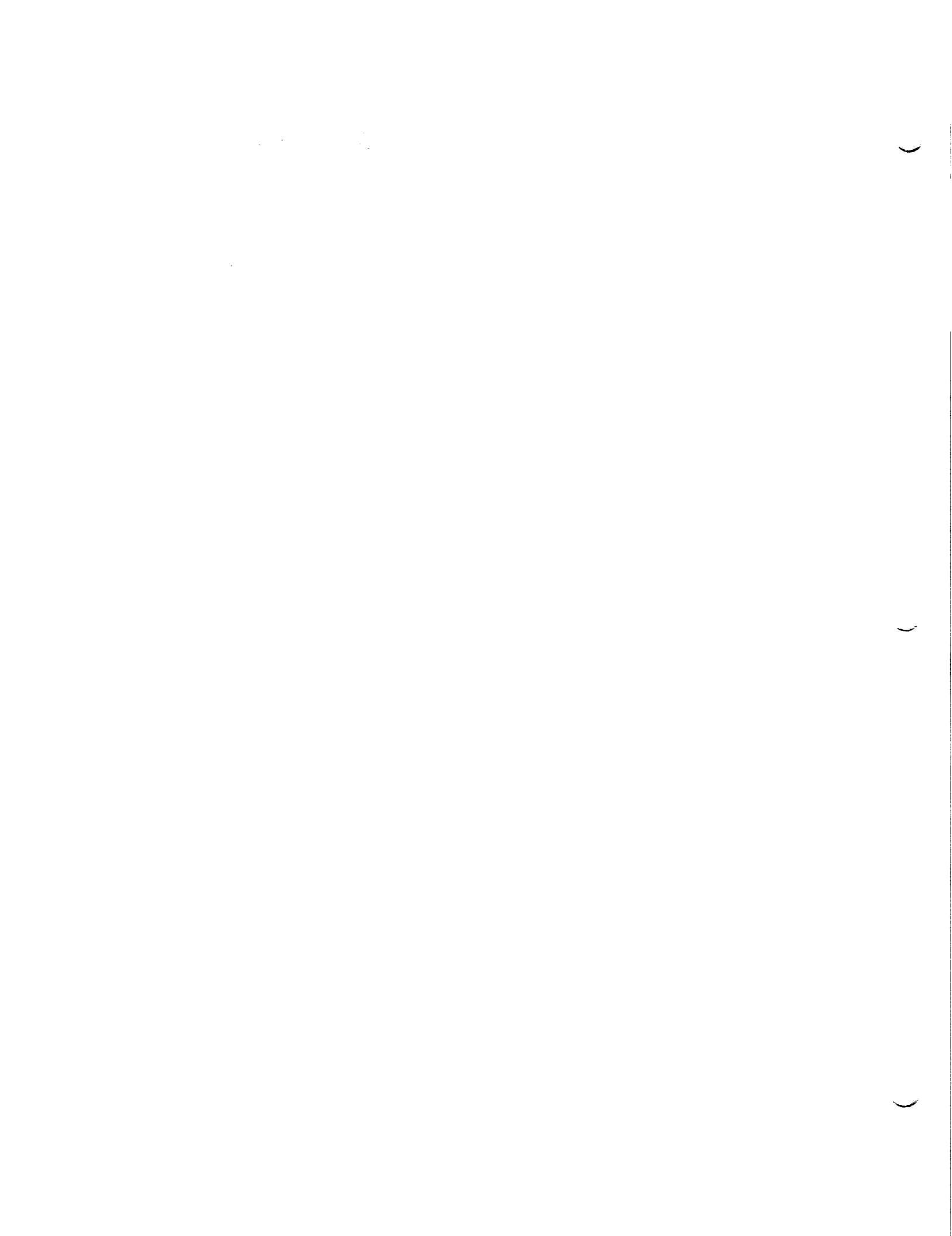
The experimental program of the Earth Sciences and Applications Division at NASA/MSFC includes development of the Lightning Imaging Sensor (LIS) for the NOAA Earth Observing System (EOS) Polar Platform. The objective is to fly a calibrated optical lightning activity imaging sensor to acquire and investigate the global distribution and variability of total lightning. This experiment is expected to fly on a sun synchronous polar orbiting platform in 1998. The lightning detector is a staring sensor with a 10 km spatial and 1 ms temporal resolution. A real time processor will identify sudden increases in brightness caused by lightning flashes. The processor will also account for the apparent movement within the field of view. The data stream relayed to the earth will include lightning event intensity, time and pixel locations.

The research plan is to use existing lightning information to generate simulated data for the LIS experiment. Navigation algorithms were used to transform pixel locations to latitude and longitude values. The simulated data would then be used to test and develop algorithms for the analysis of LIS data.

Individual frames of video imagery obtained from Space Shuttle missions provide the raw data for the simulation. Individual video frames were digitized to get the pixel locations of lightning flashes. The pixel locations will be used to locate the geographic position of the event. Because of a lack of detailed knowledge of camera orientation with respect to Space Shuttle, video scenes that contain identifiable city lights were chosen for analysis.

This project was done in cooperation with members of the Remote Sensing Branch, in particular Dr. Richard Blakeslee of the Earth Observing Team and Mr. O. Vaughan of the Sensor Technology Team. This summer the LIS scientific team was preparing for the CDCR (Conceptual Design and Cost Review) in August. I assisted with the conceptual design of the algorithms and the descriptions of the three levels of data products. I also drafted portions of the Data Management Plan for LIS.

The majority of my time was spent working on the analysis of lightning video tapes obtained by the Mesoscale Lightning Experiment. There was a dramatic improvement in the quality of the video as operational procedures were worked out. The handheld camera video is too shaky and the camera axis too undefined to quantify the discharges seen on the video. When arrangements were made for the PI to be at the Mission Control Center and advise the ground based camera controllers of where and when there would be a target of opportunity, the video from the payload bay cameras was much more stable. A particularly good set of data was obtained on the eighteenth of January 1990 when the Mission STS-32 passed over Florida during the night.

The process of locating targets on earth is a form of navigation. In this case, the location of the spacecraft is known and the target location is desired. The direction of the

camera axis when pointing at a target on earth can be determined from two angular measurements. The first angle is the tilt of the camera from a vertical nadir pointing orientation. The apparent position of the horizon can be used to find the tilt, provided the focal length of the camera is known. The second angle is the rotation of the camera axis about the vertical axis. This angle can be determined by a sighting of a known geographic location crossing the vertical center line of the image at a known time. The angle sought is then the angle between the ground trace of the orbit and the great circle path from the subsatellite point to the known location. Unfortunately there is no readout of the focal length setting of the video camera zoom lens. This value must be estimated from the contents of the image.

The lightning locations determined from satellite imagery identify the location of the illuminated cloud volume. The lightning channel is obscured by many optical thicknesses of intervening cloud. If the event is a cloud to ground stroke, the ground strike could be anywhere beneath the cloud.

The case study presented is based on two and one half minutes of video obtained on a pass over Florida. The camera is pointing toward the North West and gradually views the Southern United States from Texas to the Georgia coast. The weather analysis for that morning shows a single cold front extending from Texas to Tennessee. The GEOS imagery shows most of the South has clear skies with a line of thunderstorms in Texas, Louisiana, and Arkansas. A ground based lightning location network and a VLF radio transmission network were operational at that time.

The following analysis is based on data provided by the Mesoscale Lightning Experiment, O. H. Vaughan of NASA/MSFC, Principal Investigator, with B. Vonnegut of SUNY, M. Brook of NMIMT, and R. Blakeslee of NASA/MSFC as Co-investigators. The lightning location data was provided by EPRI and R. Henderson and R. Pyle of SUNY. The VLF transmission data were provided by U. Inan and D. Carpenter of Stanford.

The data in the table is divided into three sections. The left section of four columns is data derived from an analysis of the video. The first and second columns are the GMT for the 18th of January 1990 seven hours and twenty to twenty three minutes. The horizontal lines mark off the times when an optical flash was observed. At each of the forty times given, an optical flash corresponding to a cloud to cloud flash or a cloud to ground flash is observed.

The central section of four columns is obtained from a lightning location network. The columns are the GMT second for a cloud to ground flash, the latitude and longitude of the ground stroke and the magnitude of the current. Seven events are identified as the times of cloud to ground flashes. The remainder of the optically detected flashes are identified as cloud to cloud. In four cases the video image has been analyzed to estimate the position. The estimated locations are in satisfactory agreement with the LLP locations. In each case the optical locations of city lights were computed. The city location errors were less than 100 km. The optical locations are near the center of the illuminated cloud which may or may not be near the

ground stroke. The last flash observed is a positive flash which is located very near to the horizon. The large longitude error is due to the lack of perspective at the limb of the earth. This flash has a vertical illuminated column arising from the cloud top. Further work is being done to resolve the apparent time jitter between the two sets of measurements.

The right section of the table reports a summary of VLF propagation measurements on a path from Nebraska to Puerto Rico. There is a one to one correspondence between negative cloud to ground flashes and transmission decreases at 48.5 kHz. There is an apparent exception a 7:21:25. This is the smallest of the flashes and the decrease may be obscured by noise. A optical location will be determined on the nearest event in time to determine whether it is the same event or if this flash was not detected optically. Most of the cloud to cloud flashes did not produce a signal on this transmission path. Note that the large positive flash did not cause a VLF transmission change.

Conclusions

A method for locating the payload bay camera axis has been developed and tested. Two measurements are need, the pixel location of the apparent horizon and a timed siting of a known location passing the principal line of the image.

Individual video frames have been navigated and lightning illuminated clouds have been located on the map. Satisfactory agreement in location has been achieved for cities and LLP lightning locations.

Ground truth measurements have been compared to satellite observations.

A vertical lightning event has been identified on the horizon.

VLF transmission on this particular occasion shows a strong response to negative cloud to cloud flashes.

GMT: January 18 seven hours

MIN	SEC	LAT	LONG	SEC	LAT	LONG	MAG kA	SEC COMMENT
		OPTICAL	LOCATION		LLP LOCATIONS			
				51	32.20	-93.14	-135.60	
				6	31.38	-92.05	-76	6 NEB 2% DECREASE
				25	31.62	-92.36	-92.70	25 NEB 2% DECREASE
20	54							
20	55							
20	56	32.15	-95.29					
21	0	31.61	-94.22					
21	10							
21	11	32.17	-92.13	11	32.36	-92.40	-116	11 NEB 2% DECREASE
21	15	31.55	-92.92	15	31.96	-92.71	-170.10	15 NLK 15% PULSE
21	16	31.54	-91.50	15	31.66	-92.53	-170.10	15 NEB 6% DECREASE
21	20							
21	21							
21	24			25	32.07	-95.36	-36.10	25 NLK 10% PULSE
21	27							
21	28							
21	29			29	32.62	-93.59	-98.30	29 NLK 8% PULSE
21	30			30	32.25	-93.11	-118.10	29 NEB 2% DECREASE
21	34							34 NEB 4% PULSE
21	40							41 NEB 2% PULSE
21	41							
21	45							
21	49							
21	53							
21	55							
21	58							
22	2							
22	3							
22	6							
22	9							
22	14							
22	19							
22	20							
22	23							
22	33							
22	38							
22	43							
22	49							
22	51			51	31.87	-92.77	-71.50	51 NLK PULSE
22	51			51	31.98	-92.36	-91.80	51 NEB 13% DECREAS
23	1							
23	13							
23	25							
23	27			28	32.03	-91.81	42.50	28 NLK 10% PULSE
23	27	32.09	-88.20	28	32.13	-91.10	108.50	
				31	32.13	-94.32	-263.60	31 NEB 10% DECREAS
				48	32.06	-95.39	-162.30	48 NEB 6% DECREASE

1990

NASA/ASEE Summer Faculty Fellowship Program

Marshal Space Flight Center
The University of Alabama

Navigation in Large Information Spaces
Represented as Hypertext:
A Review of the Literature

Prepared By:	Marcus Brown
Academic Rank:	Assistant Professor
University and	The University of Alabama
Department:	Computer Science
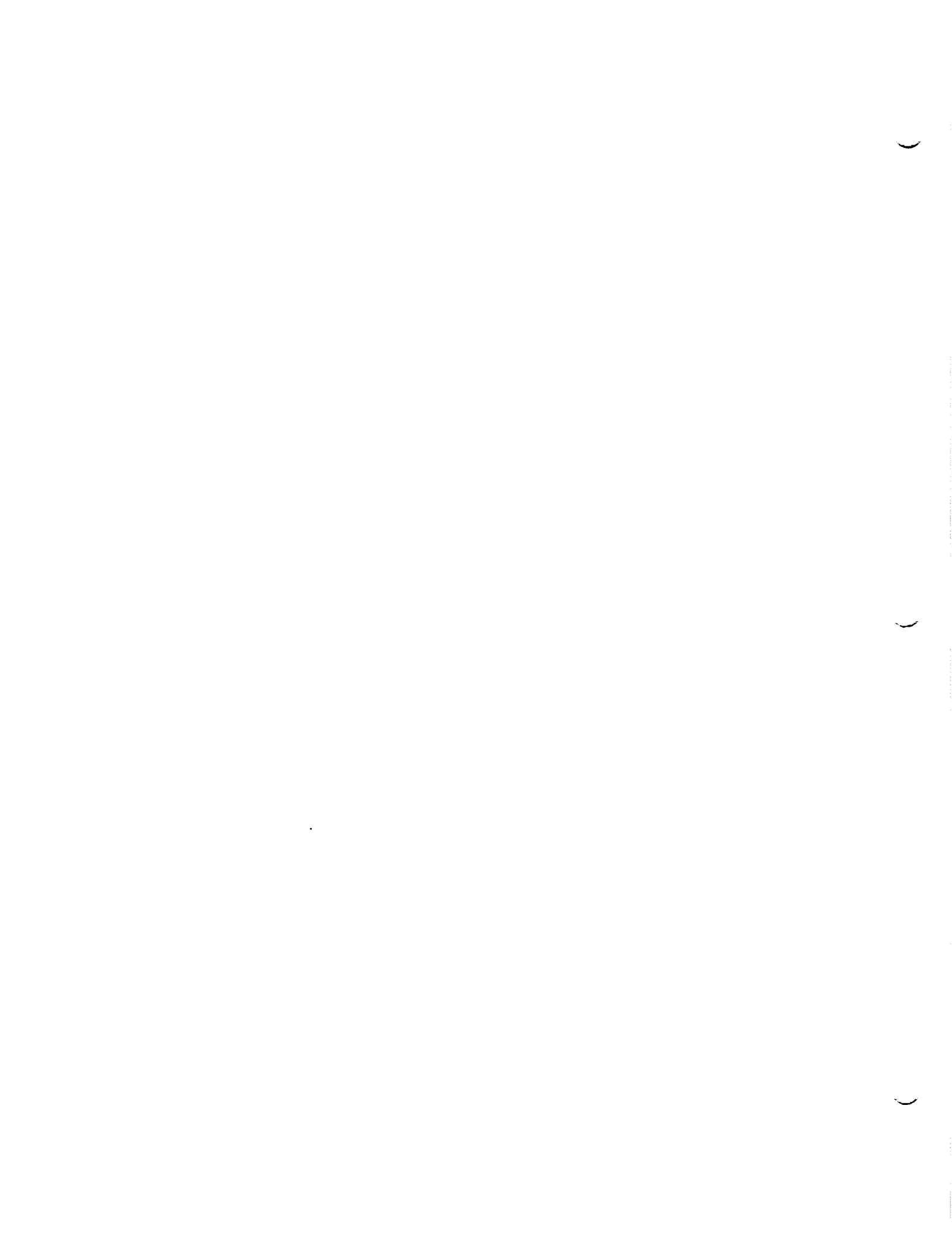
Navigation in Large Information Spaces Represented as Hypertext: A Review of the Literature

Introduction

Although Vannevar Bush first proposed a hypertext-like interface to a large body of knowledge in 1945, only in the last few years has widespread interest in hypertext and hypermedia arisen. Hypertext is usually defined as non-linear text, meaning that it consists of text nodes and links between those nodes. In some hypertext systems, the nodes may be a paragraph long, while others may have nodes which contain entire documents. The links between the nodes allow the reader to move from one node to a related node. Each node is typically linked to several other nodes, allowing the reader to move to any of them, rather than leading to a single following node like the pages of a book. Hypermedia is an extension of this concept to include not only text but also drawings, pictures, even audio and video presentations.
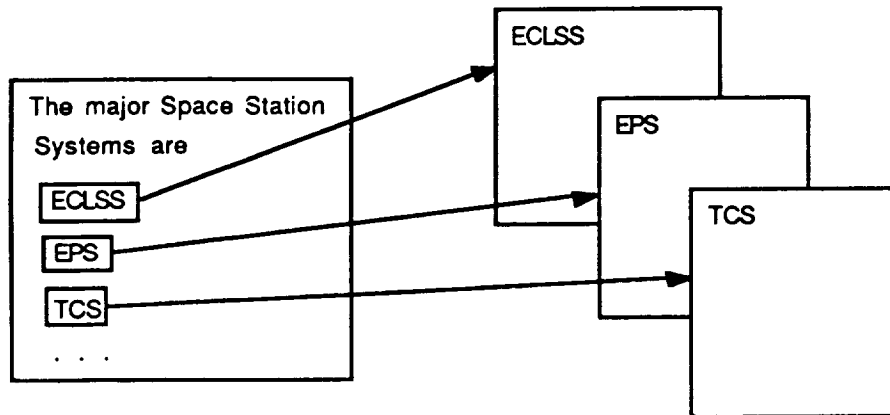
This figure may give some feeling of a hypertext system. The text node on the left has several terms about which more information is available. By selecting one of those terms, the user is taken to a node which gives additional information. Those nodes will usually lead to other nodes with further information. The user can select the information she is interested in by stepping from node to node, following only those links that interest her. This process of moving

through nodes and links is commonly called navigation of the information space.

There has been very little research into the area of navigation of large information spaces in hypertext. (By **large** spaces, we are addressing hypertexts with more than 10,000 nodes.) Several of the obvious methods used in smaller information spaces break down quickly in the larger spaces. For example, graphical maps of the hypertext quickly become too large for adequate representation on a screen. One attempt to deal with this is to reduce the amount of information portrayed at each node in the graphical browser, but when the graph approaches even 1000 nodes, showing only the nodes (even as a dot) and their relationships becomes too much to display on a screen. Further, the user is incapable of grasping any useful information from such a cluttered screen.

The basic question we must address is clear: If many of the typical tools for navigation of information spaces fail when the space grows too large, how are we to facilitate navigation in large spaces?

Our basic goal must be to provide the power of the hypertext interface in such a way as to be most easily comprehensible to the user. We must keep the user's cognitive load as light as possible. Let the computer do the grunt work, and let the user use the tool.

Information Space Topologies

One way to simplify navigation is to restrict the topology, or arrangement, that the nodes of a hypertext are allowed to have. A topology that is used in a large number of different hypertexts is the hierarchy or tree.

Hierarchical Topology
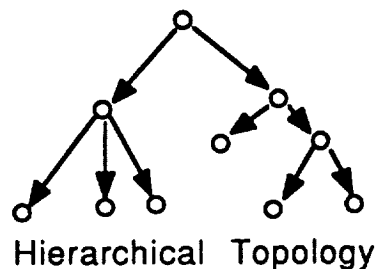
A graph based on a hierarchy has several advantages in terms of navigation and conceptualization of the information space.

Use of a hierarchy allows abbreviation of the graphical representation of the graph, since branches which diverge higher than the current location in the graph can be pruned out of the display. A hierarchically-based graph preserves a definite sense of *up* and *down*. This helps keep the user oriented with a sense of more general (up) or more detailed (down), while links to other nodes at approximately the same level of detail proceed horizontally. The basic problem with a hierarchy is that we usually put given concepts under several different hierarchies. For example, we might file 'Abbott & Costello' under 'Movies', 'Baseball', 'Comedy' and 'Literature'. In a hypertext, we would want links from all those topics to (at least some of) the nodes about 'Abbott & Costello', and links from 'Abbott & Costello' to other nodes in all of those networks. So, ideally, information about 'Abbott & Costello' would be accessible from all those hierarchies. Obviously, this means a great deal of overlap. A given node might reside in many different hierarchies at the same time.

Conclusion

It is believed that the optimal structure for information is an overlapping, simplified hierarchy. The hierarchical structure should be made obvious to the user, and many of the non-hierarchical links in the information space should either be eliminated, or should be de-emphasized so that the novice user is not confused by them. Only one of the hierarchies should be visible at any given time, but switching to another should be very simple.

This research is discussed in more detail in a report I prepared for my NASA Colleague, Joe Hale. The report is also available from me at the University of Alabama.
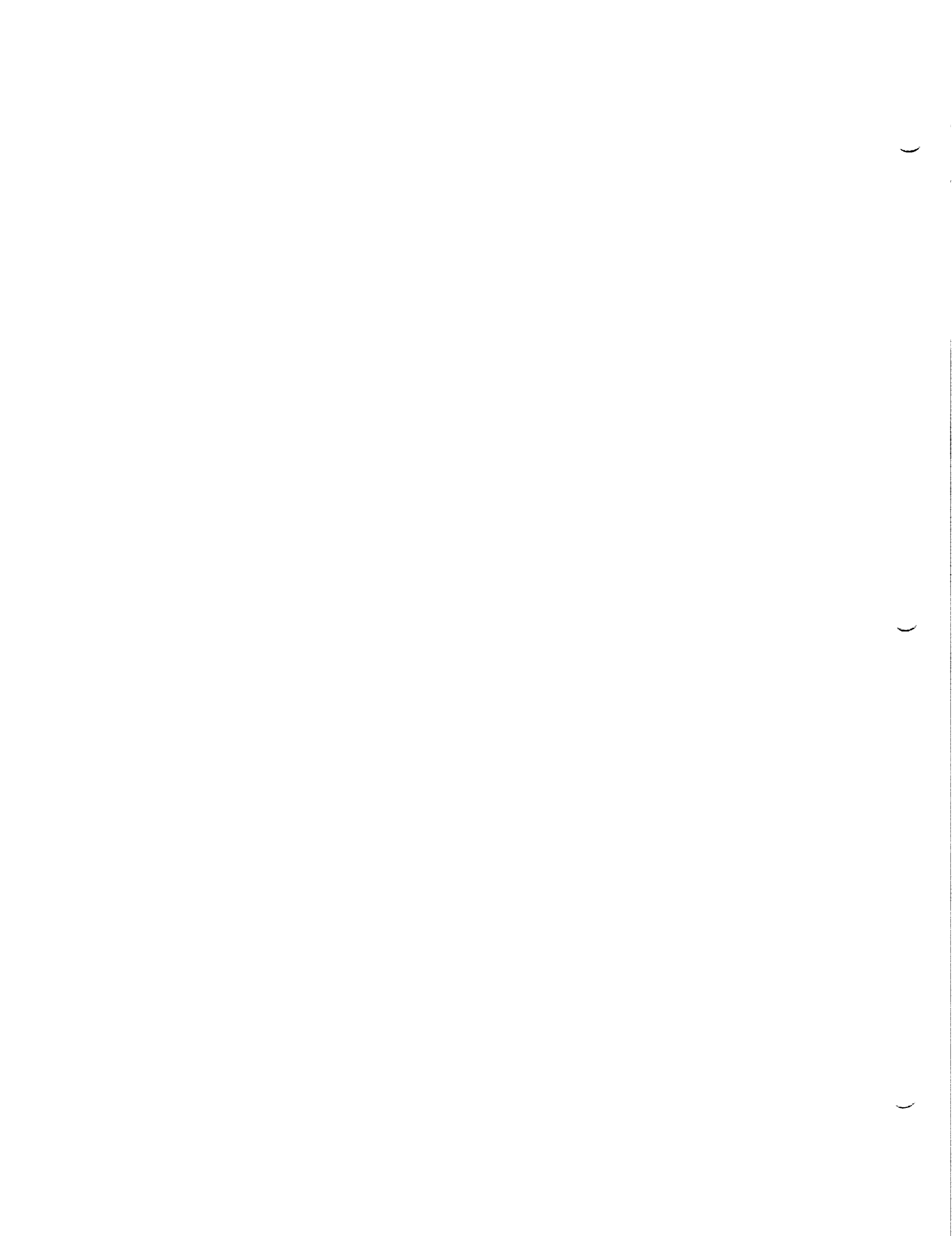
1990

NASA/ASEE SUMMER FACULTY FELLOWSHIP PROGRAM

MARSHALL SPACE FLIGHT CENTER
THE UNIVERSITY OF ALABAMA

WELDING ARC PLASMA PHYSICS

Prepared By: Bruce L. Cain

Academic Rank: Assistant Professor

University and Department: Mississippi State University
                                       Mechanical and Nuclear
                                       Engineering

NASA/MSFC:

      Laboratory: Materials and Processes
      Division: Process Engineering
      Branch: Metals Processes

MSFC Colleague: Dr. Arthur C. Nunes

Contract Number: NGT-01-002-099
                                       The University of Alabama
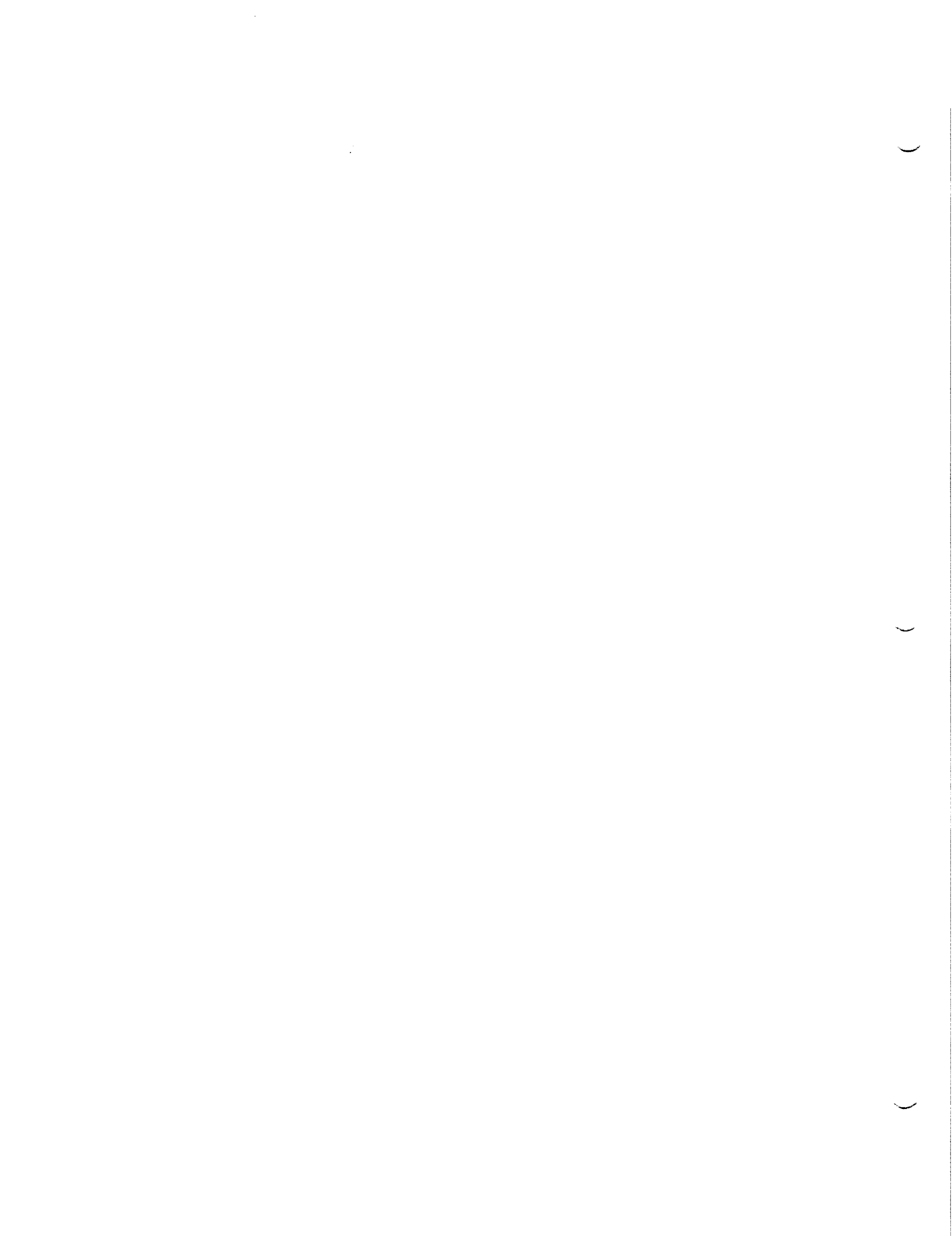
I. INTRODUCTION

The problems of weld quality control and weld process dependability continue to be relevant issues in modern metal welding technology. These become especially important for NASA missions which may require the assembly or repair of larger orbiting platforms using automatic welding techniques. To extend present welding technologies for such applications, NASA/MSFC's Materials and Processes Lab is developing physical models of the arc welding process with the goal of providing both a basis for improved design of weld control systems, and a better understanding of how arc welding variables influence final weld properties.

The physics of the plasma arc discharge is reasonably well established in terms of transport processes occurring in the arc column itself, although recourse to sophisticated numerical treatments is normally required to obtain quantitative results. Unfortunately the rigor of these numerical computations often obscures the physics of the underlying model due to its inherent complexity. In contrast, this work has focused on a relatively simple physical model of the arc discharge to describe the gross features observed in welding arcs. Emphasis was placed on deriving analytic expressions for the voltage along the arc axis as a function of known or measurable arc parameters. The model retains the essential physics for a straight polarity, diffusion dominated free burning arc in argon, with major simplifications of collisionless sheaths and simple energy balances at the electrodes.

II. ARC DISCHARGES

An arc discharge is an intense plasma with the addition of significant amounts of neutral gas which serves to replenish the loss of charged particles through electron-neutral ionizing collisions. In a welding arc, this neutral gas is normally a mixture of an inert support gas (argon or helium) and metal vapor from the work-piece. An important approximation often assumed to hold for the arc discharge is that of "local

thermodynamic equilibrium" (LTE) between all the charged and neutral particles. This allows considerable simplification in the analysis, since once the electron temperature, T_e, is found, it can then be assumed that $T_{ion} = T_{gas} = T_e$. The discharge can then be modeled as a single temperature fluid, driven primarily by electron dynamics. In a highly ionized arc discharge, electron-ion recombination is enhanced by the presence of the neutral species, producing additional energy losses by radiation. This may be significant for higher current arcs where one should also include "magnetic pressure" effects induced by the arc's self magnetic field. Unfortunately for analytic modeling approaches, these processes can only be treated realistically by numerical solution of nonlinear momentum balance equations in the bulk plasma. In the sheath regions of a high pressure arc, the plasma particles may also experience collisions due to locally high neutral densities. This adds considerable complexity in solving the sheath equations to obtain the sheath electric field.

III. SIMPLE ARC MODEL

Neglecting radiation losses, collisions in the sheaths, the influence of the arc self magnetic field, and assuming that only argon gas is present in the arc column, simplified plasma equations were solved for the cylindrical arc of Figure 1, using a Basic program outlined in Figure 2. The electron temperature was estimated based on balancing diffusive losses and ionization gains in the positive column (PC). Assuming LTE condition, the charged particle densities were determined based on equilibrium energy partitioning using the Saha equation. The ion and electron mobilities were obtained using energy averaged collision cross sections for Coulomb scattering and momentum exchange between electrons, ions, and neutrals. Then a simple current balance in the PC was used to find the electric field and drift velocities of charged particles into the sheaths.

Simple energy balances at the bounding electrodes, along with Poisson's equation, were used to obtain the cathode and anode voltage drops. This gave a Child-Langmuir potential distribution at the anode, assuming only electrons were present in the anode sheath. At the cathode, however, the charge contributions from plasma ions, J_+, plasma electrons, J_-, and surface emitted electrons, J_b, were included in the Poisson integration. These various current densities are depicted in Figure 1. The potential at the cathode was determined in terms of a parameter, $\{J_b/J_{net}\}$. This parameter was set to a nominal value of 0.85, indicating that 85% of the current at the cathode was due to surface electron emission. In general, this ratio should be independently determined based on detailed heat flux balances and known emission mechanisms. The results of this model demonstrated order of magnitude agreement with typical values for V_c, V_a, and the electric field in PC, with good trend fitting when the arc pressure was varied. However, the model failed to demonstrate important features of the arc voltage variation with arc current.

IV. FURTHER CHALLENGES

A. *Basic Model Improvements*: Several improvements in the model can be incorporated by simply relaxing assumption made in the simple model.

    1. Add arc self magnetic field effects.

    2. Add inelastic collisions (recombination and electron attachment).

    3. Add neutral gas flows. (MHD equations to obtain property flow fields.)

    4. Include vaporization of the work-piece.

B. *Plasma-Surface-Interactions*: In any model of the arc discharge, a key area of uncertainty lies in how one treats the important interaction between the discharge and the bounding electrodes. For thermionic emitting surfaces, electron emission from the electrode can be modeled by traditional thermionic and/or field assisted emission mechanisms. However, when the welding current is "reversed", the work-

piece becomes the dominant electron emitter. In addition to non-thermionic emission mechanisms, the work-piece is being rapidly melted and vaporized. Further complexities arise when this work-piece is oxidized, since the surface oxide structures must first be broken down and removed as the weld proceeds. Recent high speed photography of both reverse TIG and VPPA welding of aluminum suggests that oxide enhanced electron emission from the work-piece may also play a significant role in establishing a "dynamical equilibrium" character for the arc, via charge buildup and subsequent breakdown of the oxide dielectric layer. From this evidence, and the need to extend the plasma arc model for the reverse polarity mode, it is essential that further work extend our knowledge of emission processes.

C. *Experiments to Simplify Model Development*: Essentially all of the basic model improvements listed above involve numerical solution of non-linear partial differential equations. Such an undertaking is probably beyond the scope of interest for near term solutions for weld process development. It would seem prudent to first study the surface emission problem to establish details of the emission mechanisms, and then couple these results with a simpler model such as outlined in this work.

Due to the dynamic character of the emission problem, scoping experiments may be suggested to first illuminate the physical processes involved. In contrast to the plasma arc processes, which are reasonably well established by modern theories, these surface dominated phenomena are presently only speculatively identified. Concerning oxide enhanced electron emission effects, for example, a simple experiment would be observation of differences in arc behavior and weld quality for various configurations of oxide present on the work-piece. Similar experiments could be done using different support gases to differentiate the importance of sputtering effects. It would also be useful to obtain the voltage and current waveforms of the arc during these experiments for correlation with the differences in emission processes.

MODEL INPUT VALUES

Lo	arc length
Ro	arc radius
Po	pressure
Inet	arc current

Figure 1. Simple arc model voltage distribution.

COMPUTER PROGRAM TO FIND VOLTAGE
DISTRIBUTION IN THE ARC.

INPUT
Lo, Ro
Po, Inet

Compute T
at Equilibrium → DIFFUSION AND
IONIZATION BALANCE

Determine Ne,
Nion, Ngas → SAHA
EQUATION

ITERATION
LOOP

Estimate Mobilities
and Conductivity → COLLISION
CROSS SECTIONS

$$\vec{E} = \vec{J}/\sigma$$
$$\vec{v} = \mu/\vec{E}$$

B.C.'s → Sheath
Equations

Figure 2. Block diagram of arc model program.

1990

MARSHALL SPACE FLIGHT CENTER
THE UNIVERSITY OF ALABAMA

A SATELLITE-GROUND STUDY OF THE DYNAMICS OF THE

BULGE REGION OF THE EARTH'S MAGNETOSPHERE

Prepared by: Donald L. Carpenter

Academic Rank: Professor (Research)

University and Dept.:   Stanford University
                                      Electrical Engineering

NASA/MSFC:

    Laboratory: Space Science
    Division: Solar-Terrestrial Physics
    Branch: Magnetospheric Physics

MSFC Colleague: Barbara Giles
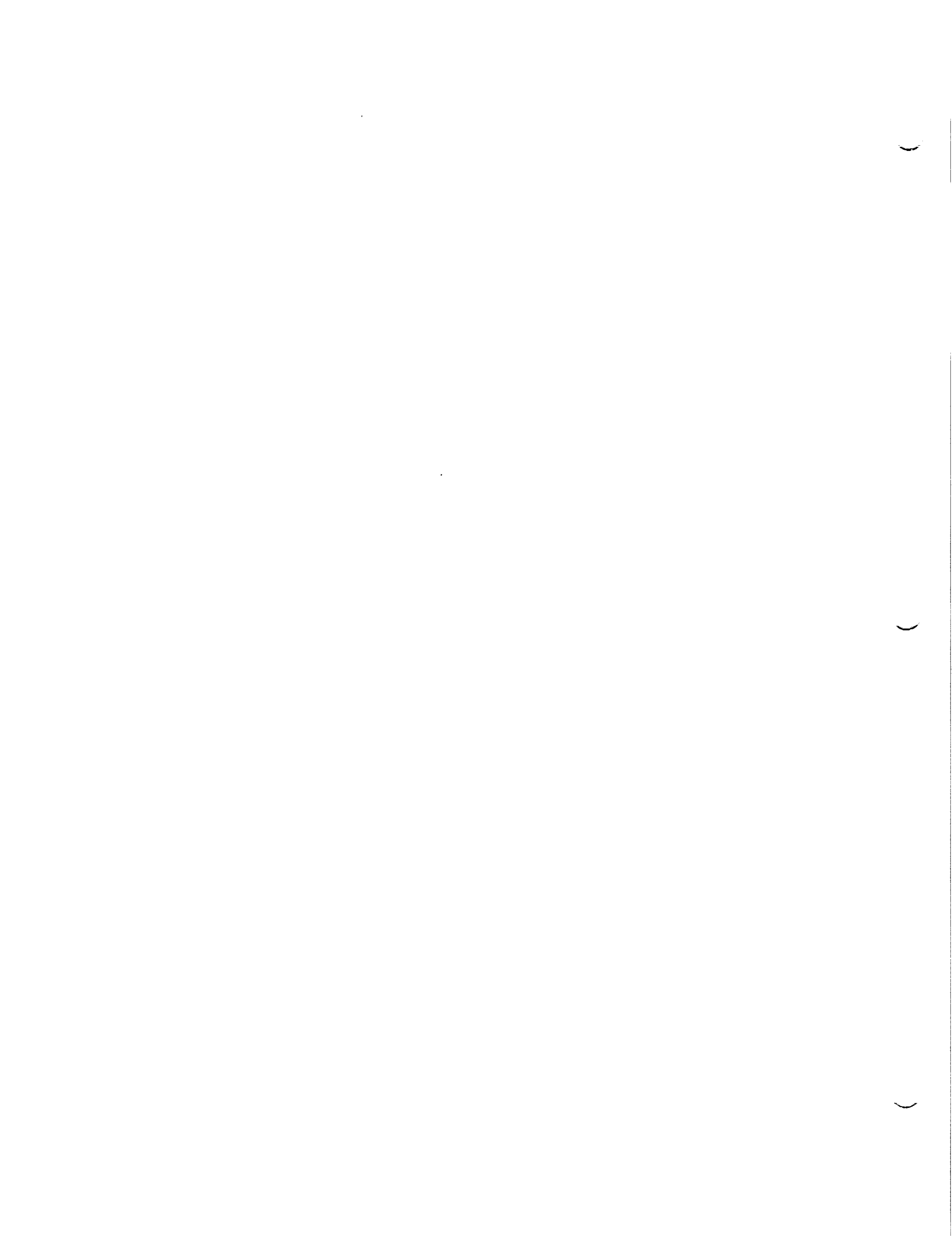
The dense plasma envelope of the Earth, called the plasmasphere, extends outward to a distance of about three to seven earth radii at the equator. At the outer limits of the plasmasphere, the plasma density usually drops sharply by a factor of from 5 to 40. This drop occurs at the so-called plasmapause; the low density region extending beyond it to the outer limits of the Earth's magnetized envelope, or magnetosphere, is called the plasmatrough.

A complex, dynamic, and poorly understood (and described) part of the the plasmasphere is the bulge region, usually located near dusk, where the plasmasphere radius is known to reach a maximum and where its shape is known to be highly variable. The bulge is a center of interest because it undergoes fast and complex changes during so-called substorms or magnetic storms, when large amounts of energy communicated to the magnetosphere by interaction with the Solar Wind are released, redistributed, and dissipated. In our research, we have been using data from multiple ground stations and satellites to see how the plasmasphere in the dusk sector is modified during these disturbances. There is clearly some type of erosion process, during which the plasmasphere is diminished in size, and it is believed that the "excess" plasma is peeled off and carried (convected) away toward the outer bondary of the magnetosphere (the magnetopause). However, very little is known about the physics of this erosion process, and about how the plasmasphere recovers during the quiet periods that follow such disturbances.

Our case studies from three multiday periods in 1982 have produced a number of new findings, including the first evidence from ground based Very Low Frequency (VLF) whistler stations of a narrow high density tail or streamer, extending sunward from the dusk side of the plasmasphere, and clear evidence from the Retarding Ion Mass Spectrometer (RIMS) experiment on DE 1 of sunward and outward bulk flow of dense plasma near dusk. The study has revealed new evidence of the accumulation of large regions of dense plasma in the afternoon sector at locations well beyond the main plasmasphere, and has raised a number of questions concerning the relation between narrow streamers, which apparently can be formed near the edge of the main plasmasphere, and the often large

outlying regions, which can extend for several earth radii along a satellite orbit.

The study has also shown that the plasmapause region after dusk is one in which irregular density structure tends to develop, and in which such structure may persist for days during a quieting/calm period. Of substantial potential importance to plasmasphere physics is our additional evidence that much of the bulge structure and activity takes place beyond an inner plasmasphere, the shape of which is strongly influenced by nightside substorm-associated plasmapause forming mechanisms. In this outer region, which is the more identifiable portion of the bulge, there appears to be a tendency for dense plasma "islands" to accumulate and to circulate in the afternoon-dusk sector in a kind of eddy flow that does not encircle the Earth in the manner of plasma flow at smaller radii.

Our work, being conducted jointly with B.Giles and C.Chappell of MSFC, R. Anderson of the U. of Iowa, P. Decreau of the U. of Orleans, and Y. Corcuff of the U. of Poitiers, is continuing into the final stages of figure preparation and interpretation, and we expect to complete our major study sometime this fall, with partial support from a grant to Stanford from MSFC.

NOTE: In addition to this main work, I have also been collaborating with D. Gallagher and P. Craven of SSL on development of an empirical model of equatorial electron density in the Earth's magnetosphere. I have also been collaborating with Bill Boeck and the lightning group at SSL on a joint study of lightning videotaped from the Shuttle in January, 1990.

1990

NASA/ASEE SUMMER FACULTY FELLOWSHIP PROGRAM

MARSHALL SPACE FLIGHT CENTER
THE UNIVERSITY OF ALABAMA

IS IT POSSIBLE TO IDENTIFY A TREND IN PROBLEM/FAILURE DATA ?

Prepared By: Curtis K. Church, Ph.D.

Academic Rank: Associate Professor

Institution: Middle Tennessee State
                                University, Department of
                                Mathematics and Statistics

NASA/MSFC:

        Office: System Safety & Reliability
        Division: Reliability &
                                Maintainability Engineering
        Branch: Problem Assessment

MSFC Colleague: Raymond Dodd, Ph.D.
                                Frank Pizzano

Contract No.:   NGT-01-002-099
                                The University of Alabama

In many scientific endeavors, researchers want to determine whether a sequence of observations taken over time exhibits some type of trend. The NASA Standard, "Trend Analysis Techniques" (NASA-STD-8070.5), describes a variety of statistical methods that could be applied to time series data. Generally, trend is regarded as a smooth broad motion of the system over a "long" term. Several techniques are currently being used. The result of these efforts is reported in "Quarterly Problem Trending Report for MSFC Shuttle Elements and Payloads" prepared by the Calspan Corporation. However, the nature of the problem/failure data poses difficulty in identifying a trend.

One of the major obstacles in identifying and interpreting a trend is the small number of data points. Future trending reports will begin with 1983 data. As the problem/failure data is aggregated by year, there are just seven observations (1983-1989) for the 1990 reports. Any statistical inferences with a small amount of data will have a large degree of uncertainty. Consequently, a regression technique approach to identify a trend is limited. Though trend determination by failure mode may be unrealistic, the data may be explored for consistency or stability and the failure rate investigated. In what follows, various alternative data analysis procedures are briefly discussed. Techniques that could be used to explore problem/ failure data by failure mode. The data used is taken from Section One, Space Shuttle Main Engine, of the Calspan Quarterly Report dated April 2, 1990.

There were four set of observations in the Quarterly Report SSME Section that had a statistically significant downward trend based on a regression analysis. There were a total of 36 data sets trended in the SSME Section. These significant trends were based on data from 1979 through 1989. Reconsidering these sets of data from 1983 on, not one of them has a significant regression fit at the .01 level, which is the level used in the Quarterly Report. If we begin with data in 1983, a significant downward trend at the .01 level of significance requires a Pearson product moment correlation coefficient of $r = -.875$, that is $r^2 = .765$. In addition to the Pearson correlation coefficient with the corresponding test of hypothesis based on the normal distribution, there are numerous nonparametric measures of association. Two widely used ones in connection with regression and trending are Spearman's rank correlation coefficient and Kendall's tau. These two procedures use the rank order of the observations rather than the actual observed value. The four sets of data that were previously fit with a regression model are summarized below with the data beginning in 1983.

Correlations and Observed Significance Levels

	Pearson	Spearman	Kendall
Fuel preburner injector			
erosion/wear	-.618(linear)	-.607	-.429
	p=.139	p=.137	p=.177
dents/etc	-.765(power)	-.857	-.714
	p=.047	p=.036	p=.024
contamination	-.675(linear)	-.685	-.488
	p=.096	p=.094	p=.111
Controller hardware			
unexplained anomalies	-.805(linear)	-.786	-.714
	p=.029	p=.054	p=.024

Another approach to exploring the data is from the perspective of consistency. That is, does the failure rate fluctuate from year to year or is it relatively stable? While this approach is not to identify a trend it may provide the experimenter with insight into the failure process. Assuming a Poisson model for the number of failures, a chi-square goodness of fit test, assuming a constant failure rate from 1983-1989, a Kolmogorov-Smirnov goodness of fit test with the same assumption, or a level of performance chart could be applied.

The chi-square goodness of fit test utilizes an assumed probability model and estimates the expected number of failures per year and then compares the observed number of failures with these expected frequencies. To specify the procedure, let X_i be the number of failures in year i and let t_i be the number of test seconds (or test starts) in year i. The expected number of failures, under the assumption of a constant failure rate, for year i is given by $\mu_i = \Theta t_i$, where Θ is the probability of a failure in a small interval. The constant failure rate estimate of Θ is given by $\hat{\Theta} = \Sigma X_i / \Sigma t_i$, where the summation ranges through the years 1983 to 1989. The chi-square test statistic is given by $T = \Sigma (X_i - \hat{\mu}_i)^2 / \hat{\mu}_i$ which is approximately distributed as a chi-square random variable with 5 degrees of freedom. The table below displays observed and expected frequencies for the 3 fuel preburner injector failure modes plus 2 other randomly selected data sets.

The .01 critical value for a chi-square distribution with 5 degrees of freedom is 15.1. The value of the test statistic T gives some idea of the agreement between the observed results and the assumption of a constant failure rate. The value of T must be cautiously viewed in cases of small expected frequencies. Consult the reference by Lawal and Upton for this consideration.

Observed and Expected Frequencies

	83	84	85	86	87	88	89
Fuel preburner injector							
erosion/wear	3	4	5	1	2	4	3
	2.73	2.52	3.83	1.21	3.95	4.30	3.5
						T=2.33	
dents/etc	13	3	7	1	1	3	2
	3.72	3.44	5.23	1.65	5.39	5.86	4.7
						T=30.60	
contamination	3	5	4	0	1	0	2
	1.86	1.72	2.61	.82	2.70	2.93	2.4
						T=12.57	
LPOTP contamination	6	10	2	3	15	13	3
	6.45	5.96	9.06	2.85	9.35	10.2	8.2
						T=15.76	
HPOTP turbine nozzle							
second stage crack	1	1	1	1	0	7	2
	1.61	1.49	2.27	.71	2.34	2.54	2.0
						T=11.39	

Another technique to explore the stability of the failure rate is a level of performance chart. It is constructed and used as a control chart. Using the Poisson probability model, the overall failure rate estimate $\hat{\theta}$ is used to compute limits of $\hat{\theta} + 3\sqrt{\hat{\theta}} / \Sigma \ t_i$. The yearly failure rate estimates $\hat{\theta}_i$ are then compared, often graphically, with these limits. Values of $\hat{\theta}_i$ outside the limits point to extreme fluctuation of the failure rates. The table below gives the yearly estimates of θ with limits based on the pooled estimate for 3 of the failure modes previously considered.

Estimates of θ by Year ($\times 10^{-3}$)

	83	84	85	86	87	88	89	Limits
Fuel preburner injector								
erosion/wear	.10	.15	.12	.08	.05	.09	.08	(.03,.16)
dents/etc	.45	.11	.17	.08	.02	.07	.05	(.06,.20)
HPOTP turbine nozzle								
second stage crack	.03	.04	.02	.08	0	.15	.05	(.01,.10)

An alternative process control technique that would monitor the yearly failure rate relative to a specified target failure rate is a cumulative sum (CUSUM) procedure. The CUSUM procedure is a sequence of Wald sequential probability ratio tests used to detect a change in the distribution of the number of problems. As before, a Poisson distribution for the number of problems is used. The CUSUM procedure is often enhanced by a fast initial response (FIR) feature. The reference by Lucas discusses a Poisson CUSUM procedure.

A cumulative sum procedure cumulates the difference between

an observed value Y_i, some normalized value of X_i, and reference value k. If this cumulation equals or exceeds the decision value h, then conclude the failure rate for that year is greater than the target rate. To detect an increase in counts, the CUSUM statistic is $S_i = \max(0, Y_i - k + S_{i-1})$. The FIR CUSUM typically uses a starting value $S_0 = h/2$. The CUSUM is restarted after indicating an out of target value.

CUSUM procedures are evaluated by calculating their average run length (ARL). The ARL should be large when the failure rate is at the target level and short when the rate is at an undesireable level.

The parameter k is the reference value for the CUSUM. Its value will be chosen to be between the acceptable failure rate (μ_a) and an unacceptable level (μ_d) that is to be detected. Although the desired level of μ_a is zero, it is usually not used since any occurence of a failure will then give a signal. The reference value for the Poisson CUSUM should be selected to be close to $k = (\mu_d - \mu_a)/(\ln \mu_d - \ln \mu_a)$.

After k is selected, the decision value h is chosen using a table look-up procedure. There are tables given in the article by Lucas. The value of h should give an appropriately large ARL when the failure rate is on target and an appropriately small ARL value when the rate is too high.

Use of a CUSUM takes more involvement from the analyst than do the goodness of fit test or the level of performance chart. The CUSUM, however, combines looking at the data for stability and checking agreement with a target value. A CUSUM procedure with an acceptable failure rate of 1 per 50,000 seconds and an unacceptable rate of 1 per 20,000 seconds has been applied to the problem/failure data. When a CUSUM value exceeds h then it is restarted with next data value. The results are comparable to those from the goodness of fit test and rate performance chart. Along with the chi-square goodness of fit test and the level of performance chart, even though simple, these techniques offer some insight to supplement the regression approach.

Trend fitting and trend estimation are very far, particularly with small samples, from being a purely mechanial process. There is great scope, even necessity, for personal judgement. Exploring the data for patterns can be a very difficult, delicate issue.

REFERENCES

1. Lawal, H. B., and Upton, G. J. G., "An approximation to the distribution of the chi-square goodness of fit statistic for use with small expectations," *Biometrika*, 67 (1980) 447-453
2. Lucas, J. M., "Counted Data CUSUM's," *Technometrics*, 27 (1985) 129-144
3. Quarterly Problem Trending Report for MSFC Shuttle Elements and Payloads, Special Study c43a-3, Calspan Corporation, April 2, 1990
4. Trend Analysis Techniques, NASA Standard 8070.5, October 1988

1990

NASA/ASEE
Summer Faculty Fellowship Program

Marshall Space Flight Center
The University of Alabama

National Launch Strategy

Vehicle Data Management System

Prepared By: David Cordes

Academic Rank: Assistant Professor

University: University of Alabama

Department   Computer Science

NASA/MSFC
      Division: Engineering Systems
      Branch: Information SystemsOffice

MSFC Colleague: Joe Pollock

Contract Number: NGT-01-002-099
                                The University of Alabama
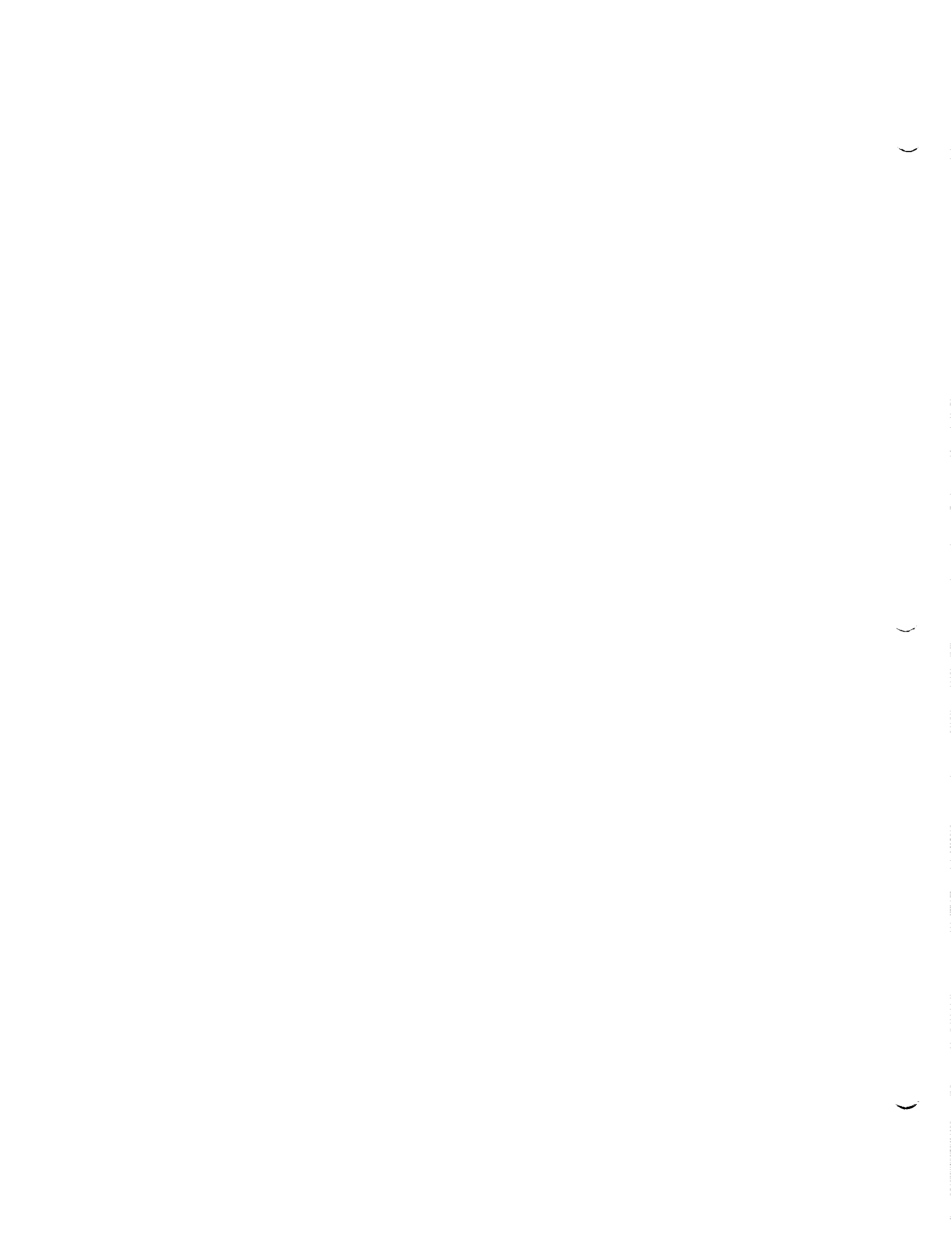
National Launch Strategy

Vehicle Data Management System

The NLS/VDMS system was developed as part of the 1990 NASA Summer Faculty Fellowship Program. The system was developed under the guidance of the Engineering Systems Branch of the Information Systems Office, and is intended for use within the Program Development Branch PD34. The development request, and primary system user, was Dr. Jim Steincamp.

The NLS/VDMS system is an on-line database system that permits the tracking of various launch vehicle configurations within the PD office. The system is designed to permit the definition of new launch vehicles, as well as the ability to display and edit existing launch vehicles. Vehicles can be grouped in logical architectures within the system. Reports generated from this package include Vehicle Data Sheets, Architecture Data Sheets, and Vehicle Flight Rate Reports.

System Overview

The system design took the following items into consideration during the course of its development. First, the system must possess a clean user interface. Second, the system should operate on a platform that the user community is familiar with. Third, the system should be straightforward, and contain on-line help for questions that might arise during its execution.

Given these constraints, the following platform was adopted for the development of this package. It will be Macintosh based, as the user community in question is familiar with the Mac, and the Macintosh also provides a clean user interface. Second, it will utilize the ORACLE database package for storing the information within the system. This decision was based on the fact that this database was available on a Mac and was already in the possession of PD34. Third, the system will utilize the SuperCard product for its hypermedia interface. SuperCard provides a hypermedia authoring system for the Macintosh, and is based heavily upon the Macintosh product HyperCard. It is a more flexible product than is HyperCard, and was also already in the possession of the PD34 group.

Initial System Development

The system proposed by the PD 34 group was built in a rapid prototyping environment. Given the time frame involved with the project, a conventional development strategy was not feasible. Instead, initial gathering of

requirements was performed with Dr. Steincamp, and then prototypes of the user interface into the system were generated. Based on Dr. Steincamp's comments regarding these interfaces, the initial system model was generated. Once the model had been established, the individual functions demanded within the model were developed.

Specific system functionality included the following: First, the system must be capable of defining, displaying and editing (with history) individual vehicles within the system. These vehicles are to be composed out of modular components. These components, other system entities, must also be able to be definable, displayable and editable (with history). Furthermore, the vehicles in the system should be able to be grouped into logical sets, called architectures. Finally, the generation of various reports was also fundamental to the project. The system must be able to generate both Launch Vehicle Data Sheets and also Architecture Data Sheets. In addition, the generation of Vehicle Flight Rate Reports was required.

As the design and implementation processes associated with this project are of little concern to the average individual, this report will instead concentrate on introducing some of the tools that were utilized to implement the system. Of particular interest are the SuperCard and ORACLE products. It was the functionality and abilities of these two products that impacted the development of this system the most.

SuperCard Hypermedia Authoring System

SuperCard is a powerful hypermedia authoring system. It is designed as a platform for the development of applications that utilize graphics, text, sound and animation. It is essentially an extension of HyperCard, Apple's commercial hypermedia system. For the NLS/VDMS system, the choice of SuperCard was based on a number of built-in features inherent to the package that permitted the speedy generation of user interfaces. Simple tasks, such as control of the mouse, were trivial within SuperCard. Other systems, such as the X-Windows system, would have demanded much more effort by the programmer.

The SuperCard system is an attempt at an object-oriented system. It is, however, not a true object-oriented system. It does possess some of the basic features inherent to object-oriented systems, such as the communication between objects by events. It lacks any mechanism for inheritance, and does not handle data types in an object-oriented manner. In fact, its data typing abilities are quite limited.

SuperCard did, however, prove invaluable in the prototyping process. The ability to quickly generate sample screens and interaction sequences was ideal for the demands of this project. The built-in primitives provided by SuperCard matched the needs of the development process very well.

The ORACLE Database

The ORACLE Database system is an implementation of a standard relational database model. The system is extremely portable, and is available on a number of hardware platforms. It utilizes the standard SQL query language in its operation. The system is both easy to learn and well-documented.

The ORACLE database was particularly attractive to this project in that it possesses a clean, simple interface into the HyperCard/SuperCard environment. The ORACLE language hypersql can be used as a bridge between SQL and the SuperTalk scripting language. The SQL commands necessary to carry out a specific function in the database can be embedded directly into the scripts of SuperCard.

The database generated for this project was constructed in third normal form. While ORACLE does not demand this of all its applications, third normal form eliminates a number of storage anomalies and also helps to eliminate data redundancy.

The database as it is used in the NLS/VDMS system is a stand-alone product. The ORACLE system does support a distributed database environment for the Macintosh, and the system could be modified so that the product could be run in a networked environment. As this was not part of the original system specifications, it is not currently implemented.

System Evaluation

The completed system is currently running in a Macintosh environment. The complete system utilizes eighteen ORACLE database tables, contains six different windows, 48 cards, 371 card buttons, 521 card fields, 52 card graphics, and 20,432 lines of object scripts. This project was generated in approximately eight weeks, with one week of initial lead time involving learning the Macintosh, ORACLE and SuperCard and one week for generation of the User's and Programmer's manuals.

In looking at the code produced in this project, the final breakdown resulted in an average generation of approximately 64 lines of code per hour. This compares

quite well with the accepted GAO standard of approximately 30 lines of generated code per day.

Additionally, a user's manual and set of developmental documentation has been prepared for the system.

Conclusions

The actual development of this product does not offer up any unique or unexpected conclusions regarding either system prototyping or system development. While it is worth mentioning that the products utilized (i.e. SuperCard) made the development process much easier, these are well-known, standard programming tools. Instead, I choose to concentrate on some concepts that are often ignored by the profession, but have been re-enforced to me over the course of the summer.

1. The ability of our profession to produce a usable product is quite poor. Recent government studies indicate that only eight percent of requested software is ever used. Over twenty-five percent of all government software developments are never even delivered to the users. Quite simply, we are not producing usable, reliable code.

2. The primary sources of error within the software process are in the requirements analysis and system specification phases. The ability to construct a complete, consistent set of functional requirements for a system is very limited. Furthermore, we lack proper techniques for extracting this information from the user population.

3. The overall success or failure of a software product can be attributed to the organizational and management techniques utilized in its development. We lack the ability to effectively organize and manage large-scale software projects.

4. The educational environment in which we develop our programming teams of tomorrow must address these concerns. We cannot simply produce outstanding hackers, but must also be able to output a programming population that possesses a basic set of both organizational and management skills.

This summer has proven very enlightening regarding the actual programming practices that are being used in a real-world situation. This information is going to be carried back directly to my Software Engineering course. By providing the class with a number of real-world scenarios for software development, their appreciation for the organization and management of software projects should be enhanced.

1990

NASA/ASEE SUMMER FACULTY FELLOWSHIP PROGRAM

MARSHALL SPACE FLIGHT CENTER
THE UNIVERSITY OF ALABAMA

A STUDY OF HYDROGEN ENVIRONMENT EFFECTS ON MICROSTRUCTURE

PROPERTY BEHAVIOR OF NASA-23 ALLOY AND RELATED ALLOY SYSTEMS

Prepared By: Ravinder M. Diwan

Academic Rank: Professor

University and   Southern University
Department: Mechanical Engineering

NASA/MSFC:

        Laboratory: Materials & Processes
        Division: Metallic Materials
        Branch: Metallurgy Research

MSFC Colleagues: W.B. McPherson and B.N. Bhat

Contract No: NGT-002-099
                                The University of Alabama
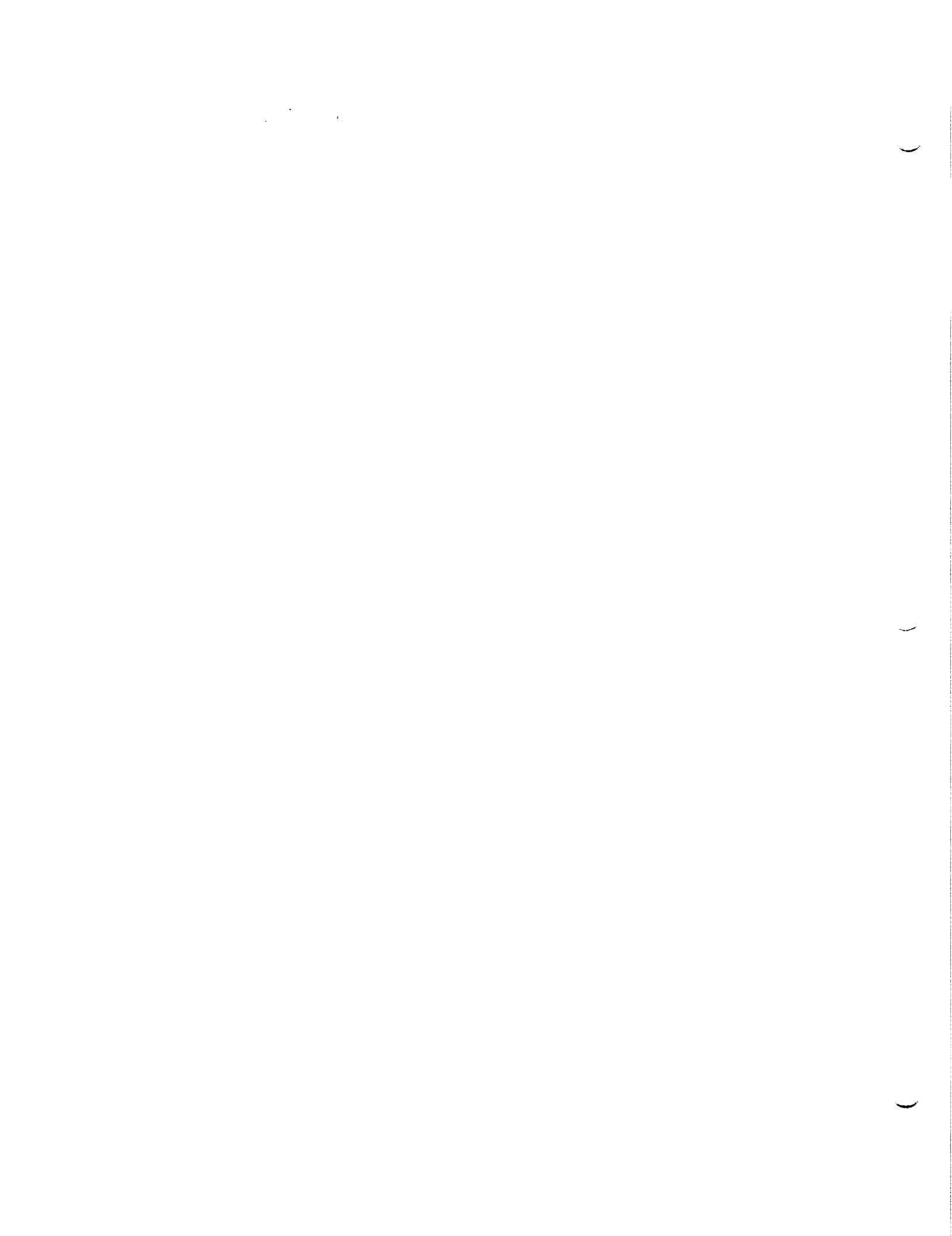
A STUDY OF HYDROGEN ENVIRONMENT EFFECTS ON MICROSTRUCTURE PROPERTY BEHAVIOR OF NASA-23 ALLOY AND RELATED ALLOY SYSTEMS

by
Ravinder M. Diwan
Professor
Southern University
Baton Rouge, Louisiana 70813

ABSTRACT

The present research work is a study into the behavior of hydrogen environment effects on microstructure property behavior of NASA-23 alloy and related alloy systems Incoloy 909, Inconel 718 and JBK-75, a modified A 286. This work is part of the overall advanced main combustion chamber (AMCC) casting characterization program of the Materials & Processes Laboratory of the Marshall Space Flight Center. The influence of hydrogen on the tensile properties and ductility behavior of NASA-23 alloy has been analyzed. NASA-23 and other referenced alloys in cast and hipped conditions have been solution treated and aged under selected conditions and characterized using optical metallography, scanning electron microscopy and electron microprobe analysis techniques. The yield strength of NASA-23 is not affected much by hydrogen under tensile tests carried at 5,000 psig conditions, however, the ultimate strength and ductility properties are degraded. This implies that the physical mechanisms operating would be related to the plastic deformation processes.

The fracture surfaces characteristics of NASA-23 specimens tensile tested in hydrogen, helium and air were also analyzed. These revealed surface cracks around specimen periphery with the fracture surface showing a combination of intergranular and transgranular modes of fracture. It is seen that the specimens charged in hydrogen seem to favor a more brittle fracture mode in comparison to air and helium charged specimens. The AMCC casting characterization program is to be continued, under which the referenced alloys have yet to be analyzed for their hydrogen behavior. As a result of this summer faculty research program, the basic microstructural factors and fracture characteristics in some cases have been analyzed.

INTRODUCTION

Development of NASA-23 alloy with a 180 ksi ultimate tensile strength and a 160 ksi yield strength and with no appreciable loss in ductility in hydrogen environments is the goal of the current advanced main combustion chamber (AMCC) program being pursued at the Materials and Processes

Laboratory of the Marshall Space Flight Center. As a part of the casting characterization plan, during the 1990 NASA/ASEE summer faculty research program , a study has been carried out of the NASA-23 and other related alloys Incoloy 909, Inconel 718 and JBK-75 alloys. Though some information related to the phase stability and effects of alloying elements in the referenced alloys is available in some references (1-7), very little is known related to the hydrogen environment embrittlement (HEE) behavior of these alloys.

The several objectives of the research that has been carried out are:

1. Evaluation of Gaseous Hydrogen environment effects and relate these to metallurgical behavior of selected basic alloy systems NASA-23, 909, 718 and JBK 75 alloys.
2. Heat Treatment and characterization of referenced alloys.
3. Test and evaluation of hydrogen environment effect.
4. Recommend future directions for research to establish fracture mode and effects of hydrogen to help development of hydrogen resistance alloys.

EXPERIMENTAL PROCEDURES

Hipped and as cast condition materials of NASA-23, Incoloy 909, Inconel 718 and JBK-75 were solution treated and aged : solution treatment times were 1 hour - at 1700 F for NASA-23 , at 1800 F for Incoloy 909 , at 1900 F for Inconel 718, and 1800 F for JBK-75 and aging treatments involved a dual aging (1325F/8hr,2hr,1150 F/8hr) for NASA-23 and 909 alloys a dual aging (1400 F/10 hr, 2hr, 1200 F/8hr) for Inconel 718 and (1325 F/16 hr) aging for JBK-75 alloy. Compositions, heat treating conditions , hardness values for all alloys are included in data presented at the Marshall Space Flight Center (8).

All solution treated and aged specimens were characterized using techniques of optical microscopy and analyzed for their microconstituents with the SEM and electron microprobe analysis techniques. In an evaluation of NASA-23 alloy , specimens were tested for smooth tensile properties and their ductility behavior under ambient air and 5,000 psig helium and 5,000 psig hydrogen environment test conditions. Test results of NASA-23 are analyzed and related to microstructural behavior and fractographic characteristics of this alloy.

Determination of total hydrogen contents using LECO analyzer on specimens charged with hydrogen under 5,000 psig at 150 F with a 10,000 sec exposure has been carried out for all alloys. An attempt was made to determine the values

of hydrogen on a local microstructural level using technique
of Schober and Dieker (9) . This was not completely
successful , though a local high concentration of silver was
seen which can be , according to the technique related to the
local hydrogen level of the specimens.

RESULTS AND DISCUSSION

NASA-23 tested in air , helium and hydrogen revealed a
loss of ductility in hydrogen in comparison to air and helium
tested samples. The optical and SEM microstructural
characterizations carried and the fractographic analyses have
revealed presence of surface cracks on the periphery of the
specimens. The fractures are seen to be of mixed transgranular
and brittle intergranular fracture mode. A characterization
of fracture surfaces using technique developed by Underwood
(9)to measure the fracture surface roughness will be highly
useful in discriminating the fracture modes and to
understand better the fracture behavior of the alloys.

The results of the several microstructural
characterizations and the fractographic analyses carried out
are detailed in the data presented (8). It is seen that the
Incoloy 909 had a higher total hydrogen about 16.9-25.5 ppm
on a 5,000 psig , 150 F exposure compared to values of 2-9.9
ppm in other alloys.

The metallurgy of the basic alloy systems studied has
been analyzed and correlated where possible with the
potential hydrogen environment behavior of the referenced
alloys. The overall AMCC casting characterization program is
a three year program and some of the results of this work and
recommendations are expected to be beneficial in modeling and
continuing research in this important area of hydrogen
environment behavior and hydrogen resistant alloy
development. Details of all research findings are in
reference 8.

ACKNOWLEDGEMENT

REFERENCES
1. W.B. McPherson, "A New High Strength Alloy for Hydrogen
   Fueled Propulsion Systems", AIAA/ASME/SAE/ASEE 22nd Joint
   Propulsion Conference Proceedings, Marshall Space Flight
   Center, AL 1986.
2. M.J. Cieslak,T.J. Headley, G.A. Knorovsky, A.D. Romig, Jr.
   and T. Kollie, "A Comparison of the Solidification
   Behavior of Incoloy 909 and Inconel 718:, MET. Trans. A
   vol 21A, Feb. 1990, pp. 479-488.
3. D.D. Krueger, S.A. Antalovich and R.H. Van Stone , "Effects
   of Grain Size and Precipitate Size on the Fatigue Crack
   Growth Behavior of Alloy 718 at 427C", Met. Trans.
   A vol 18 A, Aug. 1987, pp. 1431-1449.
4. P.S. Kotwal, "The metallurgy of Superalloys",
   Metallography, 1, 1969, pp. 251-285.
5. R. Oriani, J.P. Hirth and M.Smialouwski Ed.
   "Hydrogen Degradation of Ferrous Alloys" Noyes
   Publications, 1985.
6. R.J. Walter and W.J. Chandler, "Influence of Hydrogen
   Pressure and Notch Sensitivity on Hydrogen Environment
   Embrittlement at Ambient Temperature", Mater Sci Eng.,8
   (1971) pp.90-97.
7. R.J. Walter and W.T. Chandler, "Effects of High Pressure
   Hydrogen on Metals at Ambient Temperatures", MSFC Rocketdyne
   Report R-780-1-3, 1969.
8. R.M. Diwan, "A Study of Hydrogen Environment on
   Microstructural Property Behavior of NASA-23 Alloy and
   Related Alloy Systems", Presentation to Marshall Space
   Flight Center, Aug. 9. 1990.
9. T. Schober and C. Dieker, "Observation of Local Hydrogen
   on Nickel Surfaces", Met. Trans. A vol 14A, Nov. 1983, pp.
   2440-2442.
10. E.E. Underwood and K. Banerji, "Quantitative
    Fractography" in Fractography, 9th Ed. American Society
    for Metals, Metals Park, OH Vol 12 , 1987.

1990

NASA/ASEE SUMMER FACULTY FELLOWSHIP PROGRAM

MARSHALL SPACE FLIGHT CENTER
THE UNIVERSITY OF ALABAMA

DAMPER BEARING ROTORDYNAMICS

Prepared by: David A. Elrod

Academic Rank: Assistant Professor

University: Virginia Polytechnic Institute
                                and State University
Department: Mechanical Engineering

NASA/MSFC:

        Laboratory: Structures and Dynamics
        Division: Control Systems
        Branch: Mechanical Systems Control

MSFC Colleague: George von Pragenau

Contract No.:   NGT-01-002-099
                                The University of Alabama

INTRODUCTION

High side loads reduce the life of the Space Shuttle Main Engine (SSME) High Pressure Oxygen Turbopump (HPOTP) bearings. High stiffness damper seals have been recommended to reduce the loads on the pump and turbine end bearings in the HPOTP (Tecza, et al., 1989). The seals designed for use on the pump end are expected to adequately reduce the bearing loads; the predicted performance of the planned turbine end seal is marginal. An alternative to the suggested turbine end seal design is a "damper bearing" with radial holes from the pressurized center of the turbopump rotor, feeding a smooth land region between two rough-stator/smooth-rotor annular seals. An analysis has been prepared to predict the leakage and rotordynamic coefficients (stiffness, damping, and added mass) of the damper bearing. The following paragraphs describe:

1) governing equations of the seal analysis which has been modified to model the damper bearing,
2) differences between the upstream conditions of the damper bearing and a typical annular seal,
3) predictions of the damper bearing analysis, and
4) assumptions of the analysis which require further investigation.

GOVERNING EQUATIONS

The governing equations for the bulk-flow model of an annular seal with incompressible flow have been published by other authors (e.g., Childs, 1984, and Nelson and Nguyen, 1987): the continuity equation, and axial and circumferential momentum equations. The equations define the relationship between the clearance, pressure, axial velocity, and circumferential velocity (H, p, U_z, and U_θ) as functions of the spatial variables θ and z, and time t. Assuming small motion of the seal rotor about a centered position within the stator, a perturbation analysis is used to develop zeroth-and first-order perturbation equations. The zeroth-order solution provides the zero-eccentricity flow conditions (including the seal mass-leakage flow rate), with rotor rotation but without precession. Pressure perturbation values, part of the first-order solution, are integrated to provide the reaction forces on the rotor due to the assumed "small" circular orbit. The seal stiffness, damping, and added mass coefficients are related to the reaction forces on the rotor by the following equations:

$$F_r = -K - c\omega + M\omega^2 ,$$
$$F_\theta = k - C\omega$$

In the above equations, F_r and F_θ are the radial and tangential (i.e., tangential to the rotor "orbit") forces on the rotor, K and k are the direct and cross-coupled stiffness coefficients of the seal, C and c are the direct and cross-coupled damping coefficients, M is the "added mass", and ω is the orbit frequency in rad/sec. The cross-coupled coefficients account for

the fact that motion in one direction causes a force component perpendicular to the motion. If the tangential force is positive, it acts to support forward whirl (whirl in the direction of rotation), a destabilizing effect. The cross-coupled stiffness increases with an increasing fluid circumferential velocity component.

UPSTREAM CONDITIONS

The upstream conditions of the proposed damper bearing differ from those of the typical damper seal. For a damper seal, the upstream pressure is assumed constant; i.e., the assumed whirl motion does not cause a perturbation in the upstream pressure. The upstream fluid "reservoir" is assumed to have a nonzero circumferential component ("swirl") due to the rotation of the rotor, but no axial velocity. For the damper bearing, there are actually two seals, with the same inlet conditions. The exit pressures at the ends of the damper bearing are assumed equal. The total pressure upstream of each seal is the sum of the rotor internal pressure and the pump head due to the rotating feed holes, less the losses through the feed holes and the losses due to turning of the flow from the radial direction to the axial direction. The losses are functions of the flow velocity through the feed holes, as is the pump head if the angle of the feed holes from the radial direction is nonzero. If the feed holes are drilled at an angle opposite to the direction of rotor rotation, the swirl upstream of the seals is lower than for zero angle holes, which reduces the destabilizing cross-coupled stiffness of the seal. For a whirling rotor, the flow through the "tight" side of the seal is lower than the flow through the "wide" side. If the feed holes are drilled to reduce upstream swirl, the perturbation in the pump head and losses upstream of the damper bearing would result in a larger local pressure drop through the tight side of the seal than on the wide side. This perturbation in the upstream pressure has been included in the damper bearing analysis, and is the main difference between the damper seal and damper bearing analyses.

PREDICTIONS

The analysis has been programmed in FORTRAN, and runs in less than a minute on a personal computer. Using data from Tecza et al., and an inlet feed angle of 30 degrees from the radial direction for eight feed holes, the predicted stiffness is more than twice that predicted for the turbine end damper seal proposed by Tecza et al., (1,500,000 lb/in compared to about 700,000 lb/in), an improvement in load carrying capacity. The predicted cross-coupled stiffness (160,000 lb/in) is about 10% of the direct stiffness, as required by Tecza et al., and the direct damping is higher than required (210 lbs/in compared to a requirement of 125 lbs/in).

RECOMMENDATIONS

Based on the predictions of the present analysis, the damper bearing is preferable to the damper seal proposed by Tecza, et al. However, two aspects of the model which should be investigated further are:

1) the inlet loss model, and
2) the wall shear stress model.

Previous experimental and analytical work on annular seals in compressible flow have shown that the choices of an inlet loss model and wall shear stress model have significant effects on seal rotordynamic predictions. For example, two models with different inlet loss and wall shear stress (or friction factor) models may predict seal leakage within a few percent of experimental data, but stiffness coefficients that differ by an order of magnitude.

REFERENCES

Childs, D. W., 1984, "Finite-Length Solutions for the Rotordynamic Coefficients of Constant-Clearance and Convergent-Tapered Annular Seals," 3rd International Conference on Vibrations in Rotating Machinery, The Institution of Mechanical Engineers, York, England, Sept. 10-12.

Nelson, C. C., and Nguyen, D. T., 1987, "Comparison of Hirs' Equation With Moody's Equation for Determining Rotordynamic Coefficients of Annular Pressure Seals," *ASME Journal of Tribology*, Vol. 109, No. 1, pp. 144-148.

Tecza, J., Pinkus, O., and Buckman, P., 1989, "Damping Seal Rotor Support in Turbomachinery," Final Report, NASA Contract No. NAS8-36957.

1990

NASA/ASEE SUMMER FACULTY FELLOWSHIP PROGRAM

MARSHALL SPACE FLIGHT CENTER
THE UNIVERSITY OF ALABAMA

MECHANICAL DESIGN PROBLEMS ASSOCIATED WITH

TURBOPUMP FLUID FILM BEARINGS

Prepared By: Charles R. Evces

Academic Rank: Professor

University and   The University of Alabama
Department: Mechanical Engineering

NASA/MSFC:

        Laboratory: Propulsion
        Division: Component Development
        Branch: Turbomachinery &
                           Combustion Devices

MSFC Colleague: Henry P. Stinson

Contract No: NGT-01-002-099
                           The University of Alabama
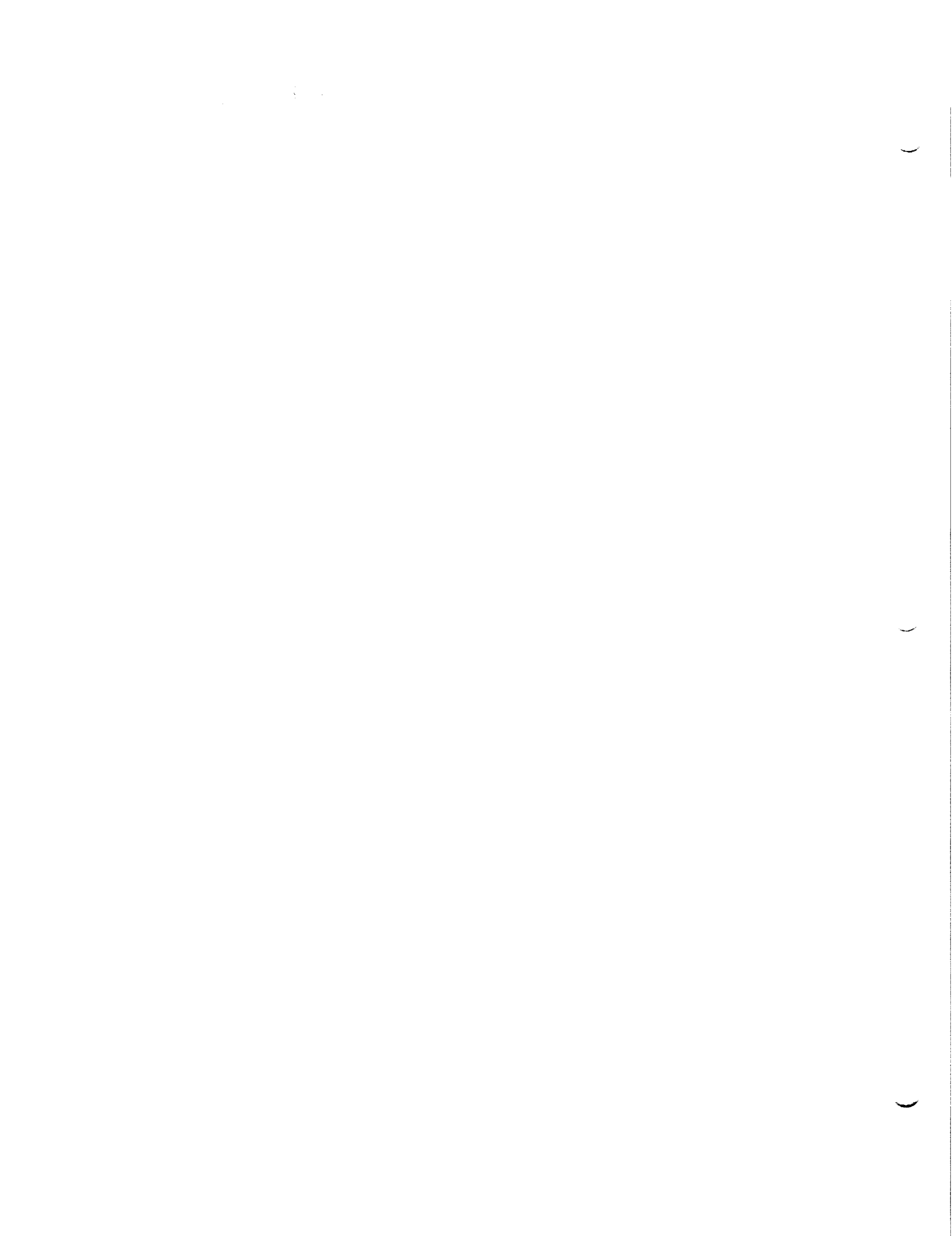
INTRODUCTION

Most high speed cryogenic turbopumps for liquid propulsion rocket engines currently use ball or roller contact bearings for rotor support. The operating speeds, loads, clearances, and environments of these pumps combine to make bearing wear a limiting factor on turbopump life. An example is the high-pressure oxygen turbopump (HPOTP) used in the space shuttle main engine (SSME). Although the HPOTP design life is 27,000 seconds at 30,000 rpm, or approximtely 50 missions, bearings must currently be replaced after 2 missions [1]. One solution to the bearing wear problem in the HPOTP, as well as in future turbopump designs, is the utilization of fluid film bearings in lieu of continuous contact bearings.

Hydrostatic, hydrodynamic, and damping seal bearings are all replacement candidates for contact bearings in rocket engine high speed turbomachinery. These three types of fluid film bearings have different operating characteristics, but they share a common set of mechanical design opportunities and difficulties. Results of research to define some of the mechanical design issues are given in this report. Problems considered include transient start/stop rub, non-operational rotor support, bearing wear inspection and measurement, and bearing fluid supply route. Emphasis is given to the HPOTP preburner pump (PBP) bearing, but the results are pertinent to high-speed cryogenic turbomachinery in general.

START/STOP RUB

The basic concept of fluid film lubrication is that the fluid film pressure prevents journal contact with the bearing. In rocket engine turbopumps, the pumped fluid is also the lubricant. At pump start up there is insufficient pressure to lift the rotor and an initial rub occurs between the rotor and bearing. The rub continues until fluid flow is sufficient for the lubricating film to form. The rub causes bearing and rotor wear, creates the danger of fire and explosion in liquid oxygen (LOX) pumps, and produces an initial backward rotor whirl.

The rub problem could be eliminated by the use of a secondary pressure source to float the rotor prior to initial rotation or by insertion of a contact bearing in parallel or series with the fluid film bearing. A secondary pressure source would require piping, valves and controls leading to an unacceptable increase in system weight and complexity. A hybrid contact-fluid bearing is more complex and has a larger space requirement than fluid bearings, and could still be a limiting factor in higher speed future generation pumps.

Fluid film bearing designs that withstand the start-stop rub problems have been available since at least 1969 [2]. A primary consideration is the appropriate bearing material for the particular cryogen. Materials testing and development is being conducted by several contractors and

agencies, but wear-related data is still relatively unavailable to the designer.

No transient start-stop rotordynamic model is available to provide the designer with quantitative or qualitative information on the number, duration and severity of rubs, what wear might occur, when rotor lift develops, or the general bearing presteady-state dynamic behavior prior to actual construction and testing of a prototype pump. This is likely due to the difficulties of developing an analytical dynamic model. The start-stop transient bearing supply pressure creates a time-variable bearing flow rate and stiffness that is perhaps also nonlinear. It is not known whether a dry friction, viscous friction, smearing or abradable rub model best represents the physics of actual rubs. Yet the rub model selected will affect the system model behavior [3]. The rotor speed and applied load transients depend upon which engine system is using the pump. In the case of hydrostatic bearings, there is likely a combined hydrostatic/hydrodynamic effect. A rigid rotor model could be sufficient for design purposes, but a flexible shaft model might provide more realistic results.

NONOPERATIONAL ROTOR SUPPORT

Fluid pressure is not available to support the rotor when the pump is nonoperational during descent from orbit, landing, ferrying and ground handling. In static equilibrium the rotor rests on the bearing surface, but due to bearing clearance is free to rattle within the bearing as the pump is moved. The magnitude of the stresses generated by motion-induced impacts between the rotor and bearing depend upon the magnitude and frequency of the the loads, the dimensions and material properties of both the rotor and bearing, and the bearing clearance. Surface damage to the bearing land and rotor surfaces could reduce bearing efficiency and rotor fatigue life.

WEAR DETECTION

Post-operational wear detection methods, without pump removal from the engine, need to be developed for fluid film bearings. Bearing wear due to rubs is not axially or circumferentially uniform. The required measurement sensitivity depends upon the amount of bearing wear permissable before performance degrades, which is probably a fraction of the few thousandths of an inch bearing clearance.

Static load-deflection methods which correlate changes in bearing stiffness with wear, similar to that used for HPOTP ball bearings, is a possible measurement technique. Signature analysis on data recorded either during or after operation could provide wear information.

FLUID SUPPLY ROUTE

The fluid supply route must be from a high pressure source to a low pressure sink. Details of the route depend upon the bearing type and pressure requirements, as well as the location of available sources and sinks. Flow is directly through a hydrodynamic journal bearing, whereas hydrostatic bearings are fed either externally through the bearing or internally through the rotor. In the case of the HPOTP pump end (PE) bearing, for either a journal or externally fed bearing design, the likely source is the preburner impeller outlet (approx. 7000 psi) with the sink at the main pump inlet (approx. 300 psi). Sufficient flow probably does not exist for an internally fed HPOTP PE bearing since turbine end coolant is drawn through the rotor cavity.

Fluid filtration must be provided in the coolant path to remove solid particles that could cause bearing damage by being trapped in the small clearances. Projected clearances for the HPOTP PE bearing are in the range of 0.0002 in to 0.0008 in whereas the maximum LOX particle size permitted for the SSME is approximately 0.032 in.

REFERENCES

[1] Butner, M.F. and Murphy, B.T.: SSME Long Life Bearings. Final Report, NASA CR-179455, July, 1986.

[2] Reddecliff, J.M. and Vohr, J.H. : "Hydrostatic Bearings for Cryogenic Rocket Engine Turbopumps". Journal of Lubrication Technology, July, 1969.

[3] Kascak, A.F. and Tomko, J.J.: Effects of Different Rub Models on Simulated Rotor Dynamics. NASA Technical Paper 2220, February, 1984.
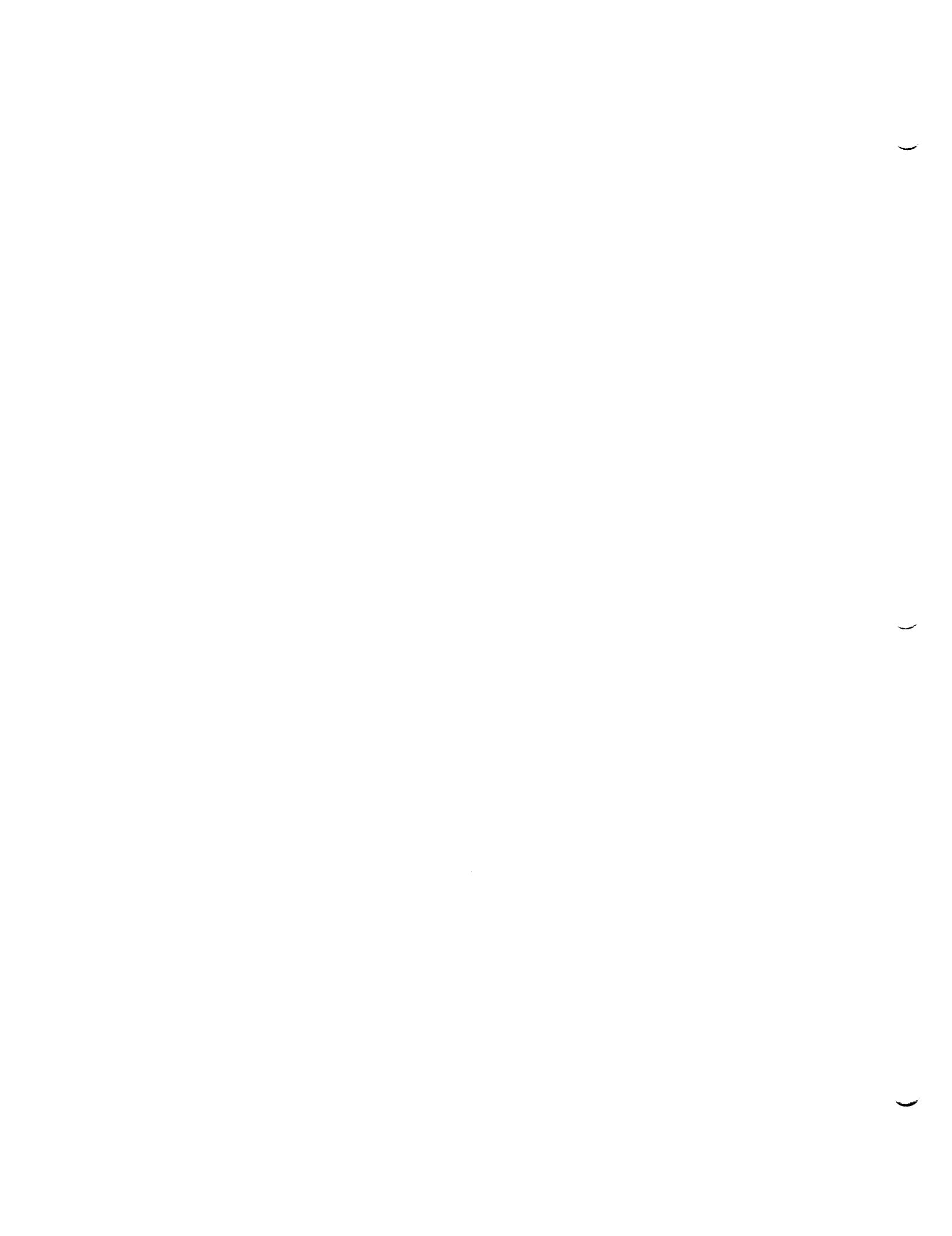
1990

NASA/ASEE SUMMER FACULTY FELLOWSHIP PROGRAM

MARSHALL SPACE FLIGHT CENTER
THE UNIVERSITY OF ALABAMA

DISK FLEXIBILITY EFFECTS ON THE ROTORDYNAMICS
OF THE SSME HIGH PRESSURE TURBOPUMPS

Prepared by: George T. Flowers

Academic Rank: Assistant Professor

University and Department: Auburn University

                                       Department of Mechanical Engineering

NASA/MSFC:

    Laboratory: Structures and Dynamics

    Division: Control Systems

    Branch: Mechanical Systems Control

MSFC Colleague: Donald P. Vallely

Date: August 10, 1990

Contract No.   The University of Alabama

                                       NGT-01-002-099
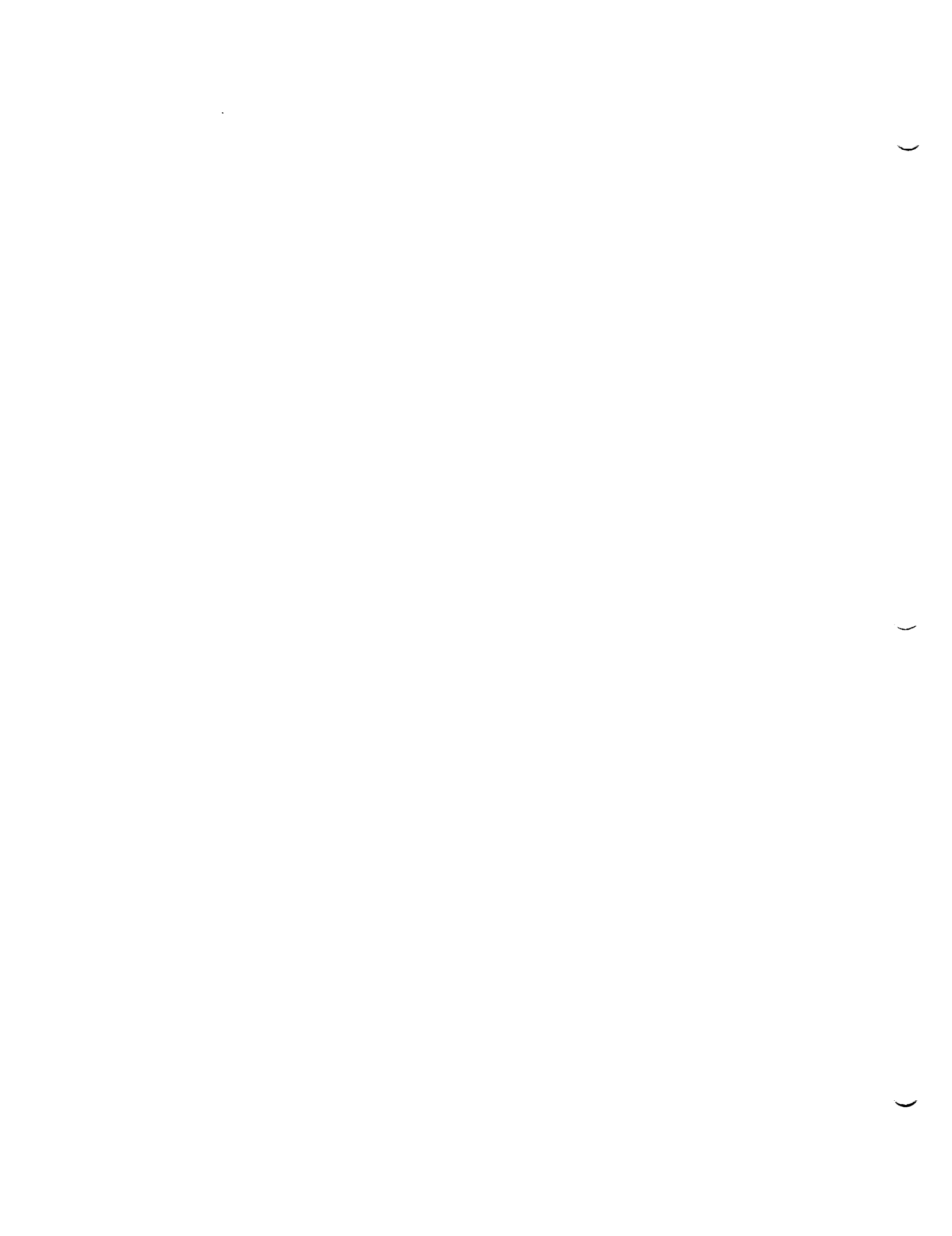
Introduction

Rotordynamical analyses are typically performed using rigid disk models. Studies of rotor models in which the effects of disk flexibility have been included indicate that it may be an important effect for many systems. This work addresses this issue with respect to the Space Shuttle Main Engine high pressure turbopumps. Finite element analyses have been performed for a simplified free–free flexible disk rotor model and the modes and frequencies compared to those of a rigid disk model. Equations have been developed to account for disk flexibility in rotordynamical analysis. Simulation studies have been conducted to assess the influence of disk flexibility on the HPOTP. Some recommendations are given as to the importance of disk flexibillity and for how this project should proceed.

Research Accomplishments

This research effort has accomplished the following tasks.

1.) A simplified finite element model of the HPOTP rotor has been developed. This model accounts for the flexibility of the first and second turbine stage disks. All the other rotor disks are modelled as rigid structures.

2.) Equations have been derived that include the effects of disk flexibility on rotordynamical behavior. The equations are quite similar in form to those typically used for rigid disk models, but two additional matrix terms are included. The resulting equations are of the form:

$$\{\ddot{q}_y\} + \Omega[\Gamma + A]\{\dot{q}_z\} + [\omega_n^2 + B]\{q_y\} + (\text{damp. and intercon. terms}) = \{0\}$$

$$\{\ddot{q}_z\} - \Omega[\Gamma + A]\{\dot{q}_y\} + [\omega_n^2 + B]\{q_z\} + (\text{damp. and intercon. terms}) = \{0\}$$

The two additional terms in these equations, A and B, are modal integrals over each rotor disk and reduce to the corresponding rigid term when the rigid disk modes are used. Axial coupling effects are neglected in this development.

3.) Modifications to include disk flexibility in the current rotordynamical analysis package have been implemented. **Stab** and **Tran** have been modified and appropriate data files have been generated to incorporate disk flexibility effects.

4.) A number of simulation and parameter variation studies have have been performed. The revised rotordynamical analysis programs have been tested with modal data from a simplified rotor finite element model. (HPOTP phase 1 rotor with flexible turbine stage disks) Eigenanalyses indicate that flexible disk effects are exhibited at frequencies significantly above the operating speed range of the HPOTP. Only minor effects are observed for synchronous vibration. Transient studies in which rub and bearing deadband are incorporated into the turbine interstage seal were also conducted (using TRAN). These studies indicate that the excitation of high frequency modes can lead to predictions of signficantly different dynamical behavior by rigid and flexible disk rotor models.

Recommendations

1.) Include disk flexibility effects in rotordynamical analyses in which supersynchronous frequencies are of interest.

2.) Develop a technique to modify contractor supplied free-free rotor frequencies and mode shapes to account for disk flexibility effects. This would serve to simplify the finite element work required to implement the analysis procedure and to insure compatibility between NASA analyses and contractor analyses.

3.) Extend the analysis procedure to include axial coupling effects.

4.) In order to develop further physical insight into the effect of rotor disk flexibility, construct appropriately scaled rotor models and study their responses using a rotor test kit.

5.) Examine dynamic data from SSME engine tests to determine if any 'anomalous' behavior can be related to disk flexibility effects.
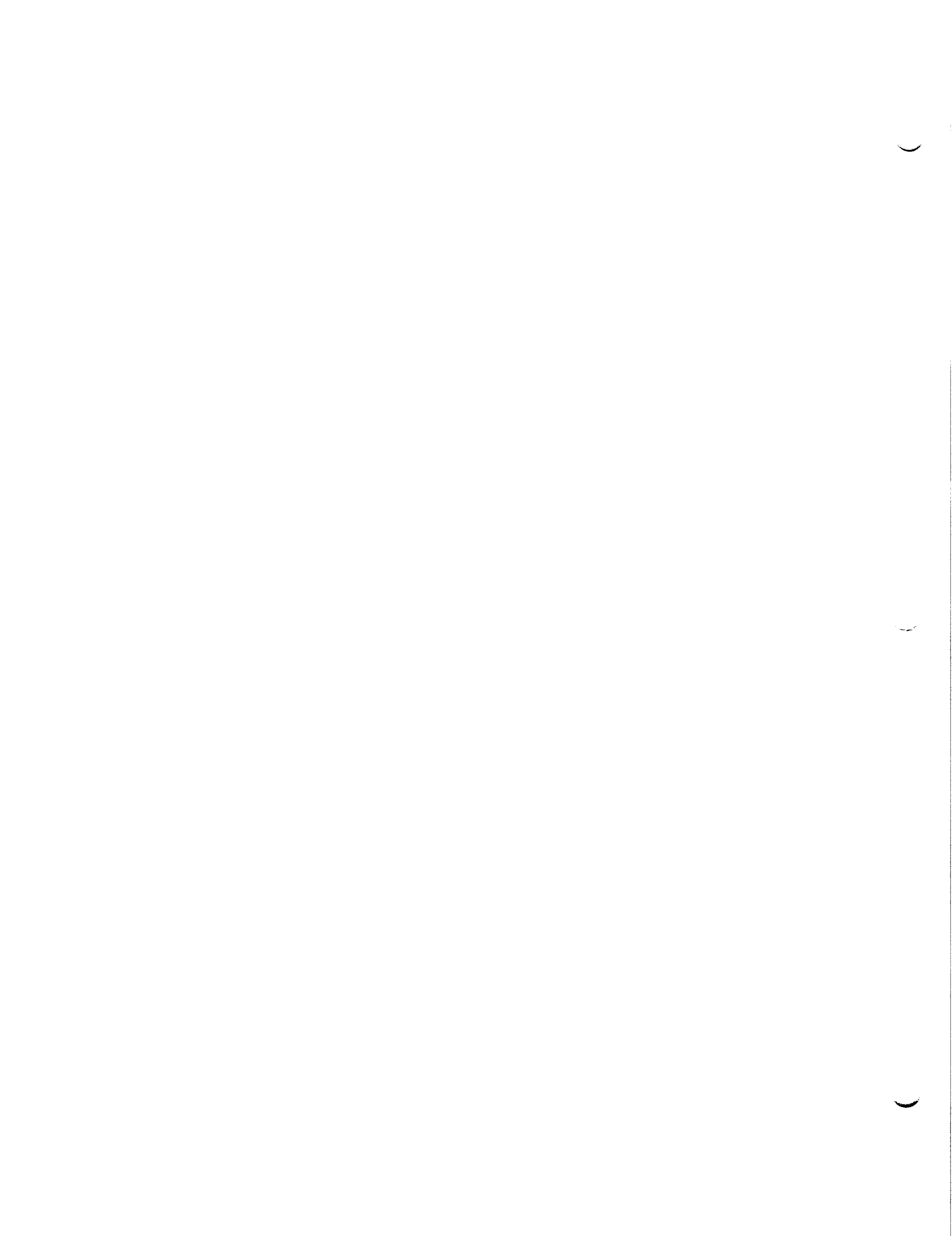
1990

NASA/ASEE SUMMER FACULTY FELLOWSHIP PROGRAM

MARSHALL SPACE FLIGHT CENTER
THE UNIVERSITY OF ALABAMA

ESTABLISHMENT OF A STRAIN ANALYSIS CAPABILITY USING
PHOTOELASTIC COATINGS

Prepared By: Samuel C. Gambrell, Jr.

Academic Rank: Professor

University and   University of Alabama, Tuscaloosa
Department: Engineering Mechanics

NASA/MSFC:

        Laboratory: Structures and Dynamics
        Division: Structural Test
        Branch: Structural Test

MSFC Colleague: Mr. G.B. Waggoner
                            Mr. D.E. Snoddy

Contract No.   NGT-01-002-099
                            The University of Alabama
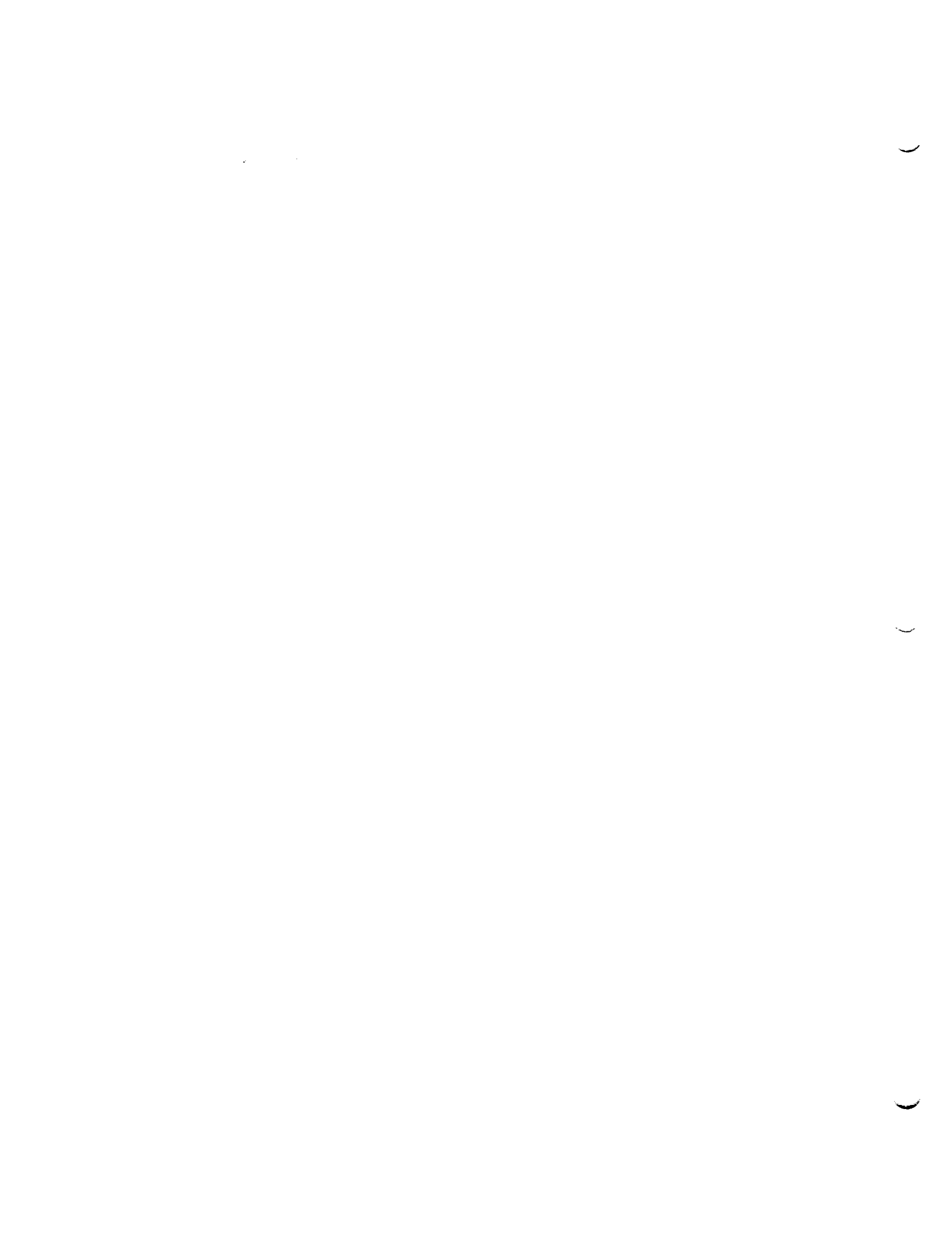
In accordance with the Research Plan prepared at the beginning of the Fellowship Program, my summer activities consisted of:

1. training personnel of the Structural Test Division of the Structures and Dynamics Laboratory in the theory and practice of strain analysis using photoelastic coatings; and

2. performing strain analysis using photoelastic coatings on appropriate test articles.

In support of these activities, the following actions have been taken:

1. equipment and supplies necessary for strain analysis using photoelastic coatings were specified, purchased, and checked out;

2. four engineers were trained in the theory and practice of strain analysis using photoelastic coatings;

3. four technicians were trained in the practice of preparing and applying photoelastic coatings to both curved and flat surfaces;

4. in addition to the final program seminar, three seminars on the fundamentals and use of photoelastic coatings were presented to a total of 43 members of the various laboratories at MSFC;

5. a photoelastic coating was applied to and used in a test of a thrust vector control corner section;

6. to further assist engineers with use and understanding of photoelastic coatings, fifteen journal articles were located and copied, and camera settings for photographing fringe patterns were determined and recorded;

7. two proposals for (a) providing technical assistance in strain analysis at MSFC and (b) testing of selected components/assemblies at the University of Alabama in Tuscaloosa have been written for submission to NASA.
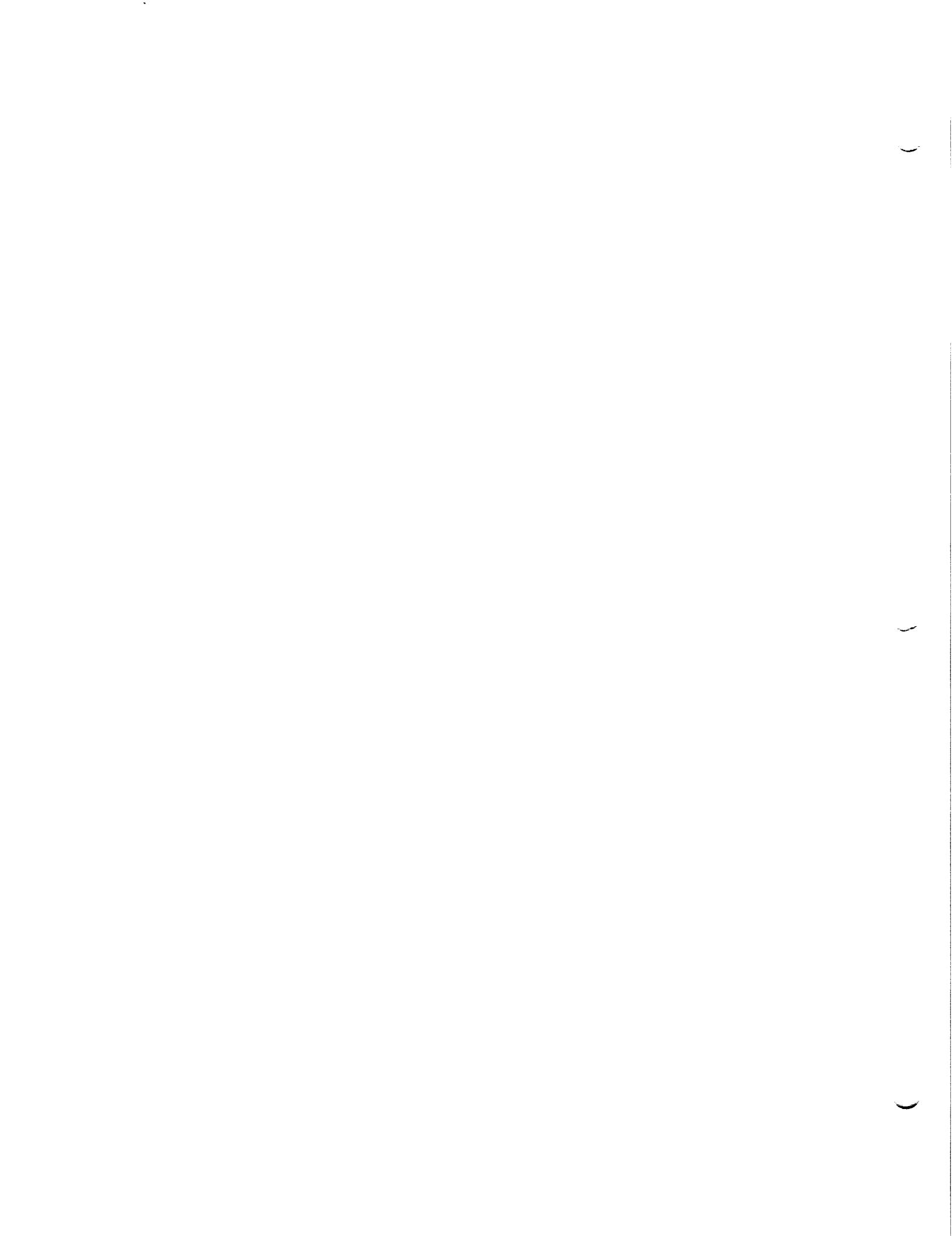
NASA/ASEE SUMMER FACULTY FELLOWSHIP PROGRAM

MARSHALL SPACE FLIGHT CENTER
THE UNIVERSITY OF ALABAMA

MULTI-BLOCKING STRATEGIES FOR THE INS3D

INCOMPRESSIBLE NAVIER-STOKES CODE

Prepared By: Boyd Gatlin

Academic Rank: Assistant Professor

University and   Mississippi State University
Department   Aerospace Engineering

NASA/MSFC:

        Laboratory: Structures and Dynamics
        Division: Aerophysics
        Branch: Computational Fluid Dynamics

MSFC Colleague: Dr. Paul K. McConnaughey

Contract No: NGT-01-002-099
                         The University of Alabama
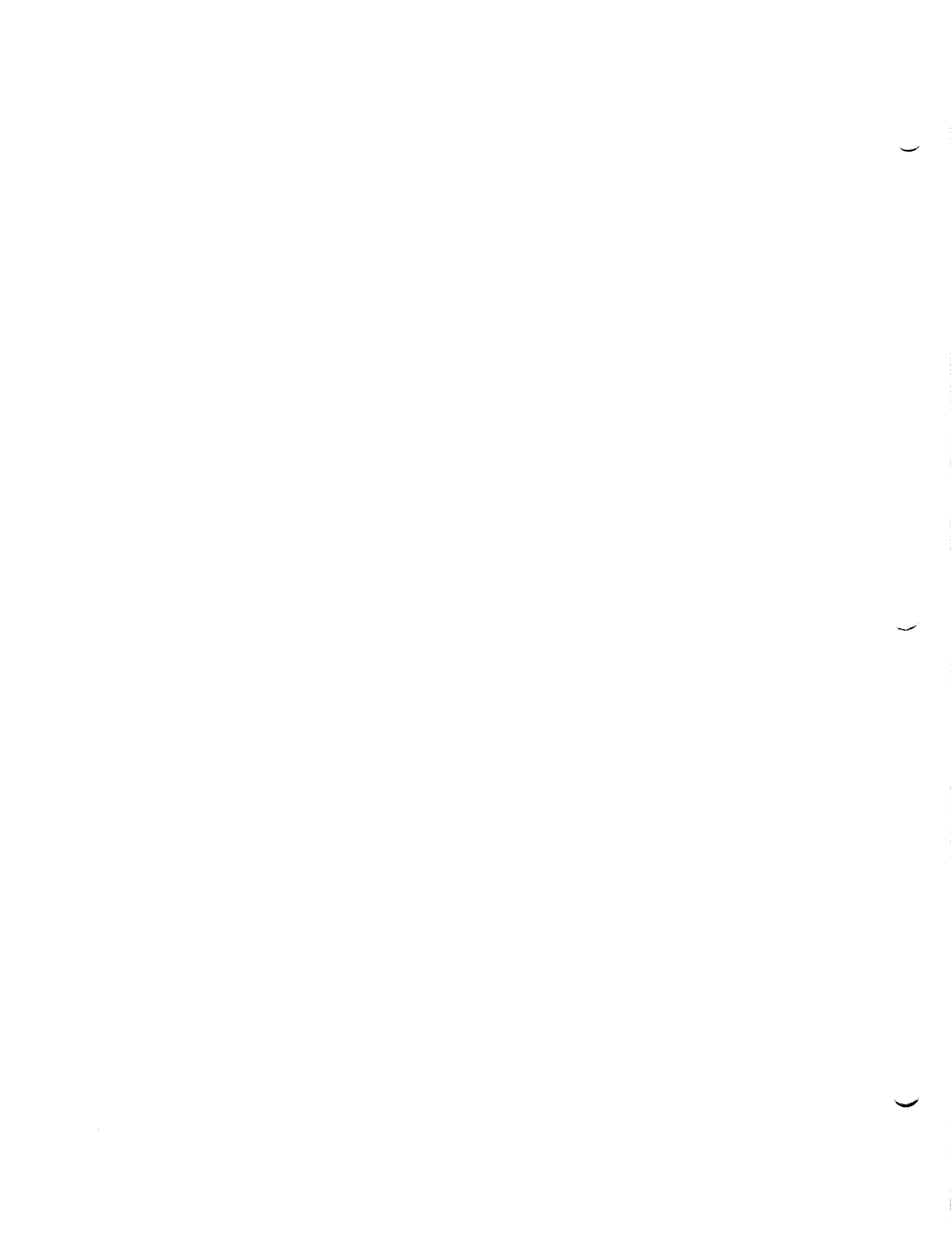
MULTI-BLOCKING STRATEGIES FOR THE INS3D

INCOMPRESSIBLE NAVIER-STOKES CODE

Boyd Gatlin
Mississippi State University

INTRODUCTION

With the continuing development of bigger and faster supercomputers, computational fluid dynamics (CFD) has become a useful tool for real-world engineering design and analysis. This is particularly true in cases where experimental data is too expensive or impossible to obtain. However, the number of grid points necessary to resolve realistic flow fields numerically can easily exceed the memory capacity of available computers. In addition, geometric shapes of flow fields, such as those in the Space Shuttle Main Engine (SSME) power head, may be impossible to fill with continuous grids upon which to obtain numerical solutions to the equations of fluid motion.

The solution to this dilemma is simply to decompose the computational domain into sub-blocks of manageable size. Computer codes that are single-block by construction can be modified to handle multiple blocks, but *ad hoc* changes in the FORTRAN have to be made for each geometry treated. For engineering design and analysis, what is needed is generalization so that the blocking arrangement can be specified by the user. This enables the engineer or analyst to concentrate on the flow problem and its solution rather than on programming.

INS3D is a computer program for the solution of steady, incompressible flow problems. Developed at NASA Ames Research Center, it is used frequently to solve engineering problems in the CFD Branch at Marshall Space Flight Center. INS3D uses an implicit solution algorithm and the concept of artificial compressibility to provide the necessary coupling between the pressure field and the velocity field. The thrust of the work reported here is the development of generalized multi-block capability in INS3D.

BLOCKING STRATEGIES

Central to the concept of multi-block computations is the requirement that only one block occupy core memory at any time. After each time step or iteration, the current block is written to an out-of-core device such as magnetic disk, and the next block is read in. This process is carried out over all blocks and then is repeated until the solution

converges to some tolerance. Clearly, the issue of communication among the blocks is immediately raised, since the solution must have the same order of accuracy at block interfaces as it does over the rest of the field. In addition, the solution must be continuous and smooth.

An obvious approach is to construct grids such that one or more surrounding layers of points of one block overlaps into the adjoining blocks. For a central-difference algorithm with second-order spatial accuracy, such as INS3D, only one such overlapping layer is needed. Points along the block interface can then be computed as field points in the usual way. The overlapping points which are interior field points in the adjoining block serve as boundary values in the current block, and vice versa. This amounts to an implicit treatment of block interfaces at the same order of accuracy as that over the rest of the field.

However, this mutual overlapping of all adjoining blocks results in a non-unique solution along block interfaces, since these points are computed in both blocks. In principle, the values would be identical at complete convergence, but as a practical matter this is not true. One treatment used in this work is to simply average the two values in order to obtain a unique solution on the interfaces.

A more sophisticated approach is to have only one of two adjoining blocks overlap into its neighbor. Under this approach, the block interface is computed in only the current block, and the interface then serves as a true boundary for the neighboring block. This requires considerably more programming logic to keep track of the relationship among several interfacing blocks. In fact, more work remains to be done on this issue for cases where several blocks share a common corner.

Since INS3D is a central-difference scheme, artificial dissipation terms are needed to damp out oscillations resulting from the odd-even decoupling inherent in the differencing molecule. At block interfaces, these can be evaluated as one-sided differences, as is done at natural boundaries. However, it was found that central differencing of these terms leads to more computational stability at block boundaries.

The effect of using overlapping solution values is, of course, to increase the size of the block to be solved by at most two in each coordinate direction. An important drawback to out-of-core storage of overlap values is that each time a block is to be computed, it must first be loaded into core, and, in the general 3D case, its boundary values must be updated by reading each of the six or more

surrounding blocks and extracting the overlapping layers, one block a at a time. The resulting I/O operations would quickly become prohibitive.

A more efficient method is to maintain in-core arrays of block interface and overlap layers. This does not result in any significantly greater core storage than would be necessary if blocks were swapped in and out of core in order to extract boundary values, since that approach would require that two blocks occupy internal storage simultaneously. However, it is much faster, since the I/O operations are drastically reduced.

USER INPUT

The relationships among the blocks in a domain are specified by user input through the NAMELIST utility, consistent with that in the original, one-block version of INS3D. In principle, arbitrary blocking configurations and boundary conditions can be treated without program modifications. In practice, however, there will inevitably be cases which will have to be treated individually through modifications to subroutines which set initial conditions and boundary conditions.

In setting up the relationship between any two blocks, one is take to be BLKA, the current block, and the other BLKB, the neighboring block. The common interface is then specified by STARTA and ENDA in BLKA and by STARTB and ENDB in BLKB, where START and END are indices of the starting and ending points of the block boundary. Each BLK is assumed to have six faces, identified in BLKA, for example as SURFA=___, where ___ indicates the face. The numbering scheme for faces is such that SRFA=1 indicates the face corresponding to the minimum value of J, the number one index in INS3D. SRFA=6, then, would refer to the face in BLKA where the number three index, L, is maximum.

Boundary conditions for all blocks are established in the same way. Block interfaces are simply treated as another type of boundary condition. For each block face, its boundary conditions are established with a simple user flag. For example, BCTYPE=1 imposes no-slip on a block boundary, while BCTYPE=4 causes the boundary to be computed using mutually overlapping layers with BLKB. Several BCTYPE options will be eliminated when the code is released to MSFC, since they invoke conditions used only experimentally during the development.

RESULTS AND SUMMARY

Only preliminary results were obtained during the
Summer Fellowship period. Several two-dimensional cases
were run successfully, but the persistent presence of
pressure disturbances in the neighborhood of block
interfaces indicates that there are subtle problems yet to
be addressed. Indications are that a way must be found to
effectively smooth the pressure field at block interfaces.
A good possibility would be to install adjustable damping
terms in the pressure equation in the neighborhood of block
interfaces.

A few three-dimensional cases were computed, including
a straight circular duct and a circular duct with a 90-
degree bend. Both cases diverged because of contamination
of the solution at block interfaces. In order to try to
isolate the problem, the straight circular duct was computed
with inviscid conditions. With no errors in the code, this
case should have converged immediately, since the initial
conditions specified were, in fact, the correct solution.
Instead, the solution diverged very slowly. Analysis of the
results indicated a false pressure gradient arising at the
block interface. The source of this problem was not
discovered by the end of the fellowship period.

However, the basic algorithm and underlying blocking
strategy are now fully developed and working in INS3D. With
additional collaborative efforts between the author and
engineers in the MSFC CFD Branch, the remaining difficulties
can be resolved.

1990

NASA/ASEE SUMMER FACULTY FELLOWSHIP PROGRAM

MARSHALL SPACE FLIGHT CENTER
THE UNIVERSITY OF ALABAMA

NASA ACCOUNTING AND FINANCIAL INFORMATION SYSTEM (NAFIS): A CRITICAL ASSESSMENT OF THE SYSTEMS DEVELOPMENT METHODOLOGY

Prepared By: Ernest Preston Goss

Academic Rank: Associate Professor

University and   University of Southern Mississippi
Department: Management Information Systems

NASA/MSFC:
        Laboratory: Institutional and Program Support
        Division: Information Systems
        Branch: Data Systems

MSFC Colleague: Mr. Alan Forney

Contract Number: NAS-837-200
                        The University of Alabama
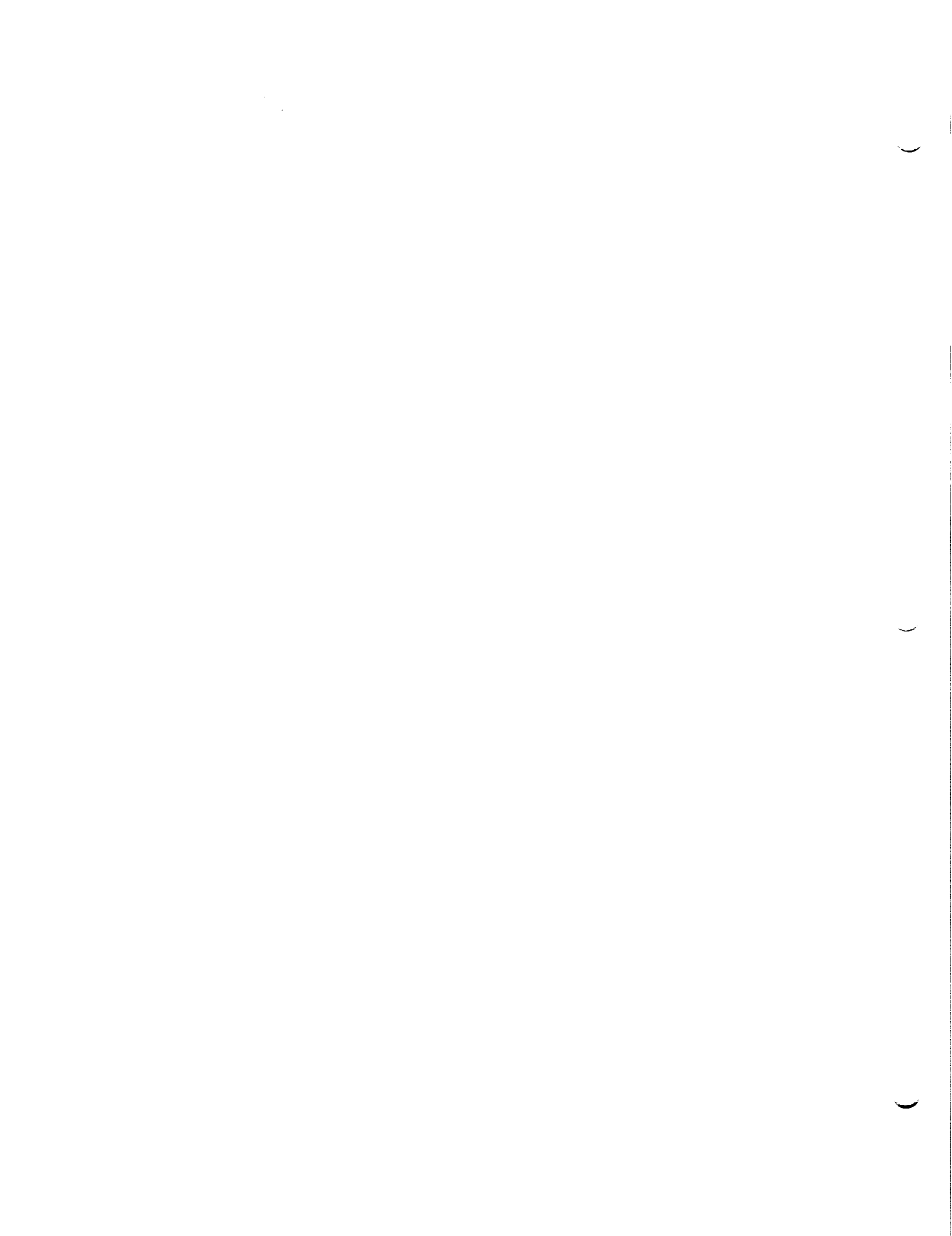
NASA ACCOUNTING AND FINANCIAL INFORMATION SYSTEM (NAFIS): A CRITICAL ASSESSMENT OF THE SYSTEMS DEVELOPMENT METHODOLOGY

In partial fulfillment of my Summer Faculty Fellowship contractual obligation, Mr. Alan Forney instructed me to examine the NAFIS systems development methodology and make recommendations to improve the process. The following comments represent a summary of my recommendations:

1. Recognize that system success is more of a function of good managerial practices than good technology and/or good coding.

2. Develop a systematic method of dealing with changes in requirements during the life cycle. Each document should outline how changes will be made during development and after implementation.

3. Clearly establish if NAFIS is a management information system (MIS) or an accounting and financial system. This must be conveyed to site managers and users early in the process since heightened expectations by users can be deadly to the perceived success of the project.

4. Undertake Independent Verification & Validation (IV&V) early in the life cycle. This could be problematic since the SRS's could be completed before an IV&V contractor is under contract. Since many of the errors occur early in the life cycle, the IV&V activity will be less effective.

5. Charge the IV&V contractor with providing periodic estimation of project costs and progress as they relate to the NAFIS plan. New estimates should be developed whenever specifications change.

6. Maintain file of potential operational and managerial problems throughout the development life cycle.

7. Develop metrics for system success. Document delivery must not serve as a metric for system success.

8. Undertake prototyping to insure that systems requirements established by upper level management satisfy those who actually use the system. This is an important task since it provides the user with a tangible product before systems implementation. Prototyping reduces the risk of being in a situation whereby be no implementation is consistent with the specification and at the same time provides the desired functionality.

9. Reduce unrealistic expectations among users. Heightened or unrealistic expectations can be a serious problem exacerbated by prototyping. Moreover due to the rapidity of prototyping, there is much less time to

recover from gaps in the SRS. Contractor must insure that prototyping does not create unrealistic expectations among users.

10. Insure that the SRS is understandable to the user. The user sees each process in a functional manner. The SRS should be compartmentalized in the same manner that the user views the system. For example, the user views travel as either a new travel request or as edit of an old travel request. To accomplish this, it is recommended that the SRS be more clearly sub-divided.

11. Don't use document delivery as a metric of project state.

12. Need to map SRS to documents that are familiar to the user. In the case of travel, the sections of the SRS should refer to portions of the travel document in a generic way since the travel documents will likely change after implementation.

13. The SRS should identify maintenance issues focusing on those events that stand a high probability of occurrence.

14. Additionally, Mr. Forney asked me to examine the Systems Requirements Specification (SRS) for the Travel Function. The following represent a summary of my comments:

14A. Specificity. If the SRS is not detailed enough, then the design process will take much longer and will be much more iterative. It is important that the SRS contain the correct level of detail to avoid the "yo-yo" effect whereby the design is changed to reflect ever changing, amorphous or misunderstood requirements. Ideally the requirements document would enumerate the reports and discuss the contents and calculation of each field.

14B. User Perspective. Document should have the user's "looking-in" perspective. A key problem in fostering communication is to have a common terminology. One objective of the SRS is to establish a common terminology.

14C. Functional and Non-Functional Requirements. The document must address both functional and non-functional boundaries and behaviors. These non-functional requirements are related to characteristics like security or project management that place boundaries on acceptable solutions.

14D. Maintenance & Documentation. Maintenance must be planned and designed into the software. For example, the SRS should address such issues as the ability to add fields to the form, table or

report? How is it done? If an signature is added to the travel document, how is it added? Maintenance consideration warrant a separate section. Ease of maintenance must include planned changes as well as repairs. Anticipated changes due to hardware evolution and changing user needs should to also be identified in the SRS. The maintenance of the code once it has been deployed will, in all likelihood, be by groups not originally involved in the design. Their training will be greatly enhanced if the requirements document can be used as a reference to design decisions and other controlling design documents. SRS should evolve to be a reference document.

14E. Mapping. The user should be able to map each portion of the SRS to a form or document that he/she is now familiar with. As the SRS currently exists, the user would be unable to map the travel forms to the SRS. This would be very helpful to the user who is most familiar with the travel forms and tends to relate processes to the actual form.

14F. Interface Requirements. For each interface, the following should be specified: a) Description of operational considerations of data transfer, such as security considerations. What protection is offered one part of system from corruption from another part? b) General description of data transfer requirements to and from the subject system and characteristics of communications media/systems used for the transfer. c)Type of anticipated interface, such as manual or automatic. d) Anticipated interface procedures, including telecommunications considerations.

14G. Prototyping. User satisfaction is diminished by the passage of time between requirements generation and system delivery. Prototyping is very useful in allaying the dissatisfaction of users. Additionally prototyping can prove to be highly effective for early identification of specification faults. Nonetheless, the prototyping does not obviate the need for a detailed SRS. Moreover, with prototyping as part of the development or life cycle process, there is much less time to recover from gaps in the SRS.. Thus a non-detailed SRS becomes problematic.

14H. Readability. Sequencing---so that the user is more able to understand the SRS, it would be very useful if the sequencing of processes were made more clear in the SRS. This could be done by sub-dividing the SRS into processes that are more understandable to the users and clearly dividing them. For example, the SRS could be color coded or tabbed. The current method of using the numbering scheme to

divide the SRS should be supplemented with more clear distinctions between sections. Page numbers could be used to more clearly divide the travel sections. It is recommended that a third digit be added to the page numbers to indicate divisions within the SRS. Printing on front and back of pages would also make the SRS less formidable. The addition of footnotes of relevant data dictionary items in the SRS would prove especially helpful in certain instances.

14I. <u>Security Requirements</u>. Are there not overall unique security requirements relevant to travel? For example, insuring travel funds are not channeled to other fund accounts. The ability of a large number of individuals to update central data stores (e.g. NPPS) could present problems. Some of the security measures should be brought out in the SRS.

14J. <u>Other Questions or Comments</u>. a) will system maintain an edit history for certain accounts and certain fields? Can it track who updated certain important fields? b) Is foreign travel really a separate entity? As presented in SRS it appears to be almost identical to domestic travel. However, examining the travel forms, they are clearly not the same. c) The ability to change personnel information in the NPPS file at many junctures appears to open up potential integrity problems. d) When error messages are displayed, the SRS does not indicate what the user will do next.

1990

NASA/ASEE SUMMER FACULTY FELLOWSHIP PROGRAM

MARSHALL SPACE FLIGHT CENTER
THE UNIVERSITY OF ALABAMA

BATSE SOFTWARE FOR THE ANALYSIS OF THE GAMMA RAY BURST

SPATIAL DISTRIBUTION

Prepared By: Jon Hakkila

Academic Rank: Associate Professor

University and   Mankato State University
Department: Mathematics, Astronomy,
                                   and Statistics

NASA/MSFC:

        Laboratory: Space Science
        Division: Astrophysics
        Branch: High Energy Astrophysics

MSFC Colleague: Dr. Charles A. Meegan

Contract No: NGT-01-002-099
                                The University of Alabama

I. Introduction

The Burst and Transient Source Experiment (BATSE) on the Gamma Ray Observatory (GRO) is designed to study astronomical gamma ray sources and to provide better positional, spectral, and time resolution about these objects than has previously been possible from one experiment.

In particular, BATSE will study the phenomenon of the gamma ray bursts. These spurious high energy emissions have no known counterparts (either quiescent or variable) at other electromagnetic wavelengths, and their astrophysical sources have been difficult to identify. Much evidence exists (such as short-timescale variabilities indicative of compact emitting regions, emission lines characteristic of positron-electron annhilation, absorption features that seem to indicate cyclotron absorption corresponding to very strong magnetic fields, etc.) to suggest that the bursts arise from material accreting onto the surfaces or into the magnetospheres of Galactic neutron stars.

As suggestive as this evidence is of a Galactic origin for the bursts, distinct association of the burst spatial distribution with either the Galactic disk or the Galactic halo has not yet been verified. This is due to (1) the limited number of bursts known from balloon experiments and orbital satellites, (2) the inherent difficulties in measuring accurate burst positions, and (3) the severe selection effects present in attempting to observe bursts.

BATSE, with its four pi steradian sky coverage (over large timescales) to faint flux limits, should resolve the burst location problem within a matter of months. However, tests that measure and interpret isotropy and homegeneity of the spatial distribution must allow for unavoidable inaccuracies in measuring burst positions and account for the numerous selection effects that will be present due to inhomogenous sampling.

II. Overview of the Analysis Techniques and BATSE Software

The procedure to be used in the analysis of the gamma ray burst spatial distribution is depicted in figure 1. Data is input from BATSE via the Gamma Ray Burst Catalog (listing individual burst positions, flux values, and associated errors) and the Sky Sensitivity Map (which summarizes observational selection effects in table format).

A FORTRAN program generates Monte Carlo burst catalogs, which are models to be compared to the actual distribution. These models can be chosen to represent a number of spatial distributions (uniform, Galactic Disk, and Galactic Halo) while the source luminosities are selected from one of several luminosity functions (mono-luminosity, Gaussian, linear topheavy, linear bottomheavy, and power law). By this, many statistical selection effects (such as the Malmquist bias) are automatically included in the Monte Carlo data sets. The Monte Carlo models are then filtered through the Sky Sensitivity Map so that they suffer from the same selection effects as the actual catalog data. Additionally, each burst position is converted into a probability distribution to mimic BATSE positional sensitivity. In this manner the Monte Carlo models are created to suffer from many of the same systematic effects as the BATSE Burst Catalog so that statistical comparisons may be directly made between them.

The Burst Catalog, Monte Carlo burst catalogs, and Sky Sensitivity Map are then passed on to an IDL program that compares the catalogs for statistical significance. The Sky Sensitivity Map is used to estimate how often each sky area is observed above the minimum flux level in question. Each burst found in this sky area is then weighted according to the frequency with which this sky area is observed (such that a few bursts observed in a poorly-studied sky area are heavily-weighted).

The catalogs are then compared via tests of homogeneity (based upon their radial distributions) and isotropy (based upon their angular distributions). Among the statistical tests used to make these comparisons: The Log(N)_Log(N>S) test (which examines the homogeneity of the distribution), the <V/Vmax> test (which examines the sample's homogeneity based upon instrumental sensitivity), multipole analysis (which studies spatial isotropy of the sample), and a source cross-correlation analysis (another isotropy test). Errors are estimated concerning the validity of the comparisons by comparing many Monte Carlo burst catalogs (all generated from the same model) with the Burst Catalog via simple summaries (such as Kolmogorov-Smirnov estimators and the fractional or "tail-area" probabilities indicating that the two samples are drawn from the same parent distribution). The results of the statistical comparisons along with graphs and charts of the summaries, are output from the IDL program for study.

III. Current Status of the Analysis Programs, and Future Work

At the present time, the interactive FORTRAN Monte Carlo Burst Generation program is close to completion. It can effectively create the spatial distributions mentioned previously using any of the indicated luminosity functions. However, smearing of the point sources into probability distributions is dependent upon an as yet unmodeled functional form (to first order on the count rate of the source and to second order on the burst position in GRO coordinates). Before sources can be removed from the Monte Carlo burst catalogs via selection effects modeled in the Sky Sensitivity Map, a dummy Sky Sensitivity Map must be generated. The structure of this map is dependent upon the as yet unchosen format for the actual Sky Sensitivity Map.

The interactive IDL analysis program is not as close to completion as the Monte Carlo one. It is currently composed of a number of dissociated (and in some cases incomplete) modules. Tested FORTRAN code exists for the multipole analysis, and a rough IDL version of the Log(N)_Log(N>S) code is operational. The codes for <V/Vmax> and positional correlation do not yet exist (although the former is very easy to install). Summaries of model comparisons and associated IDL graphs are not yet coded.

IV. Acknowledgements

BATSE Analysis Software for Determining the Spatial Distribution of Gamma Ray Bursts
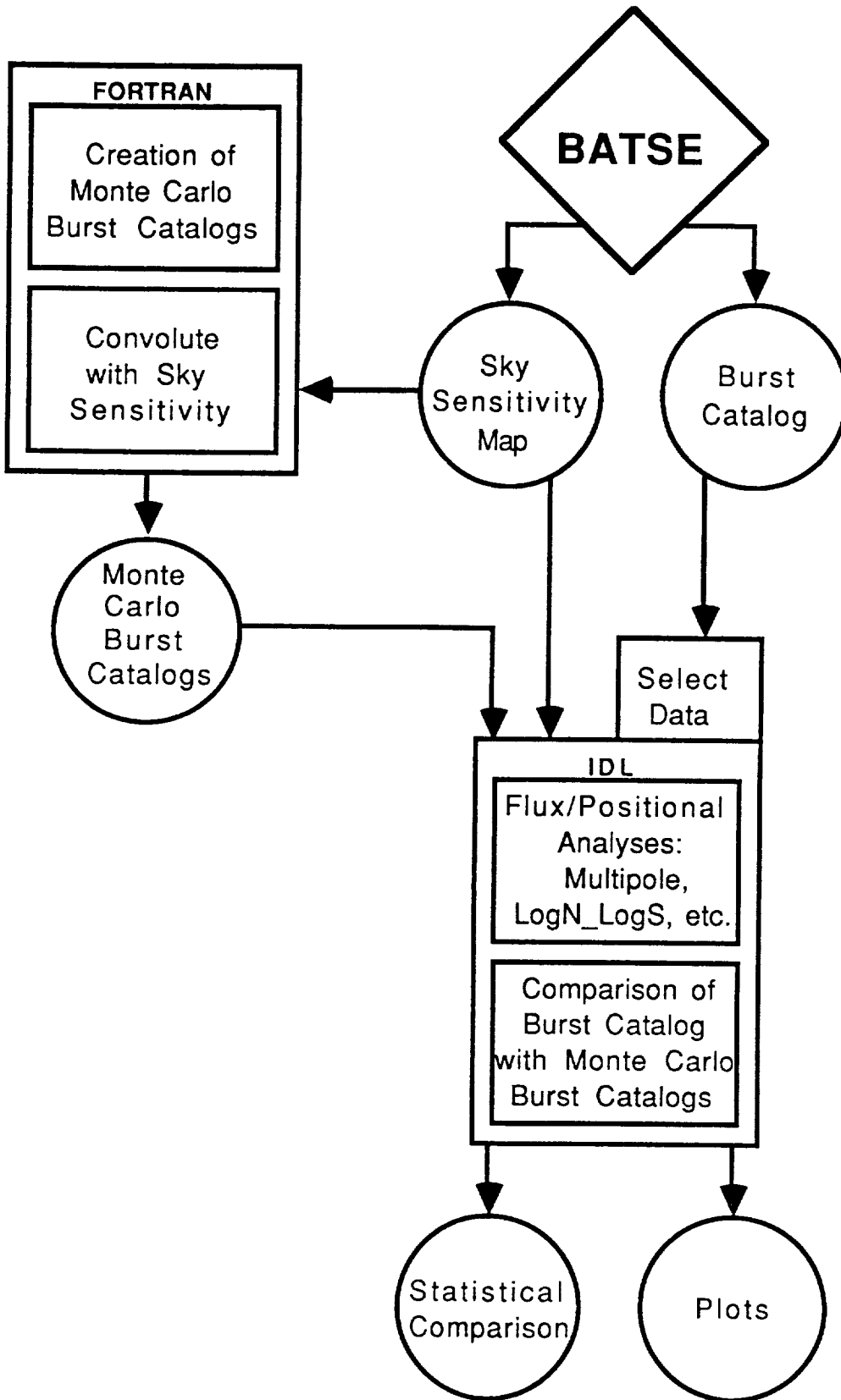
BATSE

FORTRAN

Creation of Monte Carlo Burst Catalogs

Convolute with Sky Sensitivity

Sky Sensitivity Map

Burst Catalog

Monte Carlo Burst Catalogs

Select Data

IDL

Flux/Positional Analyses: Multipole, LogN_LogS, etc.

Comparison of Burst Catalog with Monte Carlo Burst Catalogs

Statistical Comparison

Plots

1990

NASA/ASEE SUMMER FACULTY FELLOWSHIP PROGRAM

MARSHALL SPACE FLIGHT CENTER
THE UNIVERSITY OF ALABAMA

IGNITION TRANSIENT ANALYSIS OF SOLID ROCKET MOTOR

Prepared By: Samuel S. Han

Academic Rank: Associate Professor

University and   Tennessee Technological University
Department: Mechanical Engineering

NASA/MSFC:
    Laboratory: Propulsion
    Division: Propulsion System
    Branch: Performance Analysis

MSFC Colleague: Dr. Charles F. Schafer
                        Dr. S. Don Bai

Contract Number: NGT-01-002-099
                        The University of Alabama

ABSTRACT

To predict pressure-time and thrust-time behavior of solid rocket motors, a one-dimensional numerical model is developed.The ignition phase of solid rocket motors (time less than 0.4 sec) depends critically on complex interactions among many elements, such as rocket geometry, heat and mass transfer, flow development, and chemical reactions. The present model solves the mass, momentum, and energy equations governing the transfer processes in the rocket chamber as well as the attached converging-diverging nozzle. A qualitative agreement with the SRM test data in terms of head-end pressure gradient and the total thrust build-up is obtained. Numerical results show that the burning rate in the star-segmented head-end section and the erosive burning are two important parameters in the ignition transient of solid rocket motor (SRM).

INTRODUCTION

Fig. 1 shows a schematic diagram of space shuttle solid rocket motor. As the pyrogen gas from the igniter heats the surface of a solid propellent in the star-segmented section, temperature of the propellent increases until its surface temperature reaches an ignition temperature.Energy released through a chemical reaction initiates a strong convection in the chamber and the flame spreading toward the aft-end of the rocket chamber.Following the completion of flame spreading, the gas pressure in the chamber increases rapidly due to the energy and mass released from the burned solid propellent. Ignition transient (or starting transient) refers to a short period of motor operation from the ignition of igniter gas to the rapid chamber pressure build-up.

An ability to predict and control the complex transport processes in the rocket chamber is desired for an efficient design of rocket motors. Engineering design parameters include: overall transient time of a motor; reduction of motor- to-motor variation; over-pressurization; avoiding misfires and hangfires; effects of design modification such as propellent formulation, and the geometry of a rocket; variation of total thrust and the dynamic thrust.

Peretz, et. al. [1] performed experimental and analytical modeling of high velocity transient of solid rocket motors. Caveny and Kuo [2] extended their analysis to space shuttle SRM. Caveny further extended their method and compared numerical predictions with space shuttle SRM test data [3]. Total thrust build-up predicted by Caveny-Kuo's model agrees qualitatively with the test data. However, predicted transient pressure in the head-end of the motor shows an extreme departure.

The purpose of the present investigation is to analyze ignition transient of space shuttle SRM. Anew 1-dimensional numerical model is developed and numerical results are compared with the test data.

ANALYSIS

Assumptions

It is assumed that the combustion products are ideal gas of single component without the radiation effects. Chemical reaction occurs in an imaginary this surface instantaneously when the surface temperature of the propellent reaches auto- ignition temperature. All transport coefficients remain constants. Flow and temperature fields are assumed to be one- dimensional and interactions between the gas and the solid surface are adequately represented by empirical momentum and energy transfer correlations.

Equations for Gas

Mass conservation is given by

$$\frac{\partial \rho a}{\partial t} + \frac{\partial}{\partial x}(\rho u A) = \rho_{pr} r b + \dot{m}_{ig}, \tag{1}$$

where ρ is the density, A is the cross-sectional area, u axial velocity, ρ_{pr} the solid propellent density, r is the burning rate, b is the burning perimeter and m_{ig} is the rate of mass generation. All variables are functions of time (t) and axial distance (x). The Lenoir-Robillard burning rate law is employed to evaluate the regression rate of solid propellent. The conventional form of this expression is [3]

$$r = r_{ref}(P/P_{ref})^n + \alpha_e G^{0.8} P h^{-0.2} \exp[-\beta_e r \zeta_{pr}/G]. \tag{2}$$

The first term accounts for a standard burning and the second for an erosive burning. Erosive burning increases as the mass flow rate (G) of the gas increases. D_h is the hydraulic diameter, α_e and β_e are adjustable coefficients.

The axial momentum equation is

$$\frac{\partial}{\partial t}(\rho u A) + \frac{\partial}{\partial x}[A\{\rho u u - (2u + \lambda)\frac{\partial u}{\partial x}\}] = -\frac{\partial A P}{\partial x} + p\frac{\partial A}{\partial x} - \gamma_w P_w + \psi, \tag{3}$$

where γ_w is the wall shear stress and is determined by using a friction factor correlation.

The internal energy equation is

$$\frac{\partial}{\partial t}(\rho e A) + \frac{\partial}{\partial x}[A(\rho u e - \frac{k}{c_v}\frac{\partial e}{\partial x})] = -p\frac{\partial u A}{\partial x} + u\gamma_w P_w + \Phi + \frac{1}{2}\rho_{pr}u^2 r b$$

$$- q_{AS} P_w + \rho_{pr} b r h_f + \dot{m}_{ig} h_{ig}, \tag{4}$$

where Φ is the dissipation, q_{AS} is the amount of heat transfer and h_f is the enthalpy of gaseous solid propellent and h_{ig} is the enthalpy of igniter gas. The convective heat transfer to the solid is determined by using an empirical convection coefficient.

Initially the propellent and the gas in the chamber are at a thermal equilibrium with the surrounding atmosphere. The left side (x=0) of the chamber is a solid mass and the right side (x=L) is the nozzle exit. Atmospheric conditions are imposed at the nozzle exit when the flow is subsonic at the exit and a linear extrapolation is used when the flow is supersonic.

Equation for Solid
      Fig. 2 shows a schematic temperature profile in the solid propellent and a solid wall. One dimensional conduction through the solid propellent and the solid wall is governed by

$$q_{PR}C_{PR}\frac{\partial T_{pr}}{\partial t} = \frac{1}{r}\frac{\partial}{\partial r}(rk_{pr}\frac{\partial T_{pr}}{\partial r}).\qquad(5)$$

Convective boundary conditions are used at the interface between the gas and the solid and adiabatic conditions are assumed at the other surface.

Numerical Method
      A modified version of SIMPLE method [4] is used to integrate governing equations iteratively. A staggered non-uniform grid system is used. This numerical method is highly versatile and modular and is proved to be a good numerical method for combustion problems.

RESULTS

Geometry of SRM
      Physical geometry of a RSRM, including grain configuration and the attached nozzle, is selected. Total length of the propellent section is approximately 1320 inches and the nozzle is 178 inches. Radius of the propellent cross-section varies from 28 inches at the head-end to 42 inches at the aft-end of combustion chamber. Radius at the throat of the nozzle is 27 inches and 75 inches at the nozzle exit.
      Grain geometry at the head-end section is star-segmented as shown in Fig.3. To account properly for the burning surface, a burning perimeter ratio, α , is defined as

$$\alpha = \frac{\text{actual burning surface perimeter}}{\text{circumference of the cylinder}}$$

where $0 \leq \alpha \leq 6.70$.

      Igniter pyrogen gas mass flow rate is shown in Fig.4. The Autoignition temperature of the solid propellent is assumed to be 850 K. Adiabatic flame temperature of the pyrogen gas is 2450 K and solid propellent is 3361 K. All

other values of physical properties are those used in ref. 2. Total number of control volumes are 60; 20 for the chamber, and 40 for the converging-diverging nozzle.

Comparison with Test Data

Fig. 5 shows a comparison of two numerical results with test data in terms of total thrust and the head-end pressure variations. In numerical results, total thrust is divided into dynamic thrust (Fdy) and nozzle thrust (Fnoz). Dynamic thrust is caused by the change in momentum within the rocket and the nozzle thrust is due to the momentum efflux at the exit. Pressure variation in the chamber during an ignition transient is closely related to the dynamic thrust.

Numerical results show that total thrust can not reach the measured value without the erosive burning effects and a careful adjustment of burning perimeter ratio, α , is needed to match the head-end pressure variations.

CONCLUSIONS AND RECOMMENDATIONS

One-dimensional numerical model is developed to analyze ignition transients of space shuttle SRM. Ideal compressible fluid equations are solved by a variant of SIMPLE method. Comparison with test data shows a qualitative agreement. Two most dominant factors influencing ignition transients are the erosive burning rate and the burning pattern in the star-segment head-end propellent. With an accurate data for the erosive burning and head-end burning pattern, one-dimensional model may be used for parametric study of ignition transients of SRM.

Multi-dimensional analysis is needed to account for more accurate burning pattern in the star section, igniter gas expansion, complex flow in the chamber and through a converging-diverging nozzle. Erosive burning rate under highly transient dynamic conditions requires more elaborate treatments on the chemical reaction as well as flow field at the surface of solid propellant.

ACKNOWLEDGEMENT

REFERENCE

1. Peretz, A., Kuo, K. K., Caveny, L. H., and Summerfield, M., "Starting Transient of Solid Propellant Rocket Motors with High Internal Gas Velocities," AIAA J., Vol. 11, 1719, 1973.
2. Caveny, L. H., Kuo, K. K., "Ignition Transients of Large Segmented Solid Rocket Boosters," NASA CR-150162, 1976.

3.   Caveny, L. H., "Extensions to Analysis of Ignition Transients of Segmented Rocket Motors," NASA CR-150632, 1978.

4.   Patankar, S. V., Numerical Heat Transfer and Fluid Flows, Hemisphere Publishing Co., 1980.

Figure 1

Figure 2

Figure 3

Fig 4

(a) Measurement Data

$\frac{df}{dt}$
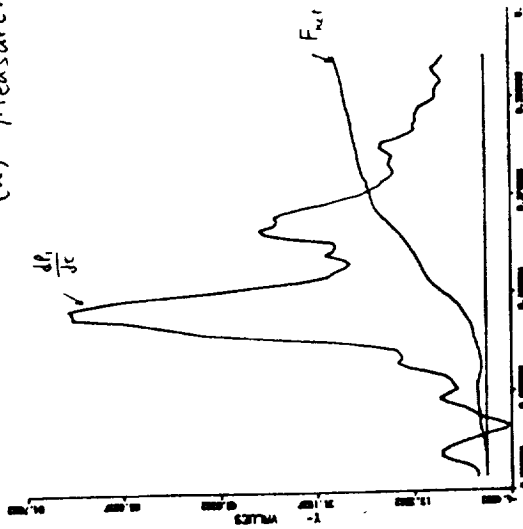
$F_{net} \times 10^{-5}$ [lbf]

$\frac{dP}{dt}$ [psi/10 ms]

(b) Numerical Data
$\alpha = 6.7$
No erosive burning
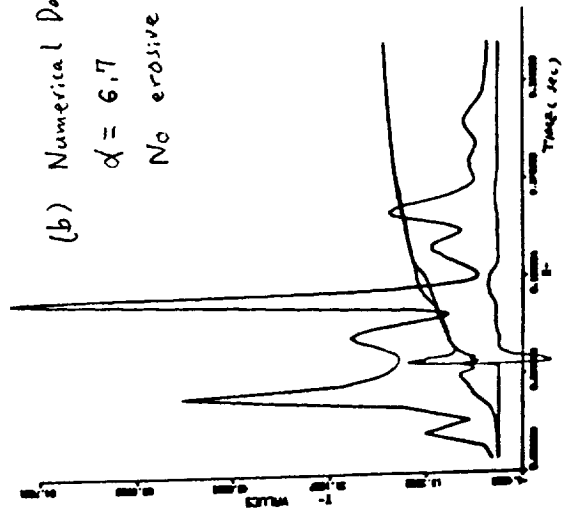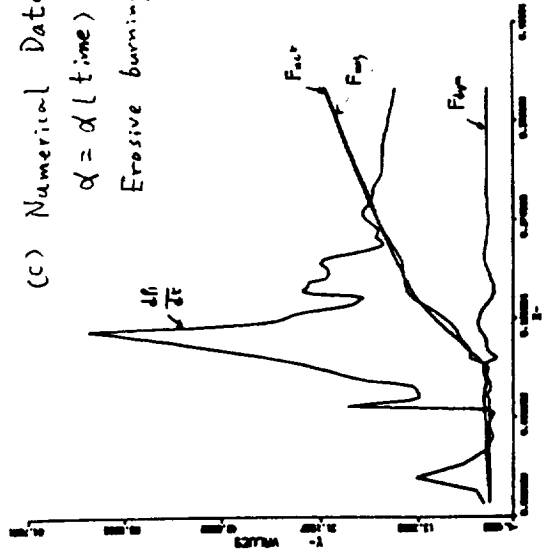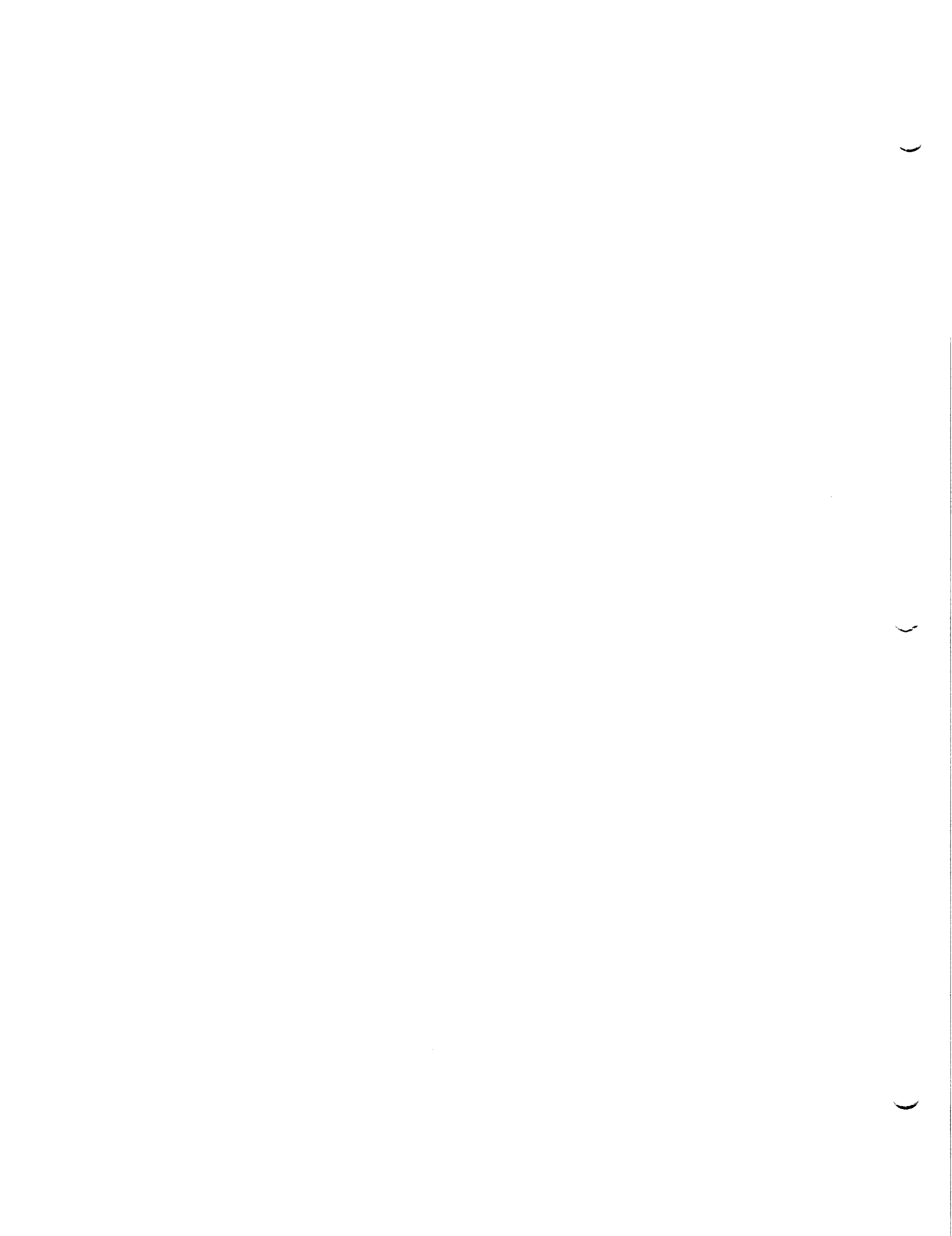
TIME (sec.)

(c) Numerical Data
$\alpha = \alpha(time)$
Erosive burning

$\frac{df}{dt}$

F_{net}

F_{erj}

F_{int}

Figure 5

1990

NASA/ASEE SUMMER FACULTY FELLOWSHIP PROGRAM

MARSHALL SPACE FLIGHT CENTER
THE UNIVERSITY OF ALABAMA

STRUCTURE FUNCTION CALCULATIONS
FOR
OSTWALD RIPENING PROCESSES

Prepared By:	Razi A. Hassan
Academic Rank:	Assistant Professor
University and Department:	Alabama A&M University Chemistry
NASA/MSFC: Laboratory: Division: Branch:	 Space Science Microgravity Science & Applications Chemistry and Polymeric Materials
MSFC Colleague:	Dr. J. Patton Downey Dr. Donald Frazier
Contract No.:	NGT-01-002-099 The University of Alabama
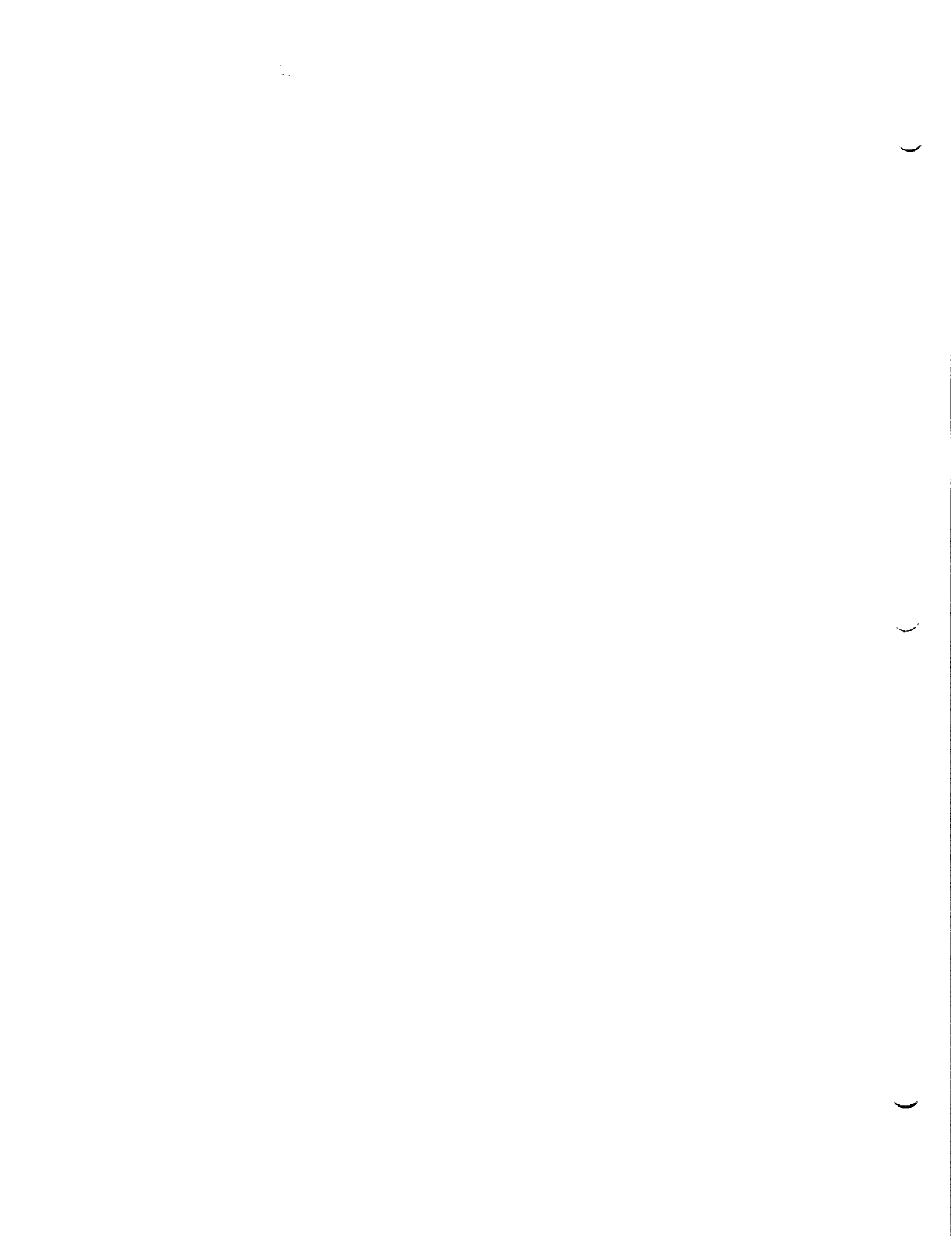
ABSTRACT

A program for computing the Structure Function for configurations involved in Ostwald Ripening has been written. The basic algorithms are derived from a mathematical analysis of a two-dimensional model system developed by Bortz, et. al (1974).

INTRODUCTION

The Chemistry and Polymeric Sciences Branch conducts experimental and theoretical research to advance the science and technology of organic and polymeric materials having applications as optical and other important devices. Studies relate to gravitational influences on solidification, crystal-growth, thin film growth, and polymerization of such materials. Space laboratories in free-fall around the earth offer an environment in which body forces on fluids can be minimized over a relatively extended period of time and range of experimental conditions. Other advantages include a quiesent environment allowing for the growth of defect-free crystals. A fundamental understanding of these low-gravity growth processes can lead to better understanding of metal fatigue in alloys, the behavior of fogs and aerosols, and, in general, almost any of the multiphase systems which covers a broad range of technology.

When a homogenous melt containing two components is cooled to a temperature at which the two components are no longer totally miscible, the melt separates into phases of differing compositions. Although equilibrium compositions are predictable by the system's phase diagram, there is no way to predict phase distribution during alloy formation. Distribution of phases is an important aspect of materials properties. Important mechanisms determining distribution on earth are sedimentation and convection. Under low-gravity conditions, sedimentation and convection dominate, affecting morphology. One such separation process is **Ostwald Ripening**.

Ostwald Ripening is a process by which larger droplets grow at the expense of smaller ones by the diffusion of mass away from droplets below a critical radius toward ones above this size. This phenomenon is important in many disciplines involving multiphase components, including long-term metal alloy integrity, foam stability, and weather phenomena. The Branch is leading a research program to perform a flight experiment which will provide data on the ripening process where gravity effects have been eliminated.

In order to draw a picture of Ostwald Ripening, imagine a solution containing two chemical components. The solution is supersaturated

with solute, and nuclei of a second phase have already started to grow. The supersaturated solution shall be called the parent phase, and the nuclei shall be termed the second phase. The nuclei shall be assumed to be large enough to have well-defined surfaces so that macroscopic theories such as thermodynamics can be applied. Such nuclei shall be called grains. Of interest to us is the grain size dustribution, which we will represent by a Structure Function.

The Structure Function can be defined as follows: The superposition of waves of different amplitudes and phases can be accomplished by vectorial addition. If f_1 and f_2 are the amplitudes of waves scattered by atoms 1 and 2, and ϕ_1 and ϕ_2, are the phases, the resultant amplitude is:

$$F = f_1\phi_1 + f_2\phi_2$$

In 3 dimensions:

$$F(hjk) = \sum_j f_j e^{2\pi i(hx_j/a + jY_j/b + kz_j/c)}$$

where h,j,k are the Miller indices of the crystal.

The expression F(hjk) is called the structure function of the system. Its value is determined by the exponential terms, which also reflect the cluster sizes of the grains formed during Ostwald Ripening.

PROCEDURE

For our computer simulation, we start with an initial state at t=0 from a completely random configuration of A and B particles. We then follow the time evolution of the random varible x_t representing the state of the system at time t. The stochastic process, an example of a Monte Carlo simulation, describing the evolution of x_t is Markovian. The algorithm used to generate our program was developed from a paper by Bortz (1974). The structure function, S(k,t), is defined as follows:

$$S(\vec{k},t) = \sum_{\vec{r}} e^{i\vec{k} \times \vec{r}} G(\vec{r},t)$$

$$\vec{k} = \frac{2}{80}\vec{\mu}$$

$$\vec{\mu} = (\mu x, \mu y)$$

$$G(\vec{r},t) = n^{-1}\sum_i [\eta(\vec{r}_i)\eta(\vec{r}_i-\vec{r})-\bar{\eta}^2]$$

$$\vec{\eta} = n^{-1}\sum \eta_i$$

$$N = N_A + N_B$$

N_A = the number of A type particles

N_B = the number of B type particles

$\vec{r}$ = describes the different positions of the system at times t.

CONCLUSION

While we expect that the values from our computer simulations will reflect Ostwald Ripening, at this point the program is still being tested. Some preliminary runs seem to justify our expectations.

REFERENCES

Baird, J.K.; Li, Kao Lee; Frazier, Donald O.; Naumann, Robert J. "Theory of Ostwald Ripening in a Two-Component System" -Center Director's Discretionary Fund Final Report (NASA Technical Memorandum), September, 1986.

Bortz, A.B.; Kalos, M.H.; Liebowitz, J.L.; Zendejas, M.A. "Time Evolution of a Quwnched Binary Alloy: Computer Simulation of a Two-Dimensional Model System", July 15, 1974.

Moore, W.J., "Physical Chemistry, Fourth Edition", Prentice Hall, Inc., 1972.
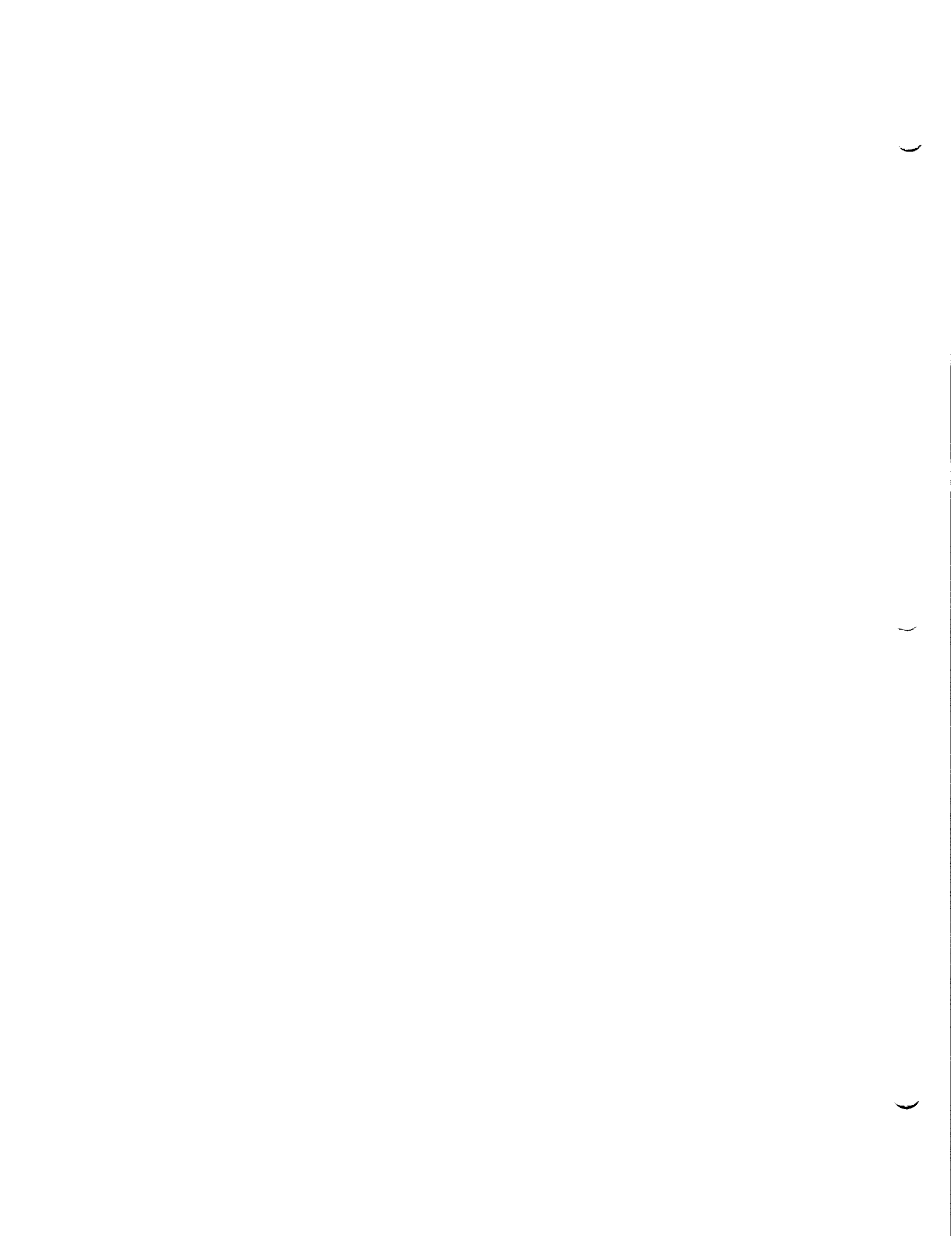
1990

NASA/ASEE SUMMER FACULTY FELLOWSHIP PROGRAM

MARSHALL SPACE FLIGHT CENTER
THE UNIVERSITY OF ALABAMA

CURRENT LIMITING REMOTE POWER CONTROL MODULE

Prepared By: Dr. Douglas C. Hopkins

Academic Rank: Assistant Professor

University and   Auburn University
Department: Electrical Engineering

NASA/MSFC:
        Laboratory: Information and Electronics
        Division: Electrical Systems
        Branch: Electrical Power

MSFC Colleague: Mr. Robert E. Kapustka

Contract Number: NGT-01-002-099
                           The University of Alabama
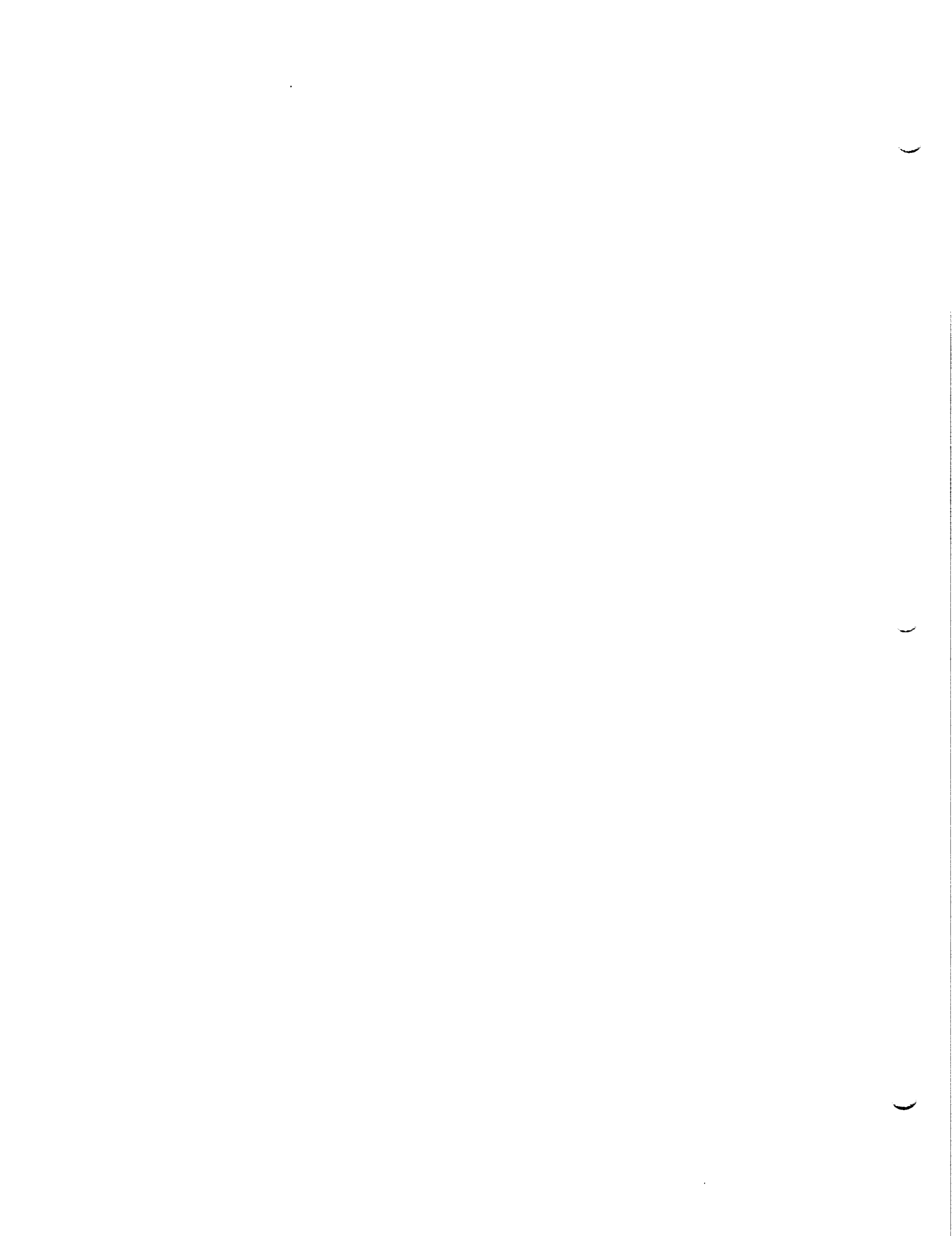
Introduction

The power source for the space station freedom will be fully utilized nearly all of the time. As such, any loads on the system will need to operate within expected limits. Should any load draw an inordinate amount of power, the bus voltage for the system may "sag" and disrupt the operation of other loads. To protect the bus and loads some type of power interface between the bus and each load must be provided. This interface is most crucial when load faults occur.

A possible system configuration is shown in Figure 1. The proposed interface shown is the Current Limiting Remote Power Controller (CL-RPC). Such an interface should provide the following power functions.

    a. limit overloading and resulting undervoltage;
    b. prevent catastrophic failure and still provide for
           redundancy management within the load;
    c. minimize cable heating; and
    d. provide accurate current measurement.

Other supervisory and management functions can be incorporated into the overall RPC. However, the intent of the work here is limited to power processing.
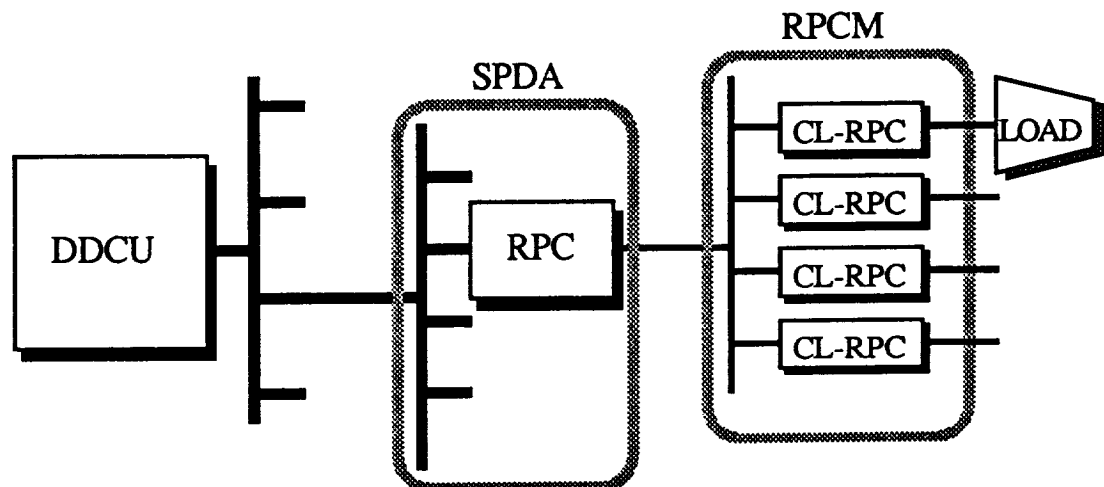
Figure 1. Power system

Design Considerations

A functional block diagram of the power processing stage of a CL-RPC is shown in Figure 2. There are four functions that drive the circuit design.

    a. rate control of current;
    b. current sensing;
    c. the variable conductance switch (VCS) technology; and

d. the algorithm used for current limiting.
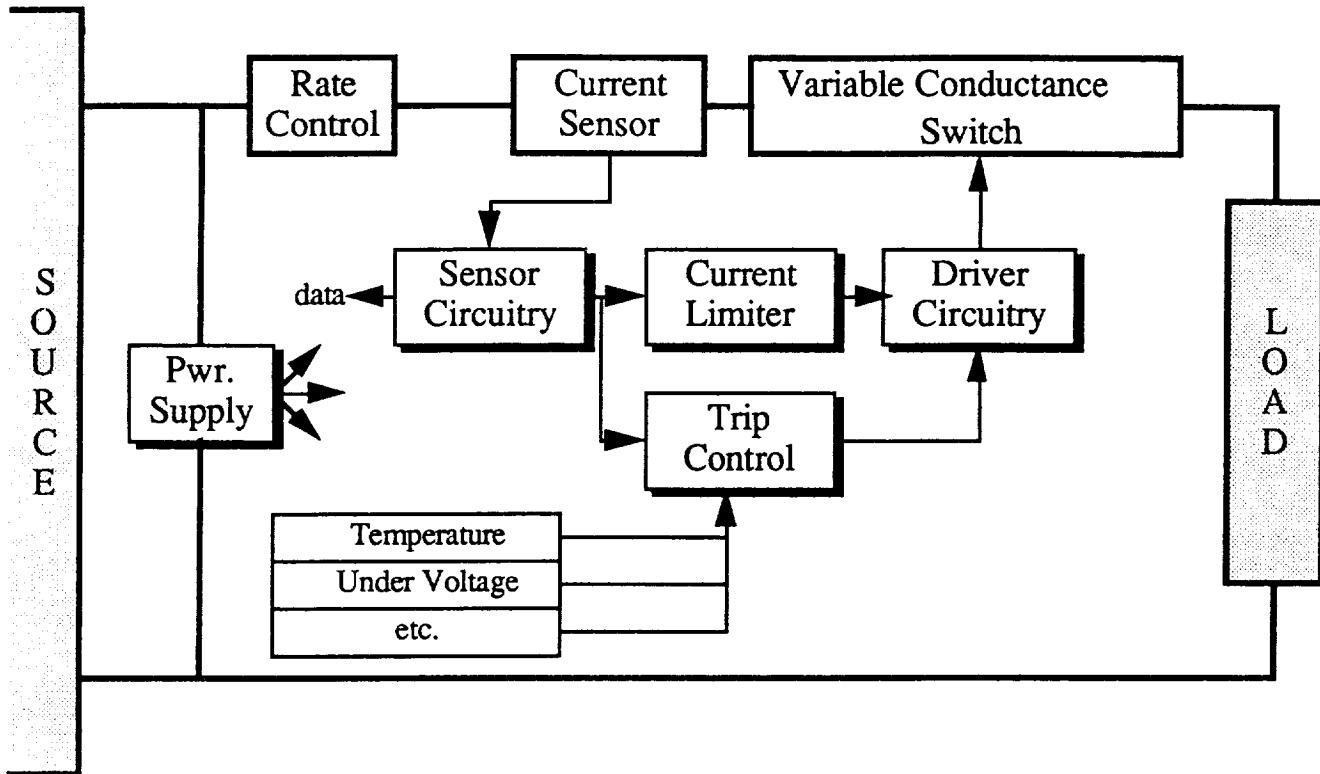
Figure 2. Current Limiting Remote Power Controller

Each function is discussed separately below.

Rate Control

Previous estimates of the bus impedance indicate that there may be as little as 2.5μH in the lines leading from the source to the load. This low inductance will allow a current occurring from a hard fault to ramp at 48A/μs worse case. The time for the current to ramp from 100% to 200% of the nominal RPC design current, and normalized to this value, is 42ns/A. Therefore, a 10A CL-RPC will need to respond in 420ns. The detection and speed of response may be too overwhelming for available electronic hardware. Either custom circuitry or a rate limiter will need to be developed and its effects on the system investigated.

Of particular interest are the ramifications of having varying proportions of distributed inductances before and after the CL-RPC and what effect the ramifications have on the CL-RPC system design. Also, what voltage effects on the system are there during a soft fault and subsequent turn-off of the RPC.

Current Sensing

Sensing methods can be divided into two categories: contact and

noncontact sensing. Regardless of the method, three evaluation criteria need to be quantified: power consumption by the sensor and circuitry (including insertion loss), speed of response, and measurement accuracy. Common contact-sensing methods include a current shunt and semiconductor current-sensing transistors. Common noncontact sensing methods include current transformers (dc bucking type) and optical fiber. An optimum sensing technique can not be determined until the bus system dynamics are well understood and the electrical requirements for the sensor determined.

Variable Conductance Switch (VCS)

The most important design consideration of the CL-RPC is the implementation of the VCS. From initial investigation of the system needs the VCS will need to operate in three modes:

a. Fully on – Typical switch operation with minimum resistance and minimum power loss. On-state voltage drop initially set at 600mV regardless of nominal current level.

b. Current limiting – VCS resistance increases to limit the load current to a specified level. The level is arbitrarily set to 200% of nominal current. The time allotted for limiting is also arbitrarily set and directly determines the thermal design of the VCS.

c. Turn off – The VCS experiences the greatest stress when an overcurrent must be terminated while the VCS is sustaining a high terminal voltage. For semiconductor switches, the SOA parameter will determine the turn off limit.

Typical devices to be investigated for implementing the VCS are BJTs, IGBTs, MOSFETs and MCTs. Of these, the MOSFETs will initially be investigated. Another factor that will impact the implementation is the configuration of the transistors and the modular form of the switch. For instance, a 10A CL-RPC can be made from four 2.5A module in parallel with each having self-protecting current limit.

The power capability of the VCS will not only depend on the size and number of the transistors but also on the packaging and, hence, thermal management. This is a materials issue that has not yet been addressed by this summer's work.

Current Limit Algorithm

The algorithm defines the electrical current versus time operation of the CL-RPC. Under normal conditions the CL-RPC offers little loss to the system and mimics an ideal switch function. During overcurrent operation the CL-RPC will constrain the current to a certain level depending on its own electrical and thermal condition. There are three levels to be determined:

a. Initial peak current – "Nuisance faults," which are of very short time duration, may exceed the current ratings of the CL-RPC. It would be advantageous to allow an initial peak current much greater than nominal to flow during these instances rather than trip or force severe design constraints on the user's equipment. There may also be a need by a user to have a momentary surge of current to clear a fuse or other device to allow for redundancy management. At present, there is no information to suggest what an acceptable level for this current is.

b. Current limit – The initial inrush or charging current of some loads may exceed the nominal current rating of the CL-RPC. Rather than trip off the equipment during starting an overcurrent limit is needed. Again, there is no information to suggest what an acceptable level for this current is.

c. Trip point – This point is reached when a maximum energy has been absorbed by the VCS during current limit. How the energy value is accumulated is yet to be determined. To mimic a circuit breaker the energy is accumulated through an I^2t algorithm. An easier alternate is $\int i(t)\, dt$.

Present Status

Literature Review

A literature search has been performed. The number of citations since 1970 is given below.

"Electronic (&) Circuit Breaker"	321 citations
"DC (&) Electronic (&) "Circuit Breaker"	30 citations
Relevant to 120Vdc	1 citation

Laboratory Results

To determine what factors effect the operation and design of a CL-RPC a hardware implementation has been undertaken. At the time of this report 70% has been completed. The systems requirements used for the design are

Nominal current - 10A
Supply voltage - 113Vdc - 126Vdc
Response time - 1μs
Overcurrent limit - 200%
Trip point algorithm - $\int i(t)\, dt$
Variable conductance switch - six HEX-5 FETs

1990

NASA/ASEE SUMMER FACULTY FELLOWSHIP PROGRAM

MARSHALL SPACE FLIGHT CENTER
THE UNIVERSITY OF ALABAMA

THEORETICAL HYPERVELOCITY BALLISTIC LIMIT FOR SINGLE OR

DOUBLE PLATES USING NONLINEAR MODAL ANALYSIS

Prepared By: David Hui

Academic Rank: Associate Professor

University and   University of New Orleans
Department: Mechanical Engineering

NASA/MSFC:
    Laboratory: Materials and Process
    Division: Non-Metallic Materials
    Branch: Polymers and Composites

MSFC Colleague: Alan Nettles
                           James Zwiener
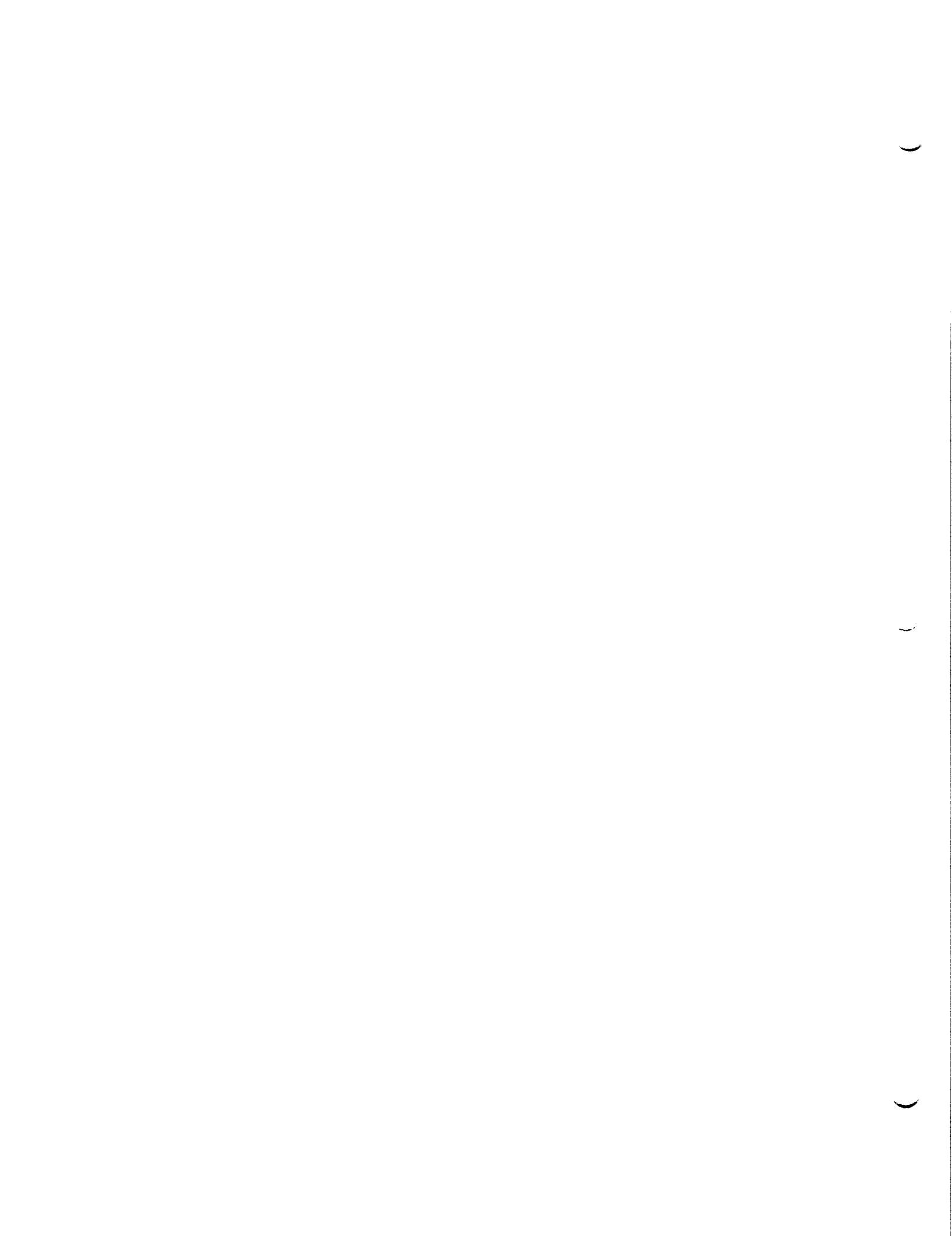
The present work deals with the original research on the use of nonlinear vibration technique to solve for the hypervelocity ballistic limit for double plates. Such structure is commonly found in typical space station design where the incoming space or man-made debris would be fragmented upon hitting the outer plate (shield) and the subsequent impact on the main wall would result in a much reduced damage of the space station or spacecraft. The existing few theoretical impact equations do not agree well with each other (Christiansen 1989). The existing computer code "bumper" used at NASA-Johnson Space Center appears to predict unconservative ballistic limit when compared with experimental data where the velocity ranges from 3 km/s to 8 km/s. Such unconservative prediction is unacceptable from a practical safe design point of view. The "bumper" code is based on Wilkinson's (1968) paper and his equations have not been improved nor modified even though they are viewed with suspicion due to lack of agreement with experiments. To make matters worse, there is not other theory which is better than Wilkinson's equation and the designers are forced to use purely empirical Nysmith (1969) or semi-empirical equations developed by Cour-Palais in 1969. The Cour-Palais equations were later modified empirically in 1989. Since the actual velocity of a space debris ranges from 10 km/s to 60 km/s and the highest experimental projectile velocity is 8 km/s (at NASA-Marshall), one is compelled to use extrapolation of existing experimental results. It is well known that extrapolation (rather than interpolation) could easily give grossly erraneous data. Since Wilkinson's equation is a purely theoretical equation based on the energy-balance mechanics concept, the extrapolation error is avoided, and when it is properly modified, it may be the only valid equation in the extremely high velocity range near 50 km/s. The purpose of the present investigation is to examine the many assumptions of Wilkinson's equation and it appears that some of the assumptions were grossly inaccurate. An attempt is made to present design charts based on the modified-Wilkinson equation so that the designer can get a "feel" of the ranges of the parameters which are of interest and "discard" a huge range of parameters, thus, significantly reducing the number of test shots required. Further discussions on the theoretical and experimental work can be found in recent memos (Abbott 1990 and Olsen 1990). The nonlinear modal analysis was discussed by the author (Hui 1990).

The analysis is based on a solution of the governing nonlinear differential equations for a plate, assuming axi-symmetric behavior using polar coordinate

$$D\nabla^2\nabla^2 W + (\varsigma)(h)\, W,_{tt} - (1/\bar{r})\,(F,_r\, W,_r),_r = 0$$

$$\nabla^2\nabla^2 F = (-Eh/\bar{r})\, W,_r\, W,_{rr}$$

where D is the flexural rigidity, E is Young's modulus, W is the out-of-plane deflection, F is the stress function, h is thickness of the main wall, ς is the density of the plate, $\bar{r}$ is the radial coordinate and ∇^2 is the differential Lagrange operator. The assumed deflection mode is:

$$w(r) = A(t)\ e^{-\bar{r}^2}, \quad w = W/h, \quad \bar{r} = (r)(2)^{1/2}$$

and this mode is more realistic than that employed by Wilkinson since it accounts for the extent of spread of the debris and it is generally accepted that the shape of the impulse should closely resemble the deflection shape at least in the very early initial response. The stress function is solved exactly (it is exact relative to the assumed deflection) and the nonlinear equilibrium is solved approximately using a Galerkin procedure. This method would predict upper bound frequencies and thus lower bound deflections. After some algebra, the nonlinear ordinary differential equation, incorporated the effect of viscous damping δ, is:

$$A(t)_{,tt} + (2\delta)A(t)_{,t} + A(t) + b^* A(t)^3 = 0$$

where $b^* = (3/8)(1-\nu^2)$ and ν is Poisson's ratio. Note that damping was not considered in Wilkinson's equation and his equation is based on quasi-static mechanics of failure as opposed to the present dynamic equations valid for extremely short duration. The inclusion of dynamic effects would give much more realistic results.

Further, the radial strain is found to be,

$$\epsilon_r(\text{at } r=0, \text{ at outer surface}) = (h/\Delta)^2\ A(t)\ (1/2)\{1 + (1/4)(1-\nu)A(t)\}$$

where is the standard deviation of the spray, the first term is the bending strain and the second term is the stretching strain.

References

Abbott, R.D., "Comparison of Wilkinson and Cour-Palais (non-optimum)
    Ballistic Limit Equations", memo to M. Bjorkman (2-H8T3, JY-34), July 1990.

Christiansen, E.L., "Comparison of Empirical Hypervelocity Impact Equations"
    NASA-SN3-89-149, NASA Johnson Space Center, October 1989.

Cour-Palais, B.G., "Meteoroid Protection by Multiwall Structures", AIAA Paper
    No. 69-372, AIAA Hypervelocity Impact Conf., April 30-May 2, 1969.

Hui, D., "Accurate Backbone Curves for a Modified-Duffing Equation for
    Vibrations of Imperfect Structures with Viscous Damping", ASME Journal
    of Vibration and Acoustics, Vol. 112, July 1990, pp. 304-311.

Wilkinson, J.P.D., "A Penetration Criterion for Double-Walled Structures
    Subject to Meteoroid Impact", AIAA Journal, Vol. 7, No. 10, Oct. 1969
    pp. 1937-1943.

Olsen, G.D., "M/D Design Activities for June 7, 1990 to July 12, 1990"
    July 12, 1990.

Nysmith, C.R., "An Experimental Impact Investigation of Aluminum Double
    Sheet Structures", AIAA Paper No. 69-375, AIAA Hypervelocity Impact
    Conference, April 30-May 2,1969.
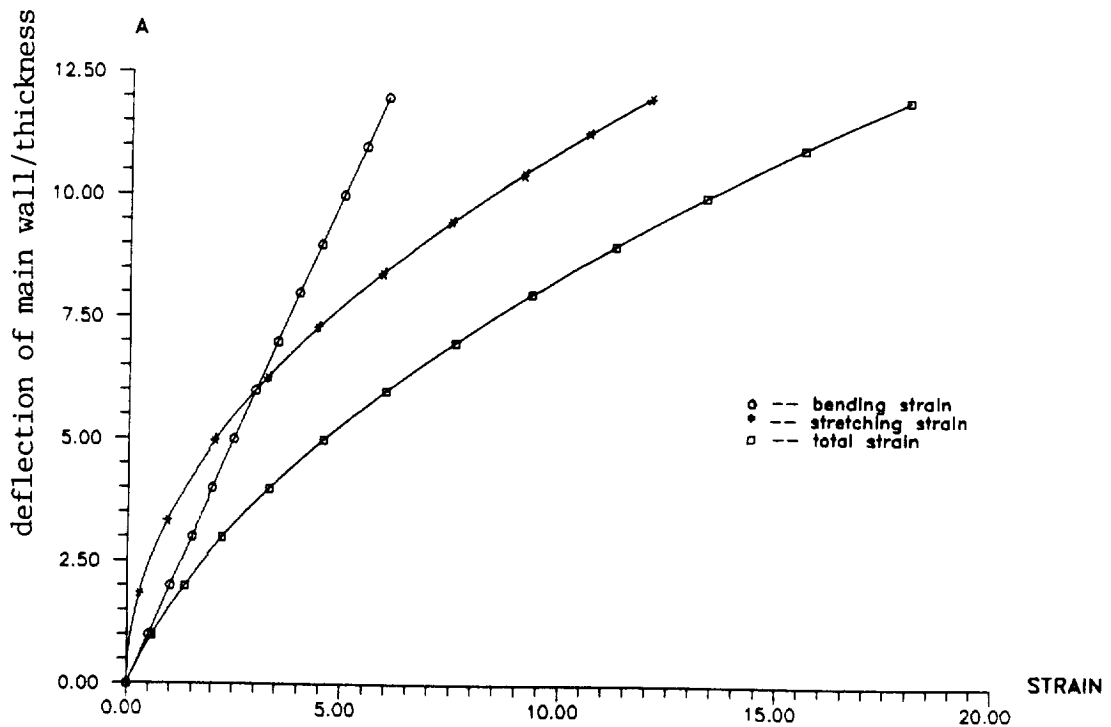
FIGURE 1

amplitude versus maximum strain of main wall

$$Z_1 = 5.1961 \, A(t) \left[1 + (b^*/2)A(t)^2\right]^{1/2}$$

$$z_1 = \left(\frac{V_p^{BL}}{(E/\rho)^{1/2}}\right)\left(\frac{\rho_p \, d_p^3}{\rho_2 \, \ell^3}\right)$$
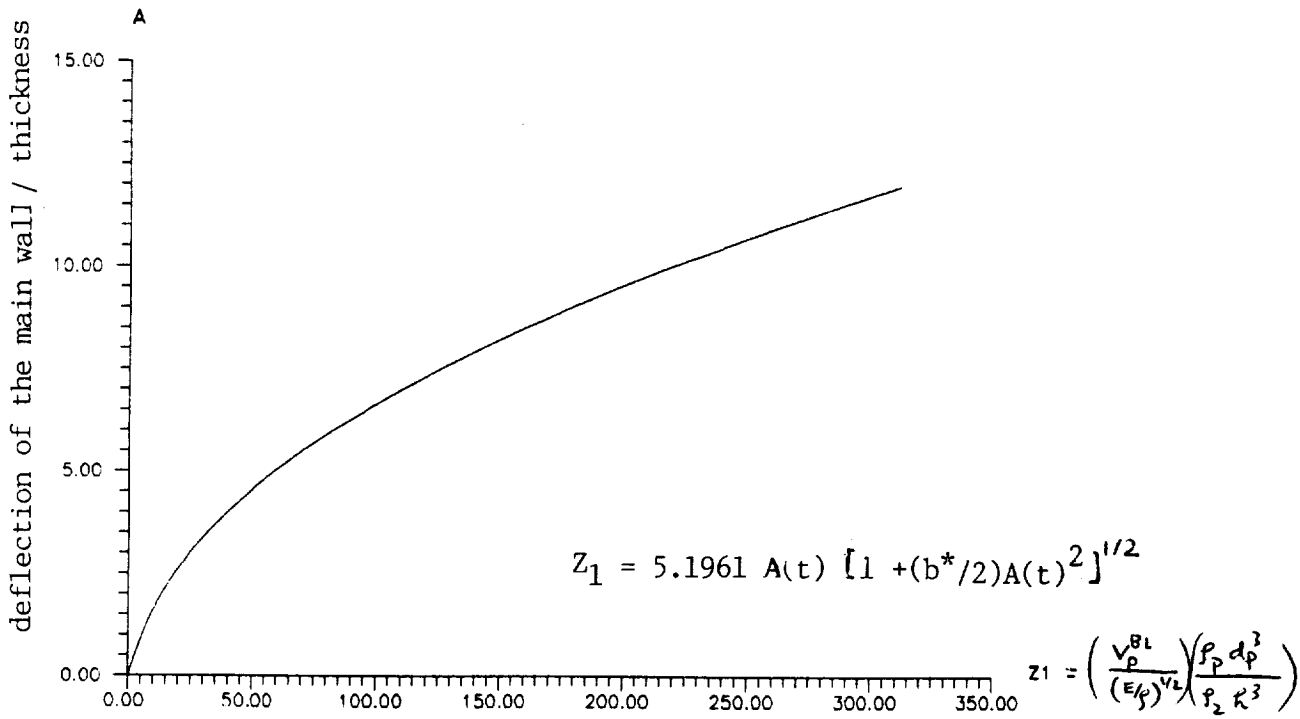
Figure 2

Amplitude versus ballistic limit velocity

$$c^{*1/2} = A(t) \left[1 + (b^*/2)A(t)^2\right]^{1/2}$$

$$SQRT(C^*) \equiv \frac{V_2(\Omega=0)}{(E/\rho)^{1/2}} \left(\frac{A}{\ell}\right)^2 \left[6(1-\nu^2)\right]^{1/2}$$
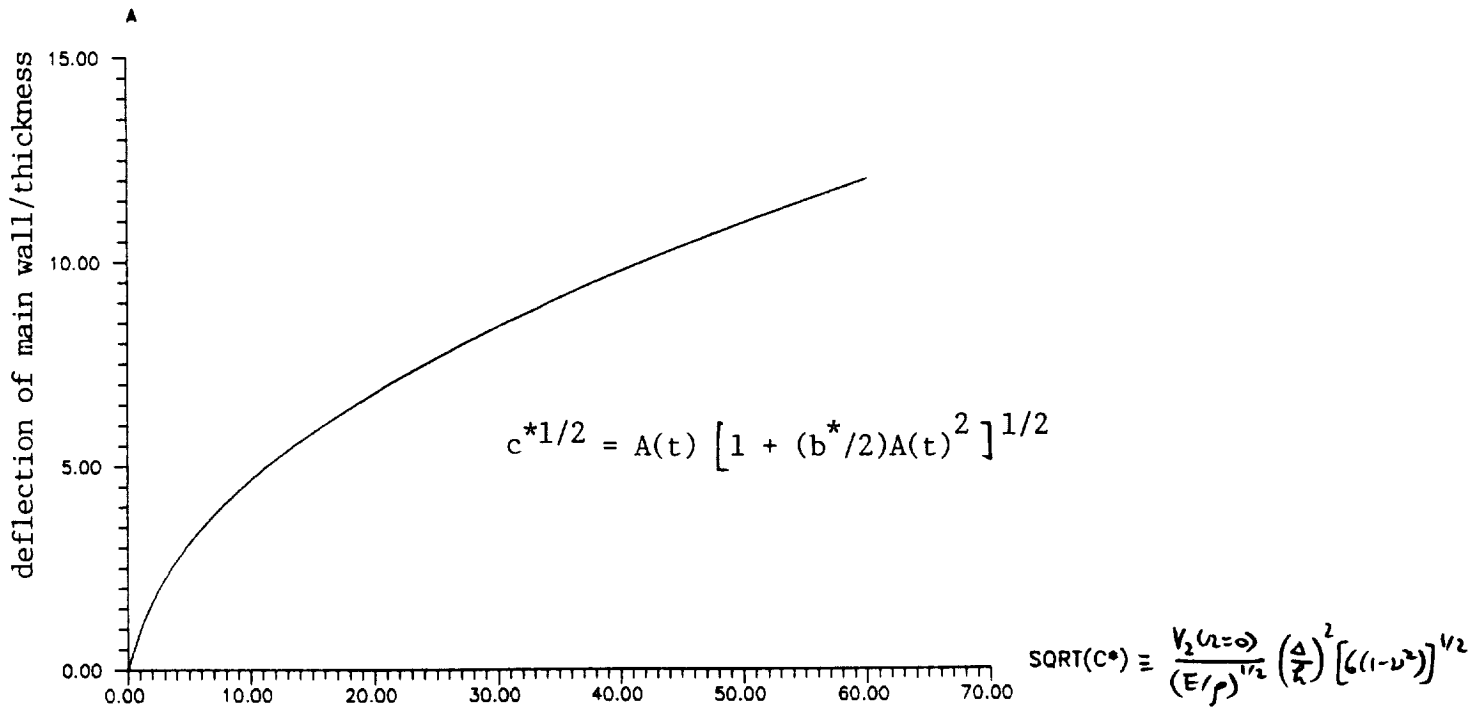
Figure 3   amplitude versus initial velocity

1990

NASA/ASEE SUMMER FACULTY FELLOWSHIP PROGRAM

MARSHALL SPACE FLIGHT CENTER
THE UNIVERSITY OF ALABAMA

SYSTEM IDENTIFICATION AND CONTROLLER DESIGN
USING
EXPERIMENTAL FREQUENCY RESPONSE DATA

Prepared by: R. Dennis Irwin

Academic Rank: Assistant Professor

University and Department: Ohio University
                                          Department of Electrical
                                          and Computer Engineering

NASA/MSFC:
        Laboratory: Structures and Dynamics
        Division: Control Systems
        Branch: Pointing Control Systems

MSFC Colleague: Dr. Henry Waites

Date: August 24, 1990

Contract: The University of Alabama
                                          NGT 01-002-099

SYSTEM IDENTIFICATION AND CONTROLLER DESIGN FOR LARGE SPACE STRUCTURES USING EXPERIMENTAL FREQUENCY RESPONSE DATA

by:

Dennis Irwin
Department of Electrical and Computer Engineering
Ohio University

Introduction

Recent findings of Guest Investigators involved in modeling and controller design for the NASA Marshall Single Structure Control Facilityhave raised questions regarding the ability of modern control design techniques and modern modeling techniques to deal effectively with the stringent modeling and control design requirements of Large Space Structure Control. In particular, these investigators have speculated that the modeling, or system identification, component of realistic control design is critical to obtaining high performance closed loop systems. This summary is a brief and general discussion of the results of investigations into the modeling and control issues performed under sponsorship of the NASA/ASEE Summer Faculty Fellowship Program.

There are several issues addressed in this report. The first is an investigation of a modeling technique based on least squares identification of individual transfer functions from measured frequency response data. The second is an investigation of multiobjective optimization techniques applied to the modeling,or system identification, problem. The third issue is an investigation into the question of whether multiobjective optimization approaches can be effectively used for control system design using only frequency response data, thereby bypassing the difficult modeling problem. The last, and most mundane, issue investigated involves the resolution of seeming discrepancies between predicted and measured control computer time delays in the Single Structure Control Facility.

System Identification from Experimental Frequency Responses

Two techniques for system identification have been investigated. The first is a least squares techniquefor estimating z-domain transfer function coefficients from frequency response data. The individual transfer functions are converted to state space form and combined to form a non-minimal multivariable state space model from which a

final minimal model is extracted. The second method utilizes multiobjective optimization techniques to directly estimate a multivariable state space model from matrix frequency responses. The two techniques have been applied to actual data from the Single Structure Control Facility and yield comparable results. The reliability (in terms of the modeling criterion used) of the models in each case appears to be mainly dependent on the quality of the data. Both of the techniques require the use of frequency dependent weighting schemes. The model quality is heavily dependent on the frequency distribution of the available data and weighting schemes are partially based on distribution dependent weighting. The various data points are also weighted depending on the reliability of the frequency response data as estimated by the associated coherence functions.

Controller Design Directly from Frequency Response Data

One of the advantages of multiobjective optimization techniques is the fact that analytical models are not always required. A design using these techniques was successfully implemented in the control facility. This single loop design was non-trivial due to the extreme modal density of the structure. Closed loop improvements in damping for four modes were greater than a factor of three. Higher frequency modes were successfully gain stabilized. These objectives were accomplished using measured frequency response data only.

As far as the author is aware, this is the first successful implementation of a controller designed using a data only approach combined with multiobjective optimization techniques. Ongoing work concentrates on modernization of the single loop classical approach to include modern robustness and performance measures for multivariable systems.

Investigation of Control Computer Time Delays

Guest investigator measurements taken in October 1989 indicated the possible presence of an unmodeled .016 second delay in the control facility HP9000/Cosmec data acquisition and control system. Since the time delay estimate was based on estimates of input/output phase lags at one frequency and obtained at high data rates (10 kHz) compared to the control computer sampling and update rate (50 Hz), it was believed that the supposedly unmodeled delay could be resolved via true sampled data analysis. A sampled-data analysis was performed on a simple model of the HP9000/Cosmec. This analysis showed that the phase shift in question was not due to a system delay but to the accumulated effects of input

and output anti-aliasing filters and the effects of sampling and data hold, which are inherently included in sampled-data controller design techniques.

1990 AFOSR Forum on Large Space Structures

The annual AFOSR Forum on Large Space Structures was attended on invitation of Harris Corporation personnel. Both government and industry speakers presented recent analytical and laboratory results. The most outstanding feature of the meeting was the amount of discussion devoted to the question of whether modern control techniques are up to the task of large space structure control design. Most speakers addressing the issue expressed the view that some recently developed techniques (e.g., H-infinity) are not presently suitable for realistic control design.

Summary

The work sponsored by this NASA/ASEE Summer Faculty Fellowship was mainly oriented toward developing techniques for modeling using frequency response data. The two techniques investigated were successfully used to identify models for a multivariable subsystem of the Single Structure Control Facility. Ongoing work involves using the identified models in conjunction with modern control techniques such as H-infinity to design controllers for the facility.

Another important result of the work performed during the Fellowship period was the successful design and implementation of a controller using only measured frequency response data and multiobjective optimization techniques. Future work in this area will be directed toward achieving modern performance and robustness specifications using multiobjective optimization.

1990

NASA/ASEE SUMMER FACULTY FELLOWSHIP PROGRAM

MARSHALL SPACE FLIGHT CENTER
THE UNIVERSITY OF ALABAMA

A GRAVITATIONAL TEST OF WAVE REINFORCEMENT VERSUS FLUID DENSITY

MODELS

Prepared by: Jacqueline Umstead Johnson, V.M.D., M.S.

Academic Rank: Assistant Professor

University/Department: Alabama A & M University, Food Science &
                        Animal Industries

NASA/MSFC:
      Laboratory: Space Science
      Division: Microgravity Sciences and Application
      Branch: Biophysics ES-76

MSFC Colleague: Helen C. Matsos
                        Dr. David A. Noever
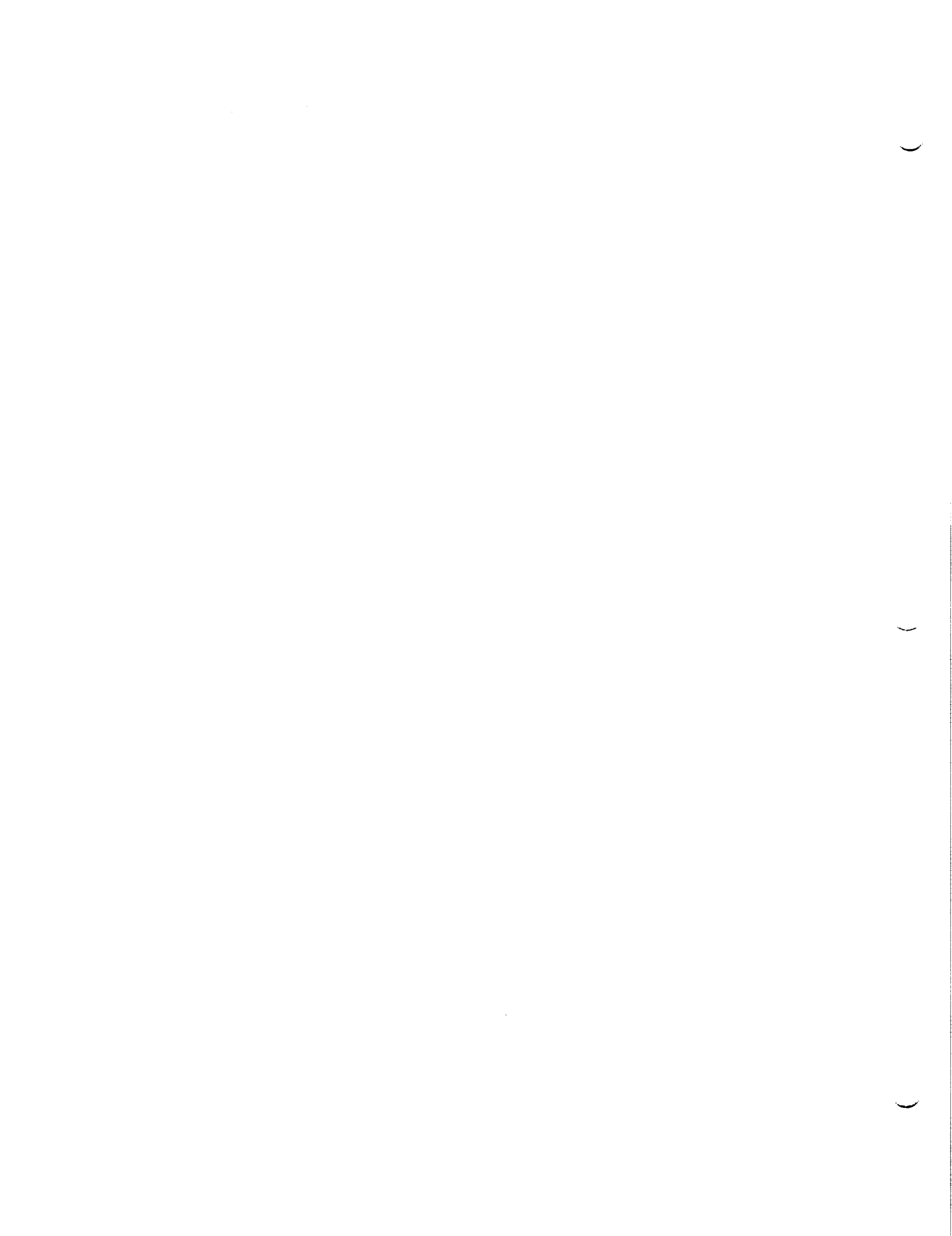
BACKGROUND

Spermatozoa, protozoa, and algae form macroscopic patterns somewhat analogous to thermally-driven convection cells. These bioconvective patterns have attracted great interest recently in the fluid dynamics community, but whether in all cases these waves were gravity- driven was unknown. The literature documents two conflicting theories, one gravity dependent (fluid density model), the other gravity independent (wave reinforcement theory). Under the wave reinforcement theory, organisms align their movements in concert, such that either their swimming strokes beat in phase or their vortices entrain neighbors to follow parallel paths. In contrast, under various fluid density models, small concentrated regions of organisms sink unstably. By observing pattern formation during low and high-gravity parabolas aboard the KC-135 research plane, a definitive existence test of bioconvective patterns was achieved. It appears that macroscopic pattern formation is consistent with the wave reinforcement hypothesis for spermatozoa and fluid density models for protozoa and algae.

Summer Research Objectives

In support of NASA/Marshall Space Flight Center Director's Discretionary Funded proposal entitled "Bioconvection in Swarming Microorganisms" (Helen Matsos, ES76, P.I/David Noever, USRA, C.I.), the primary research objectives of the summer faculty fellow were to 1) assist in sample collection [spermatozoa] and preparation for the KC-135 research experiment; and 2) to collaborate on ground testing of bioconvective variables such as motility, concentration,

morphology, etc., in relation to their macroscopic patterns.

Materials and Methods

Sealed (1.25 in diameter) chambers were used to eliminate fluid movement and surface tension effects a/nticipated during high- to low-gravity transitions. To allow for the observed pattern dependence on fluid height, three well-depths were flown for each protozoan and algal culture: 0.17, 0.25, 0.33 inches deep. Duplicate arrays were prepared for adjacent observation. Sample size and concentration were dictated by the flight hardware and time constraints to maintain viable anaerobic cultures and high speed motility. To facilitate transport and the utilization of spermatozoa aboard the KC-135 located at JSFC, unextended and undiluted semen was placed in 1.5 ml polypropylene microcentrifuge vials and stored in a Hamilton-Thorn Equitainer System. Sperm motility was preserved at 5oC until time of test.

Results

Macroscopic patterns of motility persisted in spermatozoa during all phases of variable gravity testing. In contrast both protozoa and algae showed a decreased in pattern wave number and fineness when subjected to 1.8 g. During low gravity phases, however, patterns in both protozoa and algae rapidly dispersed. Hence pattern formation of spermatozoa in variable gravity is consistent with predictive outcomes of the wave reinforcement hypothesis, while for the selected algae and protozoa, bioconvective patterns are consistent with the predictive outcome

of the fluid density model.

Planned Future Work

This study performed a definitive test of bioconvective patterns which explains earlier conflicts of these theories in the literature. As an extension of this work (/which dealt with collective behavior), a variable test of individual spermatozoa is planned. The objective will include a definitive test of sperm orientation in a velocity gradient (e.g. upstream or downstream orientation).

Figure 1. Bioconvective patterns which arise spontaneously in randomly swimming microorganisms

a) Tetrahymena cultures
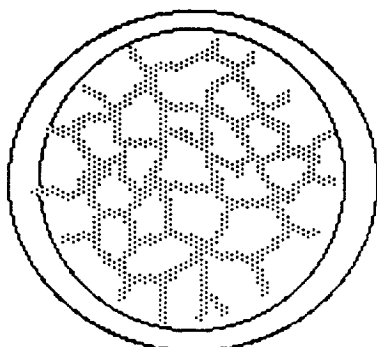
b) Euglena cultures

c) bull spermatozoa
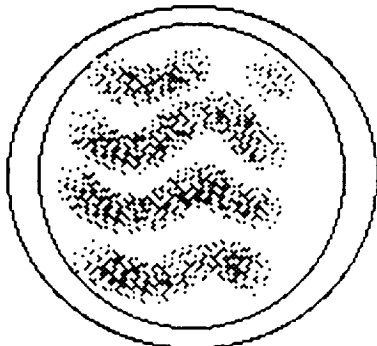
d) Glenodinium cultures
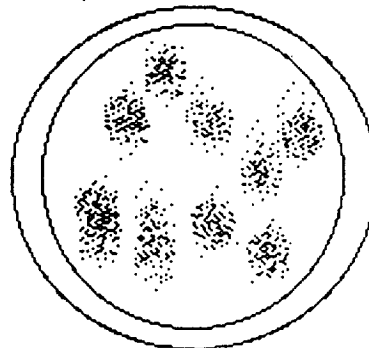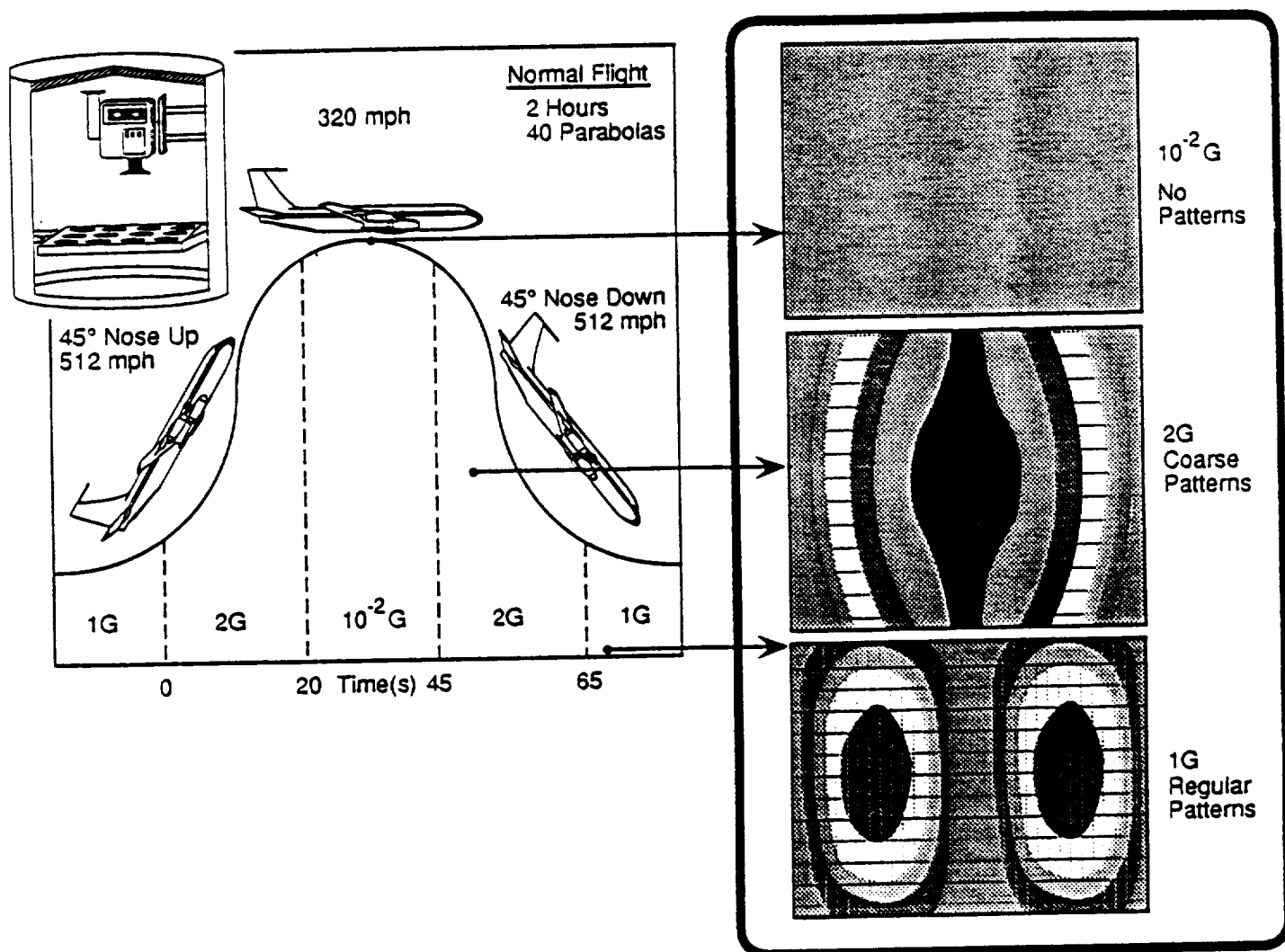
Figure 2. Schematic of aircraft parabolic flight to achieve variable gravity simulation and summary of results for protozoan and algal bioconvective patterns. The inset upper left shows a schematic of the flight apparatus. Components of the apparatus include a protective cylindrical housing; a singly mounted, plexiglass tray with 12 wells for shallow cultures; inclined illumination from the side; and a cinecamera. Flight samples included *Tetrahymena* at a concentration of 2.2×10^5 ml^{-1} and *Polytomella* at concentrations of 1.7×10^6 ml^{-1}, 3.2×10^6 ml^{-1}, 7×10^6 ml^{-1}.

Figure 3. Bioconvection patterns of Spermatozoa

1990

NASA/ASEE SUMMER FACULTY FELLOWSHIP PROGRAM

MARSHALL SPACE FLIGHT CENTER
THE UNIVERSITY OF ALABAMA

REDUCTION OF SOLAR VECTOR MAGNETOGRAPH DATA

USING A MicroMSP ARRAY PROCESSOR

Prepared By: Jack Kineke

Academic Rank: Associate Professor

Institution: Centre College
Department: Mathematics and Science

NASA/MSFC:

Laboratory: Space Sciences Laboratory
Division: Space Physics
Branch: Solar Physics

MSFC Colleague: Dr. Mona Hagyard
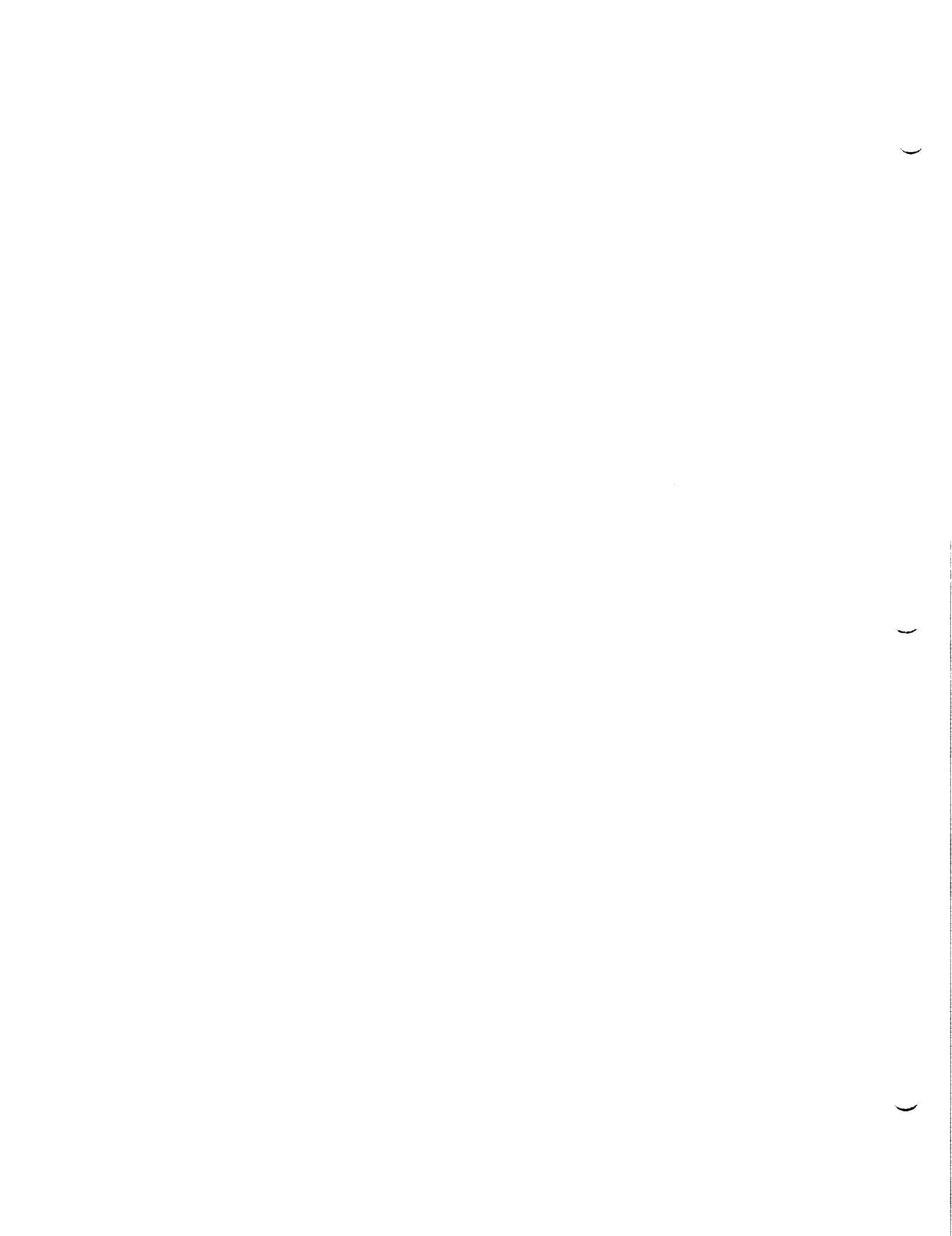
Reduction of Solar Vector Magnetograph Data
using a MicroMSP Array Processor

Background. The processing of raw data obtained by the solar vector magnetograph located at the Marshall Space Flight Center requires extensive arithmetic operations on large arrays of real numbers. A device which can perform these calculations with very high speed is the MicroMSP Array Processor produced by the Computer Design and Applications Division of the Analogic Corporation. This machine is installed in the DEC MicroVAX 3500 computer located at the MSFC Magnetograph facility, where the MicroVAX acts as the "host" computer for all array processor functions. The objectives of this study are to

(1) learn the "programming language" of the MicroMSP Array Processor and adapt some existing data reduction routines to exploit its capabilities

(2) identify other applications and/or existing programs which lend themselves to array processor utilization which can be developed by undergraduate student programmers under the provisions of project JOVE.

This work was performed during the summer faculty fellowship period from June 4, 1990 to August 17, 1990 as the initial phase of the JOint VEnture between NASA and Centre College.

Operations. The MicroMSP Array Processor (hereinafter called AP) is a high speed, multi-user vector computer which operates as a peripheral of the host. The four major subsystems of the AP are the host interface, a control processor, a vector processor and multiport memory. The host interface provides for programmed I/O and DMA (direct memory access) for all data transfers between the AP and the host. The 68020 control processor performs overall processing control of the AP system. The vector processor performs all floating point arithmetic operations, while the multiport memory provides high speed storage which is shared by the host interface, control processor and vector processor. The memory is divided to a 4MB data memory (called DMEM) and two 32KB vector memories (HMEM and LMEM). DMEM and LMEM store both integer and real numbers, while HMEM may contain only reals. Data is transferred to and from the host via the data memory.

A software library is provided with the device containing FORTRAN callable subprograms for I/O control, extensive arithmetic operations on vector arrays, some matrix operations, and a few logical operations. An additional library of image processing routines is also available. The AP is best suited for computations on real numbers, but provision is made for downloading integer quantities and conversion to real format within the AP. Real number arithmetic is performed with up to seven digits of accuracy, but it was found that consistent results are obtainable when only six significant figures are used. At present, all programs are written in VAX FORTRAN and executed on the MicroVAX. The AP library routines are called as FORTRAN functions, which execute on the AP, returning a SUCCESS flag to the host.

Computing on the AP is accomplished by using the following general programming procedure:

(1) Allocate the AP memories for array storage.

(2) Download arrays from the host to the AP data memory.

(3) Transfer arrays from data memory to vector memory.

(3) Perform arithmetic and/or logical operations.

(4) Transfer results from vector memory to data memory.

(5) Upload results to the host.

(6) De-allocate (free) the AP memories for other users.

If the memory requirements of a given application are not large, and the AP memory is managed properly, it is entirely possible that multiple users access the AP at one time. The number of users is limited only by the free AP memory available for an application. Data and results stored in any segment of an AP memory will remain there until changed or the segment is de-allocated. This allows the results (output) of one subroutine to be the data (input) to any other routine provided that the proper memory addresses are global to that routine. This is accomplished by passing the AP memory addresses as COMMON variables.

Applications. During the Summer 1990 period, two existing programs were adapted for computations on the AP in support of the operation of the Solar Vector Magnetograph at MSFC. The first of these, entitled APVMAP, is a set of routines which accept as input raw integer data proportional to the light intensities detected by charged-coupled devices for six different configurations of the polarizing optics of the magnetograph. These data are formatted in square arrays of 128 rows by 128 columns, each element corresponding to one pixel of the display of the magnetograph as it scans a 5' by 5' area on the surface of the sun. After masking the ten most significant bits (noise), the numbers are downloaded to the AP, converted to reals, loaded into vector memory, and processed to produce the sum and difference arrays used to determine the Stokes parameters Q, U, and V.[1] These results are filtered using a finite impulse respose filter if desired. A follow-on subroutine then computes the magnitudes of the longitudinal and transverse magnetic fields, the angle with the line-of-sight of the vector magnetic field, and the polarizing angle. An additional routine is called for correlation plots to determine bias and crosstalk values, while another subroutine is used for photocalibration. Results are uploaded to the MicroVAX host and stored for future plotting by conventional graphics routines. It should be noted that although the magnetograph data is stored in a two-dimensional array data structure, the AP treats these data as if they were in a one-dimensional vector having a length of 16384 elements. As of this writing, this software is undergoing beta test.

The second AP program will consist of FORTRAN subroutines to compute the components of a solar vector magnetic field by a non-linear least squares fit method using Marquardt's algorithm.[2] The first subroutine computes the derivative of the Q, U, and V Stokes parameters with respect to eight different independent variables. The rather complex arithmetic operations are performed on vectors containing up to 64 elements, each of which represents the difference between a wavelength near the center of a given spectral line and the center wavelength itself. Ultimately, when the programming is completed, the vector magnetic field components will be computed. The results of the AP derivative routine are precisely the same as those obtained from a similar routine executed on the MicroVAX. It is here that it was discovered that computations on the AP should be limited to six significant figures to avoid systematic roundoff errors.

<u>Opportunities for Undergraduate Participation</u>. Perhaps the most important purpose of the JOVE program is to involve undergraduates in "real world" research. Three students at Centre College have expressed interest, and should begin participation in the project during the fall term of the 1990-91 academic year, provided the requisite hardware and communications are made available. Clearly, AP programs can only be executed on the MSFC Magnetograph Facility's MicroVAX (or a similarly equipped machine), therefore a suitable data link to "MAGVAX" is required. After an introductory course in AP programming (taught by the author), these students should be able to produce FORTRAN code to support magnetograph data reduction at MSFC. The following problems lend themselves to student programming:

(1) Expand the subroutine which calculates magnetic fields in the APVMAP system to include those configurations of the Zeiss filter prior to October 4, 1989. The existing program is valid only for the present configuration.

(2) Modify the entire set of APVMAP subroutines to utilize an expanded vector memory in the AP. At present, the 16384 element arrays must be processed in 4KB segments. If the vector memory is increased to 128KB in each partition, a 128 by 128 array can be processed in its entirety.

(3) Continue the development of routines to implement the non-linear least squares fit method of magnetic field calculation.

The support for research in solar vector magnetic fields need not be limited to programming the AP. It is certainly possible that students can become involved in any type of programming in this project, and conceivable that their participation evolve to data analysis, definition of new observing programs and the implementation thereof.

The author is extremely grateful to Drs. Mona Hagyard, Allen Gary and Messrs. Ed West, Ed Kenny and James Smith for their assistance in "learning the ropes" of the magnetograph facility, and for making his summer a most enjoyable and intellectually stimulating period.

References

1. Hagyard, M.J.,Cumings, N.P., West, E.A. and Smith, J.E.: <u>The MSFC Vector Magnetograph</u>, Space Sciences Laboratory, NASA Marshall Space Flight Centre, AL 35812, 1981.

2. K.S. Balasubramanium, <u>Stokes Polarimetry and the Measurement of Vector Magnetic Fields in Solar Active Regions</u>, PhD Thesis, Indian Institute of Science, 1988

1990

NASA/ASEE SUMMER FACULTY FELLOWSHIP PROGRAM

MARSHALL SPACE FLIGHT CENTER
THE UNIVERSITY OF ALABAMA

GAMMA-RAY BURSTS: AN OVERVIEW

Prepared By: John Patrick Lestrade

Academic Rank: Associate Professor

University and   The University of Alabama
Department: Physics and Astronomy

NASA/MSFC:
        Laboratory: Space Science
        Division: Astrophysics
        Branch: High-Energy Astrophysics

MSFC Colleague: G.J. Fishman

Contract Number: NGT-01-008-021
                        The University of Alabama
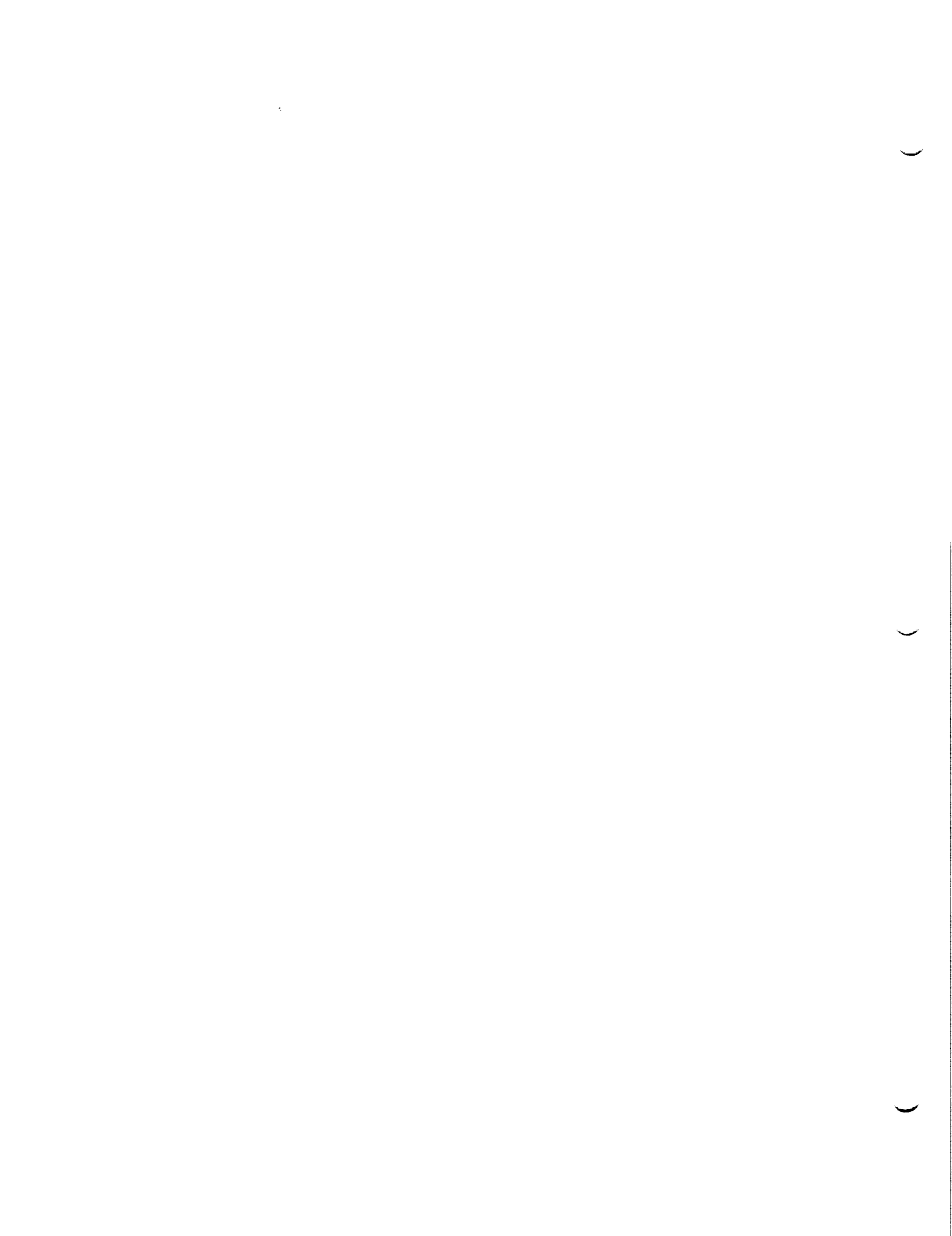
Gamma-Ray Bursts: An Overview

Abstract

Gamma-Ray Bursts were discovered in 1967 by researchers studying data from gamma-ray detectors aboard the Vela satellites. These satellites were launched with the original intent of assuring Soviet compliance with the 1963 Geneva Limited Nuclear Test Ban Treaty. Since this original discovery, over 500 bursts have been observed by more than a dozen experiments on planetary spacecraft, earth orbiters, balloon flights, and even ground based instruments.

Unfortunately, we are no closer today to describing the nature of these transient phenomena than we were two decades ago. Part of the problem lies in the large variability in their physical characteristics. This variability has spawned more than 40 γ-ray burst models. Each model claims some subset of the 500 observed bursts that conclusively proves its validity.

In this paper I present a very brief overview of the γ-ray burst phenomenon. The interested reader is referred to summary papers by Meegan (1990) and Hurley (1989).

1. Introduction:

1.1 The Discovery of Gamma-Ray Bursters

The original discovery of gamma-ray bursts was made in 1965 by Ray Klebasadel and Roy Olson from data recorded by the Vela satellite. These satellites were originally intended to discourage nuclear testing in space – presumably by the Soviet Union. Such testing was banned by the limited test ban treaty first proposed in Geneva, Switzerland and signed in 1963. Both satellites carried detectors that were sensitive to fluxes of charged particles, neutrons, x-rays, and most importantly, γ-rays.

The first two Vela satellites were launched in 1964. Placed in nearly circular orbits at an altitude of approximately 120,000 km and on opposite sides of the earth, the satellites looked for sharp increases in flux that would indicate a thermonuclear test. Several factors inhibited the early detection of cosmic bursts. First, there were many false signals, "local" events, caused by interactions of the spacecraft with the local environment. Second, each satellite tagged γ-ray events with its own local time. This made the search for simultaneous events difficult.

It wasn't until 1967, with the launch of Vela 4, that Klebasadel began to attempt correlative studies between the observations of all Velas. The first step was to convert satellite times to Universal Time (UT). A manual search was then started through the reams of output looking for simultaneous events. After a short period they found an event that was detected by both Vela 3 and Vela 4 separated by only 2 seconds. According to Klebasadel (1990),

it was clear from the time profile that this event was not due to a nuclear test, but rather, some other cosmic event. Also, the time profile and direction of the burst excluded solar phenomena as the cause.

One of the first significant characteristics of gamma-ray bursts (grb's) emerged from the Vela database: their (apparent) isotropic distribution in the sky.

1.2 Recent Observations

Since those first observations, more than 500 grb's have been detected by several different experiments. Spacecraft that have flown gamma-ray detectors include the *Pioneer-Venus Orbiters*, the Soviet *Venera* and *Phobos* missions, the Japanese *Ginga* satellite, and the recently launched French-Soviet *Granat* satellite. To date, the best "published" observations of grb's have been made by the APEX experiment on *Phobos* (Mitrofanov, 1990). These have high resolution in both time and energy. The recently launched *Granat* satellite is expected to produce better data but that has not yet happened.

The simultaneous detection of a single burst by three or more spacecraft, widely separated in space, allows the determination of the position of the burst through triangulation. This method requires relatively high resolution in the burst time profile so that unique features can be time tagged. The exact positions of the spacecraft and the time delay for arrival of the radiation at the different locations leads to position error boxes as small as a fraction of an arc-minute.

One topic that always emerges in a discussion of grb's is the lack of quiescent counterparts. With several very accurate determinations of grb positions, only one† has been associated with a counterpart. This lack of verification at other wavelengths or of an identifiable binary companion means that we do not know the distance to grb's. Consequently, we cannot calculate their luminosities. Furthermore, since counterpart searches have been carried out in known error boxes down to a level of 24th magnitude and at peak intensity the apparent visual magnitude is estimated to be +2, we are dealing with a phenomenon which changes by 22 magnitudes in apparent brightness. For comparison, supernovae show an apparent magnitude change of one-fifth this amount (i.e., +20).

A second noteworthy fact arising from all of the observations is the lack of repeaters. Of the hundreds of burst sources detected only four have been found to repeat and, based on their spectral characteristics, these four appear to be in a separate burster class.

---

† The March 5, 1979 event was peculiar for many reasons. It remains the brightest γ-ray burst in apparent magnitude. Its position is in the center of the N49 supernova remnant in the Large Magellanic Cloud (LMC). Because of the perhaps unrealistic energy output required at this distance (10^{43}-10^{44} ergs/sec) some dispute this association and think it is a chance alignment.

2. GRB Spectra:

2.1 Time Profiles

Most grb's have a duration of approximately 10 seconds. Although there have been some that have lasted for only milliseconds and others have lasted for a good part of an hour. Figure 1 shows a typical† burst time profile (Hurley, 1989). With a time resolution of 0.05 seconds, this event shows intensity structure with no apparent correlation between peaks. Apparently there are no rules. Some profiles are smooth and slowly varying, others show large random swings in intensity, and one even showed an 8-second periodicity. Some bursts show a small precursor just before the main burst while others have a long slowly decaying tail.

2.2 Energy Spectra

Most efforts to determine the physical cause of γ-ray bursts have centered around the energy spectra. Figure 2 shows a generic energy spectrum of a burst (Murakami, 1989). The most important features are the approximate power-law continuum at high energies, the absorption lines near 20 and 40 keV and the emission line at 400-500 keV. The first puzzle is the fact of the paucity of flux at x-ray wavelengths. Nearly all imagineable cataclysmic events happening near the surface of a neutron star that release γ-rays should also emit an abundance of x-rays. If this release does not come directly from the event itself, it should arise from the reprocessing of the emission by the surrounding medium and/or the stellar surface.

The second puzzle concerns the temperature of the environment where the spectrum is formed. The continuum is approximately fit by a thermal bremsstrahlung model. Such models require high temperatures, a sea of relativistic electrons, strong electro-magnetic fields, and massive particles to decelerate the electrons thus releasing radiation.

The two absorption lines at about 20 and 40 keV could be due to "cyclotron" motions of electrons in very strong magnetic fields. The shape and positions of these lines imply a magnetic field strength of approximately 2×10^{12} gauss. Such a field is consistent with the belief that bursts are associated with neutron stars. In apparent contradiction to the hot continuum, the narrowness of these absorption lines implies their formation in a cool region – where doppler and collisional broadening are reduced. One model attempts to explain this with a thin absorbing layer of gas around the neutron star overlying the hot region where electrons radiate. This layer is optically thin except at the cyclotron frequencies (Lamb, 1990). A second model avoids the absorption phenomenon completely and claims that the spectral depressions are caused by the overlap of different continua: blackbody radiation, thermal bremsstrahlung, and perhaps synchrotron continuum.

Complicating factors in the above studies include a) not all bursts show the same features, b) some show absorption and emission lines at very different energies, and c) it has recently been discovered that these spectra are variable on timescales at short as 100 msec (Mitrofanov, 1990).

---

† Many researchers in the field, with an eye on the great variability in every grb physical characteristic, would balk at using this term – for them, 'sample'

3. Conclusion

For more than two decades the study of γ-ray bursts has been hampered by poor observations and a phenomenon that is perhaps much more complicated than we first imagined. Fortunately, help is on the horizon. My work here as a NASA/ASEE fellow involves the energy calibration of a new γ-ray detector, the Burst And Transient Source Experiment (BATSE) on the Gamma-Ray Observatory (GRO). As described in my previous summer reports, detailed measurements and calculations of the sensitivity of the BATSE modules are required for the correct interpretation of burst observations.

In early 1991, GRO will be lifted into a low, earth orbit by the shuttle. This experiment will provide definitive answers to the γ-ray burst puzzle.

4. Bibliography

1. Hurley, K., 1989, Cosmic Gamma-Ray Bursts: An Overview of Recent Results, *Annals of the New York Academy of Sciences*, **571**, 442.

2. Klebasadel, R., 1990, The Discovery of Gamma-Ray Bursts, presented at the γ-Ray Burst Workshop, Taos, NM, August, 1990.

3. Lamb, D., 1990, Cyclotron Resonance Scattering in GRB Spectra, presented at the γ-Ray Burst Workshop, Taos, NM, August, 1990.

4. Meegan, C., 1990, Gamma-Ray Bursts: Current Status of Observaitons and Theory, NASA TM-100398.

5. Mitrofanov, I., *et. al.*, 1990, Study of Cosmic Gamma-Ray Bursts in the Soviet-French Experiment APEX. Models of Sources and Mechanisms of Emission, presented at the γ-Ray Burst Workshop, Taos, NM, August, 1990.

6. Murakami, T., 1989, Cyclotron Absorption in Gamma-Ray Bursts Seen with *GINGA*, *Proc. 23rd ESLAB Symp. on Two-Topicsin X-Ray Astronomy, Bologna, Italy, Sept., 1989.*
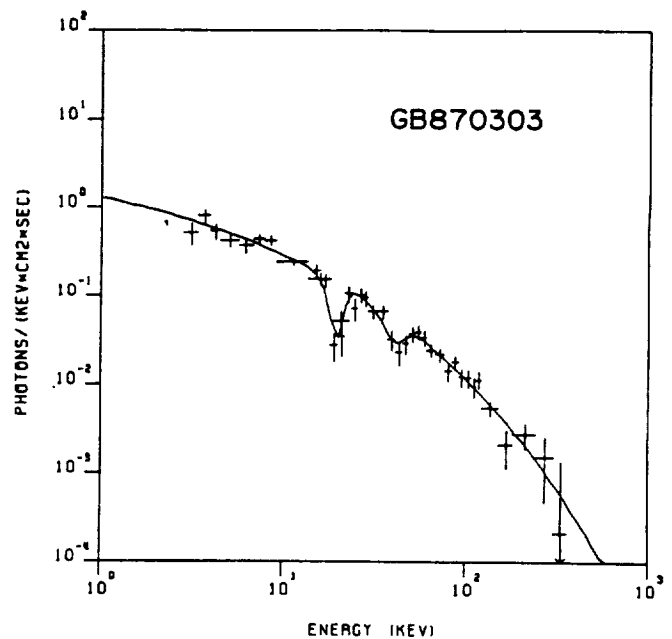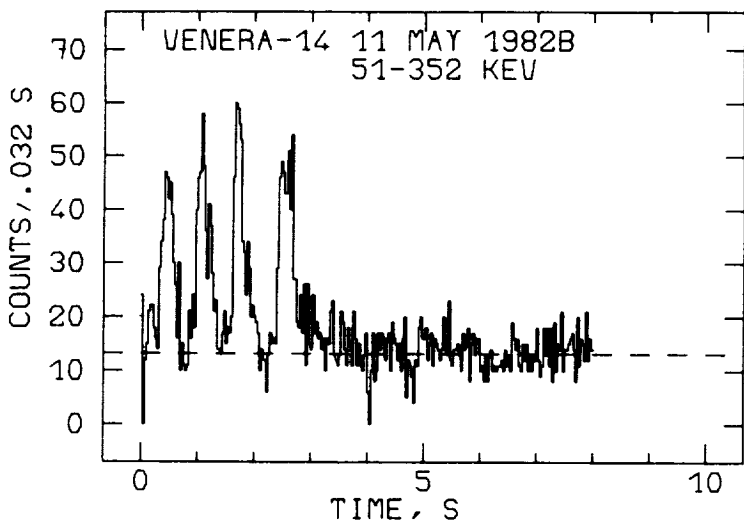
NASA/ASEE SUMMER FACULTY FELLOWSHIP PROGRAM

MARSHALL SPACE FLIGHT CENTER
THE UNIVERSITY OF ALABAMA

VISUALIZATION OF YEAST CHROMOSOMAL DNA

Prepared by: Seth Lubega

Academic Rank: Professor

University and   Oakwood College
Department: Department of Biological Sciences

NASA/MSFC:

    Laboratory: Space Science
    Division: Microgravity Science & Application
    Branch: Biophysics

MSFC Colleague: Dr. Robert S. Snyder

Contractor No.:   NGT-01-002-099
                                   The University of Alabama
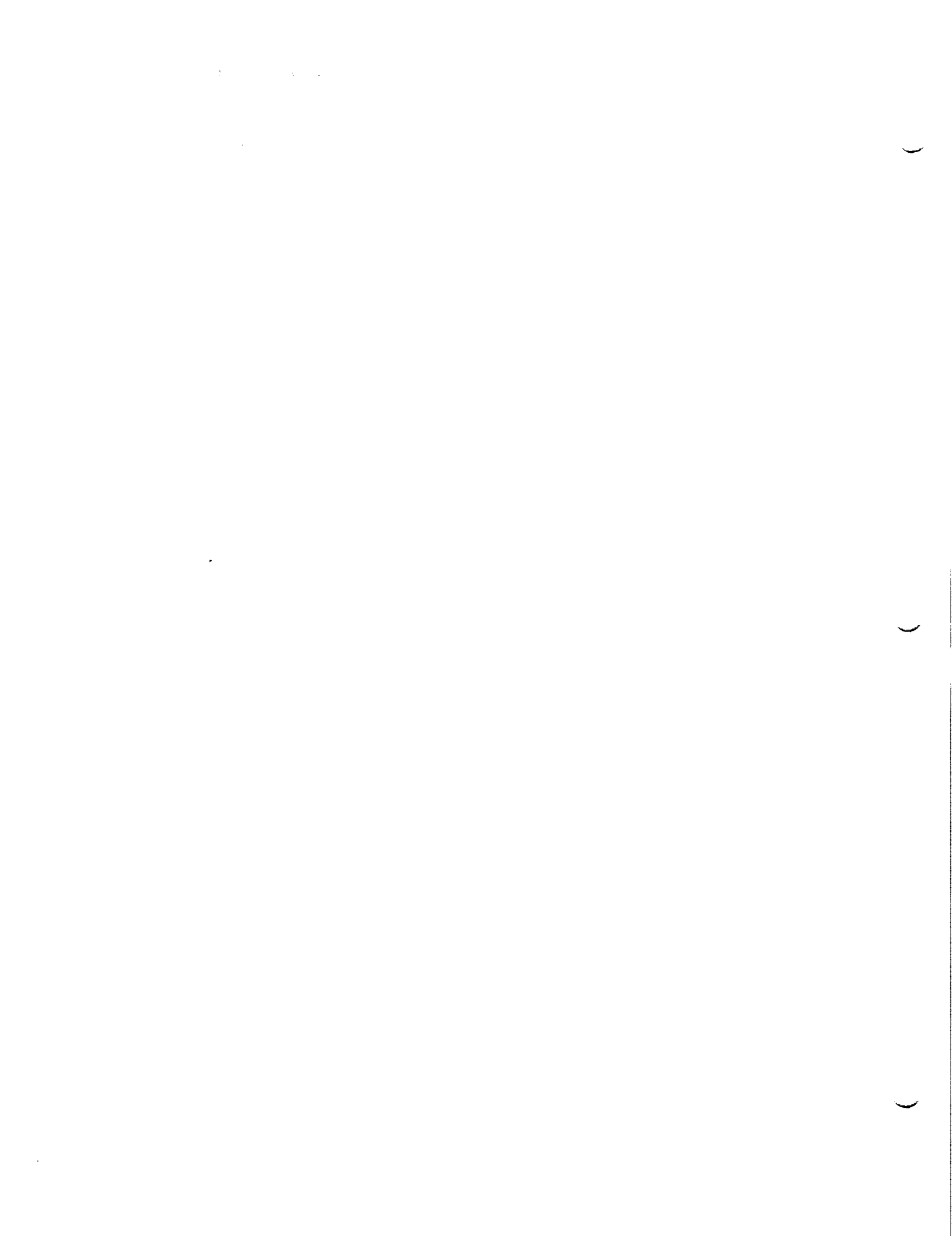
VISUALIZATION OF YEAST CHROMOSOMAL DNA

Introduction

The DNA molecule is without doubt the most significant life molecule since it codes the blue print for other structural and functional molecules of all living organisms. It is also by far the largest. Some chromosomal DNA molecules are as long as several centimeters. With a diameter of only 20 Å, the aspect ratio may be to the magnitude of $10^6 - 10^7$. This makes it extremely fragile. Agarose gel electrophoresis is now being used widely to separate DNA of virus, bacteria, and lower eukaryotes (fungi and protozoa). Individual chromosomal DNA molecules have been observed using the fluorescent microscope but the physical basis of their behavior is still poorly understood. Dr. Robert Snyder and his team have undertaken the task of reviewing the existing methods of DNA fractionation and microscopic visualization of individual chromosomal DNA molecules by gel electrophoresis as a basis for a proposed study to investigate the feasibility of separating DNA molecules in free-fluids as an alternative to gel electrophoresis. It has been an exciting experience to learn the various techniques as I worked with the team this summer. Since the study is in its initial stages, negotiations are under way for some arrangements to make it possible for me to continue to work with the team through the academic year. This will be necessary for me to keep up with the progress of the study and be ready to work with the team next summer.

The chromosomes of lower eukaryotes such as fungi and protozoa have poor mitotic and meiotic visualization and present a challenge for both genetic and cytogenetic studies. On the molecular level, agarose gel electrophoresis is being widely used to separate chromosomal DNA according to molecular weight. Carl and Olson (1985) separated and characterized the entire

karyotype of a laboratory strain of <u>Saccharomyces cerevisiae</u>. Smith et al. (1989) and Schwartz and Koval (1989) independently reported the visualization of individual DNA molecules migrating through agarose gel matrix during electrophoresis. The techniques used by these researchers are being reviewed in our laboratory as a basis for the proposed studies.

Preparation of Intact Chromosomal DNA

'The separation of chromosomal DNA based on molecular weight requires that that DNA remain intact without breakage. For DNA of 50 kb or less from most biological sources, standard methods of purification such as phenol extraction, alcohol precipitation, and micropipetting are quite effective. Larger molecules, especially those above 300 kb in size cannot be effectively purified by these methods without breakage. Schwartz and Cantor (1984) developed a method of preparing DNA samples by <u>in situ</u> lysis of cells or spheroplasts in a semi-solid matrix. Several modifications of this method have been developed but they all employ an agarose matrix. The intact cells or spheroplasts are suspended in low gelling agarose. The liquid-cell mixture is poured in molds known as inserts and allowed to solidify before treating with reagents to lyse the cells and remove the proteins leaving the naked DNA in the stable gel. The insert is then treated with 0.5 M EDTA to reduce nuclease activity to levels where no double stranded breaks will occur. In this form the insert can be stored at 4 °C for long periods of time although best results are obtained when electrophoresis is carried out within 2 weeks.

Separation of DNA by Pulse Field Gradient Gel Electrophoresis (PFGE)

Most chromosomal DNA molecules are extremely large. Small molecules 50 Kb or less are easily separated on the basis of their molecular weight using polyacrelamide or agarose gel electrophoresis. DNA molecules larger than 50 kb tend to migrate at the same rate making separation by these methods impossible. Schwartz and Cantor (1984) described a method that effectively separates large DNA molecules by agarose gel electrophoresis. The Pulse Field Gel Electrophoresis (PFGE) method is based on the fact that DNA molecules in solution behave like a worm-like coil. The pores in the agarose are smaller than the dimension of the coils formed by molecules more than 30 kb in size. When a large DNA molecule enters such a gel in response to an electric field, the coils must elongate parallel to the field. When the field is shut off and a new field is applied perpendicular to the long axis of the DNA molecule, it finds itself lying across the openings of several pores. It will have to reorient itself and enter one of them. The key to separation is the fact that larger molecules take longer to reorient than smaller ones. As the cycle is repeated each molecule will have a characteristic net mobility along the diagonal of the gel.

Visualization of Individual DNA Molecules During Agarose Gel Electrophoresis

The visualization of individual DNA molecules migrating through agarose gel matrix during electrophoresis using a fluorescent microscope was a giant step toward the understanding of the dynamics involved in the orientation of these macromolecules. Smith et al. (1989) and Schwartz and Koval (1989) both observed that DNA molecules advanced lengthwise through the

gel in an extended configuration. They alternately contracted and lengthened as they moved. Often they became hooked around obstacles in a U-shape for extended periods and displayed elasticity as they extended from both ends at once. The obstacles may be due to the fact that commercial agarose is contaminated with other polysaccharides, salts, and proteins.

Smith et al. also observed an aqueous layer under the cover slip on the slide on which the gel was. In the absence of an electric field the DNA molecules in the aqueous layer could be seen "tumbling and wriggling" in response to Brownian motion while the DNA in the gel was virtually motionless. In an electric field the DNA in the quueous layer "tumbled and streamed" quickly toward the positive electrode. The DNA in the gel underwent a slower and more constrained motion as described above.

The studies of chromosome-sized DNA fractionation and visualization reported to date involve viral, prokaryotic (bacteria), and lower eukaryotic (fungi and protozoa) DNA. Higher plants and animals have much larger and more complex chromosomal DNA's that will require other methods of preparation.

Our team is in the initial stages of reviewing the established techniques as a basis of improving on them. Our initial challenge is the investigation of the feasibility of developing a method of visualizing and separating DNA-sized molecules in free-fluids. We hope that this method will have the capability of visualizing and separating chromosomal DNA of higher eukaryotes (plants and animals) and provide an invaluable tool in genetic studies of these organisms.

References

Carle, George F., and Maynard V. Olson (1985): "An Electrophoretic Karyotype for Yeast (DNA/Chromosomes/Orthogonal-Field-Alteration Gel Electrophoresis)," Proc. Natl. Acad. Sci. USA, Vol 82: 3756-3760.

Carle, George F., and Maynard V. Olson (1987): "Orthogonal-Field-Alternation Gel Electrophoresis" Methods in Enzymology, 155:468-475.

Schwartz, David C., and Charles R. Cantor (1984): "Separation of Yeast Chromosome-Sized DNAs by Pulsed Field Gradient Gel Electrophoresis, Cell. 37:67-75.

_____ and Michael Koval (1989): "Conformational Dynamics of Individual DNA Molecules During Gel Electrophoresis," Nature, Vol. 338, No. G215, pp. 520-522.

Smith, Steven B., Paul K. Aldridge, and James B. Callis (1989): "Observation of Individual DNA Molecules Undergoing Gel Electrophoresis," Science, 243:203-206.

1990

NASA/ASEE SUMMER FACULTY FELLOWSHIP PROGRAM

MARSHALL SPACE FLIGHT CENTER
THE UNIVERSITY OF ALABAMA

"TECHNIQUE FOR ASSESSING VEGETATION-INDUCED MOISTURE FLUX,

WITH IMPLICATIONS FOR GLOBAL CLIMATE MODELING"

Prepared By: Emir Jose Macari

Academic Rank: Assistant Professor

University and   University of Puerto Rico
Department: Civil Engineering

NASA/MSFC:

        Laboratory: Space Science
        Division: Earth Science and Appl.
        Branch: Special Projects

MSFC Colleague: Dr. N. C. Costes

Contract No.:   NGT-01-002-099
                           The University of Alabama

General

The Mission to Planet Earth has as main objective the study of the changes that the planet has and is undergoing. Mission to Planet Earth describes a focused effort in satellite remote sensing and the associated ground-based research from a variety of fields that will characterize the global environment as an interacting system. The Earth Observing System (EOS) is an integral part of Mission to Planet Earth and is dedicated to providing the new observations, data and information necessary to understand the way the Earth works as a natural system.

With the development of EOS, scientists will be able to observe and understand many of the key variables and processes of the global-scale cycles of energy and water. Water plays a global role of enormous variety of Earth system processes. Water is considered to be the most powerful agent of topographic change. Water is also necessary for life on Earth, playing a major role in climate regulation. In addition to its role in ocean circulation and precipitation, water can also affect climate in the continents through transpiration within plant and soil ecosystems. Short term hydrological events, such as droughts or large precipitation activity can cause substantial ecological changes on regional scales.

Large scale hydrologic studies are essential to the NASA/MSFC EOS initiative in order to better understand hydrological flux processes that are a main ingredient in global biosphere interactions. One of the most important questions for modeling the global hydrologic cycle includes the interrelationship between land surface and atmospheric processes for variable spatial and temporal scales. Global climate models have shown that proper modeling of the Earth's surface (which is commonly modeled as a boundary layer) is of great importance to the results obtained in such modeling studies.

Introduction

Recent simulation experiments on the sensitivities of climate to hydrological processes have been conducted by Mintz (1984) and Ye (1989). Hydrological processes have been found to significantly affect terrestrial climate. Yeh et al. (1984) showed that in addition to affecting the planetary boundary layer, ground hydrological processes can be felt through the whole troposphere.

The relationship between vegetation and soil (especially in the rooting zone) is crucial to both the heat and water balance. Only through vegetation can water in the deep soil layers be connected with the atmosphere and take part in the hydrological processes. Hydrologically, the

three main factors controlling this are: the time between storms, the duration of storms, and the storm depths, (Eagleson, 1978). This research project attempts to study each of these features, in relation to vegetation controls on the disposition of rainfall. It is proposed that understanding the movement of water between the vegetation and soil (including evapotranspiration and infiltration) will be the gateway for modeling atmospheric flux and improving global climate models.

Despite increasing efforts by hydrologists and atmospheric scientists to measure short-term rainfall intensity, it may not be the important variable for soil water physical interpretation. As indicated above, rain does not fall directly upon the earth surface where soil physical measurements are made. It is funnelled there by the resident vegetation; either throughfall or stemflow. These plants may act as 'lenses' and focus the water, so that the local flux density of water application to the surface may be substantially above the recorded rainfall rate. Therefore, the vegetation plays a critical role in the transmission of rainfall to the surface and deeper soil deposits.

Objective

The overall goal of the proposed research effort is to develop a field/laboratory methodology which will provide a better understanding of vegetation-induced water movement. Water flow initiated from stemflow of wooded slopes feeds soil water pathways, which in turn feed the deeper groundwater system and give rise to stream response. This is balanced by more water inputs via throughfall, where it percolates the soil matrix and allows much greater rates of evapotranspiration and atmospheric/soil moisture flux. Until now, soil physicists and hydrologists have not treated the vegetation-soil interface in any detail. In fact, most studies have disregarded the effect of rainfall 'funnelling' and modeled surface hydrologic flux solely on the basis of evenly applied rainfall. Calculation of soil moisture flux requires frequent measurement of soil suction during a storm. This research study seeks to gain an understanding the effect of vegetation on soil moisture, and the effect of this 'differential' wetting on resulting evapotranspiration and atmospheric flux.

Instrumentation

A small forested research plot on the Redstone Arsenal has been instrumented with an intensive network of electronically multiplexed tensiometers, throughfall and stemflow collectors, rain gauges and soil moisture sampling devices. The overall instrumentation set-up is managed and operated by two Campbell 21X field data-loggers which are programmed to gather and store the appropriate data, a

sketch of the apparatus. The research site is located in the immediate proximity of Building 4372. A mobile trailer, located on the high ground (west side) of the site houses the data-loggers and acts as the control room to the research site. The data-loggers are powered by DC current and are kept recharged by means of solar energy. Solar panels were mounted on the north-east corner of the site and are connected to each of the six sets of 12 volt batteries located in the middle of each instrumentation grid.

The research site is discretized into six identical grids. Each grid consists of four sets of tensiometers and one set of soil moisture sampling devices. Each of the grids is connected to a centrally located multiplexer that is excited by one of the two data-loggers (located inside the field laboratory). Each set of both the tensiometers and soil moisture sampling devices, is composed of three instruments which were installed to depths of 1, 2, and 3 feet from the surface elevation. Also, a seventh grid was instrumented located away from base of one of the trees in the site. This last grid is composed of 9 sets of tensiometers and 4 sets of soil moisture sampling devices and will enable the identification of soil zones of high flux density, where vegetation 'funnelling' through the tree roots may occur. The total number devices in the research site is 99 tensiometers and 30 soil moisture sampling devices. In addition, six tipping bucket rain gauges were installed. One of them was installed in the north-east corner of the site (as far away from the trees) in order to measure the total volume of rain during a given event. Another rain gauge is fed by a stemflow receptacle installed on the trunk of one of the down slope trees in order to measure quantities of water that travel to the surface via the tree trunk. The remaining four rain gauges were installed below the tree canopies in order to measure the canopy rain throughfall.

An above ground sprinkling system was installed at the site. Artificial sprinkling experiments will be conducted to enable specific tests of observed phenomena. By controlling water application, vegetation-induced moisture flux can be correlated to pre-storm antecedent wetness condition. This will greatly enhance data collected from natural events, and place results within the context of seasonal and annual conditions.

Soil Conditions

In order to assess the soil conditions at the indicated research site, three soil borings were drilled and soil samples were obtained from each of these borings. The results of the test drilling indicated a topsoil cover at each of the test locations ranging in thickness from approximately 1.0 to 1.5 feet. Below the topsoil cover the

test borings encountered an upper stratum of sandy lean clay extending to depths ranging from approximately 6 to 9 feet below the surface elevations. The tests borings were terminated in an underlying stratum of fat clay with variable proportions of leached limestone fragments. The borings were terminated at approximately 10 feet below the surface elevation.

Operation of the Site

The data-loggers have been programmed to excite the multiplexers and hence record data from the pressure transducers (tensiometers) and the rain gauges at given time intervals. These time intervals will depend on the meteorological forecast. During anticipated rain events the sampling intervals will vary between 15 and 20 minutes in order to obtain as much data as possible. During anticipated dry periods the sampling intervals will be expanded to every hour in order to minimize non-usable data. The data obtain during the sampling periods is collected by the data-loggers and then stored into two detachable storage modules. In order to analyze the data the storage modules can be plugged into a personal computer by means of an RS232 connector and specially developed software retrieves and converts the data into ASCII format spreadsheets that can be readily accessed by any spreadsheet software package.

Conclusions

The expected results can be used for improving hydrologic sub-models of global climate change. With information obtained during the experiments outlined above, specific questions regarding the nature of vegetation-induced moisture flows can be addressed.

The experimental and numerical methods developed through this research could be used in future large-scale experiments on hydrologic and atmospheric flux. These efforts involve remote sensing applications, to predict regional-scale processes. Knowledge gained in the proposed study will be used to develop a Vegetation-Soil-Water index for regional atmospheric flux and hydrological models.

1990

NASA/JOVE PROGRAM

MARSHALL SPACE FLIGHT CENTER
THE UNIVERSITY OF ALABAMA

TEST IMAGES FOR THE MAXIMUM ENTROPY

IMAGE RESTORATION METHOD

Prepared By: James E. Mackey

Academic Rank: Professor

University and
Department: Harding University
Physical Science

NASA/MSFC:

Laboratory
Division: Space Science
Branch: Solar Terrestrial Physics
Solar

MSFC Colleague: Dr. Jim Dowdy
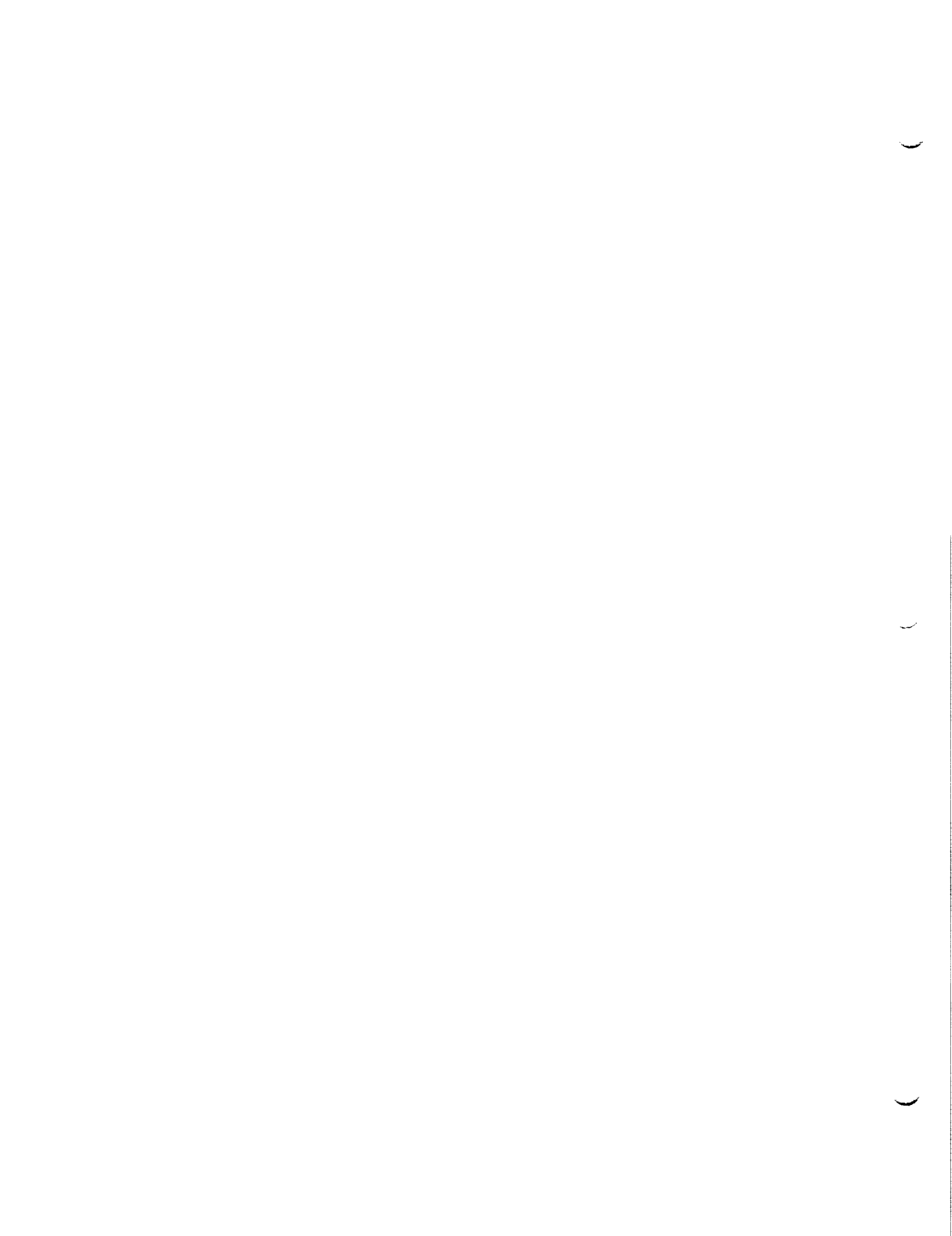
Test Images for the Maximum Entropy
Image Restoration Method

One of the major activities of any experimentalist, in addition to data collection, interpretation and subsequent communication of information, is data analysis/reduction. It is in this step that actual physical data as collected by a variety of instruments and techniques is transformed into information that can be effectively utilized in making interpretations of and drawing conclusions about the physical system being studied. In solar physics, remote observations are made of the sun in a variety of wavelengths and circumstances. In no case is the data collected free from the influence of the design and operation of the data gathering instrument as well as the ever present problem of noise. In analyzing the data, which is, in some fashion, always truncated and digitized fourier transform techniques have been extensively employed. The process can be simply represented as

$$d(x) = h(g(x)) + n(x)$$

where $d(x)$ represents the collected data, $g(x)$ the actual solar information, $h(x)$ represents the given instrument and measurement procedure, and $n(x)$ is the noise. In theory one merely inverts this relationship to obtain $g(x)$ as an inverse operation of $h(x)$, however, the presence of the noise and the fact that data $d(x)$ is a limited representation of the true information $g(x)$ makes this in practice impossible. To actually obtain the true information one characteristically makes assumptions about the data and extends the data into regions in which it is not actually known. The correlation function is normally evaluated at the points (called lags) where the sample data is actually known. One then takes the

fourier transform of the correlation function to obtain the information desired. In the process of taking this transformation we find that there are a very large number of spectral functions that are consistent with the measurements we have. It is then common to extend the range of known correlation functions into the unknown region and typically assume that the extended values are all zero (conceivably one could make other assumptions about these values other than zero, but they remain **assumptions** and not true data). When this occurs the investigator has interjected an a priori statement and included an experimental bias. All of this is true apart from a consideration of noise. The present of significant noise (significant meaning too large to be neglected) invalidates the simple inversion procedure regardless of the range of known correlation functions.

The Maximum Entropy Method (MEM) attempts to perform this inversion by making minimal assumptions about the data. In simplistic terms the method chooses the correct restored data by requiring that the entropy (or information) of the process be maximized subject to constraints such as the total energy being constant or the sum of the probabilities being one, etc.

To provide a means of testing the MEM and characterizing its sensitivity to noise, choice of point spread function, type of data, etc., one would like to have test images of known characteristics that can represent the type of data being analyzed. Such images could provide an answer to objections that the apparently enhanced information obtained by MEM is nothing but a computer artifact of the restoration procedure and not real data.

In beginning to construct such images a choice was made to

initially begin with images with a highly symmetric octagonal symmetry. This allows for easy construction of 512 by 512 pixel images from a 128 by 128 pixel square unit cell. A sample test image is shown as Figure 1. The area between the octagons models the network regions on the sun while the interior of the octagons models the cells. The distribution of area between the network and cells was chosen to reflect typical values for solar images. To allow for the influence of the instrument on the data, the test image is convolved with a point spread function appropriate to the particular instrument producing the data set, in this case the Harvard EUV Spectroheliometer flown on the 1973 Skylab missions. The point spread function or PSF is shown in Figure 2. The convolution of the test image and the PSF is shown in Figure 3, and the smoothing effects of the instrument PSF are clearly shown. Since the original data was 120 pixels by 60 pixels, it was subsequently expanded to form a square image by expanding each pixel by 5 horizontally and by 10 vertically (because of oversampling, the effective resolution on the surface of the sun was 2.5 arc seconds horizontally and 5 arc seconds vertically with one arc second corresponding to approximately 725 km on the solar surface). To approximate this data with our convolved test image we sampled the image for each 5th column and 10th row with every other row shifted by two pixels. The resulting sampled image is shown in Figure 4. Once the sampled image was constructed it was necessary to add noise appropriate to the instrument. Since the data was taken as instrument counts, the error can be taken as Poisson error. The modeled noise image is shown in Figure 5. A deviation of up to 10% from Poisson statistics was allowed. The resulting test image, shown in Figure 6, was constructed by adding

the noise to the sampled image and shifting the byte threshold to make all the intensities positive.

The next step in test image construction, which is already in progress, is to add fine scale features to the original test image and repeat the above procedure to determine the size of fine scale features that can be seen in the images. These images will then be treated with the Maximum Entropy algorithm to see to what extent the fine scale detail can be recovered. Once the MEM has been verified to our satisfaction, it will then be applied to images of the quiet sun to attempt to recover small scale structure and determine the significance of the contribution from small scale magnetic loops in the solar network to the energy emitted from the networks. If the method can be adequately validated for such images, it can potentially be applied to a very wide range of other types of data that have been or will be collected by space instruments and probes.
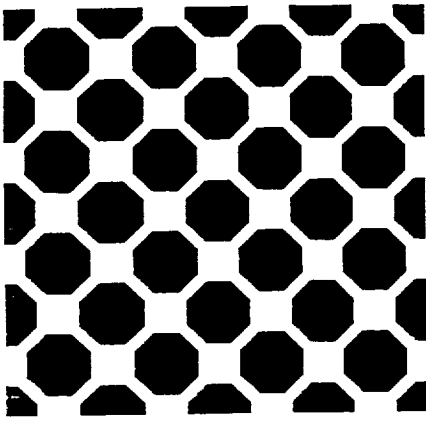
Fig.1
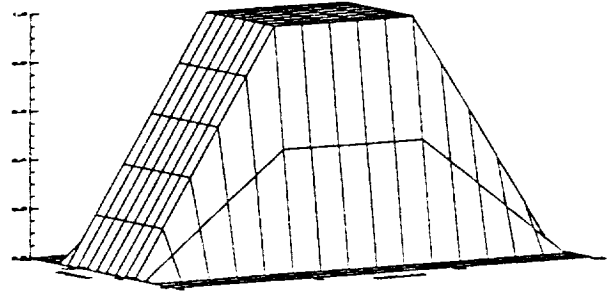
Fig.2
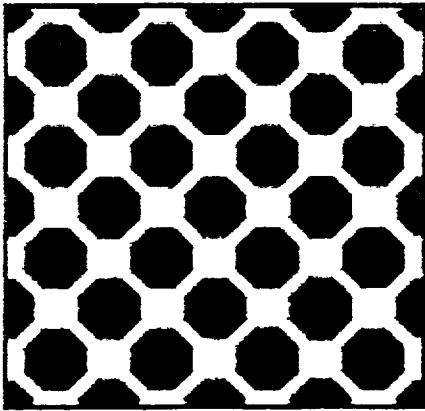
Fig.3
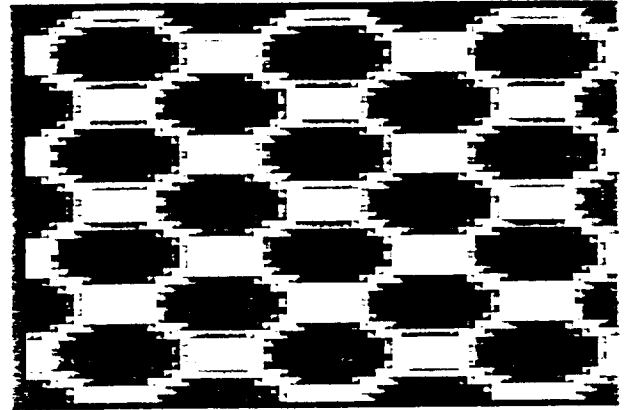
Fig.4
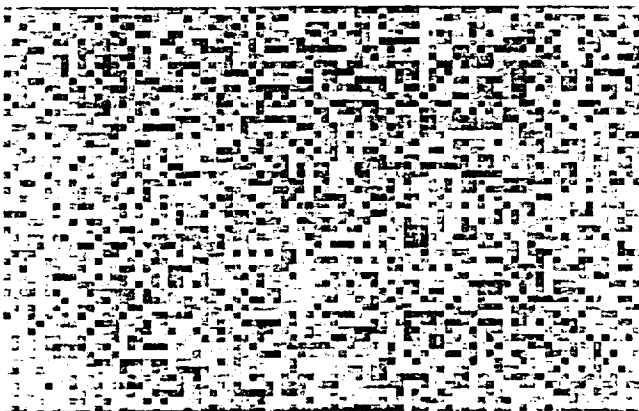
Fig.5
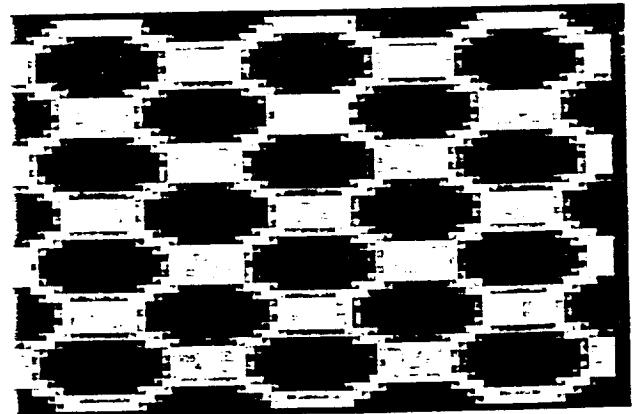
Fig.6

1990

NASA/ASEE SUMMER FACULTY FELLOWSHIP PROGRAM

MARSHALL SPACE FLIGHT CENTER
THE UNIVERSITY OF ALABAMA

FEASIBILITY STUDY OF ROBOTIC NEURAL CONTROLLERS

Prepared By: Mario E. Magana

Academic Rank: Assistant Professor

University and   Oregon State University
Department: Electrical & Computer Engineering

NASA/MSFC:
    Laboratory   Information and Electronic Systems
    Division: Guidance, Control & Opt. Systems
    Branch: Control Electronics

MSFC Colleague: Ralph Kissel

Contract Number: NGT-01-002-099
                          The University of Alabama
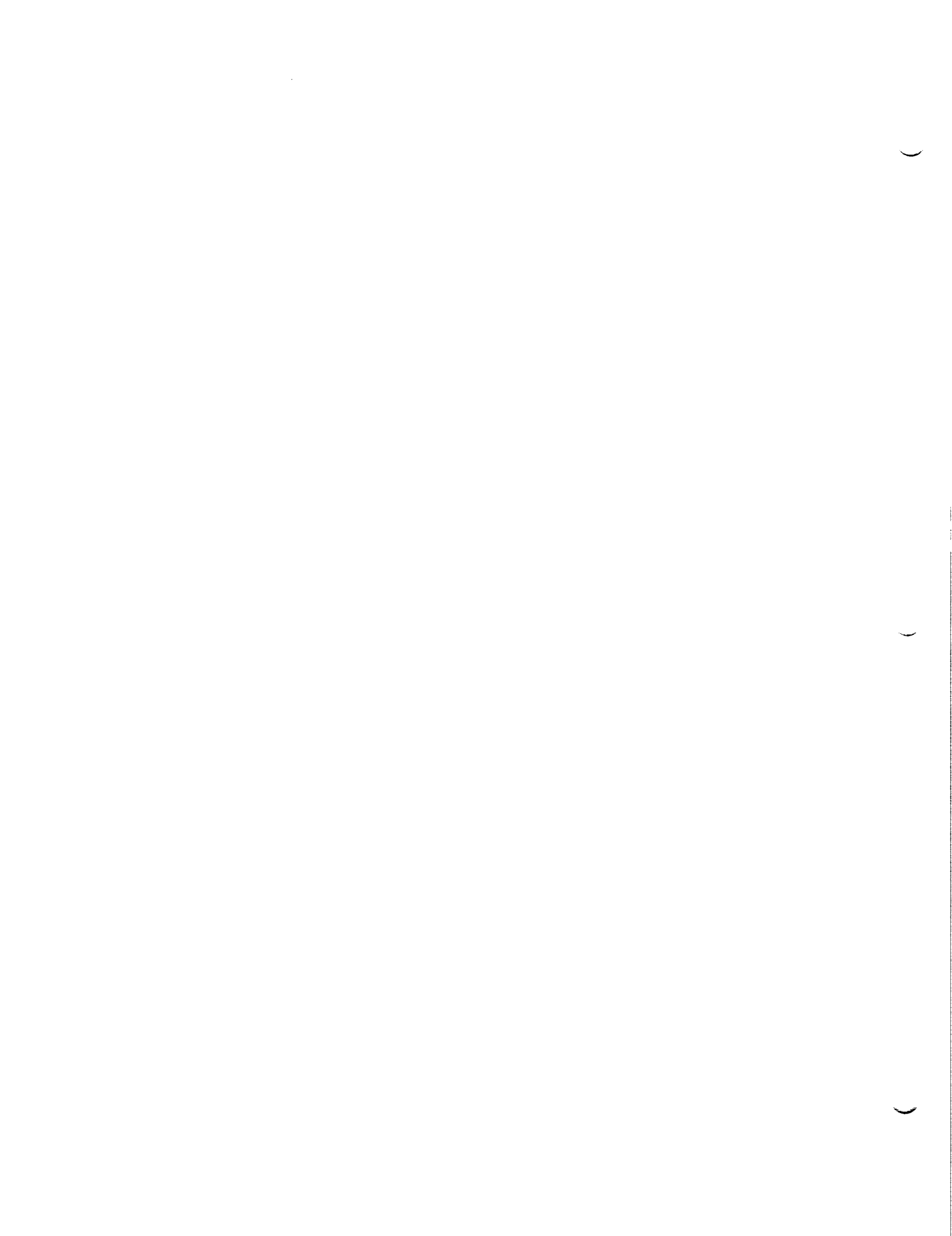
FEASIBILITY STUDY OF ROBOTIC NEURAL CONTROLLERS

by

Mario E. Magaña
Assistant Professor
Department of Electrical & Computer Engineering
Oregon State University
Corvallis, OR 97331

ABSTRACT

This work is the result of a feasibility study performed to establish if an artificial neural controller could be used to achieve joint space trajectory tracking of a two-link robot manipulator. This study is based on the results obtained by Hecht-Nielsen [4], who claims that a functional map can be implemented to a desired degree of accuracy with a three-layer feedforward artificial neural network. Central to this study is the assumption that the robot model as well as its parameters values are known.

INTRODUCTION

The recent explosion of artificial neural networks applications in virtually every science and engineering discipline has motivated control engineers to look into the possibility of using these types of networks to solve problems whose solutions are very hard to find [1], e.g., a robust controller for a nonlinear system.

Researchers [2,3] have already shown that multilayer feedforward artificial neural networks can be used to solve pattern recognition (mapping) problems. Furthermore, Hecht-Nielsen [4] has "shown" mathematically that an L_2 function (mapping) from $[0,1]^n$ to $\mathbf{R}^m$ can be implemented to any desired degree of accuracy with a three-layer feedforward artificial neural network.

Let us now consider the dynamic model of an n-degree of freedom robot manipulator with revolute joints given by

$$\tau = M(\theta)\ddot{\theta} + V(\theta,\dot{\theta}) + F(\dot{\theta}) + G(\theta) , \qquad (1)$$

where τ $\triangle$ nx1 vector of joint torques.

$\theta, \dot{\theta}$ and $\ddot{\theta}$ $\triangle$ nx1 vectors representing the angular positions, velocities and accelerations, respectively, of the links.

$M(\theta)$ $\triangle$ nxn inertia matrix.

$V(\theta,\dot{\theta})$ $\triangle$ nx1 vector of torques arising from centripetal and coriolis forces.

$F(\dot{\theta})$ $\triangle$ nx1 friction torque vector.

$G(\theta)$ $\triangle$ nx1 vector of torques due to gravity.

Let

$$f(\theta,\dot{\theta},\ddot{\theta}) \triangle M(\theta)\ddot{\theta} + V(\theta,\dot{\theta}) + F(\dot{\theta}) + G(\theta) ,$$

then

$$\tau = f(\theta, \dot{\theta}, \ddot{\theta}) \ . \tag{2}$$

If f is a continuously differentiable function, i.e., every term on the right-hand side of (1) is continuously differentiable (this is a somewhat restrictive requirement for a practical manipulator), then in the light of the result obtained by Hecht-Nielsen [4] the function f that represents the robot dynamics can be implemented (identified) with a three-layer feedforward artificial neural network.

Let $N_f[\theta, \dot{\theta}, \ddot{\theta}; w]$ denote the feedforward artificial neural network that identifies $f(\theta, \dot{\theta}, \ddot{\theta})$, where w represents the weights or input strengths to the artificial neurons, then if the number of neurons in the hidden layer increases to infinity, $N_f \to f$ (see [5]). Furthermore, if

$$\tau = N_f[\theta, \dot{\theta}, \ddot{\theta}; w] + \dot{e} + k_r e \ , \tag{3}$$

where $e \triangleq \theta_r - \theta$,
θ_r ▲ nx1 vector of reference trajectories,
k_p ▲ nxn diagonal positive definite matrix,

then upon substitution of (3) into (1) yields $\dot{e} + k_p e \to 0$ also, i.e., $e \to 0$ which implies that $\theta \to \theta_r$.

The controller (3) is the equivalent of the well-known method of computed torque [6].

IDENTIFICATION OF ROBOT DYNAMICS USING ARTIFICIAL NEURAL NETWORKS

Consider the two-link direct drive robot manipulator shown in Fig. 1.
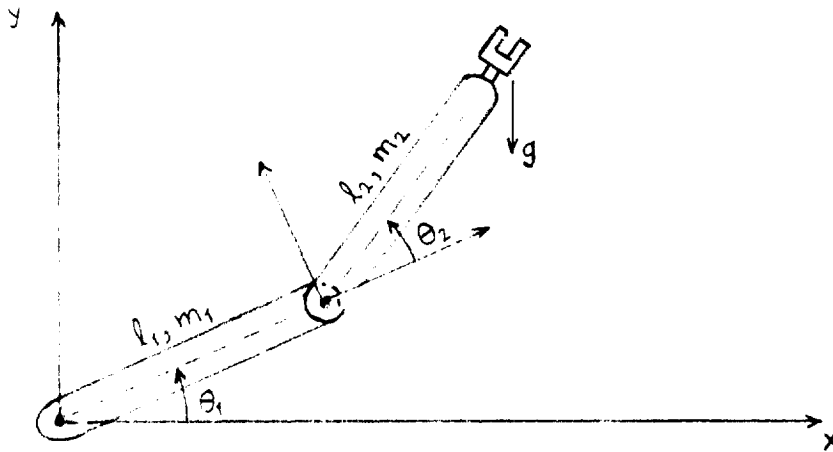
Fig. 1. Two-link robot manipulator.

The dynamic model of this manipulator (excluding friction and external loads) is given by [7]

$$\begin{bmatrix} \tau_1 \\ \tau_2 \end{bmatrix} = \begin{bmatrix} a_1 + a_2\cos\theta_2 & a_3 + \dfrac{a_2}{2}\cos\theta_2 \\ a_3 + \dfrac{a_2}{2}\cos\theta_2 & a_3 \end{bmatrix} \begin{bmatrix} \ddot{\theta}_1 \\ \ddot{\theta}_2 \end{bmatrix} + \begin{bmatrix} -a_2\left(\dot{\theta}_1\dot{\theta}_2 + \dfrac{\dot{\theta}_2^2}{2}\right)\sin\theta_2 \\ \dfrac{a_2}{2}\dot{\theta}_1^2\sin\theta_2 \end{bmatrix} + \begin{bmatrix} a_4\cos\theta_1 + a_5\cos(\theta_1+\theta_2) \\ a_5\cos(\theta_1+\theta_2) \end{bmatrix}$$

$$\tag{4}$$

where $a_1,...,a_5$ are constant parameters that depend on the lengths (ℓ_1, ℓ_2) and the masses (m_1, m_2).

For this particular study, we will use the numerical values of the link parameters that correspond to links 2 and 3 of the Unimation Puma 560 robot manipulator [7], i.e., $\ell_1 = \ell_2 = 0.432$ m; $m_1 = 15.91$ kg and $m_2 = 11.36$ kg. Using these values, we get:

$$
\begin{aligned}
a_1 &= 3.82 \\
a_2 &= 2.12 \\
a_3 &= 0.71 \\
a_4 &= 81.82 \\
a_5 &= 24.06.
\end{aligned}
$$

Postulating the problem in the framework of artificial neural networks, we would like to design a network to synthesize the mapping $\tau = f(\theta, \dot{\theta}, \ddot{\theta})$, where

$$
f(\theta, \dot{\theta}, \ddot{\theta}) = \begin{bmatrix} (3.82 + 2.12C_2)\ddot{\theta}_1 + (0.71 + 1.06C_2)\ddot{\theta}_2 - 2.12S_2\left(\dot{\theta}_1\dot{\theta}_2 + \frac{1}{2}\dot{\theta}_2^2\right) + 81.82C_1 + 24.06C_{12} \\ (0.71 + 1.06C_2)\ddot{\theta}_1 + 0.71\ddot{\theta}_2 + 1.06S_2(\dot{\theta}_1^2) + 24.06C_{12} \end{bmatrix} \quad (5)
$$

where $C_i \triangleq \cos\theta_i$
$S_i \triangleq \sin\theta_i$
$C_{ij} \triangleq \cos(\theta_i + \theta_j)$

In our approach we use a so-called connectionist architecture that attempts to identify the complete dynamic equation [8]. This is shown schematically in Fig. 2.
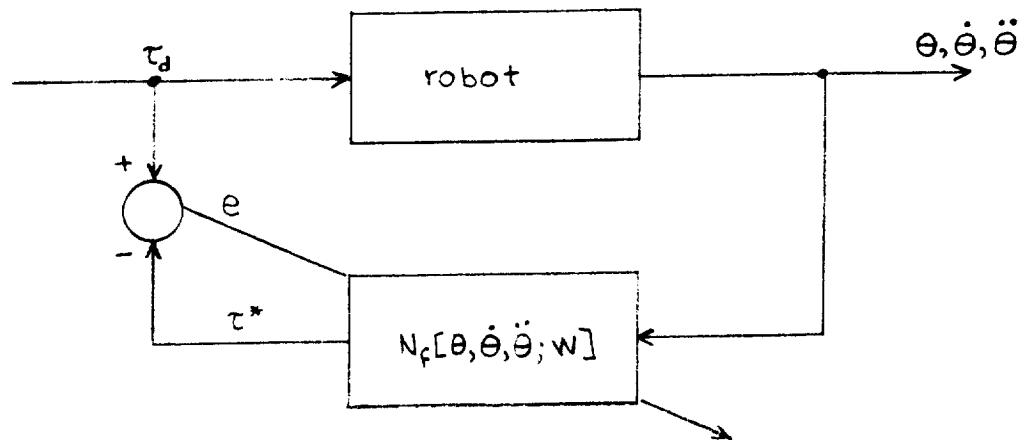
Fig. 2. Learning robot dynamics.

where $\tau_d \triangleq \begin{bmatrix} \tau_{d1} \\ \tau_{d2} \end{bmatrix}$ = desired torques

$\tau^* \triangleq \begin{bmatrix} \tau_1^* \\ \tau_2^* \end{bmatrix}$ = torques generated by the artificial neural network

$e \triangleq \tau_d - \tau^*$

Although the input and output spaces for the two-degree of freedom manipulator is not as large as that of a six-degree of freedom one, it was found experimentally using 4000 8-tuplets (inputs), a four-layer feedforward network with 200, 300, and 400 neurons in each of the two hidden layers and several learning rates (0.7, 0.8, 0.9, 1.0, 1.1), that learning stalled at about 10% of the input-output pairs. In fact, every one of these training runs took several days to execute.

We would also like to point out that three-layer networks with a large number of neurons in the hidden layer were found to perform even worse than the four-layer networks.

It therefore appears that multilayered feedforward artificial neural networks as presently formulated are not of practical use in the identification and control of relatively simple robotic manipulators despite the claims made by many researchers.

CONCLUSIONS

Although Hecht-Nielsen [4] "has proved" that a function (map) can be implemented to a desired degree of accuracy with a three-layer feedforward artificial neural network, a great deal of care must be exercised in interpreting his result, because a very large number of neurons in the hidden layer may be required to learn a functional map, thus rendering these types of networks impractical to implement true neural controllers for robotic manipulators. Therefore, in the opinion of the author, feedforward artificial neural networks as presently conceived, are of no practical use to control robots.

REFERENCES

[1]   P.J. Antsaklis, "Neural Networks in Control Systems," *IEEE Control Systems Magazine*, Vol. 10, No. 3, 1990.

[2]   T.J. Sejnowski and C.R. Rosenberg, "Parallel Networks that Learn to Pronounce English Text," *Complex Syst.*, Vol. 1, pp. 145-168, 1987.

[3]   B. Widrow, R.G. Winter, and R.A. Baxter, "Layered Neural Nets for Pattern Recognition," *IEEE Trans. Assp.*, Vol. 36, No. 7, pp. 1109-1118, July 1988.

[4]   R. Hecht-Nielsen, "Theory of Backprogration Neural Network," *Proc. IEEE 1989 Intl. Conf. on Neural Networks*, pp. I-593 to I-605.

[5]   M. Arai, "Mapping Abilities of Three-Layer Neural Networks," *Proc. IEEE 1989 Intl. Conf. on Neural Networks*, pp. I-419 to I-423.

[6]   J.J. Craig, *Adaptive Control of Mechanical Manipulators*, Addison-Wesley, 1988.

[7]   H. Seraji, "Decentralized Adaptive Control of Manipulators: Theory, Simulation, and Experimentation," *IEEE Trans. Robotics and Automation*, Vol. 5, No. 2, April 1989.

[8]   D.F. Bassi and G.A. Bekey, "High Precision Position Control by Cartesian Trajectory Feedback and Connectionist Inverse Dynamics Feedforward," *Proc. IEEE 1989 Intl. Conf. on Neural Networks*, pp. II-325 to II-331.

NASA/ASEE SUMMER FACULTY FELLOWSHIP PROGRAM

MARSHALL SPACE FLIGHT CENTER
THE UNIVERSITY OF ALABAMA

NEURAL NETWORKS AS A CONTROL METHODOLOGY

Prepared By: Claire L. McCullough

Academic Rank: Assistant Professor

University and   University of Alabama in Huntsville
Department: Electrical & Computer Engineering

NASA/MSFC:
    Laboratory: Structures & Dynamics
    Division: Control Systems
    Branch: Pointing Control Systems

MSFC Colleague: Dr. Henry Waites

Contract Number: NGT-01-002-099
                        The University of Alabama
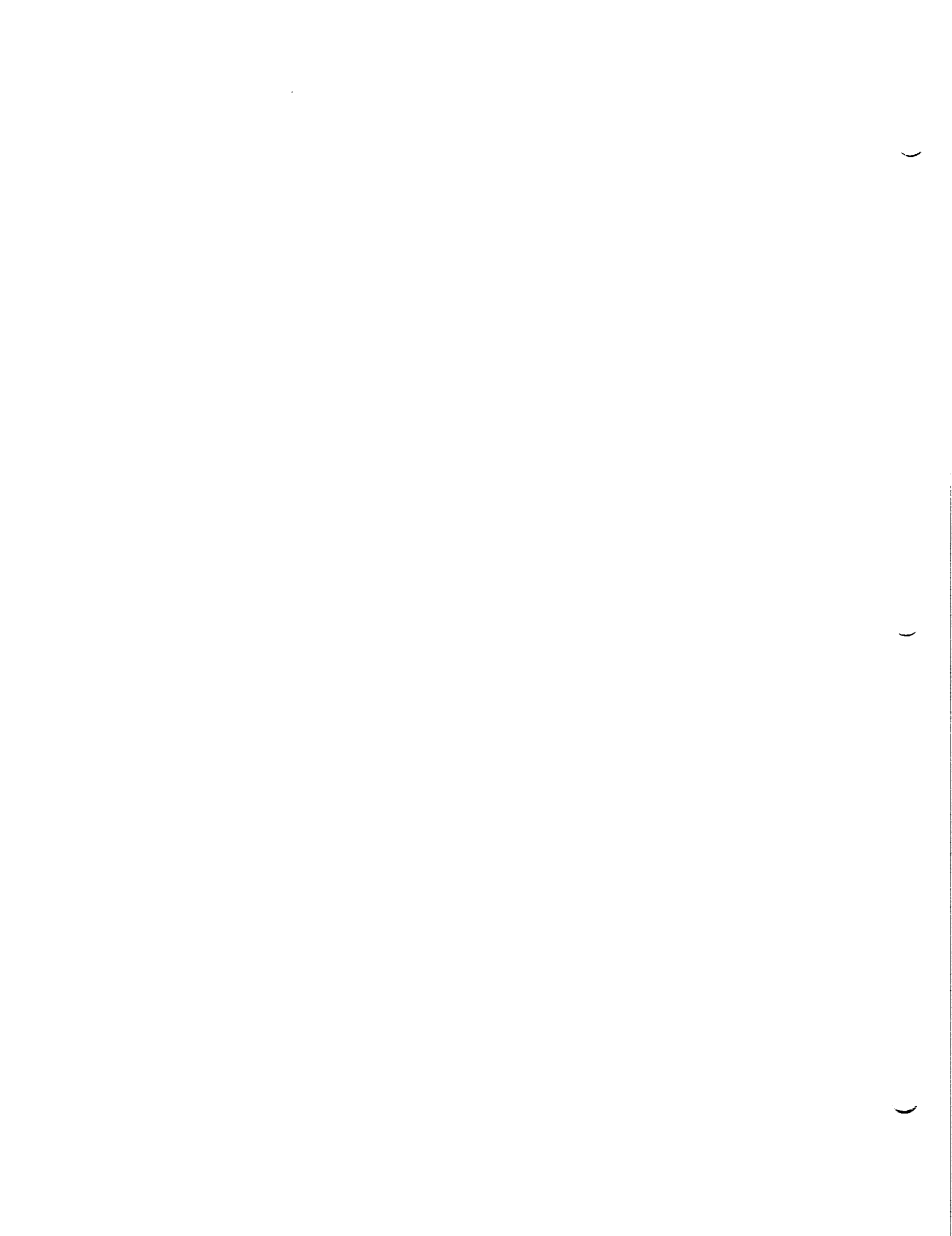
While conventional computers must be programmed in a logical fashion by a person who thoroughly understands the task to be performed, the motivation behind neural networks is to develop machines which can train themselves to perform tasks, using available information about desired system behavior and learning from experience.

Goals of the project begun under the Faculty Summer Fellowship program were threefold:

1) to evaluate various neural net methods and generate computer software to implement those deemed most promising on a personal computer equipped with Matlab

2) to evaluate methods currently in the professional literature for system control using neural nets to choose those most applicable to control of flexible structures

3) to apply the control strategies chosen in 2) to a computer simulation of a test article, the Control Structures Interaction Suitcase Demonstrator, which is a portable system consisting of a small flexible beam driven by a torque motor and mounted on springs tuned to the first flexible mode of the beam.

At the present time, the first two goals have been met, and work on the third is on-going. Results of each will be discussed below.

Using many references, the currently available methods for training neural nets were examined and evaluated for ease of implementation, reliability, computer requirements, and applicability to control systems. Some methods were rejected because of the vast numbers of neurons required to work practical problems (e.g., Bidirectional Associative Memories); some, for example Boltzmann machines, because of the very large amount of computer time required to train the nets; and some, like Hopfield nets, for the extreme difficulty of implementation (in order to utilize a Hopfield net, a Lyapunov function must be generated for system "goodness" and appropriate weight adjustments based on that Lyapunov function must be determined--a procedure requiring vast "mathematical expertise and ingenuity" [1]). While there is currently no optimum method for neural nets, after careful evaluation, back-propagation was chosen as the most practical choice for implementation. This method changes network weights proportional to the partial derivative of the system error function with respect to each weight. This approximates a gradient descent procedure, and therefore assures that the system will reach an energy minimum. Difficulties with back-propagation include possible network paralysis if neurons saturate, the possibility of reaching a local rather than a global minimum, and long training times. However, the method is very easy to implement algorithmically, and is used in the majority of the controls applications appearing in the current literature. Methods have been proposed to fix difficulties with back-propagation, but each has its own associated problems (for example, Cauchy training eliminates the problem of convergence to local minima, but has a greater instance of network paralysis than systems using back-propagation, and a training time one hundred times that of the already lengthy back-propagation training). Thus back-propagation was chosen as the neural net training method to be implemented.

Using Matlab, software was generated implementing a back-propagation trained neural net on an IBM compatible personal computer. For a given problem, number of layers and number of neurons must be "empirically determined," [2] so neural nets of several sizes and configurations were compared. Some authors have hypothesized that fewer neurons may be used for a given problem if those neurons are arranged in more layers [1]. In the trials conducted, no network was found which failed to converge eventually, so no evidence was obtained to support or disprove this hypothesis. However, empirical evidence does suggest that given that both will eventually converge to a solution, a neural net with fewer layers will converge more quickly. Figure 1, showing the error measure

(total sum square error) versus number of training epochs for a two-layer neural net (with one nonlinear hidden layer and a linear output layer) and a three-layer net (with two nonlinear hidden layers and a linear output layer), is typical of the results generated.

In the second phase of the project, recent publications in the professional literature regarding applications of neural nets to control problems were examined and compared. Methods currently available can be divided into roughly three categories:

a) methods in which a neural net is trained to emulate a currently existing controller, whether human or computerized (such as [3]);

b) methods in which nets generate some state or function which is then used in a standard controller design (for example, [4] in which the neural net is used to generate estimates of unknown nonlinear system parameters, which are then used in a standard adaptive controller);

c) methods in which the neural net generates a controller for an unknown system without human intervention [2].

Of the three types, the third is by far the most sophisticated, as it assumes no mathematical knowledge of the system to be controlled, and does not require a human to be able to control the system or to generate a controller which successfully does so. This would mean that nonlinear systems which could be modeled poorly, if at all, theoretically could still be successfully controlled by a trained neural net. It was decided that such a method would be the best candidate for controlling flexible space structures.

The particular method choosen for application to the test system was that in [2]. This is a time back-propagation system. First, a neural net must be trained to emulate the behavior of the unknown system using standard back-propagation methods. This trained emulator is then used to train the controller as follows:

1) A time trajectory for system behavior is generated, with the untrained controller generating essentially random inputs to the emulator.

2) The final emulator output is compared to the desired output.

3) The error is propagated back through the emulator to generate an equivalent controller error, which is used to train the controller.

4) The process is continued, propagating back through each time step of the trajectory until the controller has been trained for all time steps.

5) Steps 1-4 are repeated for many trajectories.

Currently on-going is work applying the method in [2] to the test article. The neural net chosen for use had one hidden nonlinear layer containing 35 neurons and a linear output layer of 10 neurons to scale the outputs. One problem in implementing the method was difficulty in obtaining accurate training data for the CSI Demonstrator; the final data was generated by Mark Whorton and John Sharkee of NASA, using a Matlab simulation of the system.

Another difficulty encountered was ill-conditioning of the data. Although it was mentioned nowhere in the literature, it was discovered that if inputs to the neural net vary by several orders of magnitude, as is the case of the Demonstrator, the nonlinear neuron layer soon saturates, so that training of that layer comes to a virtual standstill. This causes the nonlinear layer to send the same input to the linear layer regardless of the system input, causing the linear weights to grow without

bound as they try to adjust to give varying outputs a constant input. This causes the error measure to grow without bound. This problem was solved by scaling the trajectories of very large system states to bring them down to the level of the others and prevent layer saturation.

It was also discovered that the 8088 PC being used for software development was too slow to be practical in training a neural net to emulate the test article; currently the software is being run on an 80386 machine with 10,000 training patterns comprising a single epoch (a single epoch takes approximately 45 minutes on the 80386 and over 24 hours on the 8088). As yet, the emulator has not converged to zero error, but to a TSS of approximately 4. Figure 2, of TSS versus epoch number, shows this convergence. When state trajectories for both the system and the emulator are compared, results for different states range from that in state X_1 where the emulator does not adequately follow the system response (Figure 3) to state X_3 (Figure 4) in which the two are practically identical. Possible reasons for this include an inadequate training set (i.e., one which does not fully span the state space) and a neural net with an inadequate number of neurons and/or layers. Work to perfect the emulator is continuing. At such time as the emulator adequately predicts all system states, the controller will be trained as part of an on-going effort during the coming academic year. Once the controller is trained, its performance may be compared to the currently existing controllers for the system in terms of computation requirements, robustness, etc. Other neural net strategies, such as using the neural net as an estimator for system parameters needed by standard adaptive controllers, could also be addressed at some future time.

While neural nets have yet to be fully evaluated as a tool for control of nonlinear or poorly modeled systems, they show great potential in this area, and deserve further consideration and study.

REFERENCES

[1] Wasserman, P. D., *Neural Computing: Theory and Practice,* Van Nostrand Reinhold, New York, N. Y.,1989.

[2] Nguyen, D. H. and Widrow, B., "Neural Networks for Self-Learning Control Systems," *IEEE Control Systems Magazine*, April 1990, pp. 18-23.

[3] Guez, A. and Selinsky, J., "A Trainable Neuromorphic Controller," *Journal of Robotic Systems,* vol. 5, no. 4, 1988, pp. 363-388.

[4] Chen, F. C., "Back-Propagation Neural Networks for Nonlinear Self-Tuning Adaptive Control," *IEEE Controls Systems Magazine*, April 1990, pp. 44-48.

2 & 3 Layer Nets with Random Training Set

TSS

Epoch Number
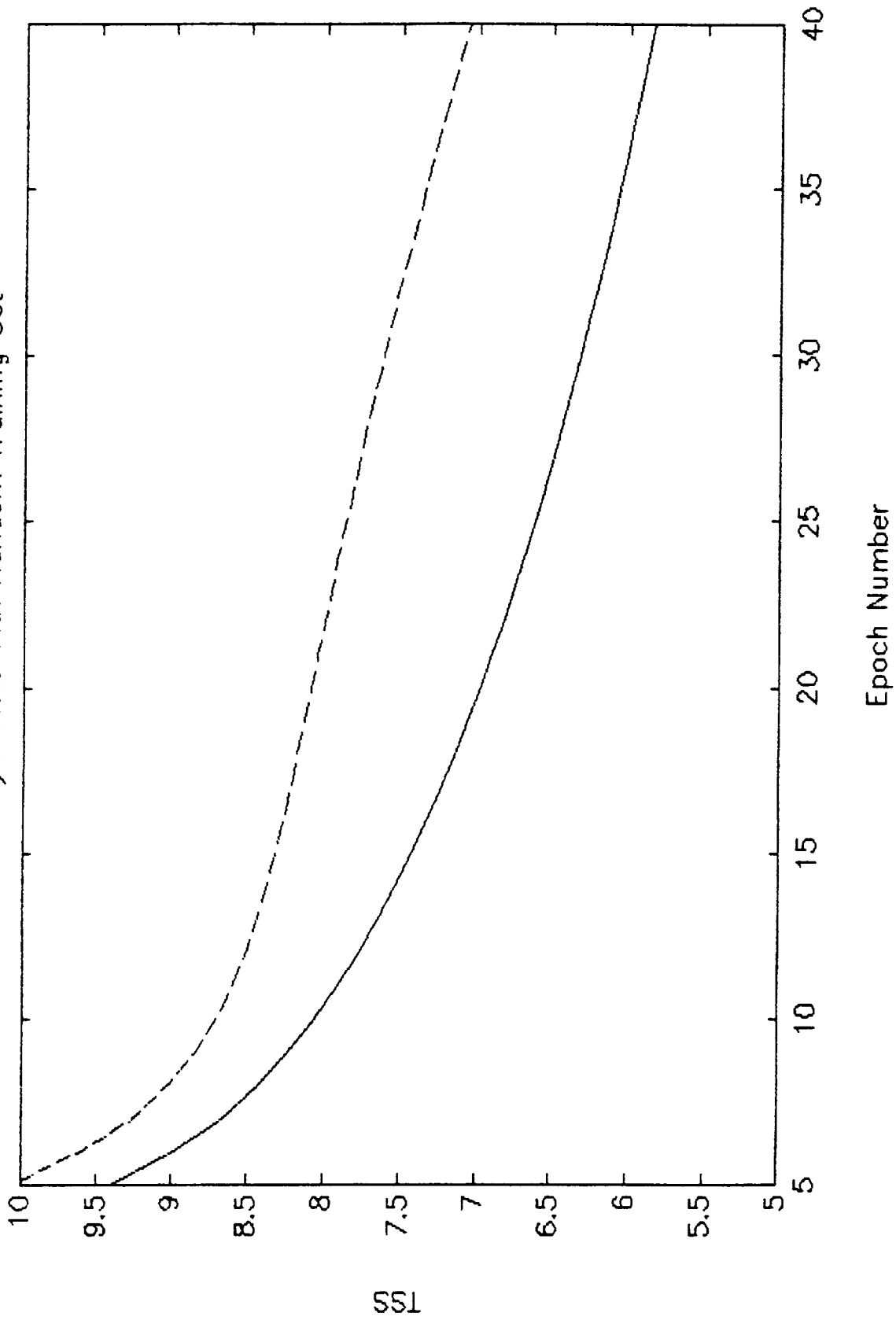
weight convergence, case 2
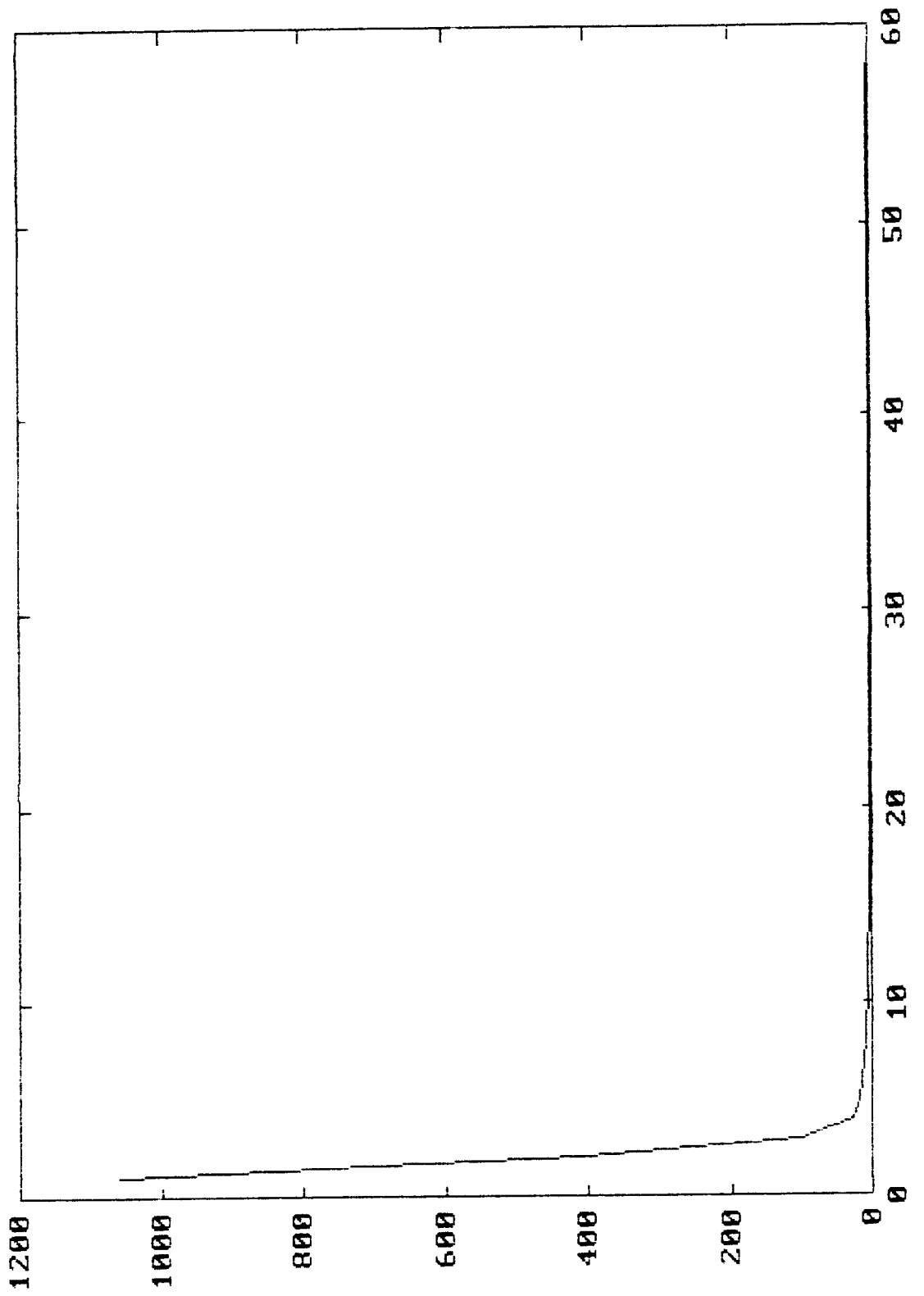
plant & net time responses, Case 2

plant & net time responses, Case 2
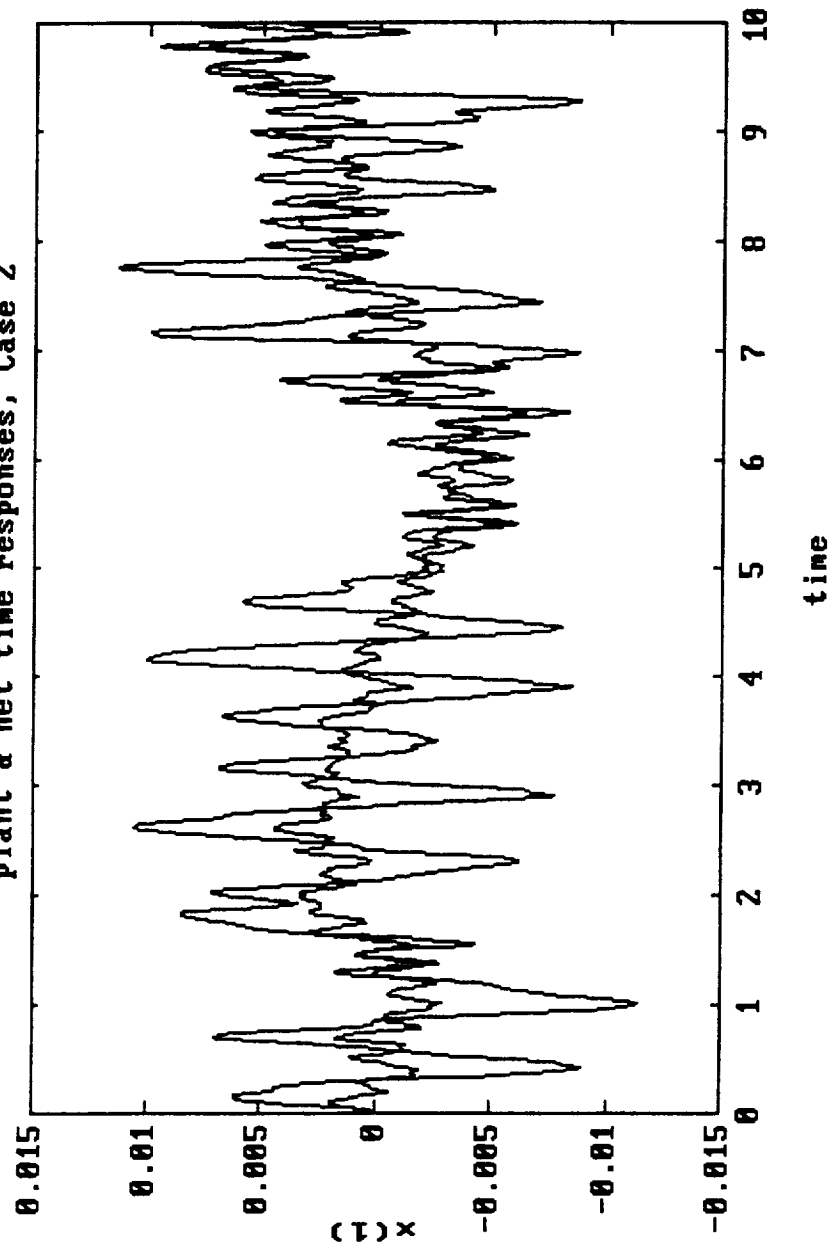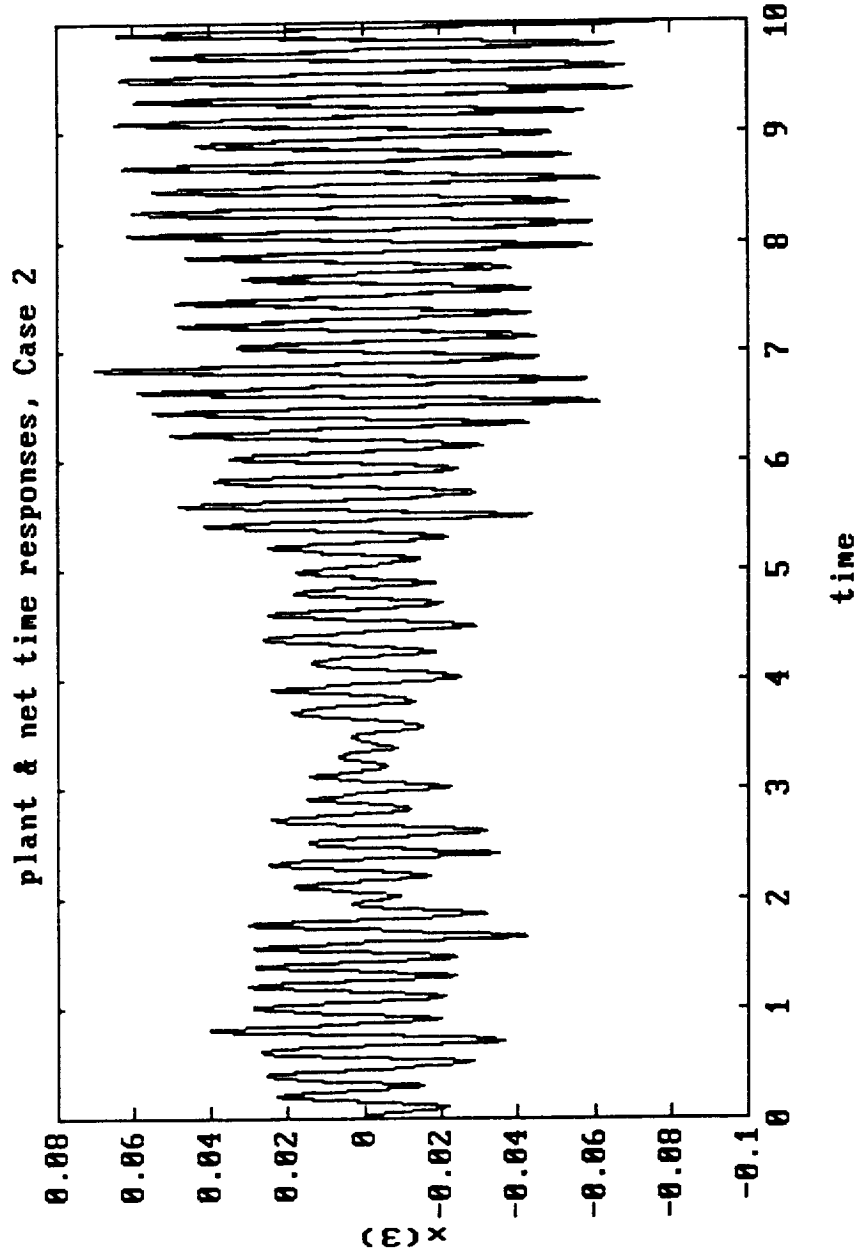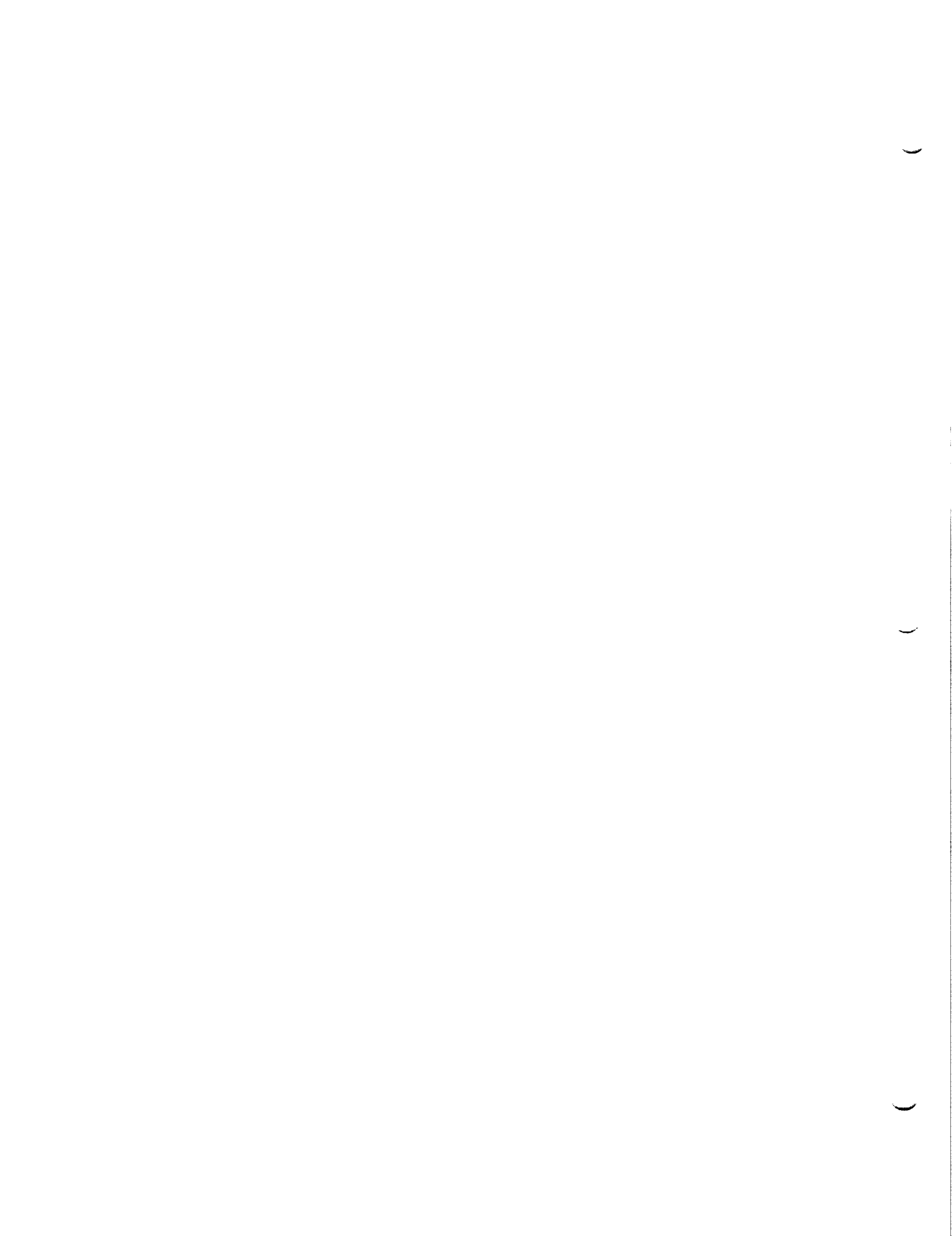
1990

NASA/ASEE SUMMER FACULTY RESEARCH FELLOWSHIP PROGRAM

MARSHALL SPACE FLIGHT CENTER
THE UNIVERSITY OF ALABAMA

THERMAL ANALYSIS SIMULATION FOR A
SPIN-MOTOR USED IN THE ADVANCED MAIN COMBUSTION CHAMBER
VACUUM PLASMA SPRAY PROJECT
USING THE SINDA COMPUTER PROGRAM

Prepared by: Gary H. McDonald, Ph.D., P.E.

Academic Rank: Assistant Professor

University and Department: The University of Tennessee
                                        at Chattanooga
                                      Mechanical Engineering -
                                        Mechanics

NASA/MSFC:

    Laboratory: Propulsion

    Division: Component Development

    Branch: Turbomachinery and
                                      Combustion Devices

NASA colleague: Kathy S. Tygielski

Date: August 16, 1990

Contract No.:   NGT 01-002-099
                                      The University of Alabama
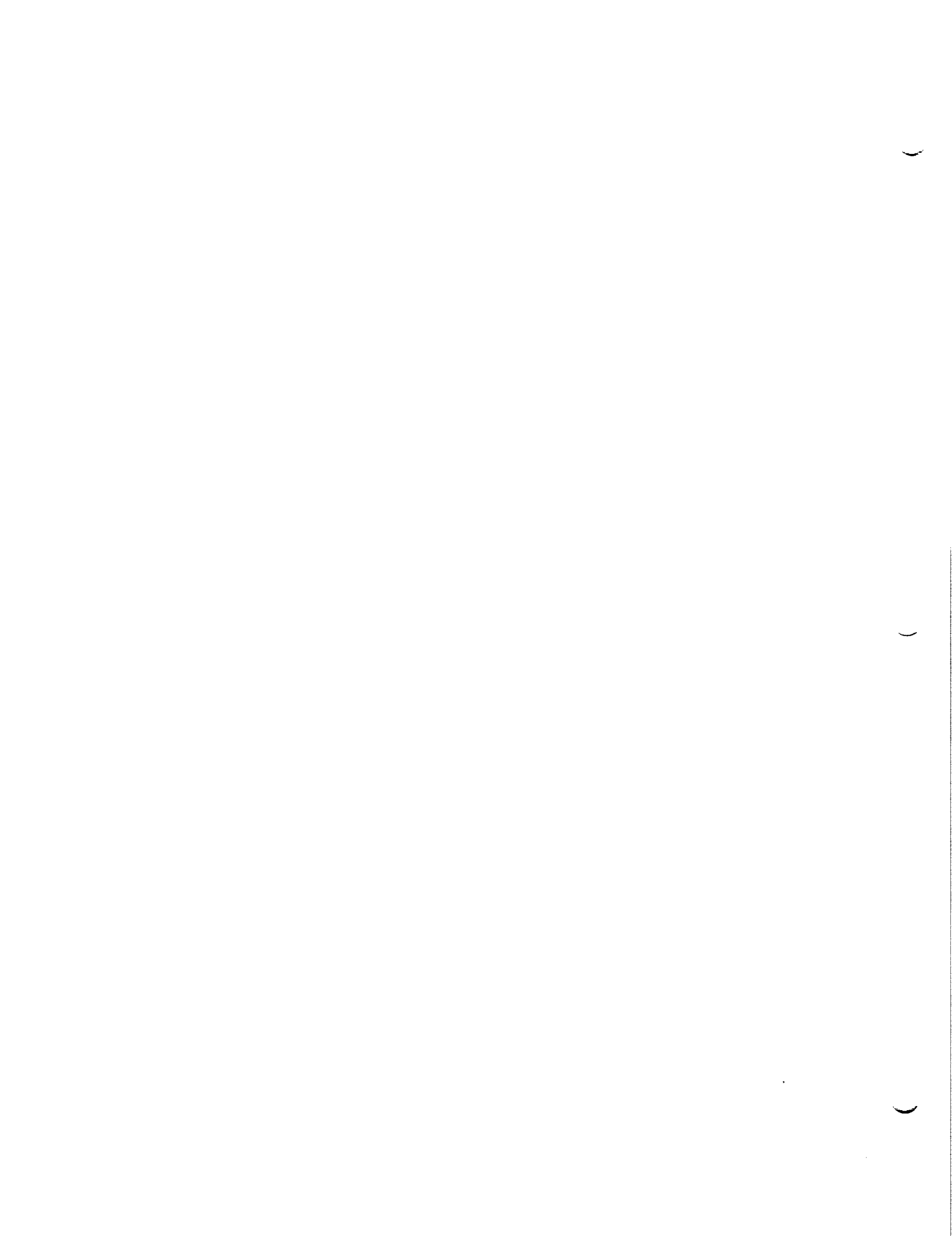
INTRODUCTION

In the space shuttle main engine (SSME), the mixing of liquid hydrogen (LH2) fuel and liquid oxygen (LOX) oxidizer occurs in the main combustion chamber (MCC). Stored in separate compartments inside the external tank, the LH2 and LOX are pumped by high and low pressure fuel and oxygen turbopumps into the MCC for ignition and combustion. By expelling its combustion products through the nozzle, thrust is produced to propel the shuttle from earth.

The current MCC construction consists of welding many components to form the converging - diverging chamber shape. This process takes about four years to complete at a cost of 3.2 million dollars per chamber. The advanced main combustion chamber (AMCC) is designed to simplify the process for construction and reduce any critical-failure modes by reducing the number of welds. The proposed construction time is about one year with a cost of 1.2 million dollars per chamber.

The proposed improvements are to cast the AMCC jacket out of weldable hydrogen resistant superalloy. In order to line the casting, the vacuum plasma spray (VPS) process will be used to spray Narloy Z, a copper based alloy, inside the casting. This process will be performed by three plasma guns spraying Narloy Z at 1500 ^{0}F inside a vacuum chamber. The AMCC will be bolted to a turntable driven by a spin-motor and spindle assembly inside the chamber in order to keep the plasma guns perpendicular to the inside surface throughout the duration of the spraying. Three spray guns are necessary for the spraying process. One gun will spray the top section, one will spray the bottom section and one will spray the critical throat section of the AMCC. This system is shown schematically in Figure 1. The proposed benefits of the VPS process are to reduce the number of welds and eliminate all blind welds, to eliminate copper plating from the hydrogen barrier, to reduce maintenance and need for weld inspections and to decrease manufacturing time and thereby reduce the cost.

One of the many design challenges of this project is predicting the thermal effects due to the environment inside the vacuum chamber on the turntable and spin-motor spindle assembly. The objective of this study is to model the spin-motor using the computer program SINDA, System Improved Numerical Differencing Analyzer. By formulating the appropriate input information concerning the motor's geometry, coolant flow path, material composition, and bearing and motor winding characteristics, SINDA should predict temperatures at various predefined nodes. From these temperatures, hopefully, one can predict if the coolant flow rate is sufficient or if certain mechanical

elements such as bearings, O-ring seals or motor-windings
will exceed maximum design temperatures.

THE PROBLEM DEFINITION

The spin-motor turntable assembly is schematically
shown as a one-half scale drawing in Figure 2. The spin-
motor housing is approximately 11.25 inches in height and
13.25 inches in diameter. The motor is composed of the
housing, coolant water flow path, two ball bearings, rotor-
stator-resolvers, silver slip-ring for electrical
conductance, and a central hollow shaft. The spin motor
material is 304 stainless steel, the bearing material is
440C steel, the motor windings are AISI 1010 steeland
vanadium steel, and the coolant is water. The motor will
have 60 ^{0}F and 60 psi water flowing into it. The chamber
temperature will be 300 ^{0}F and the three VPS guns will bring
the AMCC turntable and spin-motor spindle assembly up to
1500 ^{0}F. The Narloy Z liner will overspray from the AMCC
onto the turntable and spin-motor housing. This overspray
will effect the heat transfer into the motor and
temperatures inside the housing. However, it will not be
considered in this initial study. The modes of heat
transfer present will be conduction, both axial and radial
to the central shaft, convection between the motor
components and coolant flow, and radiation of the vacuum
chamber and AMCC-VPS environment to the motor housing. The
spin-motor is proposed to turn the turntable at 100 RPM
throughout the period of spraying. The estimated load of
the AMCC and turntable on the spin-motor is approximately
1000 pounds. The bearings are a 95 mm bore diameter top
bearing and a 80 mm bore diameter bottom bearing. Both
bearings are SKF single-row deep groove ball bearings. [1]
The motor components are Inland motor model number BMS-7101.
[2]

BUILDING THE SINDA MODEL

SINDA is a software system which possesses capabilities
that make it well suited for solving lumped parameter
representations of physical problems governed by the
diffusion-type heat equation. The system was designed as a
general thermal analyzer accepting resistor-capacitor (RC)
network representation of thermal systems. SINDA consists
of three main parts: (1) the preprocessor, (2) the
execution (integrating heat transfer equations), and (3)
operation (post-processing and output). In the
preprocessor, the lumped capacitance of a region is called a
node assigned by some arbitrary reference number. A node
represents capacitance of defined region which is the
product of density, specific heat and volume. The three
types of nodes are diffusion nodes, arithmetic nodes, and

boundary nodes. The heat conduction paths between the defined nodes are considered conductors which are also assigned some arbitrary reference number. The types of conductors available are linear conductors, radiation conductors, and one-way fluid conductors. A linear conductor can be either axial, radial or convective conductances. Axial conductance is the product of thermal conductivity and area perpendicular to heat flow divided by the length of flow path. Radial conductance is the product of 2 times pi times length of path divided by natural logarithm of the outer radius divided by the inner radius. Convective conductance is the product of the convection heat transfer coefficient and area perpendicular to heat flow. A radiative conductance is the product of emissivity, surface area, Stefan-Boltzmann constant and a surface configuration view factor. A one-way fluid conductance is the product of mass flow rate and specific heat. Other parts of the preprocessor are source data and constant or array data. Source data represents any internal heat generation source within the system imposed on a particular node. The constant data represent material properties that are constant throughout the simulation. Array data represent material properties that are either a function of time or temperature in the simulation. The execution uses forward finite differences to solve the heat transfer equations to find temperatures. The operation blocks are unique to each simulation representing FORTRAN statements controlling iterations and output. [3]

The construction of the preprocessor data took most of the time in this study. First, the motor was subdivided into 30 regions defined by diffusion nodes. Next, arithmetic nodes were defined between differing materials inside the motor and boundary nodes defined the exterior of the motor housing. Next, volumes of each region were calculated. Then, capacitances of each region were determined where specific heat is a function of temperature from the array data.

Once the capacitances were defined, axial and radial conductances were determined. For both cases, the length of heat flow path is represented by variable L, and the thermal conductivity is a function of temperature from the array data. For axial conductance, area A, is perpendicular to the heat flow and for radial conductance, r_o and r_i are outside and inner radii, respectively.

Convection conductances were found by calculating the appropriate liquid-solid contact surface areas. Then, the convective heat transfer coefficient, h, was found using a turbulent correlation for circular cross-section (Dittus Boelter correlation). The convective heat transfer coefficient is a function of temperature using the appropriate material properties at the desired temperatures.

The convective heat transfer coefficient versus temperature data were found in the array data for the coolant flow rates of 10 and 20 gallons per minute (gpm). One-way fluid conductances were calculated using either the 10 or 20 gpm converted to mass flow rate and the specific heat as a function of temperature from the array data.

Radiative conductances were found by setting emissivity to 0.9, calculating total housing surface area to be 455.4 square inches and view factor to be 1. This conductance equalled 0.1714×10^{-8} Btu/hr-ft$^{2-0}$R. The only heat generation sources were due to the motor windings and bearings. After extensive calculations, the top and bottom bearing heat generation rates were 14.6 and 10.3 Btu/hr, respectively. The motor-winding heat generation rate was 755.5 Btu/hr.

The array data consisted of thermal conductivity and specific heat versus temperature for 304 stainless steel, 440C steel, AISI 1010 steel, vanadium steel and water. Also, for water, viscosity, density and Prandtl number versus temperature were listed. For two coolant flow rates, 10 gpm and 20 gpm, convective heat transfer coefficient versus temperature were formulated using the Dittus-Boelter correlation.

At this time, no significant solution from SINDA has been determined.

RECOMMENDATIONS

Several recommendations can be made to further this study.

1. To complete the operation blocks and debugging of the SINDA codes to obtain verifiable results.

2. To add the effect of Narloy Z overspray from the AMCC-VPS on the motor housing.

3. After detailing of the design is complete and some preliminary chamber tests occur, try to correlate experimentally determined data with model predictions to obtain confidence with the model constructed.

4. To perform some parametric studies of the effects of coolant flow rate variation, chamber temperatures variations and other necessary parameters to better understand the thermal environment of the AMCC-VPS support equipment.

Hopefully, based on these recommendations, a useful numerical model of the AMCC, turntable and spin-motor spindle assembly can be constructed. These models could become an important source of information when comparing the results to future experimental AMCC test data. Also, parametric studies using this model can provide a relatively economical means to predict possible problem areas. However, for the SINDA model results to be a reliable predictor of the thermal effects, it must have reliable input data based on experimental or empirical formulations. As the AMCC develops from the design and development phases into the construction and test phases, the SINDA model can become an important evaluation tool for predicting motor, turntable, or even AMCC thermal conditions.

REFERENCES

1. SKF Product Guide Manual, SKF Industries, Philadelphia, PA, 1988.

2. Inland Motor, Kollmorgen Corporation, Brushless D.C. Motor and Servo Amplifiers, Radford, VA, 1988.

3. SINDA User's Manual with Sinflo addition, COSMIC Program # GSC - 12671 Computer Software Management and Information Center, Athens, GA (revised by Sperry Support Services), Huntsville, AL, 1980.
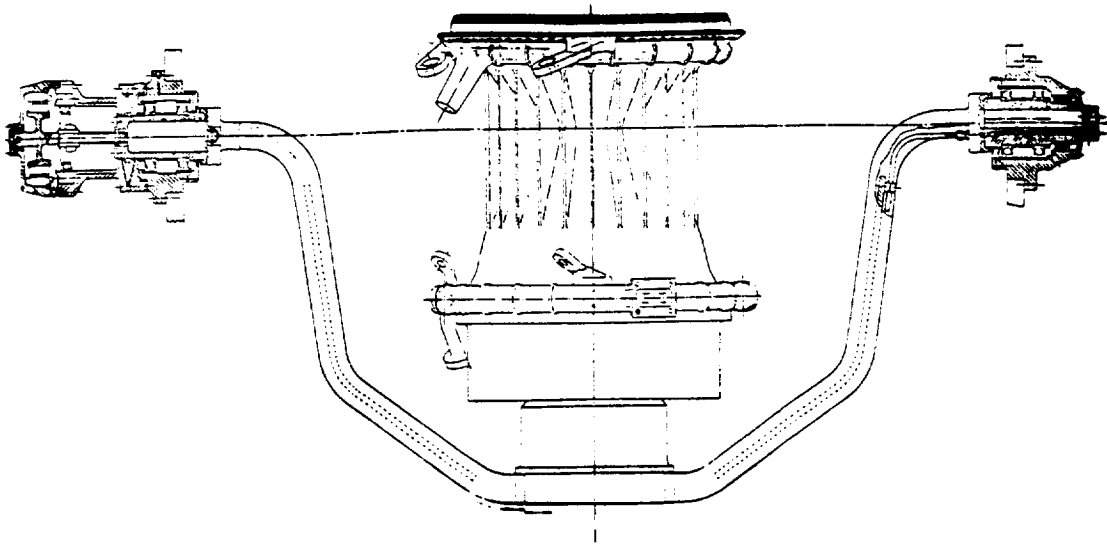
Figure 1:   The AMCC, Turntable, Spin-Motor with Spindle
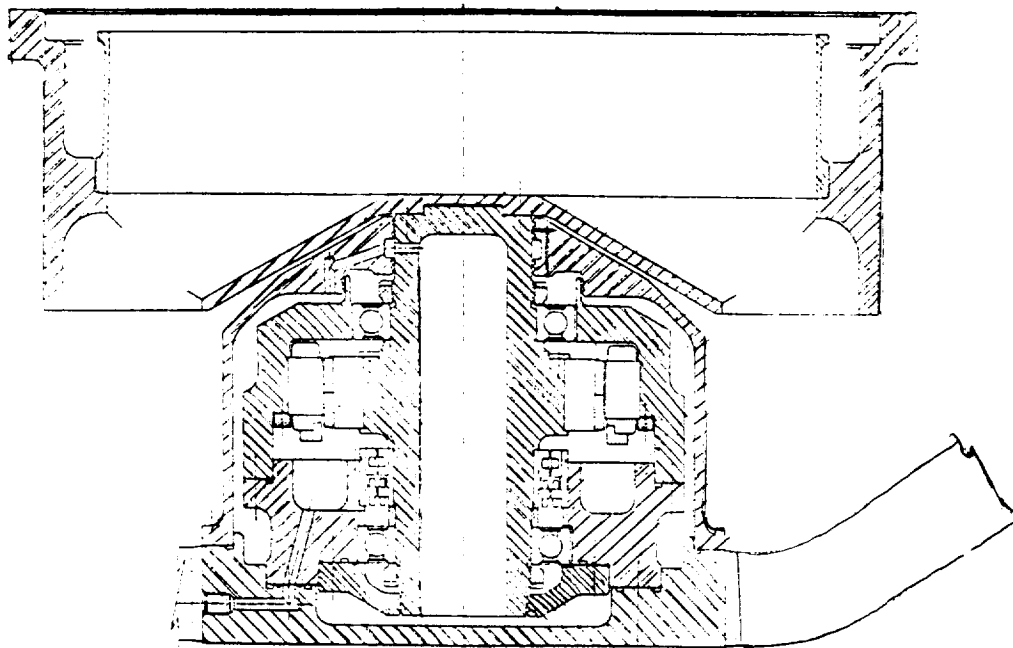
Figure 2:   The Spin-Motor and Turntable Assembly

1990

NASA/ASSE SUMMER FACULTY FELLOWSHIP PROGRAM

MARSHALL SPACE FLIGHT CENTER
THE UNIVERSITY OF ALABAMA

INFORMATION AND PROBLEM REPORT USEAGE IN

SYSTEM SAFETY ENGINEERING DIVISION

Prepared by: Stephen J. Morrissey

Academic Rank: Associate Professor

University and   University of Wisconsin-Platteville
Department: Industrial Engineering

NASA/MSFC

  Office: Safety, Reliabilty, Maintainability,
                            and Quality Assurance

  Division: System Safety Engineering
  Branch: Project Safety Engineering

MSFC Colleague: John M. Livingston

Grant Number: NGT-01-002-099
                           The University of Alabama
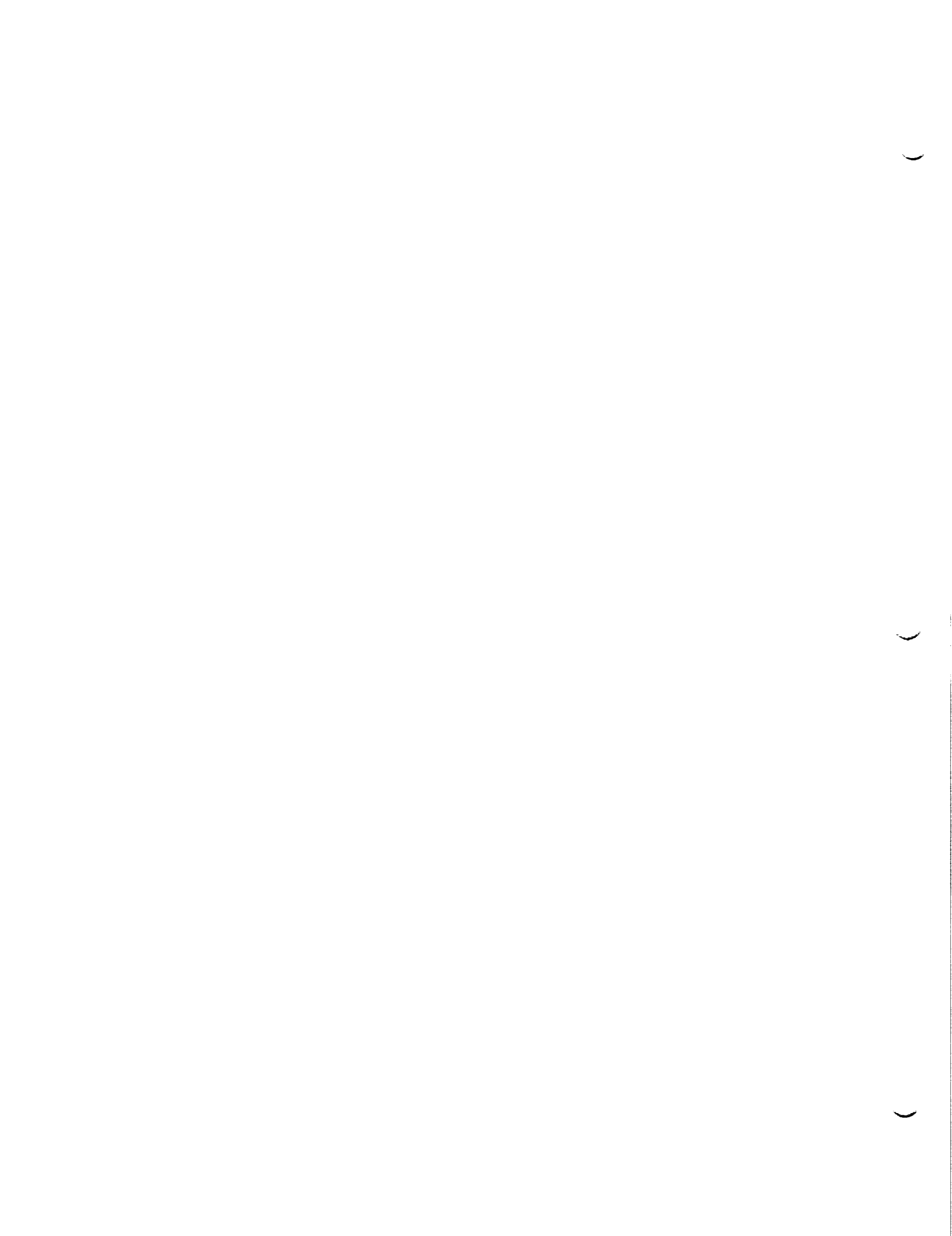
SUMMER FACULTY REPORT
System Safety Engineering, CT - 21, Marshall Space Flight Center

Stephen J. Morrissey, Ph.D., Summer, 1990

SUMMARY
This report summarizes the findings of the problems I was asked
to address during my stay. There were five basic problem or
question areas. Four of the five are examined individually in the
following pages, the fifth is was to provide recommendations,
these are included with each of the four major problem areas.

1: EVALUATE ADEQUACY OF CURRENT PROBLEM/PERFORMANCE DATA BASE

Problem and performance identification and evaluation is defined
by PRACA requirements, with each of the major system contractors
having their own contractual arrangements which are also based on
PRACA. Under this system, reports of problems or unusual and
unexpected events or conditions come from the contractor, from
acceptance/qualification testing, in-flight and post flight
analyses(PFA). When problem report data is received it is
evaluated for its criticality and uniqueness. If an observed
problem is deemed to meet these requirements, it is entered as a
problem report and enters the reporting and evaluation procedure.

1. Data Acquisition: Calspan is automating the data reporting
and trending efforts. This is a relatively new project and will
allow for identification of trends in data for established
(previously identified) problems and for classification of
newly reported problems or unusual events that do not have
FMEA-CIL numbers. This effort uses the traditional data sources
described above and is working to also integrate data from
contractor's internal data bases.

Comments:
*This effort can be improved by more contractor cooperation in
sharing their data bases, by inclusion of data derived from
standard repair procedures, and by improving the communication
between MSFC and contractors at other locations. Several
contractors are providing excellent data from their internal
data bases.

*Because of the importance of understanding the PFA problem
identification methods, it is recommended that responsible
individuals participate in these sessions at least once a year.
This can be by live participation or by viewing the video
taped activites. In a similiar fashion, individuals who are
required to evaluate other systems should have exposure to the
contractors actual operations. This will enhance their
understanding of the physical hardware and how it is prepared,
tested and evaluated.

*It has been observed that different divisions within SRM&QA are
working on projects or have contractor projects that are of
great interest and use to other sections. Knowledge of other

divisions projects is not totally comprehensive, and while there is no evidence of attempts to prevent other groups and divisions from knowing what is being done, communication is not as complete as it should be. It is recommended that some method of cross communication be established, perhaps a session in which each group leader gives a short presentation which outlines active projects and their groups current and future operational needs. From these discussions better understanding of each groups capabilities and needs will be possible, and a more coordinated effort result.

*The post flight analysis is primarly done by engineering personnel, and considerable experience has been gained. This experience base is now sufficiently developed so that this activity can be taken over by quality oriented rather than design oriented personnel. Such a change in orientation should improve the reviews if the knowledge and experience base gained in PFA inspections can be translated into inspection criteria possibly with an expert system. Such a shift in orientation should also allow for a better understanding and control of the variety of design waivers that exsist on any system. This inclusion of quality personnel should also facilitate problem quanitification and hazard analyses.

2. Data Evaluation-Reporting: Calspan develops a monthly report called the Open Problems List (OPL) that lists and trends problem reports that have been filed or closed during the reporting interval. These reports are grouped by system (ET, SRB, SRM), and whether the reports have been closed or are still open at the end of the reporting interval. The OPL is distributed to a variety of users to help managers and other personnel identify problems in the various systems.

An important issue has been how to deal with problem reports and hazards that do not have FMEA-CIL numbers or that are new or unique. This has been resolved by assigning problem reports without FMEA/CIL numbers a citicality of one. These reports are then grouped together and in a review session evaluated as to their apparent criticality, and assigned to project groups to develop FMEA-CIL documentation. This procedure should allow for rapid identification and entry of new hazards into the FMEA/CIL data base. In the last review of this type, 580 reports did not have FMEA/CIL numbers. Of these, 440 were considered as "non-problems", the remaining 140 have been assigned to project groups to develop FMEA analyses and related CILs. The amount of active participation by system safety in these reviews is not clear.

Comments:
*A better method is needed to trace reported problems to their basic or root cause(s) so that proper counter measures or corrective designs can be developed. This includes problems that result from device/system failures, to problems that result from devices being out of tolerance, but still functioning, and human errors. This may also require better

reporting of problems arising from standard repair procedures. While this type of reporting is a sensitive issue to some contractors, this data is needed to insure proper tracking of problems. It can be argued that to provide this data would require substantial additional reporting and accounting efforts by contractors. However, this data should already be internally available to the contractors. A possible compromise would be to have contractors supply their own measure or ratio of units accepted(of some particular type) to units sent (of some particular type).

*A computerized, real time system to cross reference Hazard Reports, CIL Numbers, FMEA Numbers and problem report numbers and any waivers or proposed engineering changes needs to be implemented.

*The current system for problem reporting developed by Calspan has great protential. It should be expanded to allow the following:

   1. Interactive searching of the data base by non-Calspan personnel. this is a relatively new program, this may develop naturally with maturity.
   2. A survey needs to be made of SRM&QA personnel to determine what other information would be useful for presentation in the monthly OPL report.

2: EVALUATE METHODS OF PERFORMING TREND ANALYSIS

Currently there are two major efforts under way that involve trend analysis. These are Performance Trending and Problem Trending.

Performance Trending: Data from past launches is being used by ATI to develop envelopes of nominal performance. Real time data for a particular system or element across its operational time is statistically evaluated to develop templates or control chart limits describing the upper and lower values for the parameter over time that have been observed 95% of the time. These upper and lower limits provide a window within which real time values of the parameter can be plotted allowing determination of the "acceptability" of the parameter compared to past performance at that point in operational time.

Comments:
 *This method has great usefulness for both real time LCC decisions and for development of test/acceptance criteria.

 *This method should be expanded to allow development of multivariate plots, not just individual (sub)system responses.

 *The performance envelopes developed by this method may be quite different from the "red-line" values. A method of quantifying the risk associated with observations in this region needs to be developed.

Problem Trending: is being addressed in two different ways. The first is the OPL report discussed earlier that lists problems by system and criticality, and corrective actions (if any) that have been taken in the past reporting period (typically one month). The second effort is the "problem trending report" that is issued every six months. This report uses all available current and historical data for systems, elements, and subsystems, and develops a variety of different trend analyses for these data. Analyses typically are trend reports for systems and elements, with detailed studies performed on various elements or systems according to frequency or criticality of events, and visibility. These trend analyses use graphical and statistical methods, and can be used to describe the effectiveness of design changes, or point out areas needing control. The purpose of these efforts is to provide management guidance and oversight to managers, and facilitate tracking of problems and the effectiveness of correction.

*Trending is a powerful tool to facilitate understanding and control of the systems described. However the feedback loop to insure compliance is not always present. In the trending reports there is evidence of systems or components in which design changes have been made, yet the rate of problems has not changed, and in some cases, the problem rate has increased. Trend analysis is only as good as managers choose it to be.

3: METHODS AND SOURCES OF DATA FOR PROBABLISTIC RISK ASSESSMENT
There have been substantial efforts in the area of PRA to determine basic and time dependent reliabilities for elements, systems and subsystems, and towards life cycle characterizations. Data used for these evaluations comes from the basic sources of data already identified. These analyses have been oriented towards traditional reliability studies, and their system safety impact or inputs are not totally characterized, nor have system safety inputs been sought in any systematic fashion.

Comments:
*Facilities and personnel are available to perform PRA at many different levels of complexity and sophistication. However this resource is not sufficiently recognized nor utilized as a source to develop PRA criteria for FMEA/CILs or other types of hazard analysis.

4: HOW IS RISK ASSESSMENT DOCUMENTATION UPGRADED/UPDATED?
This is currently performed by problem review boards or by individuals raising concerns and initiating these changes and modifications. Until the trending analysis efforts had been developed, this was the only way by which hazards and needed revisions could be identified. The updating of documentation is a different issue and hazard reports and CILs may often have waivers and inprocess modifications and engineering change proposals active. Keeping track of these is difficult, and

currently is performed as much by word of mouth as by formal lines of communication.

*This condition obviously needs to be improved, possibly by using a more formalized procedure which would flag hazard reports, FMEA-CILs whenever a waiver or engineering trend proposal that references them is active.
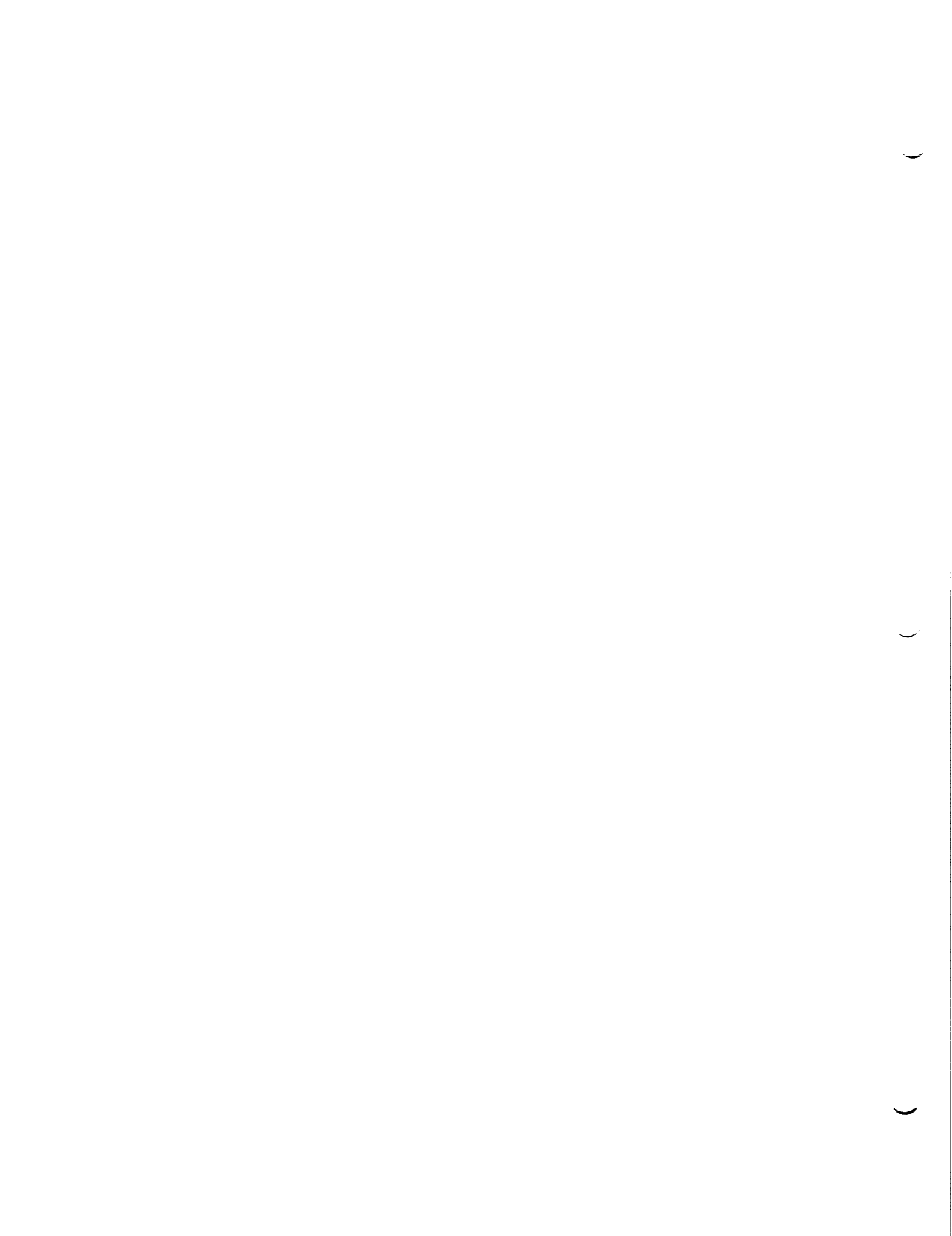
1990

NASA/ASEE SUMMER FACULTY FELLOWSHIP PROGRAM

MARSHALL SPACE FLIGHT CENTER

THE UNIVERSITY OF ALABAMA

CONSTRUCTION OF THE 16 METER LARGE LUNAR TELESCOPE (LLT)

Prepared By: Husam Anwar Omar

Academic Rank: Assistant Professor

University: University of South Alabama

Department: Civil Engineering

NASA/MSFC:

     Laboratory: Program Development
     Division: Lunar and Mars Exploration
     Branch: 16 Meter LLT

MSFC Colleague: Max Nein

Contract No.:   NGT-01-002-099
                     The University of Alabama

Introduction

NASA is currently involved in studying the possibility of constructing a 16 meter telescope on the moon's surface that is capable of UV, visible and IR observations. This telescope will be scanning the skies looking for extraterrestrial life on planets that could not be seen using earth based telescopes.

Lunar based telescopes offer distinct advantages over earth and space telescopes. The moon's gravitational forces (Although only one sixth of earth's gravity) add stability to the telescope structure. In addition, the superstructure can be anchored in the moon's surface, thus eliminating a lot of vibrations and wobbling that is observed in space telescopes. Furthermore, the absence of any atmosphere on the moon eliminates any interference with the incoming light and thus provides a more clear picture than any earth based telescope. Furthermore, the long lunar nights (about 28 earth days) provide astronomers with longer viewing time than is possible using earth based or space telescopes.

There are many concerns that have to be addressed when designing a structure for a telescope of this magnitude. First, the large size of the primary structure that holds the primary mirror (16 meter diameter) results in excessive flexibility thus causing large deformations. Secondly, Due to the sensitive nature of the instruments used in the telescope, the total deflection between any two mirror clusters should be limited to one millimeter. Thirdly, there always are uncertainties when dealing with the stress-strain characteristics of the lunar soil. This makes it difficult to predict settlements that can be expected under the foundations. The fourth concern deals with the difficulty in construction and site preparation on the lunar surface. The fifth concern deals with packaging and transporting the telescope components to the moon.

Material Availability

Reinforced concrete was the first material considered. There are several advantages to using concrete on the moon. They include among others fire and heat protection for equipment housed inside the structure, protection from solar radiation, and low coefficient of thermal expansion (10×10^{-6} m/m/°C). Most research done on producing concrete on the moon describe two methods of production. The first, is the conventional method of mixing cement and aggregates with water in a sealed and pressurized environment to produce concrete that is similar to terrestrial concrete. The other method involves sintering compacted lunar regolith to form a glass like material which has strength characteristics similar to those of terrestrial concrete.

Although both methods of producing concrete on the moon described above are possible, the author feels that it is not feasible to utilize concrete at this stage because of the following reasons. The first method requires water to mix with the cement and aggregates, but water will be a precious commodity on the moon and will be used for drinking rather than mixing concrete. In addition, the mechanics of mixing concrete and the properties of the mixed concrete on the lunar surface are not well understood. Furthermore, concrete transporting, mixing and placing is labor intensive, something we normally try to avoid in lunar construction because of the limited labor resources. The method of sintering is time consuming if we use solar energy for heating.

There are several Aluminum alloys existing today that have a wide range of properties. The main advantage of Aluminum is that it is a light weight and strong material. Aluminum alloys have lower modulus of elasticity than steel. Welding is normally difficult in Aluminum alloys and produce weak joints around welds. The coefficient of thermal expansion of most Aluminum alloys is approximately 23×10^{-6} m/m/$^\circ$C.

At this stage of telescope's development, the material used for the pedestal is not important because new and better materials will be developed by the time the telescope is ready to be built. Materials with high modulus of elasticity, low coefficient of thermal expansion and high tensile and compressive strengths should developed and used. For the model developed in this study an Aluminum-Manganese alloy was used because of its low CTE (9×10^{-6} m/m/$^\circ$C).

Structural Design of the Telescope's Pedestal

The mass of the mirror clusters and their driving hardware are currently estimated at 30 Kg/m^2. The primary structure is basically a truss comprised of thin Graphite Epoxy tubes. The total mass of the primary structure including the mirrors was estimated to be 30,000 Kg. The motor turning the telescope about its vertical axis applies a torque of 1200 N.m to rotate the telescope. This torque will cause torsional stresses to develop in the pedestal that have to be taken into account in the design. Although theoretically the load from the primary structure should be concentric because we are using counterweights to balance the load, a minimum eccentricity of 3 meters was considered in the design. This should account for any accidents that might occur during construction.

The pedestal will house the motors that drive the pointing system and a Coude' mirror. Therefore, a tube structure was chosen for the pedestal to provide protection for the motors and

mirror from lunar dust contamination and impact of micro-
meteoroids.

The pedestal's structure was designed to support the primary
structure with minimum lateral and vertical deflections. Several
pedestal configurations were considered and analyzed to obtain
the optimum structure.

Figs. 1 and 2 show the front and top views of the designed
pedestal, respectively. It consists of three segments. Each
segment is a tube four meters high and three meters in diameter.
Eight vertical and two horizontal stiffeners are used for each
segment to increase stiffness and reduce possibility of buckling.
The circular horizontal stiffeners are 25 cm wide and 25 mm
thick. While the vertical stiffeners are 3.95 meters high and
have thicknesses that vary depending on the applied loads. The
three segments can be either transported completely assembled or
unassembled depending on volume limitations of the transporting
vehicles. It is recommended that the three pedestal segments be
attached using bolts or rivets and not welding to eliminate the
possibility of creating weak joints normally caused by welding in
Aluminum.

Design of Telescope's Foundations

Excavation on the lunar surface is a difficult and tedious
operation. There is not enough traction for the excavating
machinery to operate effectively. In addition, low gravity on the
moon requires special anchoring procedures of the construction
machinery. Furthermore, the subsurface conditions at the tele-
scope's site are not well established. It is difficult to predict
the density of the soil at a given depths at a given location.
Preliminary studies show that the density of the soil tends to
increase with depth. At depths exceeding 2 meters at some loca-
tions, the soil density was close to that of limestone rock which
is extremely difficult to excavate. Therefore it is recommended
that shallow foundations be used. Three different shallow founda-
tion systems were considered and are presented here.

The first system, shown in Fig. 3, is called the Spudcan
footing developed at the University of New Mexico. This footing
will cause minimum soil disruption and will be placed using a
vibration machine. The footing is filled with lunar regolith to
give it stability. This footing requires minimum site
preparation. However, the vibrating machine has to be transported
to the moon thus increasing the weights to be transported. In
addition, the vibration will cause dust scattering on the site
which might cause dust contamination of sensitive instruments and
construction machinery.

The second system, shown in Fig. 4, is a spread footing. This footing is efficient if the solid dense soil is no more that two meters below the surface. It consists of a thin walled Aluminum container that is filled with condensed lunar regolith for added stability and strength. The contact diameter of the footing is five meters. The spread footing system requires excavating the site to a depth where the solid soil id found, cleaning and grading the site so that it is flat.

The third system, shown schematically in Fig. 5, utilizes the Lunar Excursion Vehicle (LEV) as a base support for the telescope's pedestal. The LEV legs should have automatic leveling devices to correct for any settlements in the soil. Transportation experts indicate that LEVs are designed as expendable vehicles that will be discarded after their fifth mission. The pedestal will be attached to the LEV on its final trip to the lunar surface where it will land on the prepared site of the telescope. Several problems have to be addressed before considering this option feasible. A study should be conducted to investigate the strength and stiffness requirements that should be imposed on the LEV so that it can be used for this purpose. Furthermore, a damage assessment should be made to study the effects of landing on the different components of the LEV and the telescope's pedestal. Since the LEV is in its design stage, the findings of such a study should be communicated to the LEV designers to see if it is practical to design the vehicle for this particular application.

Summery

In this study the different materials that could be used to design the pedestal were identified and comparisons were made. The most appropriate material so far is an Aluminum alloy. The material that should be used should have low coefficient of thermal expansion, high modulus of elasticity and high compressive and tensile strengths. Two different pedestal designs have been presented. The first design is complete, while the second, the telescopic pedestal, is still under investigation. Preliminary studies of the telescopic pedestal show promising results and should be investigated further.

Due to variations in lunar soil conditions both vertically and horizontally, three foundation systems have been presented. The spudcan footing can be used in the case where dense soil is very deep (more than three meters). The spread footing is recommended where the dense soil is between one and three meters below the surface. Finally the LEV support requires a prepared site. The soil should be compacted and stabilized if necessary to reduce settlements.
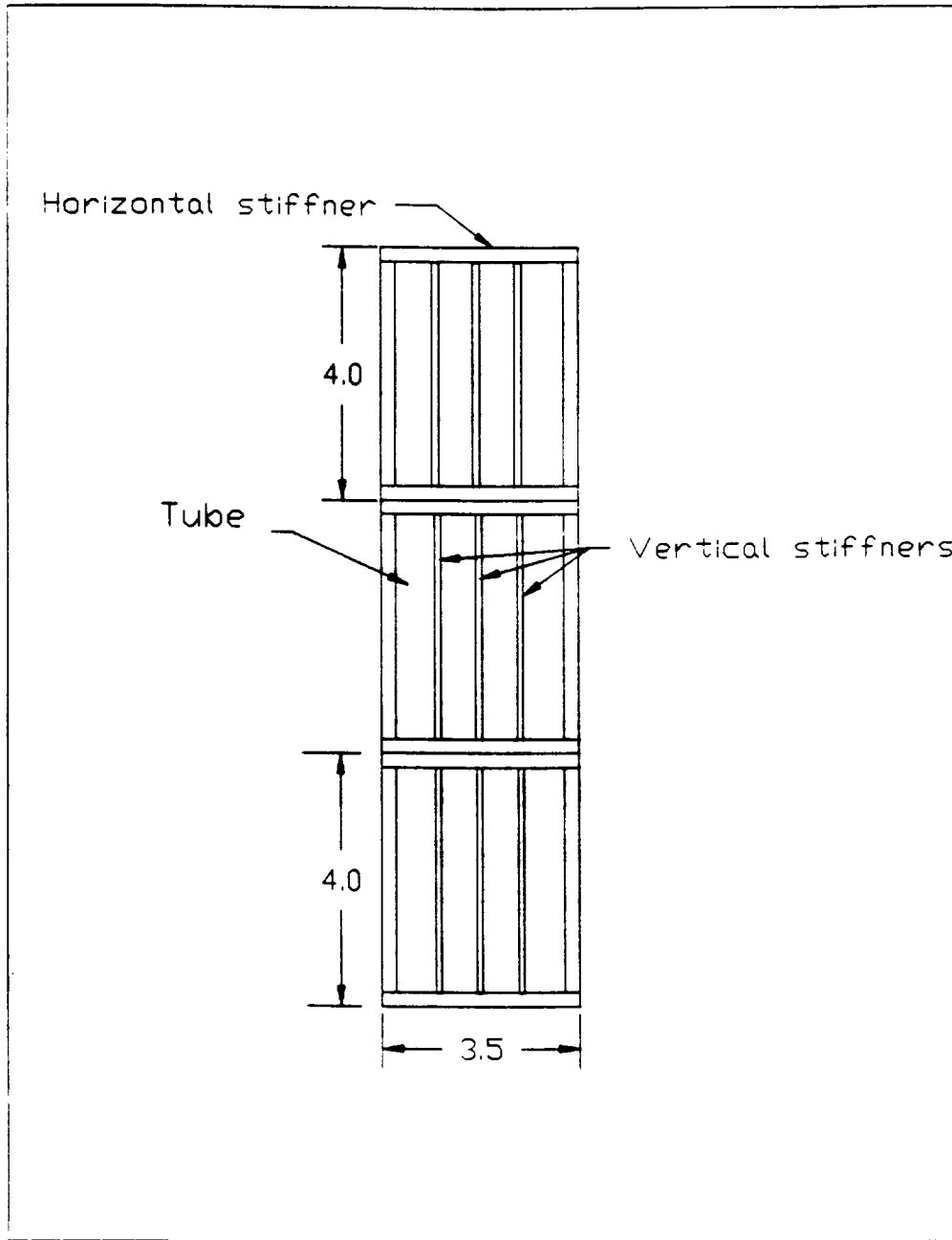
Fig. 1: Front View of pedestal
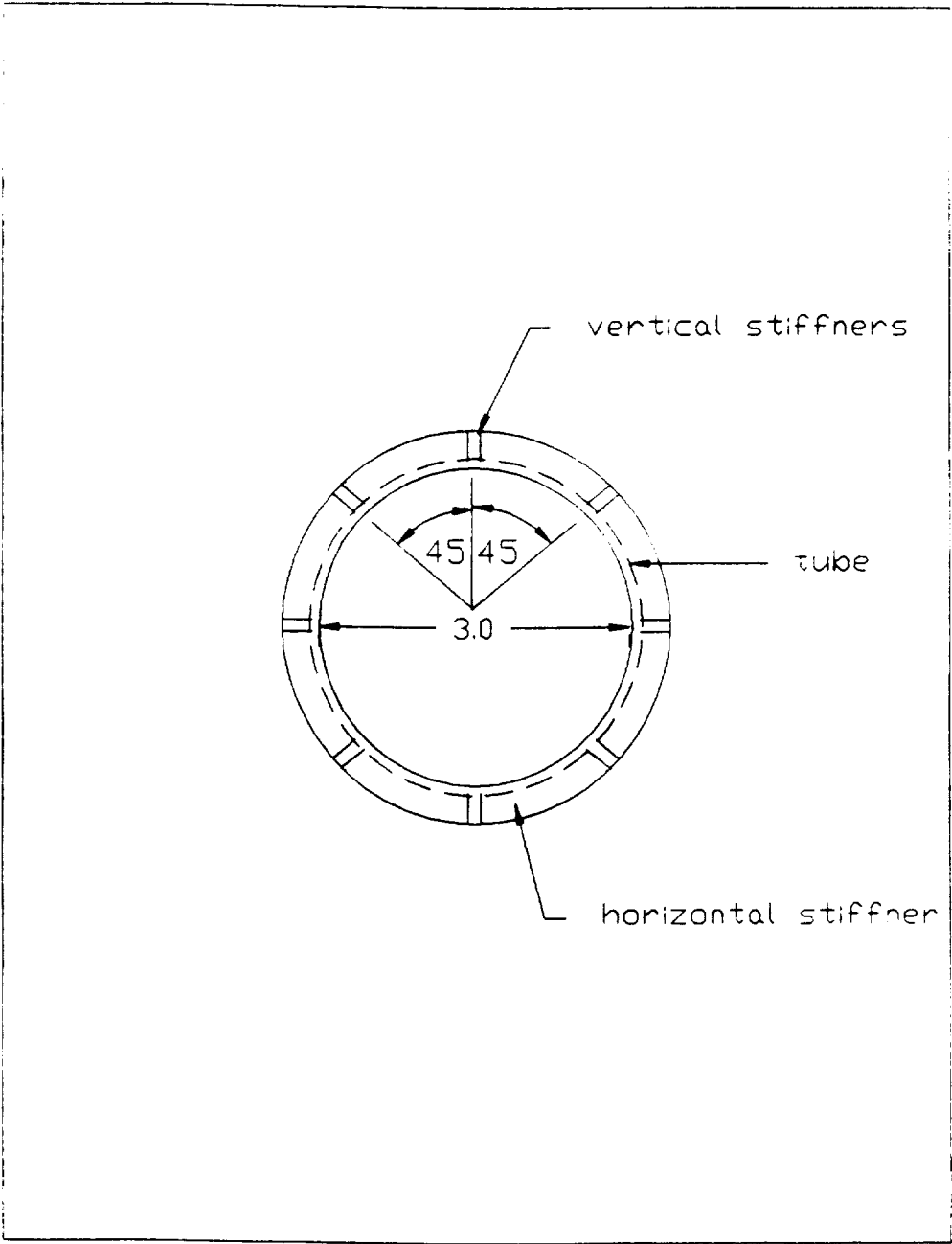
Fig. 2: Top View of Pedestal

Fig. 3: Spucan Footing

Thin circular plate
filled with compacted
regolith

1.0

0.50

Dense regolith
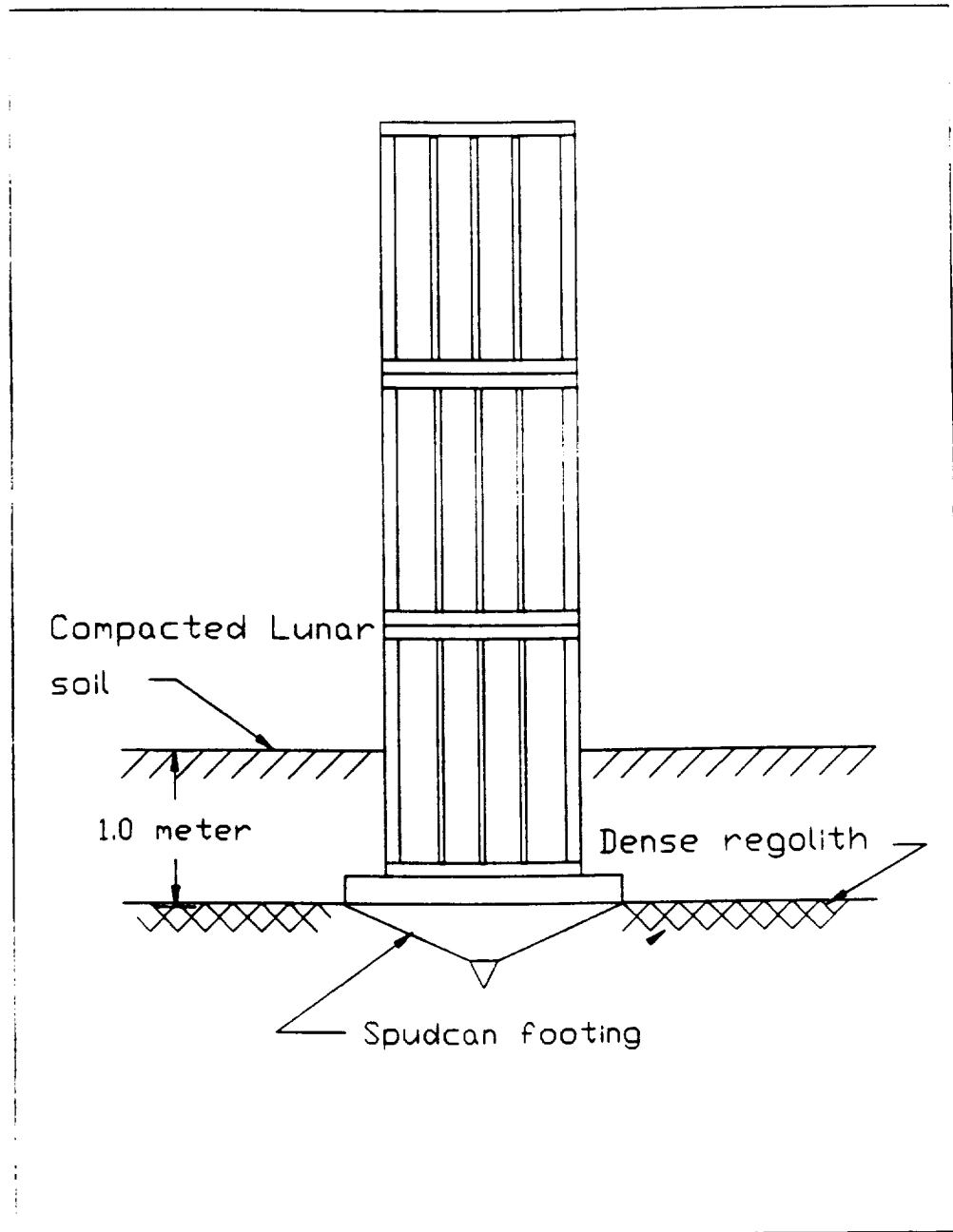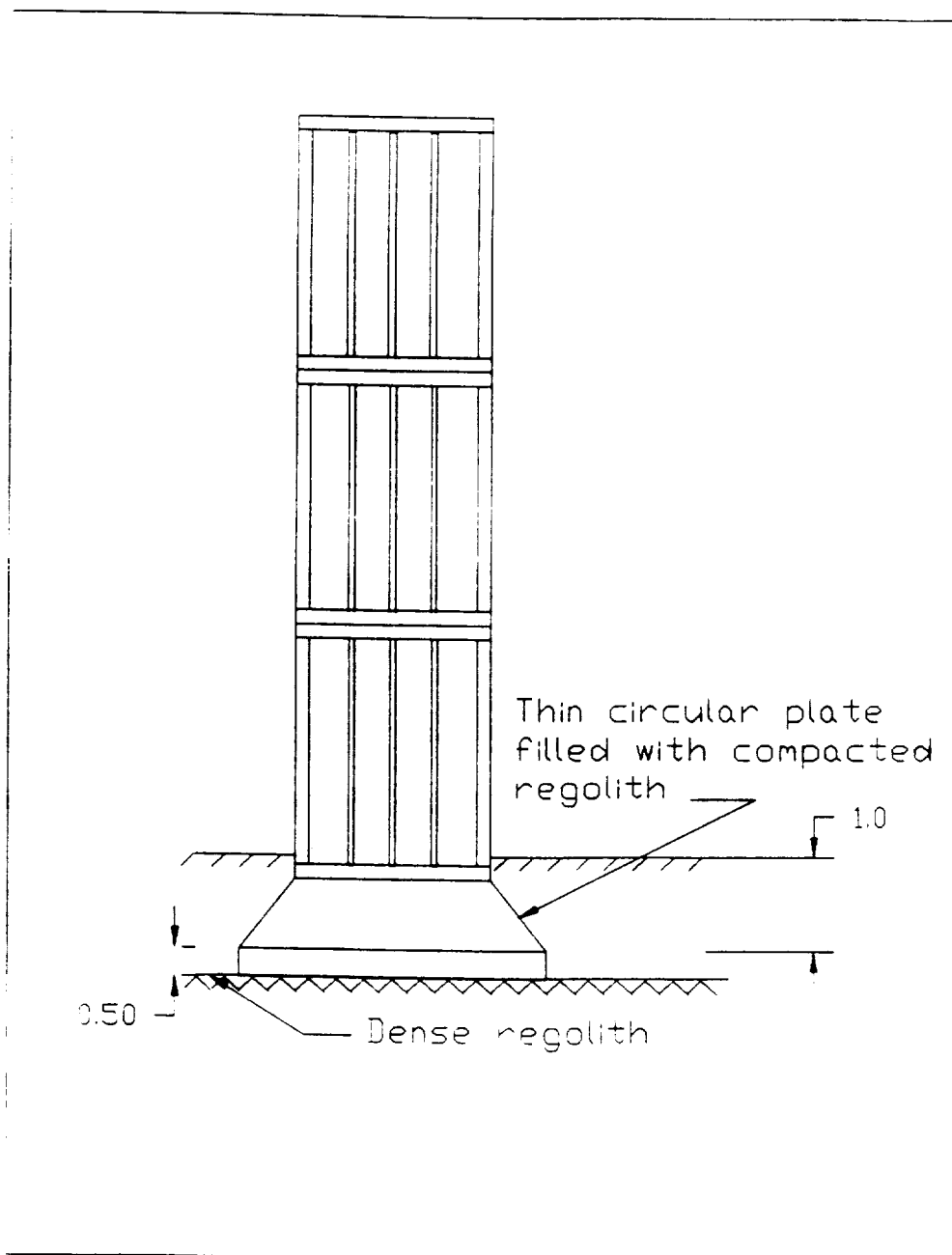
Fig. 4: Spread Footing

Fig. 5: LEV Support
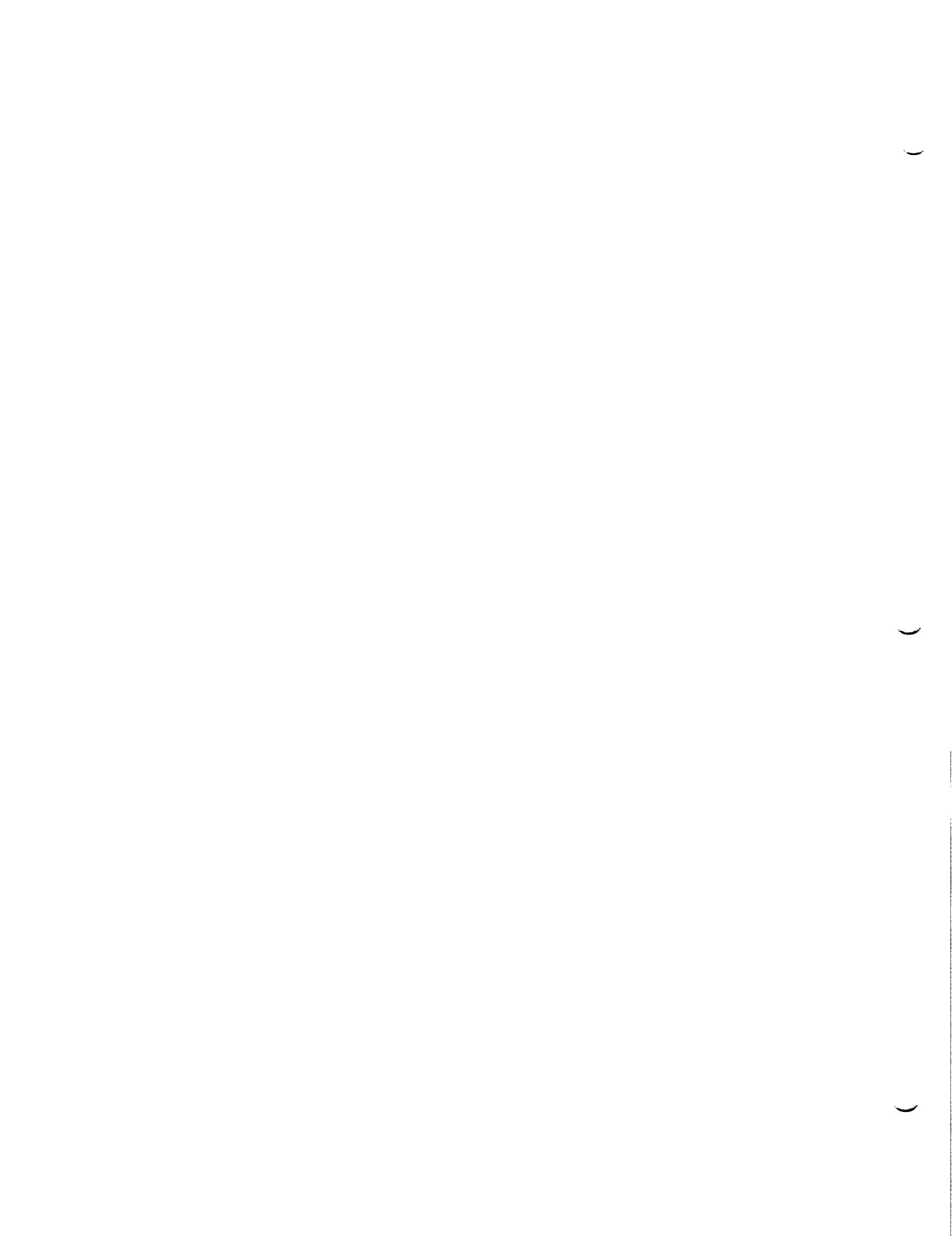
1990

NASA/ASEE SUMMER FACULTY FELLOWSHIP PROGRAM

MARSHALL SPACE FLIGHT CENTER
THE UNIVERSITY OF ALABAMA

A SURVEY OF TECHNIQUES FOR REFRIGERATION, RELIQUEFACTION, AND PRODUCTION OF SLUSH FOR HYDROGEN

Prepared By: Dan Overcash

Academic Rank: Associate Professor

University and   Lenoir-Rhyne College
Department: Physics and Earth Science

NASA/MSFC:
        Laboratory: Propulsion
        Division: Propulsion Systems
        Branch: Space Propulsion

MSFC Colleague: Leon Hastings

Contract Number: NGT-01-002-099
                          The University of Alabama
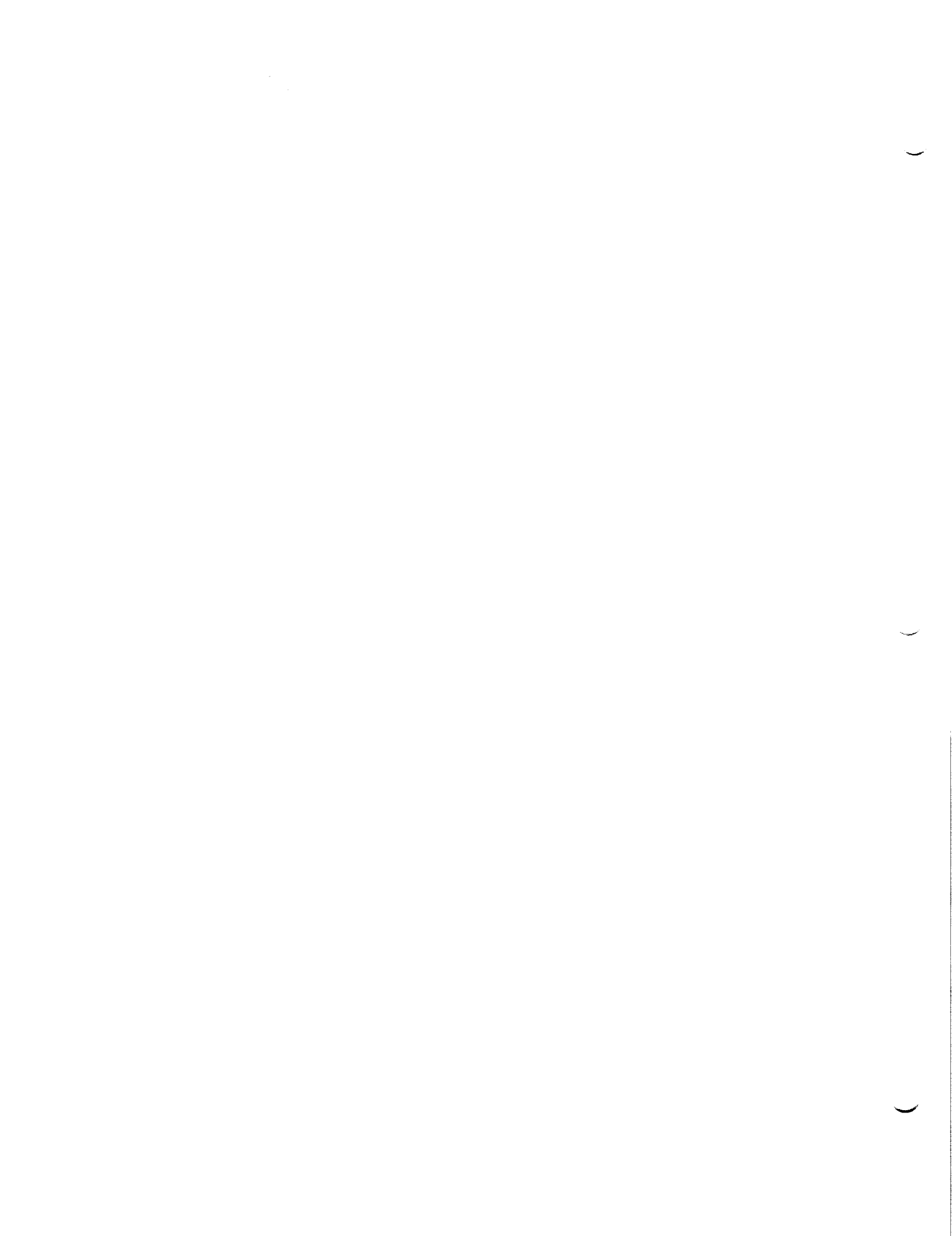
A Survey of Techniques for Refrigeration, Reliquefaction, and Production of Slush for Hydrogen

Techniques surveyed for hydrogen reliquefaction were: Auger; Bubbling Helium; Simon desorbtion; Peltier effect; Joule-Kelvin expansion - Stirling, Brayton, Viulleumier, Rotary reciprocating; Dilution Refrigerator; Adiabatic demagnetization of a paramagnetic salt; and Adiabatic magnetization of a superconductor.

First, I'll briefly consider commercial applications for hydrogen liquefaction then, I'll discuss space refrigeration.

Auger: One end of an auger made of high heat conducting material is immersed in liquid helium and the other end is rotated in hydrogen gas. The cooling power depends on the size of the auger and is slow, massive, and requires liquid helium.

Bubbling Helium Gas: Bubbling liquid helium gas through hydrogen gas slowly forms hydrogen slush but this technique also requires liquid helium and is slow because of the small specific heat of helium.

Simon Desorption: Refrigeration occurs as helium is absorbed by charcoal. This requires liquid helium and has a limited temperature range 20K-50K (36R-90R)[1].

Petlier Effect: Heat can be extracted by passing a current through a thermocouple. A difference in temperature between thermocouple junctins produces a voltage and a current produces a difference in temperature. The peltier heat is equal to the product of the temperature and the Seebeck coefficients. A current of 10 amps through 10 junctions of a Cu-Fe thermocouple at water ice temperature produces 0.74 watts of cooling[1]. In 1838, Levy used an Sb and Bi thermocouple and succeeded in freezing a drop of water[1]. Semiconductors have larger Seebeck coefficients, and good electrical conductivity, but poor thermal conductivity. A p-n junction as gives a heat current of 35 watts but is not usable for hydrogen because the heat is proportional to the temperature (20K) and large currents are needed with the resulting large Joulian heat dissipation.

Joule-Kelvin Expansion: *Stirling cycle*. On a pressure and volume plot, the difference in positive and negative work is the heat absorbed by the refrigeration cycle. In the operation of an ideal stirling refrigerator, a gas is compressed and heat is rejected. The pressure is then lowered at constant volume and the temperature of the gas drops. The gas then expands so the pressure drops and heat is absorbed. The final step in this cycle is a constant volume increase in pressure. In 1982, Myrtle[2] built a

conical Stirling refrigerator to cool from 300K to 9K. Elegant for its simplicity with only one moving part, no moving seals, and 0.6 m x 0.1 m in size, but 8 hours are needed to refrigerate to 9K with its 1 milliwatt cooling. They are sold by North American Phillips, A.D. Little, and Hughes Aircraft. These cycles have a large temperature range and cooling power of 500 watts and can produce 400 liters/hour of liquid hydrogen.[3] They are good commercial refrigerators but their space application is limited by their volume, mass, and support equipment - 5m x 10m x 2m (328 ft^3) for 100 gallons/hour. In a commercial Russian J-K expansion refrigerator, in the condenser, the refrigerant is at as low a temperature as can be obtained and a high pressure. The refrigerant, as a saturated liquid, passes through a narrow opening to a region of lower pressure adiabatically. This "throttling" process occurs at constant enthalpy. Liquefaction of gases by the Joule-Kelvin effect involves isenthalps on a pressure and temperature graph. On an isenthalpic plot for hydrogen, in a region with positive slope, a decrease in pressure causes a decease in temperature. For hydrogen, refrigeration can be obtained for pressure drops in the range 25K to 200K. At 77K (liquid nitrogen) for the maximum pressure to throttle hydrogen is 15MPa (2000 psi).[1] Refrigerators use adiabatic reversible expansion to achieve temperatures within the inversion curve and then Joule-Kelvin expansion is used to liquefy them.

Brayton. Cycles have lower operating pressure levels and have been analyzed by Maddocks and others. They use compressors with after coolers to remove the heat of compression and heat exchangers and expanders. Too many components!

Viulleumirer. A thermal compressor device that offers the possibility of long life and reduced electrical power requirements.

Dilution Refrigerator: Proposed in 1951 and built in 1978, the temperature of a He^3 - He^4 mixture is lowered and the mixture spontaneously separates into two phases. The He^3 floats on top. Lowering the temperature further, the He^4 acts like a vacuum for the dilute gas of He^3 atoms. Upper He^3 atoms are more densely packed and are dispersed among the He^4 atoms, similar to evaporation cooling. Cooling is when the He^3 from the concentrated phase crosses the phase boundary into the dilute phase. A vacuum pump is used to remove the He^3 atoms from the dilute phase, thereby cooling. Transport of He^3 will continue across the boundary because of the 6.4% solubility of He^3 in He^4. He^3 is removed from the dilute phase by osmotic pressure and returned to the still.
    Suppliers of dilution refrigerators are Phillips Research Laboratories, Netherlands, and Astronautics Corp. Many articles may be found in "Cryogenics" articles

concerning: faster He pumps, heat exchangers, condensation stages, without He pumps, entropy of transfer, heat of transport, and dissipation effects.

Recent articles in "Cryogenics" indicate that low temperatures will be essential for some experiments in future space missions but this survey is from 10K-20K and a cooling power of less than 74 Joules per mole of He[3] for dilution refrigerators is small even though they continue to refrigerate below 1.2K and can produce millikelvin temperatures.

Gravity plays an important role in the separation of the lighter He phase from the heavier He phase. H.W. Jackson[3] has demonstrated that electrostriction (5000 volts across a gap of 0.5 mm) is well suited for a mixing chamber aboard spacecraft. Vermeulen and Frossati describe a "powerful" dilution refrigerator but its support equipment is several cubic meters in volume for the necessary pumps.

Astronautics Corporation of America has developed magnetic heat pump which use the magnetocaloric effect to produce refrigeration. Between 2K and 20K, gadolinium garnet (GGG) is used. On an entropy and temperature diagram, a cycle starts by rotating a paramagnetic salt into a magnetic field. This requires work to increase the magnetic energy in the GGG and liberates heat. A heat exchanger removes the heat and from the GGG at a constant temperature as the field is increased and the entropy drops. As the GGG is rotated out of the magnetic field, the temperature drops. A rotating wheel of GGG has been used to produce hydrogen slush. For each kilowatt of cooling power, 34.3 pounds per hour of NPB liquid hydrogen, and 0.93 kW of electrical power and used.

As the GGG rotates into the magnetic field, heat is removed from the wheel by boiling liquid hydrogen. As the wheel rotates out of the field, hydrogen freezes on the wheel and is removed by strippers. J.A. Waynet[5] describes a 1 kilowatt magnetic refrigerator which produces 50% slush @ 550 liters per hour and has a mass of 370 kg and a volume of about 1 cubic meter. A 7 tesla magnetic field is used and the current necessary for this field can be provided by solar cells to a superconducting magnet but a superconducting magnet requires liquid helium. The infrared telescope has successfully used liquid helium in space for a year. This 1 kW refrigerator also uses 27 tons per day of liquid nitrogen. Other candidate cycles in magnetic refrigeration are the Brayton and Ericsson cycles which increase the temperature span and use external thermal agents which act as a thermal flywheel. Superconductors, which can be used as thermal switches in these refrigerators as magnetic fields, are used to turn on and off superconductivity and, therefore thermal conductivity. An active magnetic refrigerator with ortho to para hydrogen

converters, span 77K to 10K, 10 carnot cycle devices are needed. The active magnetic refrigerator (AMR) uses a packed bed of material sandwiched between a hot and a cold reservoir. A heat transfer fluid is shuttled back and forth through the bed by pistons. The bed is magnetized with no flow. Fluid is then passed from the hot reservoir with the bed magnetized. The bed is then demagnetized with no flow. Fluid is then passed from the hot reservoir through the cooled bed. Magnetic refrigerators need to be flight tested and paramagnetic salts with higher specific heats should be found. For the NASP X-30[4], slush hydrogen maintenance by conventional methods are not compatible. The freeze thaw method requires large vacuum pumps and heat exchangers. The auger and helium gas injection system requires large helium refrigeration systems. The largest helium refrigerator ever built is at BNL and provides 10 kwatts of cooling but has 5 cold exchangers which are the size of a gasoline tanker.

Flippen[6] has found for the type II superconductor, Nb, adiabatic magnetization provides cooling. Applying a magnetic field makes the superconductor a normal conductor and refrigerates.

All the refrigerator cycles discussed for adiabatic demagnetization of a paramagnetic salt should be investigated for the magnetization of a superconductor.

Cooling is obtained by converting from ortho to paro hydrogen. The 7 or 8 tesla magnetic field, 70,000 gauss magnetic fields needed for magnetic refrigerators is now obtainable with superconducting magnets with liquid helium cooling and are available from Janis. Future high temperature superconductors, if developed, may bring transition temperatures below space temperatures and provide long term space magnets for magnetic refrigeration to liquify hydrogen. Electrical engineers say high currents may be obtained from solar cells if low power is needed as for superconductors. If spacecraft can be turned so that ceramic superconductors are below 125K, 225R, as of 1987 with 1-2-3 superconductivity is now possible.

Lawless and Clark[7], in 1988 specific heat measurements, found an interesting magnetocaloric stabilization mechanism. Ceramic and epoxies were found that have magnetocaloric cooling and could be used in magnet windings and paramagnetic wheels in cryorefrigerators.

At the Fifth International Cryogenic Conference, R.W. Vance of Aerospace Corporation in California reviewed the state-of-the-art small refrigerators that may be capable of performing in space.

Mason and Stephens described a supercritical helium (SHe) system for a 6 month life time of liquid hydrogen.

A reversed Brayton cycle refrigerator with four expanders was described where high pressure gas passes through a series of counterflow heat exchangers. The compressor rotates 100,000 revolutions/min and are supported by gas bearings that assure long life but these systems are extremely inefficient, less than 1% at 10K.

A Vuileumier refrigerator has a potential long life, low power demands and uses and isotope for thermal compression.

One unit has been flight tested for a short period. Slow piston speeds and low bearing loads produce long life.

Liquid and solid cryogenic propellants, when stored in properly designed dewars, will require small refrigeration loads which can be handled by several of the refrigerators described in this paper for space flights of one year in length.

I encourage this group to investigate and design space cooling systems for the high temperature reservoirs for these refrigeration systems. Since radiation cooling depends on the fourth power of the temperature, higher temperature heat exchangers give increased radiation cooling and higher efficiencies.

I would like to spend the next academic year investigating and testing high temperature superconductors for use is adiabatic refrigerators. Both as magnetic field producers and as a working material for magnetocaloric refrigerators.

Endnotes

1. Zemanski, <u>Heat and Thermodynamics</u>, 6th ed., pp. 25, 441, & 328.

2. K. Myrtle, C. Winter, and S. Gygax, <u>Cryogenics</u>, March 1982, p. 139.

3. H.W. Jackson, <u>Cryogenics</u>, February 1982, p. 59.

4. J.A. Waynet, J.A. Barclay, R.W. Foster, <u>A Portable Magnetic Refrigerator for X-30 Slush Maintenance 5th National Aerospace Plan Technology Symposium</u>, October 1988.

5. J.A. Waynet, J.A. Barclay, P. Claybaker, R.W. Foster, S.R. Jaeger, S. Kral, C. Zimm, <u>Production of Slash Hydrogen Using Magnetic Refrigeration</u>, 7th Intersociety Cryogenic Symposium, Boulder, Colorado, January 1989.

1990

NASA/ASEE SUMMER FACULTY FELLOWSHIP PROGRAM

MARSHALL SPACE FLIGHT CENTER
THE UNIVERSITY OF ALABAMA

ELECTRON TEMPERATURE AND CONCENTRATION IN A THERMAL ATOMIC OXYGEN SOURCE

Prepared By: Patrick Dennis Pedrow

Academic Rank: Assistant Professor

University and   Washington State University
Department: Electrical Engineering

NASA/MSFC:

          Laboratory: Materials and Processes
          Division: Engineering Physics
          Branch: Physical Sciences

MSFC Colleagues: Mr. R. C. Linton
                                 Mr. M. R. Carruth

Contract No: NGT-01-002-099
                                 The University of Alabama
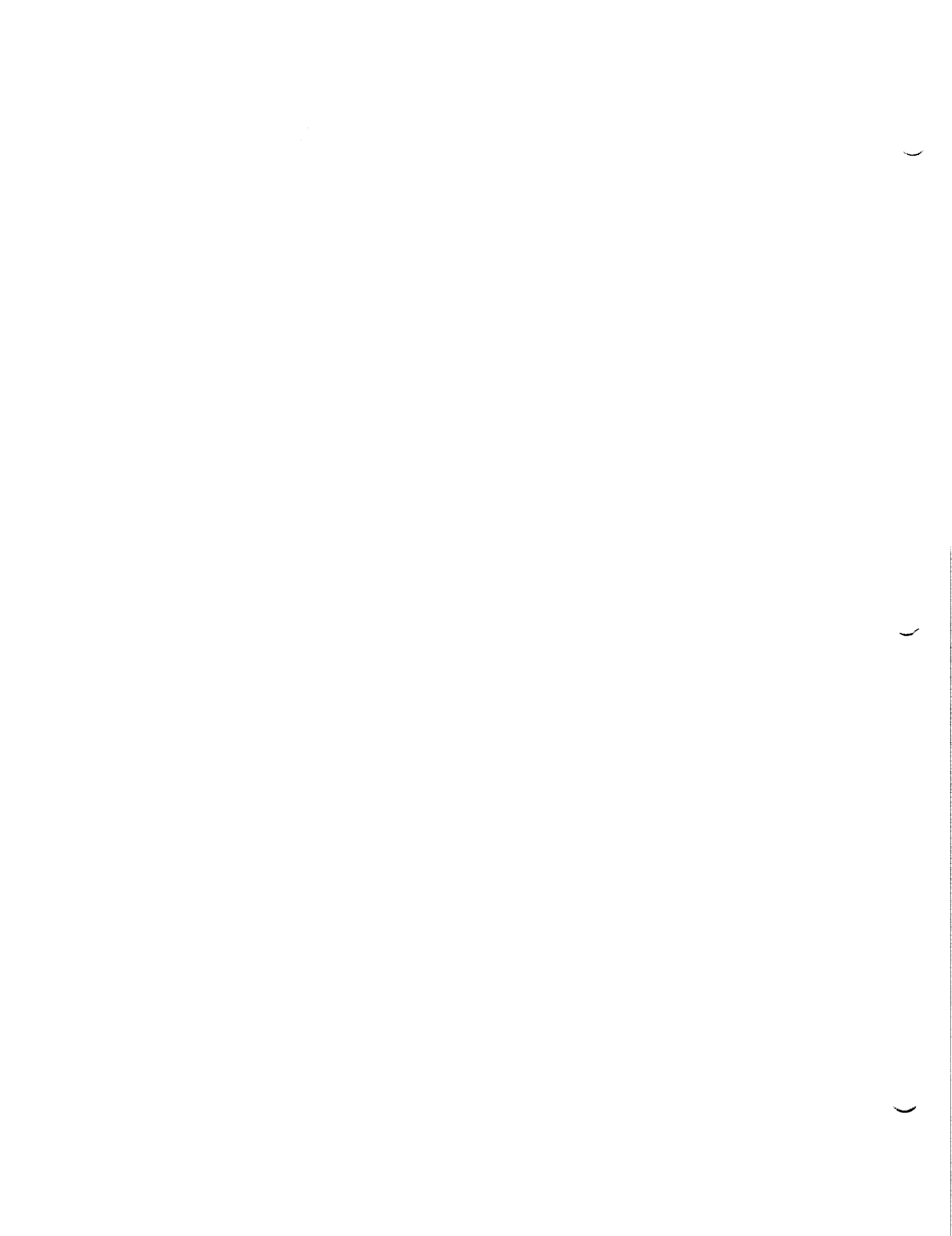
I. Introduction

The lower earth orbit environment erodes materials primarily due to the presence of atomic oxygen at concentrations on the order of $10^9 cm^{-3}$.[1] Corresponding electron concentrations are on the order of $10^5 cm^{-3}$ with an electron temperature on the order of 0.15 eV. [2] A thermal atomic oxygen source for materials screening has been built for NASA by Boeing Aerospace.[3] This device is shown in Figure 1. Plasma is created by 13.56 MHz rf power applied to oxygen flowing in a 7.6 cm ID glass tube. Charged and neutral particles from the plasma flow downstream to the "T" region where the small glass tube connects to a 15.2 cm ID glass tube. Materials are typically exposed near the aluminum flange located at x=24.1 cm with power, pressure, and flow set to 100W, 100mtorr, and 6.7 sccm, respectively. The objective of the work described here was to use a microwave interferometer and Langmuir probes to characterize the electron concentration in this thermal atomic oxygen source.

II. Apparatus

Two flat (0.5mm thick) 304 stainless steel Langmuir probes were used; one was a round disk with exposed area $2.04 \times 10^{-4} m^2$ and the other was a square with area $1.16 \times 10^{-2} m^2$. The small disk probe was used at x=0 and 10 cm while the large square probe was used at x=10, 16.5, and 25cm. The 9cm x 60cm 304 stainless steel ground plate shown in Figure 1 was found to be essential for stable Langmuir probe measurements. Bias voltage was supplied by batteries attached to an integrated circuit voltage regulator. Bias voltage was measured with a Fluke 8020B Multimeter and probe current was measured with a Phillips PM3365 100MHz oscilloscope in conjunction with viewing resistors with values 10.3kΩ, 95.8kΩ, and 1MΩ (oscilloscope input resistance). To minimize rf noise, all electrical connections were made with coaxial cables. Langmuir probes have been summarized in several texts [4,5,6] and the circuit used for these measurements was described previously.[7]

The microwave interferometer passed 9.2 GHz microwaves through the walls of the glass tube and through the plasma via transmitting and receiving horn antennas. Microwave interferometers for plasma diagnostics have been described in the literature.[8,9] The interferometer used in this work is very similar to that shown in Figure 6.7 on p. 201 of Reference 8. Basically, power from the microwave source was split into a plasma path and a reference path. Microwaves from these two paths were then added and detected. The electron concentration in the plasma changed the phase of the plasma path microwaves resulting in a detector output voltage that was proportional to electron concentration.

III. Results

Typical operating conditions in the thermal atomic oxygen source were found to produce electron concentrations at the center of the "T" in Figure 1 that were well below the detection threshold of the interferometer ($10^8 cm^{-3}$). Hence, we calibrated (with the interferometer) the circular Langmuir probe at an artificially high plasma density and then

used the circular and the square Langmuir probes to measure the low electron concentrations that exist during materials exposure tests.

To create this high density plasma, argon gas was used at a pressure of 350 mtorr, a flow rate of 19.5 sccm and an output power of 200W with 72W reflected back to the rf power supply. These conditions filled both the vertical and horizontal tubes with a very bright dense plasma. Using standard Langmuir probe techniques, the electron temperature of this plasma was measured to be 4.71±0.82 eV. Figure 2 shows calibration of the Langmuir probe with the interferometer. For this data, the horns of the interferometer and the circular probe were located at x=0. The probe was oriented in a horizontal position that minimized reflected microwave power. The probe was biased to -42V to insure that it was collecting saturation ion current. As shown in Figure 2, the rf source was pulsed on and off for times on the order of 5 seconds. The interferometer and Langmuir probe measured electron concentrations of 4.03×10^9 and $3.39 \times 10^9 \text{cm}^{-3}$, respectively. This gives a ratio of 1.2, which is excellent agreement between the two techniques.

The atomic oxygen source was then set to more realistic operating conditions: power in the range 50 to 200W with zero reflected power, oxygen pressure 100 mtorr, and flow rate 6.7 sccm. Figure 3 shows typical Langmuir probe volt-ampere characteristics for the square probe located at x=25cm with power settings of 50, 100, 150, and 200W. Electron temperature was obtained from a semilogarithmic plot of the logarithm of electron current versus probe voltage. Electron current was obtained by subtracting saturation ion current from the probe current. In Figure 3 the electron temperatures for 50, 100, 150, and 200W were 0.56±0.11, 0.63±0.05, 0.55±0.04, and 0.69±0.04 eV, respectively. That is, for these conditions the electron temperature was nearly independent of power setting, an observation that is consistent with others.[10,11]

Electron concentration was found by assuming singly charged ions, invoking the plasma condition $n_i = n_e$, and using the expression

$$n_e = n_i = \frac{I_{si}\sqrt{\dfrac{m_i}{kT_e}}}{0.607Ae} \tag{1}$$

where I_{SI}, m_i, and A are the saturation ion current, the ion mass, and the probe area, respectively. This is from Equation (3.2.20) on page 60 of Reference 5. For this analysis, we assumed that the dominant positive ion was O_2^+ which is consistent with the work of others.[12] In Figure 3 the electron concentration for 50, 100, 150, and 200W were $1.33\pm.45 \times 10^4$, $6.87\pm.94 \times 10^4$, $1.40\pm.12 \times 10^5$, and $2.97\pm.33 \times 10^5 \text{cm}^{-3}$, respectively.

Similar measurements at x=0, 10, and 16.5 cm showed that the electron concentration could be expressed as a function of power and position by the expression

$$n_e = 973 P^2 \exp\left(\frac{-x}{5.21}\right)$$ (2)

where n_e is electron concentration in cm^{-3}, P is power in W, and x is distance in cm. Plug flow analysis[13] of ambipolar diffusion [14] predicts that dependence in the x direction would be

$$n_e \propto \exp\left(\frac{-x}{\lambda}\right)$$ (3)

with

$$\lambda = \frac{0.174 R^2 u_x}{D_a}$$ (4)

where R, u_x, and D_a are the tube radius, the flow velocity and the ambipolar diffusion coefficient, respectively. Figure 4 compares all measured data points with this analytical expression. Figure 5 shows contours of constant electron concentration in the x-P plane.

While electron temperature was nearly constant with power at each location, it was found to be a function of x. For example, at a power setting of 100W, the electron temperature at x=0, 10, 16.5, and 25 cm was 2.51±0.17, 1.22±0.05, 0.80±0.06, and 0.63±0.05eV, respectively.

IV. Conclusions

Electron concentration was measured as a function of power and position. The electrons were lost to the walls through ambipolar diffusion and their concentration was accurately described by Eq. 2. That is, electron concentration was proportional to power squared and decayed exponentially with distance.

V. Recommendations

Data similar to Figure 5 should be generated for erosion rate and for atomic oxygen concentration as measured with a catalytic thermocouple probe.[15] Additional plug flow analysis should be used to develop an analytical model for concentrations of all species of interest. Laser-induced fluorescence (LIF) should be investigated for measuring atomic

oxygen concentration and to identify reactant species emitted from the surface of materials exposed to atomic oxygen.

VI. References

1. M. F. Rose, IEEE Transactions on Electrical Insulation, *EI-22*, pp. 555-571, 1987.

2. R. L. F. Boyd, *Space Research by Rocket and Satellite*, New York:Harper & Brothers, 1960, Chapter 1.

3. NASA Contract NAS8-36586, 1986-1989.

4. R. H. Huddlestone and S. L. Leonard, editors, *Plasma Diagnostic Techniques*, New York: Academic Press, 1965, Chapter 4.

5. I. H. Hutchinson, *Principles of Plasma Diagnostics*, New York: Cambridge University Press, 1987, Chapter 3.

6. O. Auciello and D. L. Flamm, editors, *Plasma Diagnostics*, Volume 1, New York: Academic Press, 1989, Chapter 3.

7. P. D. Pedrow and A. M. Nasiruddin, IEEE Transactions on Plasma Science, *17*, pp 17-23, 1989.

8. M. A. Heald and C. B. Wharton, *Plasma Diagnostics With Microwaves*, New York: Robert E. Krieger Publishing Co., 1978.

9. Hotston and M. Seidl, J. Sci. Instrum., *42*, pp 225-230, 1965.

10. J. E. Heidenreich, III, et al., J. Vac. Sci. Technol. B, *5*, pp 347-354, 1987.

11. J. Felts and E. Lopata, J. Vac. Sci. Technol. A, *5*, pp 2273-2275, 1987.

12. T. H. Lin, et al., IEEE Transactions on Plasma Science, *16*, pp 631-637, 1988.

13. I. Stakgold, *Green's Functions and Boundary Value Problems*, New York: John Wiley, 1979, pp 11-13.

14. F. F. Chen, *Introduction to Plasma Physics and Controlled Fusion*, Vol. 1, New York: Plemum Press, 1984, pp 159-169.

15. M. R. Carruth, et al., Rev. Sci. Instrum., *61*, pp 1211-1216, 1990.
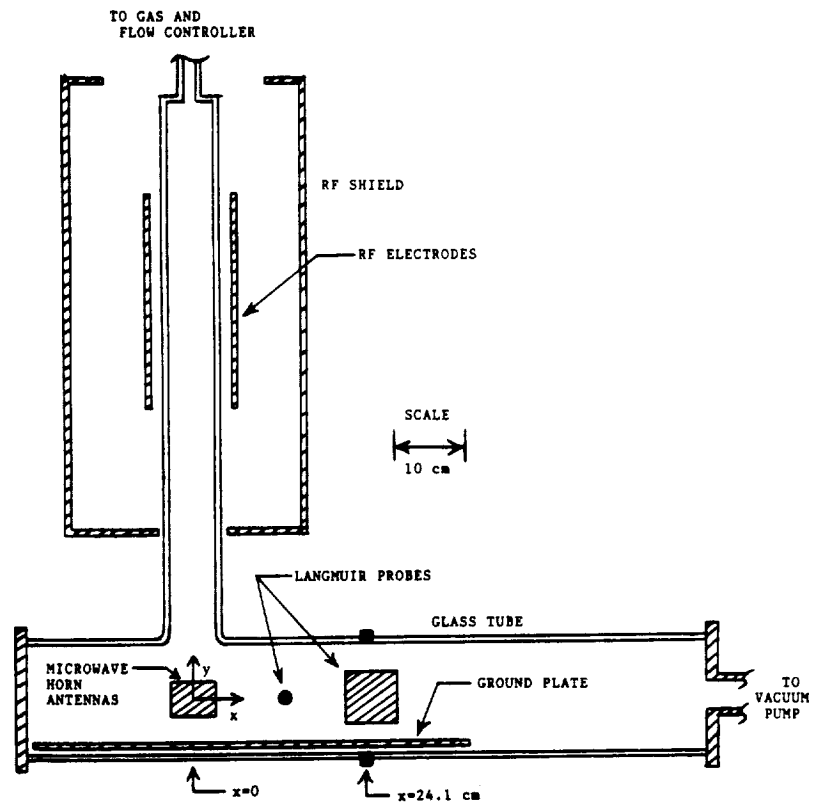
Figure 1. Thermal atomic oxygen source.
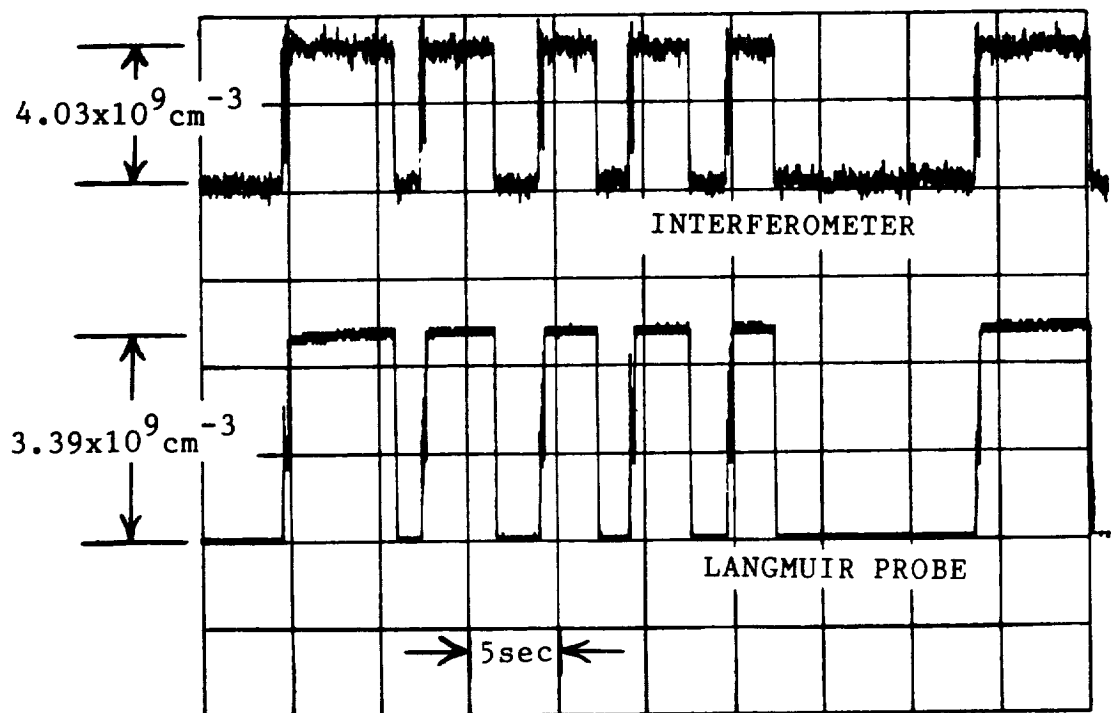
Figure 2. Calibration of Langmuir probe with microwave
interferometer.

LANGMUIR PROBE IN OXYGEN
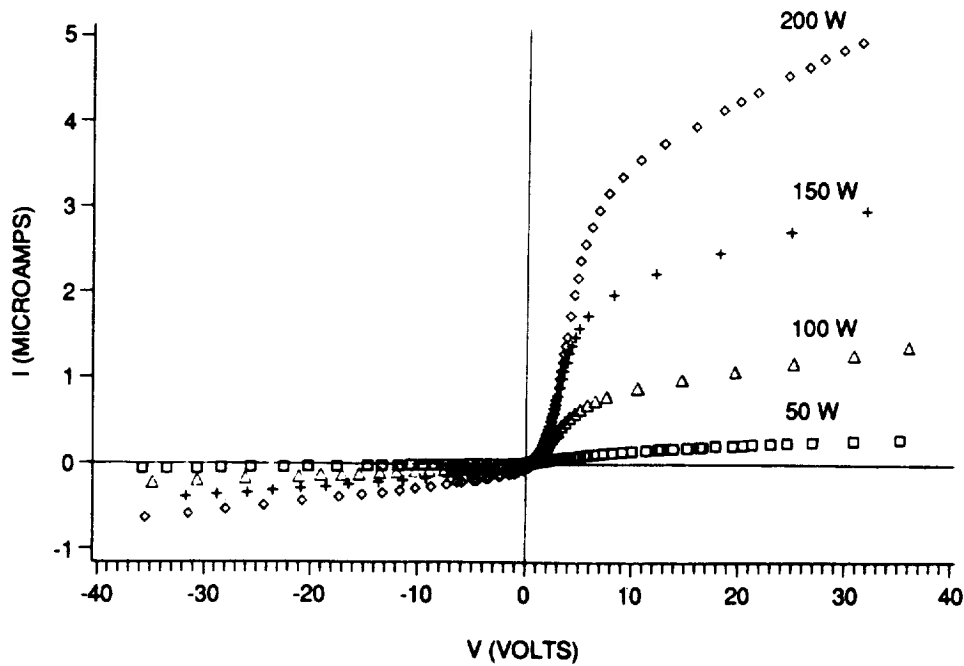
Figure 3. Square Langmuir probe at x=25cm with 100mtorr oxygen.

MEASURED VERSUS ANALYTICAL
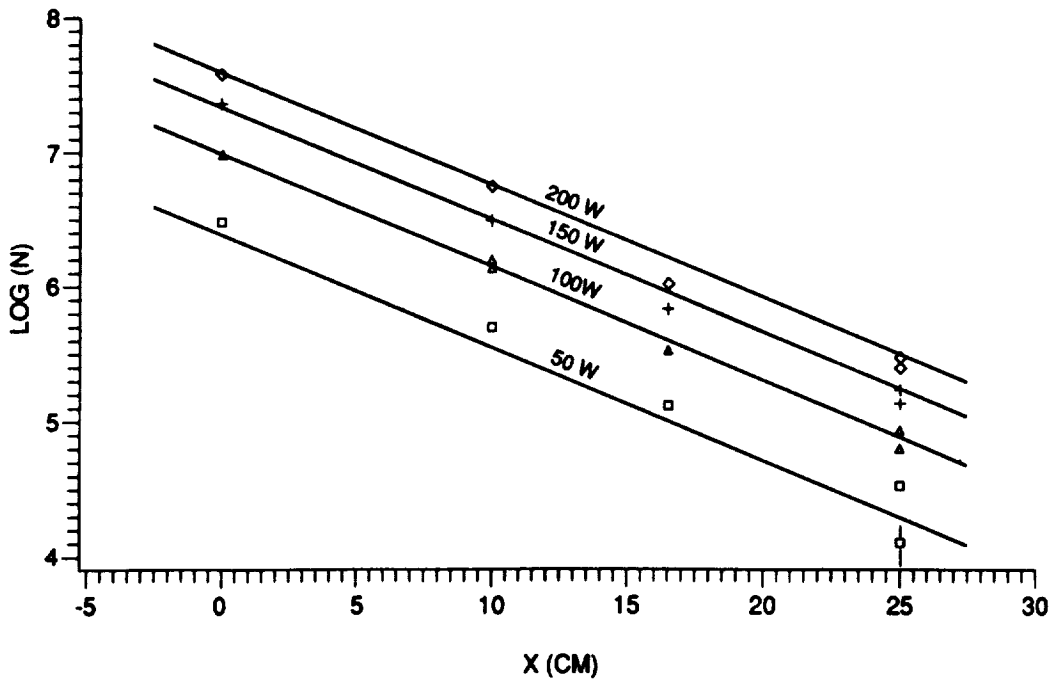
Figure 4. Analytic expression (solid lines) compared to measured data (symbols).

ELECTRON CONCENTRATION
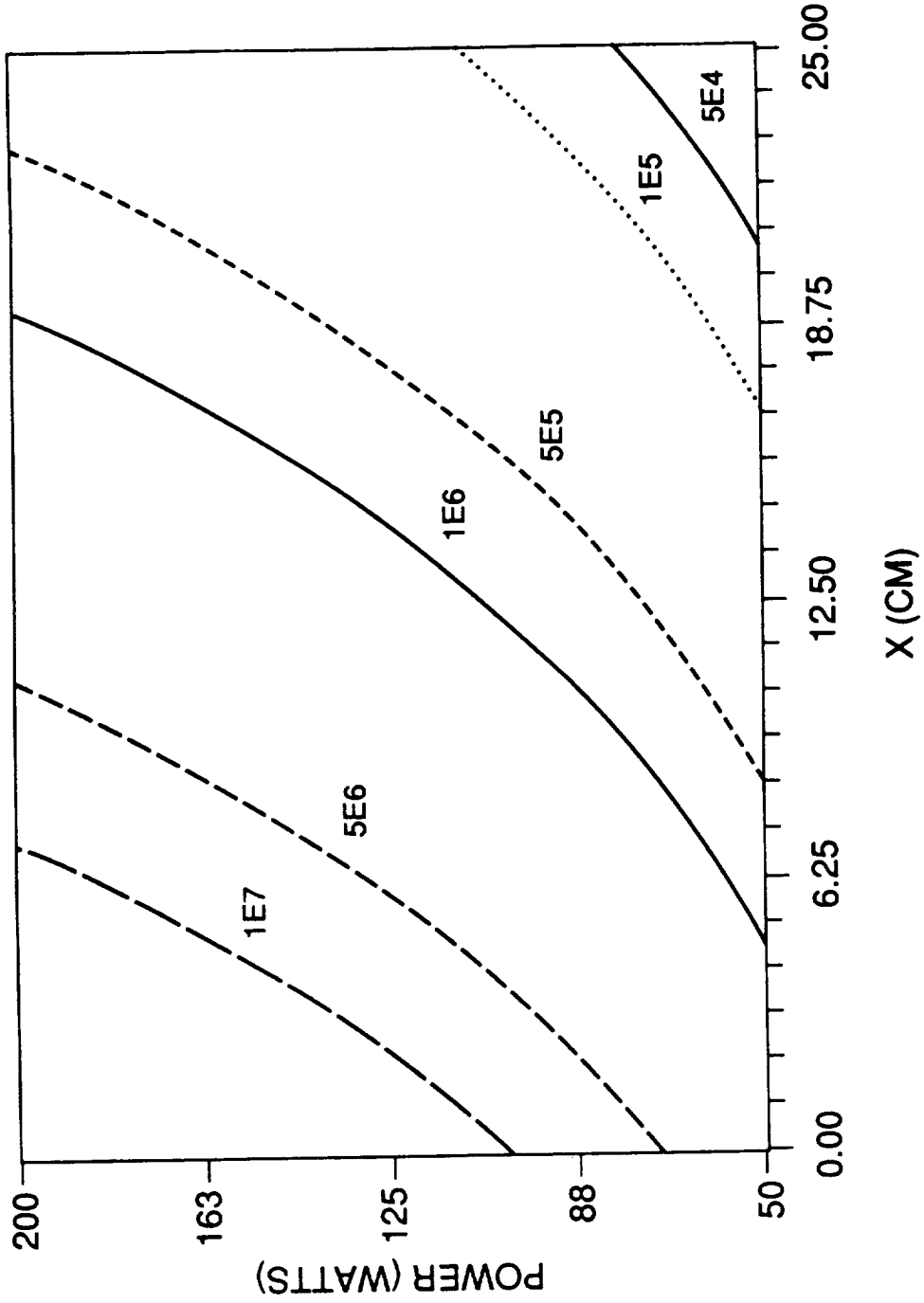
Figure 5. Contours of constant electron concentration in units of cm-3. Oxygen at 100mtorr and 6.7sccm. From Eq. 2.
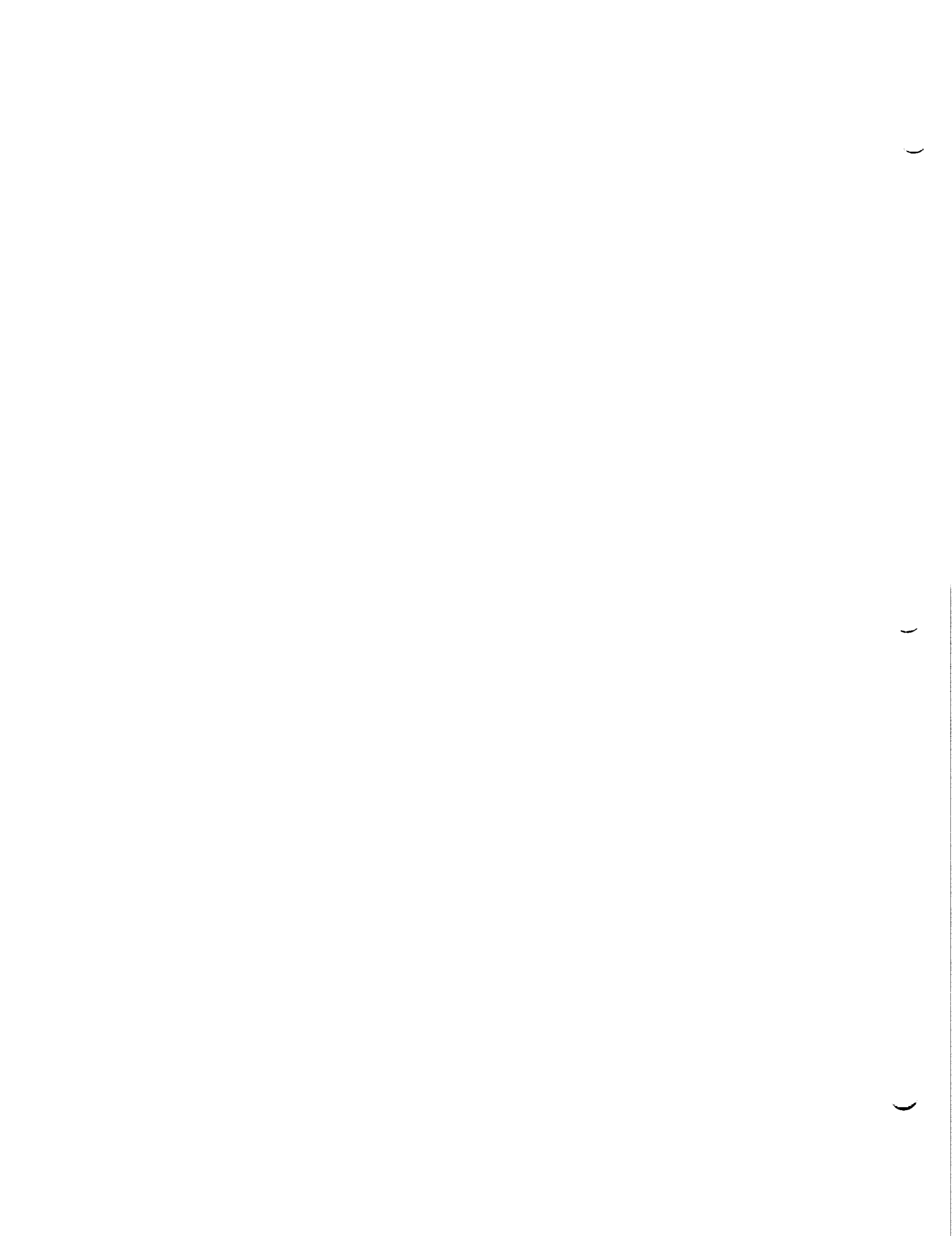
1990

NASA/ASEE SUMMER FACULTY FELLOWSHIP PROGRAM

MARSHALL SPACE FLIGHT CENTER
THE UNIVERSITY OF ALABAMA

ANALYTICAL STUDY OF THE EFFECTS OF CLOUDS ON THE LIGHT

PRODUCED BY LIGHTNING

Prepared By: Dieudonne D. Phanord

Academic Rank: Assistant Professor

University and   The University of Alabama
in Huntsville
Department: Mathematical Sciences

NASA/MSFC:
     Laboratory: Space Science
     Division: Earth Science/Applications
     Branch: Remote Sensing

MSFC Colleague: Richard J. Blakeslee
Douglas Mach
Hugh Christian
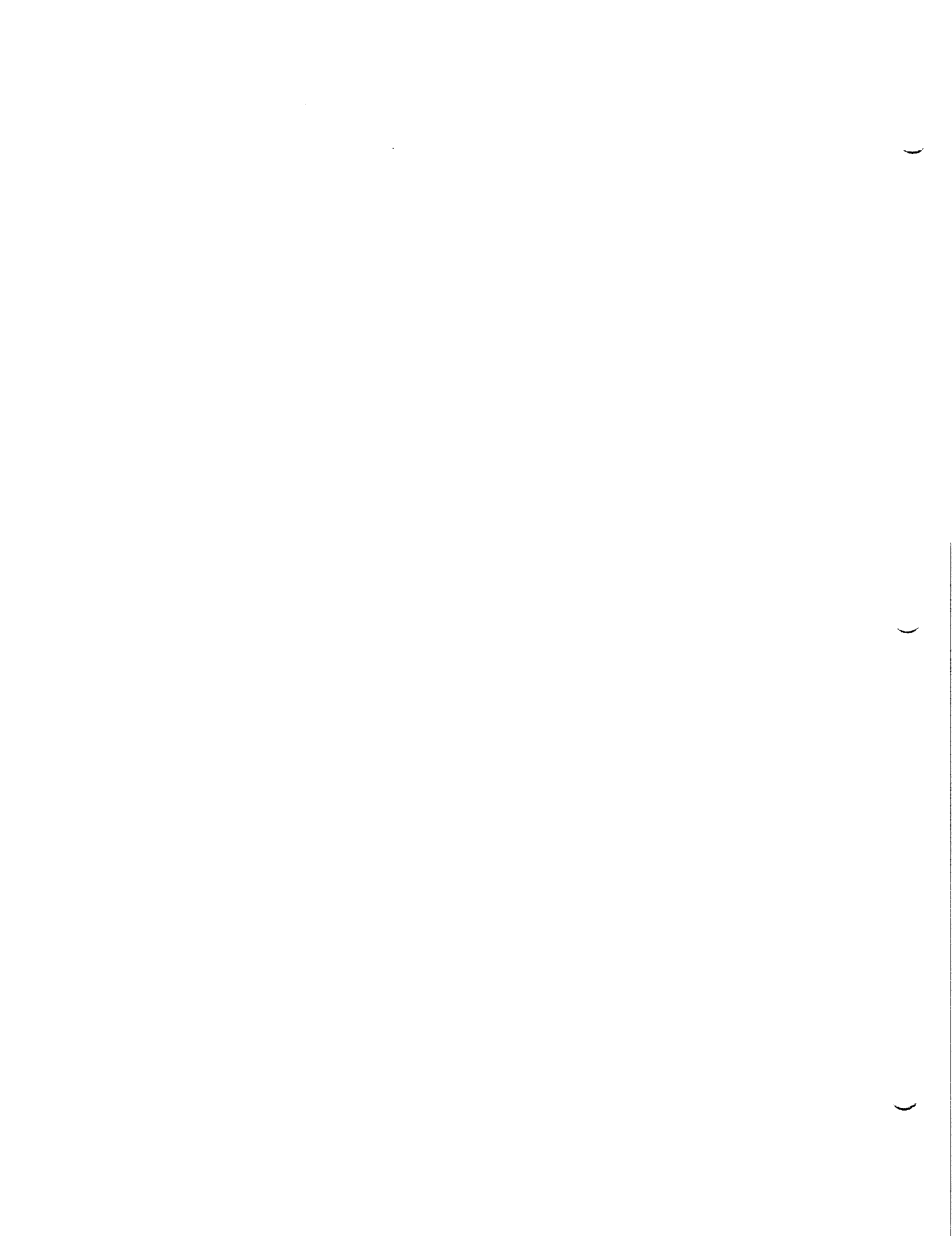
I. INTRODUCTION

We consider the scattering of light (visible or infrared) due to lightning by cubic, cylindrical, and spherical clouds. A typical cloud is represented by a statistically homogeneous ensemble of configurations of N identical and aligned spherical water droplets whose centers are uniformly distributed in its volume. The incident light is from point sources inside the penetrable cloud.

The optical effects of clouds on the light produced by lightning have received great interest for many years. Different techniques have been used in trying to explain the complicated nature of these effects. In particular, we mention the Monte Carlo method [9] which is a computer simulated technique. In a Monte Carlo program, we follow the path of the photons emitted into the cloud by lightning. A photon is said to be scattered if it escapes from the cloud after colliding with the spherical droplets. Otherwise, it is considered as being absorbed by the cloud [1 to 8]. The Monte Carlo method is time consuming, expensive and it is very difficult to obtain from it reliable statistics [9].

Here, we extend to cloud physics the work done by Twersky [10 to 12] for single and multiple scattering of electromagnetic waves. We solve the interior problem separately to obtain the bulk parameters for the scatterer equivalent to the ensemble of spherical droplets. With the interior solution or the equivalent medium approach, the multiple scattering problem is reduced to that of a single scatterer in isolation. Hence, the computing methods of Wiscombe [13] or Bohren [15] specialized to Mie scattering with possibility for absorption have been used to generate numerical results in short computer time.

II. MATHEMATICAL ANALYSIS

We model the incident point source as $\vec{\phi} = \hat{a}\dfrac{e^{i\kappa r}}{r}$, $\kappa_1 = k\eta'$, and η' being the complex relative index of refraction for the host medium inside the cloud, the total outside solution

$$\vec{\psi} = \vec{\phi} + \mathbf{u}_o \tag{1}$$

satisfied the following differential equation obtained from Maxwell's equations after suppressing the harmonic time dependence

$$\left[\vec{\nabla} \times \vec{\nabla} \times +\kappa_1^2\right]\vec{\psi} = 0, \vec{\nabla} \cdot \vec{\psi} = 0. \tag{2}$$

Here,

$$\kappa_2 = \kappa_1 \eta'' = k\eta'\eta'', \tag{3}$$

with η'' being the complex relative index of refraction for the medium inside the spherical water droplet.

Similar to Twersky [11], we have from (1)

$$\vec{\psi} = \hat{a}\frac{e^{i\kappa r}}{r} + \left\{ \tilde{h}(\kappa_1|\mathbf{r} - \mathbf{r}'|), \mathbf{u}_o(\mathbf{r}') \right\}. \tag{4}$$

Asymptotically, for $\kappa_1 r \gg 1$, we can write

$$\mathbf{u}_o(\mathbf{r}) = h(\kappa_1 r)\mathbf{g}(\hat{\mathbf{r}}, \hat{\kappa}_1 : \hat{a}), \hat{\mathbf{r}} \cdot \mathbf{g} = 0, \tag{5}$$

and the scattering amplitude

$$\mathbf{g}(\hat{\mathbf{r}}, \hat{\kappa}_1 : \hat{a}) = \left\{ \tilde{\mathbf{I}}_t e^{-i\hat{\kappa}_1 \cdot \mathbf{r}'}, \mathbf{u}_o(\mathbf{r}') \right\} \tag{6}$$

are evaluated from Mie scattering theory.

From the general reciprocity relation

$$\left\{ \Psi, \vec{\psi}_a \right\}_t = 0 \tag{7}$$

for any arbitrary direction of incidence, we derive as in [11] the self-consistent integral equation for the multiple configurational scattering amplitude

$$\mathbf{G}_t(\hat{\mathbf{r}}) = \tilde{\mathbf{g}}_t(\hat{\mathbf{r}}, \hat{\kappa}_1) \cdot \hat{a} + \sum_m' \int_c \tilde{\mathbf{g}}_t(\hat{\mathbf{r}}, \hat{\mathbf{r}}_c) \cdot \mathbf{G}_m(\hat{\mathbf{r}}_c) e^{i\hat{\kappa}_{1c} \cdot \mathbf{R}_{tm}}. \tag{8}$$

We take the average of (8) over a statistically homogeneous ensemble of configurations to obtain [11] the dispersion relation determining the coherent parameters

$$\mathcal{G}\left(\vec{\kappa}_1 | \vec{K}\right) = -\frac{\rho}{c_o(K^2 - \kappa_1^2)} \left\{ \left[e^{-i\vec{K} \cdot \mathbf{R}}, \mathbf{U} \right] \right\}$$

$$+ \rho \int_{V_\infty - v} [f(\mathbf{R}) - 1] e^{-i\vec{K} \cdot \mathbf{R}} \mathbf{U} d(\mathbf{R}). \tag{9}$$

Equation (9) solves formally the interior problem for the cloud. To obtain numerical results, one can apply stationary phase method [12] on (8) and reduce (9) to

$$K - \kappa_1 \sim -\frac{ig\sigma_0}{2\eta}\mathfrak{L}^{-1}$$

$$and$$

$$\mathfrak{L} = \left\{ 1 - \rho\frac{g\sigma_0}{2\eta}\int_0^\infty [f(\mathbf{R}) - 1]e^{i(\kappa_1 - K)R}d(\mathbf{R}) \right\}. \tag{10}$$

From equation (10), the leading term approximation gives

$$\eta^2 = \epsilon$$

$$\epsilon = 1 + \frac{3\mathfrak{F}}{1 - \mathfrak{F}},$$

$$\mathfrak{F} = \omega_0\left(\frac{\epsilon' - 1}{\epsilon' - 2}\right), \tag{11}$$

$$\omega_0 = \frac{\omega}{1 + \omega}.$$

For

$$\epsilon' = \left(\eta_r' + \eta_i'\right)^2, \tag{12}$$

and the bulk index of refraction is

$$\eta^2 = \epsilon,$$

$$\begin{matrix}\eta_r \\ \eta_i\end{matrix} = \left\{\frac{\epsilon_r}{2}\left[\left(1 + \frac{\epsilon_i^2}{\epsilon_r^2}\right)^{\frac{1}{2}}\right] \pm 1\right\}^{\frac{1}{2}}. \tag{13}$$

The bulk parameters reduce the multiple scattering to a problem of a single equivalent scatterer. (See tables for numerical results).

III. CONCLUSION

Due to the complexity of the problem, only results for the leading term approximation are given here. The multiple scattering problem has been reduced to that of a single scatterer in isolation. Depending on the size parameter of the cloud particles as compared to the wave length of the incident light, either Rayleigh or Mie scattering technique can be used to determine Qext, Qscat, and Qbacs.

With the bulk parameters, we can use Wiscombe's computer code to obtain in short computer time, acceptable numerical results for a medium with a complex relative index of refraction which is an improvement of Bohren [15]. The equivalent medium approach gives naturally the polarizations and the angular distributions of photons which escape the cloud surface.

IV. REFERENCES

1. Aida, M., 1977: Scattering of solar radiation as a function of cloud dimensions and orientation. J. Quant. Spectrosc. Radiat. Transfer, 17, 303–310.

2. Bucher, E. A., 1973: Computer simulation of light pulse propagation for communication through thick clouds. Appl. Opt., 12, 2391–2400.

3. Danielson, R. E., D. R. Moore and H. C. van de Hulst, 1969: The transfer of visible radiation through clouds. J. Atmos. Sci., 26, 10778–1087.

4. Davies, R., 1978: The effect of finite geometry on the three dimensional transfer of solar irradiance in clouds. J. Atmos. Sci., 35, 1712–1725.

5. Davis, J. M., S. K. Cox and T. B. McKee, 1979: Vertical and horizontal distributions of solar absorption in finite clouds. J. Atmos. Sci., 36, 1976–1984.

6. McKee, T. B., and S. K. Cox, 1974: Scattering of visible radiation by finite clouds. J. Atmos. Sci., 31, 1885–1892.

7. Plass, G. N., and G. W. Kattawar, 1968: Monte Carlo calculations of light scattering from clouds. Appl. Opt., 1, 126–130.

8. Van Blerkom, D., 1969: Diffuse reflection from clouds with horizontal inhomogeneities. Astrophys. J., 166, 235–242.

9. Thomason, L. W., and E. P. Krider, 1982: The effects of clouds on the light produced by lightning. J. Atmos. Sci., 39, 2051–2065.

10. Twersky, V., 1977: Coherent scalar field in pair-correlated random distributions of aligned scatterers. J. Math. Phys., 18, 2468–2486.

11. Twersky, V., 1978: Coherent electromagnetic waves in pair-correlated random distributions of aligned scatterers. J. Math. Phys., 19, 215–230.

12. Twersky, V., 1983: Propagation in correlated distributions of large-spaced scatterers. J. Opt. Soc. Am., 73, 313–320.

13. Wiscombe, W. J., 1979. Mie scattering calculations: Advances in technique and fast, vector-speed computer codes, NCAR/TN-140 +STR, National Center for Atmospheric Research, Boulder, Colo.

14. Twersky, V., 1983: Wavelength-dependent refractive and absorptive terms for propagation in small-spaced correlated distributions. J. Opt. Soc. Am., 73, 1562–1567.

15. Twomey, S., and C. F. Bohren, 1980: Simple approximations for calculations of absorption in clouds. J. Atmos. Sci., 37, 2086–2094

V. ACKNOWLEDGMENT

SPHERE SCATTERING PROGRAM

REFMED= 0.1000E+01   REFRE= 0.500000E+00   REFIM= 0.000000E+00
SPHERE RADIUS = 15.000   WAVELENGTH = 0.4880
SIZE PARAMETER= 0.1931E+03

QSCA= 0.205700E+01   QEXT= 0.205700E+01   QBACK= 0.233708E+00

ANGLE	S11	POL	S33	S34
0.00	0.100000E+01	-0.542434E-13	0.100000E+01	0.355165E-14
9.00	0.101441E-03	-0.240238E+00	0.958169E+00	0.155556E+00
18.00	0.809887E-05	-0.679672E+00	-0.337390E-01	-0.732740E+00
27.00	0.151475E-04	0.524835E+00	0.821119E+00	0.224302E+00
36.00	0.468224E-04	-0.431056E+00	0.807469E+00	-0.402721E+00
45.00	0.459087E-04	-0.490314E+00	0.814878E+00	-0.309139E+00
54.00	0.506346E-05	0.860585E-01	0.181473E+00	-0.979623E+00
63.00	0.334143E-04	-0.523285E+00	0.311479E+00	-0.793192E+00
72.00	0.172027E-04	-0.359514E+00	0.371604E+00	-0.855956E+00
81.00	0.258653E-04	0.271532E+00	0.770260E+00	-0.577036E+00
90.00	0.165587E-04	0.313426E-01	0.366425E-01	-0.998837E+00
99.00	0.171157E-04	0.358241E+00	-0.168439E-01	-0.933477E+00
108.00	0.378746E-04	0.464737E-01	0.602422E+00	-0.796824E+00
117.00	0.112762E-04	0.220812E+00	0.704808E+00	-0.674157E+00
126.00	0.355094E-05	0.933251E+00	0.354882E+00	-0.556950E-01
135.00	0.366420E-05	0.734118E+00	-0.677763E+00	-0.413374E-01
144.00	0.132568E-05	0.468369E+00	-0.751838E+00	-0.464080E+00
153.00	0.318972E-05	0.106089E+00	-0.724534E+00	-0.681026E+00
162.00	0.127502E-05	-0.103156E+00	-0.968058E+00	-0.228521E+00
171.00	0.315999E-05	0.264331E+00	-0.962842E+00	-0.553618E-01
180.00	0.590261E-05	-0.236712E-10	-0.100000E+01	0.313251E-10

REFMED= 0.1000E+01   REFRE= 0.132900E+01   REFIM= -0.329000E-06
SPHERE RADIUS = 0.480   WAVELENGTH = 0.8600
SIZE PARAMETER= 0.3507E+01

QSCA= 0.227020E+01   QEXT= 0.227020E+01   QBACK= 0.395052E+00

ANGLE	S11	POL	S33	S34
0.00	0.100000E+01	0.000000E+00	0.100000E+01	0.000000E+00
9.00	0.922420E+00	0.563351E-02	0.999969E+00	0.550071E-02
18.00	0.721860E+00	0.217153E-01	0.999490E+00	0.23414E-01
27.00	0.474803E+00	0.448205E-01	0.997282E+00	0.584701E-01
36.00	0.257936E+00	0.645601E-01	0.990661E+00	0.120096E+00
45.00	0.112784E+00	0.485908E-01	0.973895E+00	0.221737E+00
54.00	0.393514E-01	-0.103252E+00	0.933106E+00	0.344495E+00
63.00	0.135274E-01	-0.498173E+00	0.849299E+00	0.174686E+00
72.00	0.901806E-02	-0.368455E+00	0.791493E+00	-0.487627E+00
81.00	0.945430E-02	0.197477E+00	0.763149E+00	-0.615421E+00
90.00	0.897089E-02	0.567128E+00	0.716241E+00	-0.406650E+00
99.00	0.734485E-02	0.710871E+00	0.699117E+00	-0.767998E-01
108.00	0.561621E-02	0.574907E+00	0.782048E+00	0.240588+00
117.00	0.432635E-02	0.147739E+00	0.941330E+00	0.303432E+00
126.00	0.360259E-02	-0.404131E+00	0.912331E+00	-0.658133E-01
135.00	0.362801E-02	-0.715242E+00	0.365618E+00	-0.595611E+00
144.00	0.468960E-02	-0.586591E+00	-0.393778E+00	-0.707707E+00
153.00	0.682983E-02	-0.314769E+00	-0.829044E+00	-0.462175E+00
162.00	0.953647E-02	-0.124406E+00	-0.970944E+00	-0.204428E+00
171.00	0.118259E-01	-0.284236E-01	-0.998368E+00	-0.495403E-01
180.00	0.127243E-01	-0.877489E-14	-0.100000E+01	-0.102374E-13

REFMED= 0.1000E+01   REFRE= 0.132500E+01   REFIM= -0.124000E-01
SPHERE RADIUS = 100.000   WAVELENGTH = 5.0000
SIZE PARAMETER= .01257E+03

QSCA= 0.226582E+03   QEXT= 0.441131E+01   QBACK= 0.647478E+03

ANGLE	S11	POL	S33	S34
0.00	0.100000E+01	-0.203204E-11	0.100000E+01	-0.425569E-12
9.00	0.310327E-01	-0.998188E+00	-0.531018E-01	-0.283038E-01
18.00	0.716488E-02	-0.981093E+00	0.172648E+00	-0.874618E-01
27.00	0.212244E-02	-0.979733E+00	0.173917E+00	0.993747E-01
36.00	0.142130E-02	-0.956971E+00	0.189002E+00	-0.220192E+00
45.00	0.205954E-03	-0.933447E+00	-0.251622E+00	0.255661E+00
54.00	0.433484E-03	-0.775018E+00	0.601301E+00	0.194380E+00
63.00	0.114486E-03	0.532359E+00	0.662261E+00	-0.527262E+00
72.00	0.413065E-04	0.700565E-01	-0.642471E+00	-0.763101E+00
81.00	0.142686E-03	0.858127E+00	0.958247E-02	0.513349E+00
90.00	0.241022E-03	-0.241273E+00	0.391307E+00	-0.888069E+00
99.00	0.119656E-03	0.655108E+00	0.702851E+00	-0.277189E+00
108.00	0.130419E-02	-0.769865E+00	-0.404472E+00	-0.493669E+00
117.00	0.463362E-02	-0.938115E+00	-0.178932E-02	0.346320E+00
126.00	0.736716E-02	-0.972399E+00	-0.106992E+00	-0.207350E+00
135.00	0.147604E-02	-0.730593E+00	0.300318E+00	0.613224E+00
144.00	0.102740E-02	-0.433089E+00	-0.693427E+00	0.575841E+00
153.00	0.723232E-03	-0.170305E+00	-0.525661E+00	-0.833473E+00
162.00	0.346430E-03	0.373583E+00	-0.920732E+00	-0.112645E+00
171.00	0.734864E-03	-0.750297E+00	-0.597476E+00	0.282979E+00
180.00	0.597202E-02	-0.152443E-11	-0.100000E+01	-0.877348E-12

1990

NASA/ASEE SUMMER FACULTY FELLOWSHIP PROGRAM

MARSHALL SPACE FLIGHT CENTER
THE UNIVERSITY OF ALABAMA

DEVELOPMENT OF SEDS DATA SYSTEM FLIGHT SOFTWARE

Prepared By: William E. Pierson

Academic Rank: Professor

University and   West Virginia Institute of Technology
Department: Electrical Engineering

NASA/MSFC:

    Laboratory: Program Development
    Division: Payload and Orbital Systems Office
    Branch: Orbital Support Systems Group

Contract No: NGT-01-002-099
                         The University of Alabama
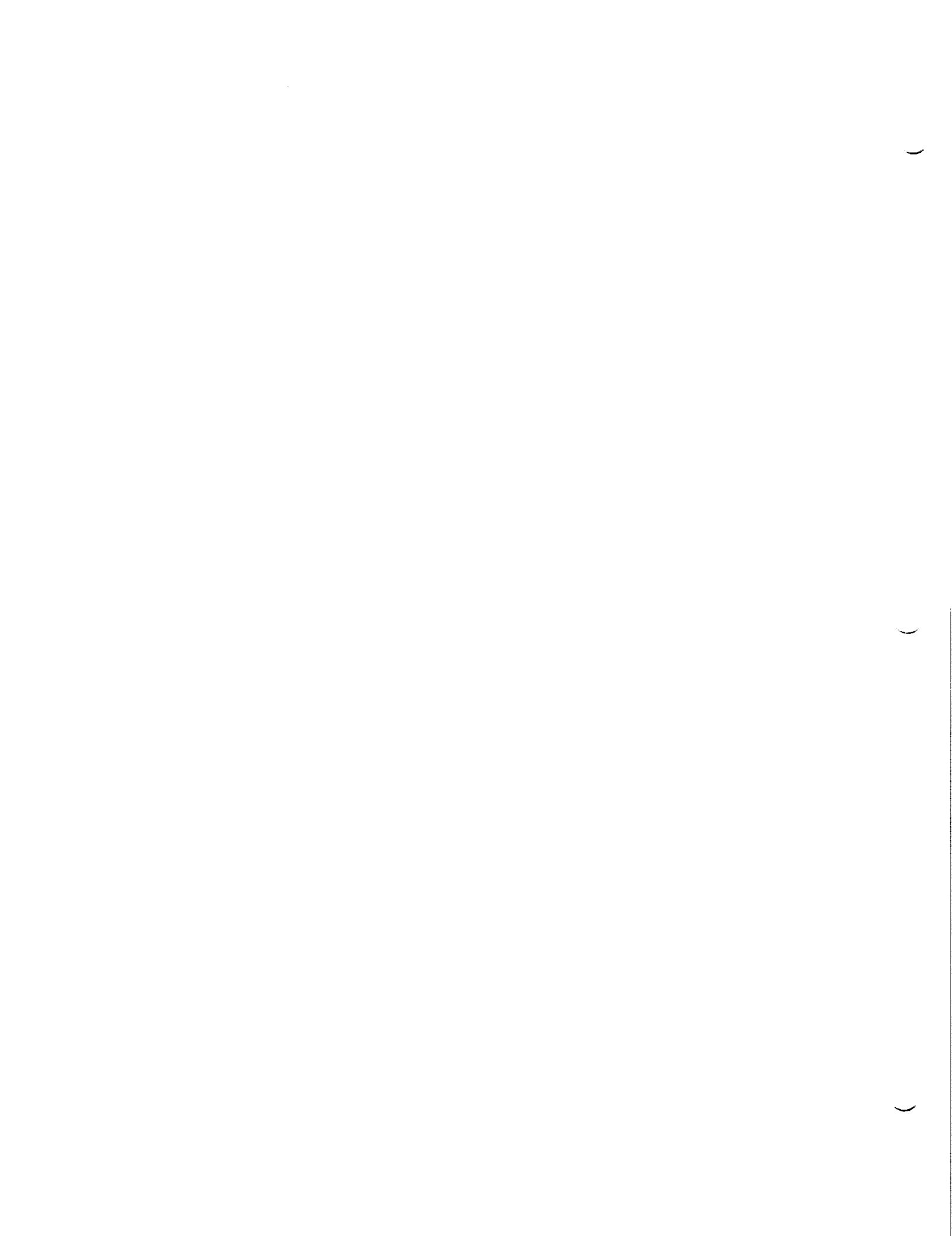
DEVELOPMENT OF SEDS DATA SYSTEM FLIGHT SOFTWARE

July, 1990

Background

The Small Expendable-tether Deployer System (SEDS) is being built for a 1991 flight on a Delta II launch vehicle. SEDS will deploy a 50 lb (23 kg) instrumented satellite as an end mass at the end of 20 km tether. This end mass is being developed by Langley Research Center. The objective of the experiment is to test the SEDS design concept by demonstrating that the system will satisfactorily deploy the full 20 km tether without stopping prematurely, come to a smooth stop on application of the brake, and cut the tether at the proper time after it swings to the vertical. SEDS will also collect data that will be used to test the accuracy of tether dynamics models for this type of deployment. The experiment will last about 1.5 hours (or one orbit) with actual deployment lasting about 85 minutes.

Radar tracking of the experiment is planned. In addition, the SEDS on-board computer system will record, store, and continuously transmit data over the Delta II S-band telemetry channel. The system will count the tether windings as the tether unwinds, log the time of each turn, monitor tether tension, and record various temperature readings. The computer will also control the stepper-motor brake system and activate the tether cutter mechanism.

Two major sections of the flight software were developed under the 1990 NASA/ASEE Summer Faculty Fellowship Program: the data telemetry software and the data collection software. Initial testing of the software under simulated flight conditions was performed, also. These tests used both assembly language routines running on SEDS data systems and C-language routines running on an IBM-PC.

SEDS Hardware

The SEDS data system uses a National Semiconductor NSC800 CMOS microprocessor, which has the same instruction set as the Zilog Z80 microprocessor. The system includes various support circuitry to provide additional resources such as parallel and serial I/O, analog-to-digital conversion, and timers. Also provided is ROM for storing the flight software and RWM in the form of main memory and mass RAM for storing program constants and recording flight data. The system is powered by 28VDC, supplied by the Delta II, and operates at a 2MHz clock rate.

Measurements and Events

Table 1 summarizes the measurements taken by the SEDS computer. In addition to logging the time of each software counter change in mass RAM, the times corresponding to a software turns counter which is an exact multiple of 512 is logged into main memory. This serves as a backup source of information should mass RAM fail and also allows real-time monitoring of the tether length.

Two light-activated switches located 180 apart on the tether spool are used to sense tether unwindings. Using two sensors oriented in this manner allows detection of false triggers due to tether flutter and also provides some hardware redundancy. The software is capable of detecting a sensor failure and will record the failure in a Counter Failure Flag, which is transmitted along with measured data. Should one sensor fail, the software will continue to operate, however, false triggers will no longer be detectable by the SEDS data system.

Although the turns counters are updated asynchronously, the hardware counter values are written to the data storage buffers once every two seconds, and the software counter value is written once every five seconds. All measurements except the tension snapshot are taken and updated continuously for the duration of the flight. The tension snapshot measures and stores the high tension range for 16-second intervals at various stages during the flight. This will allow post-flight frequency analysis to be performed on tension data for critical flight periods. Since the tension is being sampled at 500 sps, frequency components as high as 250Hz can be detected.

Normal tether tension is collected as a one-second average. This tension may originate from the low-scale reading or the high-scale reading, and the measurement will carry two extra bits to indicate the scale from which the tension reading was taken.

TABLE 1
Summary of Data Collected During SEDS Flight

Measurement or Event	Data Length (Bytes)	Stored Length (Bytes)	Buffer Length (Bytes)	Flight Time (sec/min)	Sample Interval (sec)
Main Memory					
Turns Count A	2	1	3000	6000/100	async.
Turns Count B	2	1	3000	6000/100	async.
Software Turns Count	2	1	1200	6000/100	async.
Tension, 1-sec Average	2	2	12000	6000/100	1
High Tension Snapshot	1	1	8000	N/A	.002
Software Count Log Time	3	3	300	6400/107	async.
Temperature Readings	4	4	2400	6000/100	10
Turns Counter Failure	4	4	4	N/A	async.
Mass RAM					
Log Time of Software Counter Update	2	2	128K	8192/136	async.

Each measurement has been allocated sufficient memory to allow at least 6000 seconds (100 minutes) of data to be collected. In the event that the flight should exceed this duration (the data buffers become full), provision has been made to reset buffer pointers and restart the data collection process.

Flight Software

Five major modules to be used by the flight software were developed under the 1990 NASA/ASEE Summer Faculty Program. These modules perform two primary functions:

1) collect and store data from on-board sensors, and
2) continuously transmit data over an RS232 communications port.

A brief description of each module is provided below.

TXINIT: initializes data buffers, mass ram, program constants, and timer and turns counter interrupts

TXMT: foreground program which continuously transmits contents of data buffers and mass RAM using predefined formats

TXMT2: low-level serial output routines which interface with the RS232 port of the SEDS data system

TXINTR: background interrupt service routine for the 2ms timer interrupt; maintains real-time clock and monitors the occurrence of turns counter events; data buffers and mass RAM are updated at the prescribed intervals

TXLOG: routine to place a time stamp into mass RAM whenever the software turns counter changes

The data telemetry software formulates and transmits frames of information organized into two formats: data frames and master frames. One master frame is sent for each 15 data frames transmitted. Master frames allow the data frames to be interpreted by indicating the starting point of the various measurements. In addition, the master frame records the event of a counter failure and allows a real-time display of certain flight data. Data frames contain actual flight measurements.

Software Tests

Several levels of tests were performed to verify correct operation of the data telemetry and collection software. During the first testing phase simulated flight data was generated and stored in an unused area of the SEDS data system's main memory rather than being transmitted over the serial port. The data was later transmitted to an IBM-PC using the PROCOMM communications software and stored on the hard disk for further evaluation. This initial testing phase uncovered several programming errors, which were corrected.

The second phase of testing allowed the SEDS data system to communicate in real time with the IBM-PC over an RS232 communications channel. The test software was written so that sets of frames

from the beginning, middle, or end of the simulated flight could be collected for analysis. The data collected by the PC software was converted to an ASCII (readable) format once data transmission had ceased. Additional errors were uncovered and corrected during the second phase of the software testing. The software written for the IBM-PC to perform the second phase of testing was written using the C programming language (Turbo C by Borland, Inc.) and C Async Manager, a interrupt-driven set of PC communications functions by Blaise Computing, Inc.

The final tesing phase tested both the data collection software and the data telemetry software running under simulated flight conditions. In order to perform realistic testing of the combined data collection and data transmission routines, signals emulating turns counter inputs were generated using a second prototype SEDS data system (serial number 1). This second system was programmed to generate well-behaved turns counter inputs for both hardware counters occurring once every 200ms. Test data was collected using an IBM-PC and revealed several programming errors which have been corrected.

Summary and Recommendations

The original objectives outlined for the NASA/ASEE Summer Faculty Program have been achieved. That is, software to collect and transmit SEDS flight data has been written and tested to the extent available resources will allow. Additional testing will have to be performed over the next few months to further assure that the software operates as intended. As the software now stands, relatively few additions are needed before the entire set of flight software is complete. Specifically, modules need to be added which will initiate the collection of tension snapshot data, activate the tether brake, and activate the tether cutter. Finally, the complete set of flight software needs to be tested in near-flight conditions to verify proper operation and results.

References

1. Harrison, J. K. and Rupp, C. C., "Small Expendable-Tether Deployer Systems (SEDS) Development Status", Paper Presented at the AIAA Third International Conference, May 1989.

2. "SEDS Data System Functional Requirements", Energy Sciences Laboratories, Inc. and Program Development, MSFC, May 1988.

3. SEDS Data System Data Collection and Telemetry Software", Final Report, NASA/ASEE 1990 Summer Faculty Fellowship Program, Contract No. NGT-01-002-099, Marshall Space Flight Center, Huntsville, AL.

1990

NASA/ASEE SUMMER FACULTY FELLOWSHIP PROGRAM

MARSHALL SPACE FLIGHT CENTER
THE UNIVERSITY OF ALABAMA

EMERGENCY EGRESS REQUIREMENTS
FOR
SPACE STATION FREEDOM

Prepared By: Paul S. Ray

Academic Rank: Assistant Professor

University and   The University of Alabama
Department: Industrial Engineering
                                Tuscaloosa, Alabama

NASA/MSFC:

        Division   Systems Safety Engineering
        Branch: Project Safety Engineering

MSFC Colleague: Mark G. D'Agostino
                                Richard Siler

Contract No: NGT-01-002-099
                                The University of Alabama
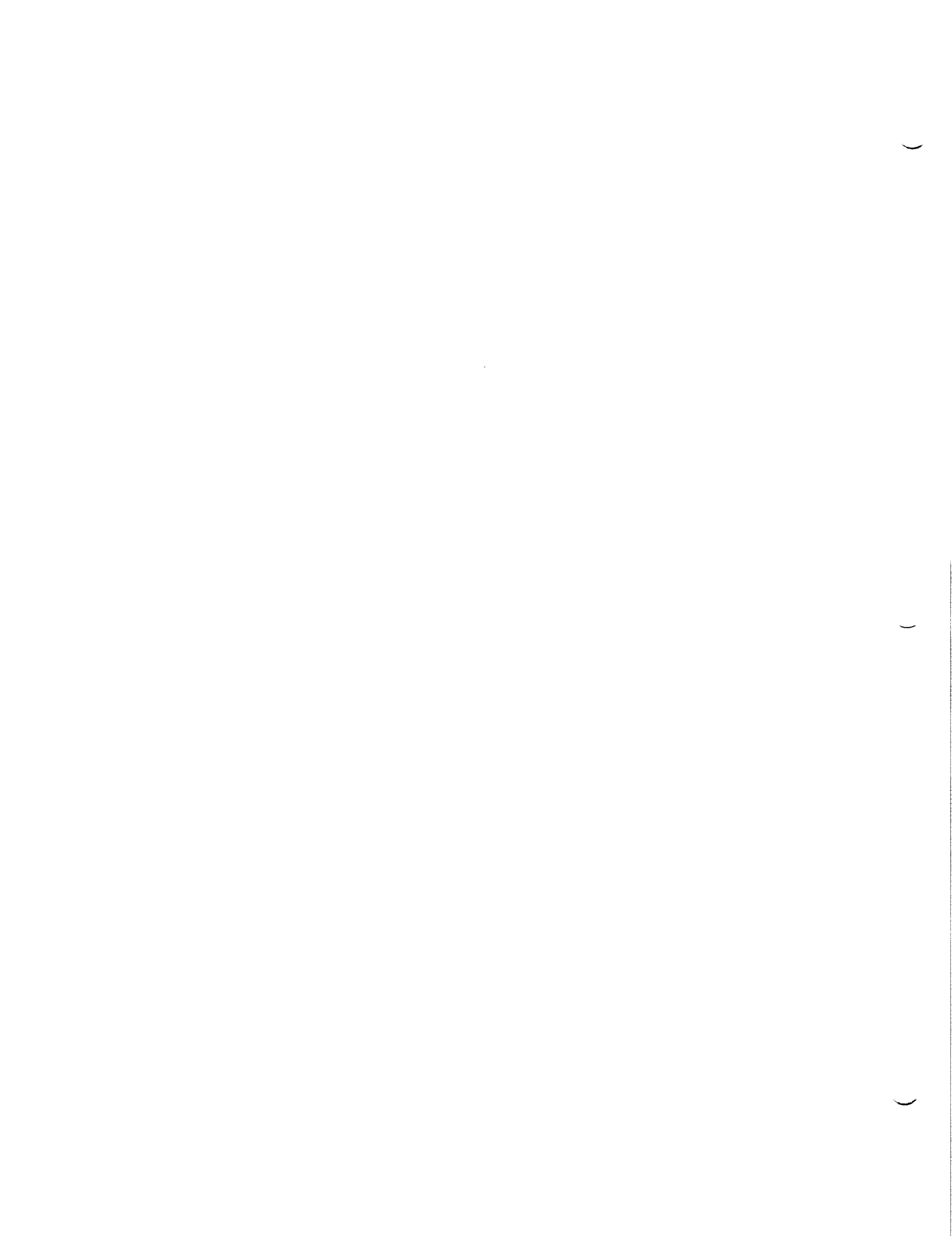
Introduction

There is a real concern regarding the requirements for safe emergency egress from the Space Station Freedom. The possible causes of emergency are (a) depressurization due to breach of the station hull by space debris, meteoroids, seal failure, or vent failure, (b) chemical toxicity, and (c) a large fire.

The original considerations including nodes at the end of international modules, egress aids, zoning of equipment and clear isles have been discarded in favor of the current specification requiring time of egress not to exceed three minutes. However, the tasks required for safe emergency egress in three minutes were not fully analyzed and the requirement has been recently used to 'avoid' design instead of making it safer.

Objectives

The objectives of the current study were to (a) Identify the tasks required to be performed in emergencies, (b) establish time required to perform these tasks, and (c) review the human-equipment interface in emergencies.

Assumptions

The study has been based on the following assumptions that resulted from previous studies:

1. Space Station Configuration established in PDR/5-4/GRFX-07/17/90.

2. Hatch Operation is manual.

3. All hatches remain open during normal operation.

4. Crew members can maintain a translation speed of one meter per second in the induced airflow caused by a 4 inch diameter hole in the station hull.

5. Probable translation speed range is from 0.75 to 2.0 ft/second depending on translation path restrictions. These values are based on the Skylab experience and empirical data obtained from the Astronauts.

6. Aisle passages are unobstructed at the onset of an emergency exit.

Emergency Egress Tasks

The emergency egress tasks consist of:

1. Perceiving the emergency warning
2. Recognizing the voice synthesized advice
3. Translating to safe area
4. Closing the hatches on both sides of the
   affected element

Assessment of the Emergency Egress Times

Emergency egress times were estimated for three unfavorable
situations. Each scenario begins with all crew members located
at the Habitation (Hab) module, while an emergency occurs in (a)
Node #3, (b) at the mid-length, and (c) at one end of the Hab.
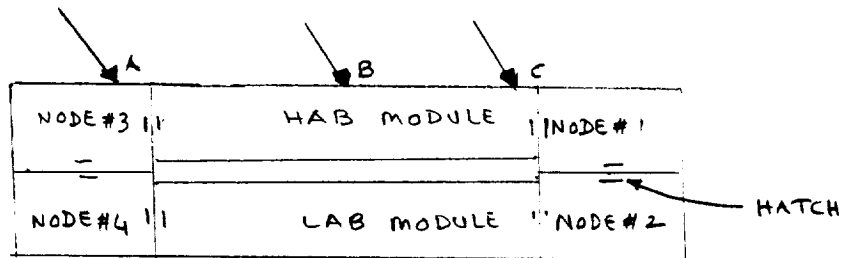
Sketch of the Space Station Configuration

The estimated times for the three cases were:

Case	Egress time (sec)
A	166
B	102
C	194

In case 'C', egress may be accomplished in 178 seconds if the
hatch between Node #1 and Node #2 is closed instead of the one
between Node #1 and the Hab module. But in this case Node #1
will be lost in addition to the Hab module.

Human-Equipment Interfaces in Emergencies

The emergency interface equipment identified are:

1. Hatch
2. Hatch Cover Plate Handle
3. Hand Crank for securing hatch cover plate
4. Pressure Gauge
5. Mobility Aids
6. Foot Restraints

Appropriate design specifications for these elements have been suggested to insure improved human performance of the emergency egress tasks. These specifications relate to human factors considerations and operational safety. The principal specifications are given below:

1. Hatch: The railings of the hatch operating mechanism should be enclosed.

2. Handle: The handle should be designed for power grip of a gloved hand and be of circular cross section. Recommended dimensions:
   Diameter = 1.5 inches
   Length = 5.5 inches
   Clearance = 2.0 inches

3. Hand Crank:
   Crank Arm = 8.0 inches
   Crank Handle:
   Diameter = 1.5 inches
   Length = 2.0 inches
   Operation at both sides of the Cover Plate should be decoupled

4. Pressure Gauge: Recommended Specifications:
   Graduation Range = 1-15 psia
   Graduation Interval = 1 psia
   Graduation Mark = 5 psia
   Conform to Specification No. MIL-M-18012B

5. Mobility Aids: Fixed Handrails and Kick Surfaces should be provided at suitable locations and for Hatch operation in emergencies.

6. Restraints: Foot Restraints are to be provided for Hatch operation in emergencies.
   Recommended Dimensions :
   Length = 8.25 - 11.5 inches
   Breadth = 4.5 inches
   Adjustable to fit different foot widths
   Portable, and
   Lockable on the floor

Summary

The study observations are summarized as follows:

1. A fixed time value specified for egress has shifted focus from the basic requirements of safe egress.

2. In some situations the crew members may not be able to complete the emergency egress tasks in three minutes without sacrificing more than half of the station.

3. Increased focus should be given to the Human Factors aspects of the station design.

Recommendations

1. Emergency Egress requirements for the Space Station should be directly linked to the following basic needs of safe egress before:

   A. Incapacitation due to low ambient pressure,
   B. Contamination from toxic chemicals, or
   C. Suffocation from smoke caused by fire.

2. A Flashing Display in Grid system should be evaluated as an alternative to the Voice Synthesizer for directing crew members in emergencies. This alternative appears to have some potential for reducing egress time and will also eliminate the masking effect of noise on the message.

3. Suggested specifications for emergency equipment should be considered for inclusion in the design of the Space Station.

4. The following procedures and design considerations should be finalized at an early date:

   A. Appropriate locations for suitable mobility aids and Restraints.
   B. Protective clothing and their stowage locations.
   C. Egress procedures and aids for single node attachments (PLM, ESA, JEM).
   D. Emergency decontamination procedures and facilities.

5. Ability of the crew members to perform emergency egress tasks should be experimentally verified under micro-gravity conditions for different sizes of hull penetration i.e. different induced air flow rates.

1990

NASA/ASEE SUMMER FACULTY FELLOWSHIP PROGRAM

MARSHALL SPACE FLIGHT CENTER
THE UNIVERSITY OF ALABAMA

The Effect of Friction
in the Hold Down Post Spherical Bearings
on Hold Down Post Loads

Prepared By: James A. Richardson

Academic Rank: Assistant Professor

University and   University of Alabama
Department: Civil Engineering

NASA/MSFC:

    Laboratory: Structures and Dynamics
    Division: Structural Dynamics
    Branch: Systems Response

MSFC Colleague: Dr. John Townsend
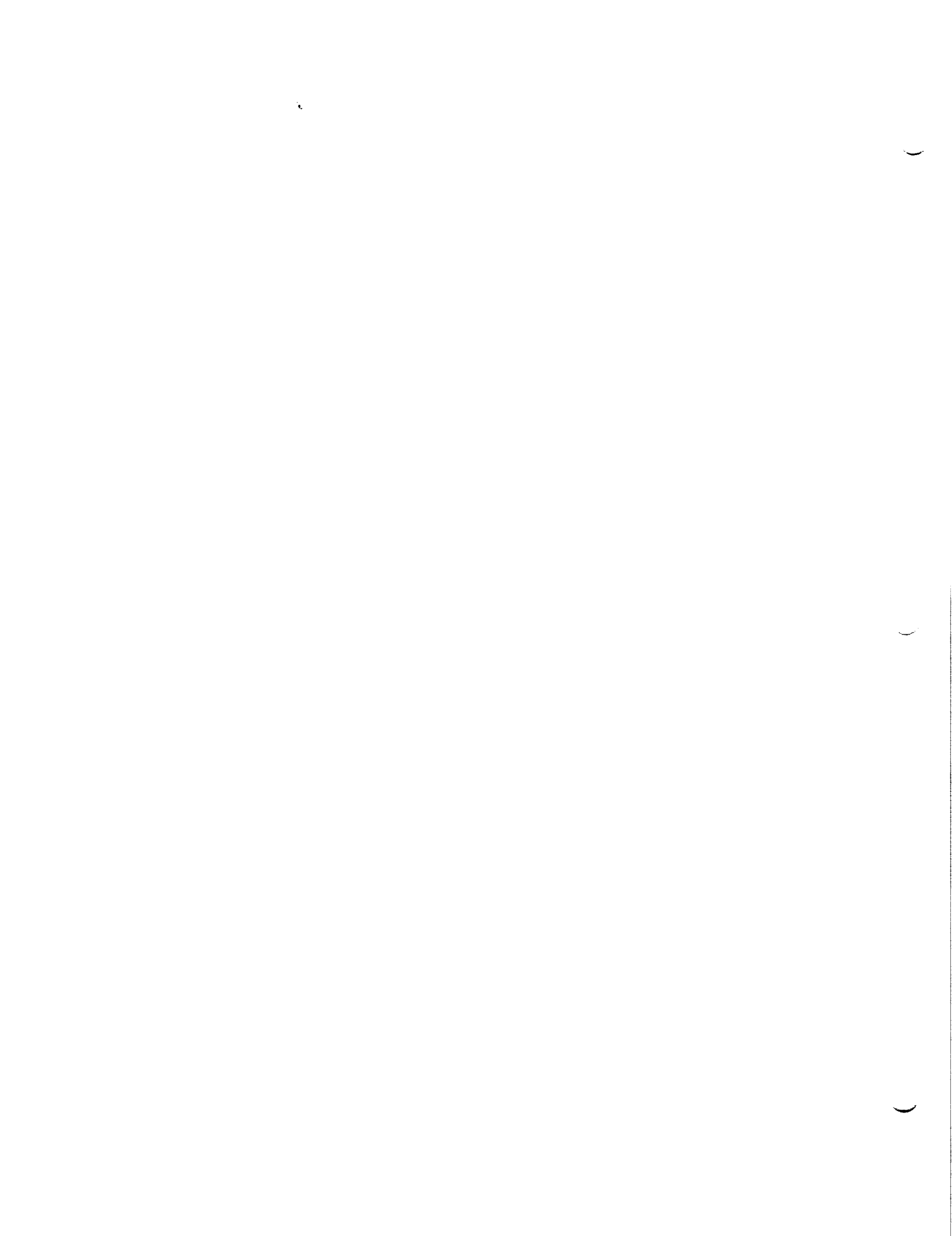
Abstract

The effect of friction at the connection of the SRB aft skirt and the MLP hold down posts was analyzed. A simplified model of the shuttle response during the SSME buildup was constructed. The model included the effect of stick-slip friction for the rotation of the skirt about the spherical bearing. Current finite element models assume the joint is completely frictionless in rotation and therefore no moment is transferred between the skirt and the hold down posts. The model was partially verified against test data and preliminary parameter studies were performed. The parameter studies indicated the coefficient of friction strongly influenced the moment on the hold down posts. The coefficient of friction had little effect on the hold down post vertical loads, however. Further calibration of the model is necessary before the effect of friction on the hold down post horizontal loads can be analyzed.

Background

During tests of the aft skirt, the skirt has consistently failed to reach the required 140% of the design loads. The maximum design loads on the skirt occur when the shuttle is on the mobile launch platform (MLP) and the space shuttle main engine (SSME) is developing full thrust (SSME buildup).

There is uncertainty about the loads on the skirt during SSME buildup. The hold down posts (HDP's) have been instrumented with strain gages and measurements have been recorded for many shuttle launches. An anomaly was observed concerning the horizontal (Z-direction) HDP loads. The total Z-direction load on the HDP's was apparently in the direction opposite to the SSME thrust, for part of the buildup period. The existence of friction at the skirt/HDP interface would cause a bending moment to be applied to the HDP, however, and may account for the anomaly.

A model of the shuttle response during SSME buildup was developed in this project which included the effects of friction at the interface between the SRB aft skirts and the MLP hold down posts. Specifically, friction between the aft skirt shoe as it rotates about the HDP spherical bearing was modeled (see Figure 1). The purpose of this project was to analyze the effects of friction at this interface on HDP loads. These loads are important because the HDP loads are equal and opposite to the loads on the aft skirt, a critical component in the shuttle.

Simplified Model of Shuttle During Buildup

The response of the shuttle during SSME buildup was analyzed with as simple a model as possible. Only the response of the shuttle in the X-Z plane was modeled, (see Figure 2). The model included the equivalent stiffness, mass, and damping properties of the shuttle, as described below, and considered gravity and thrust loads. The incremental equation of motion for the system was solved using a step-by-step integration procedure. A FORTRAN computer program was written to perform the integration and other calculations.

The stiffness of the MLP and HDP's was modeled using boundary element springs. This was thought justified due to the much greater stiffnesses of the MLP/HDP compared to the aft skirt. With hindsight, these springs are not adequate because the actual MLP/HDP stiffnesses are coupled; e.g. a horizontal HDP deflection causes a HDP bending moment. An improved model will include the appropriate coupling terms.

The aft skirt stiffness was calculated by the following procedure. A NASTRAN finite element model (FEM) of the skirt was released at all degrees of freedom (DOF's) except the nine DOF's needed for the 2-D model. A unit displacement was applied at one of these nine DOF's and the resisting forces at the nine DOF's were calculated by the NASTRAN model. These forces represented one column of the aft skirt stiffness matrix. The procedure was repeated eight times to yield the full 9 X 9 skirt stiffness matrix.

Initial versions of the model proved to be too stiff compared to measurements because the model did not consider the relative rotation between the bottom of the SRB and the top of the aft skirt. A rotationally soft element, of unit length, was attached to the top of the aft skirt to account for the "free play" in the skirt/SRB connection. This element had the SRB axial and shear stiffness, but a soft rotational stiffness. There were no coupling terms in this element's stiffness matrix in order to prevent large horizontal deflections due to the artificially soft rotational stiffness. The stiffness of the SRBs was modeled with a normal beam element.

The mass distribution in the axial (X) direction of each shuttle component was used to calculate the center of mass (C.M.) of the shuttle. The rotational inertia of the shuttle about the horizontal axis through the C.M. was then calculated. Only two lumped masses were used in the model: the translational mass at the C.M. and the rotational inertia.

Viscous damping equal to 1% of critical was applied at the two mass DOF's described above. Coulomb damping due to sliding friction at the skirt/HDP interface was also accounted for. The model checked to see if slip occurred at the interface by comparing the resisting force to the load on the interface. The force resisting slip was calculated by multiplying the normal force times the coefficient of static friction. If slip occurred for a particular time step, then the elastic stiffness of the HDP for that DOF was set equal to zero, and the Coulomb damping force was calculated. Similarly, if no slip occurred, the elastic stiffness of the HDP was included, and the Coulomb damping force was set equal to zero.

Results

The model was calibrated by comparing its predictions to test results and launch data. Unfortunately, the error modeling the MLP/HDP's (described above) was not observed until the final week of the project. Therefore, the anticipated parameter studies were not finished. Initial parameter studies, however, indicated that the coefficient of friction has a large effect on the bending moment loads on the HDP's. Slip occurred for values of static coefficient of friction up to 0.20. The friction coefficient had practically no effect on the horizontal HDP loads. This was contrary to expectations, however, and was thought to be due to neglecting the coupling terms of the MLP/HDP stiffness.

Conclusions

A simplified model of the shuttle response during SSME buildup was constructed. The model demonstrated that interface friction forces can cause large moments to develop between the SRB aft skirt and the MLP HDP's. Refinement of the model should improve our understanding of the role of friction on critical aft skirt loads.
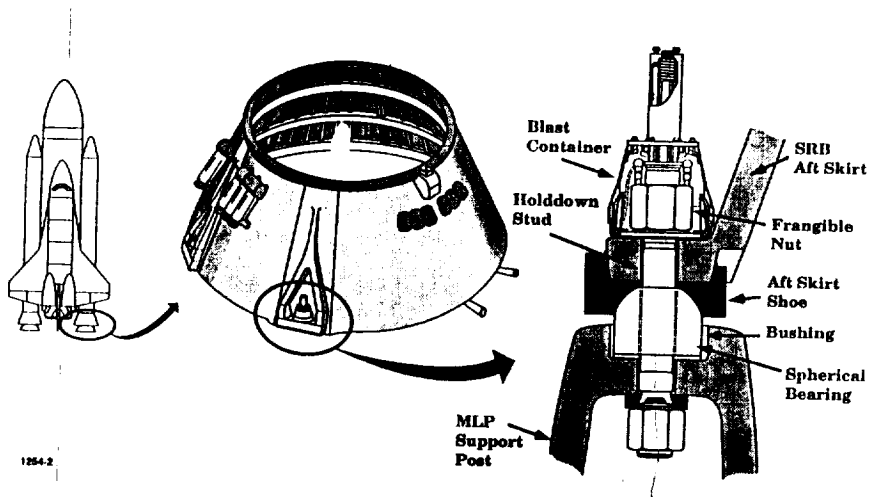
Figure 1. SRB Aft Skirt/MCP HDP Connection
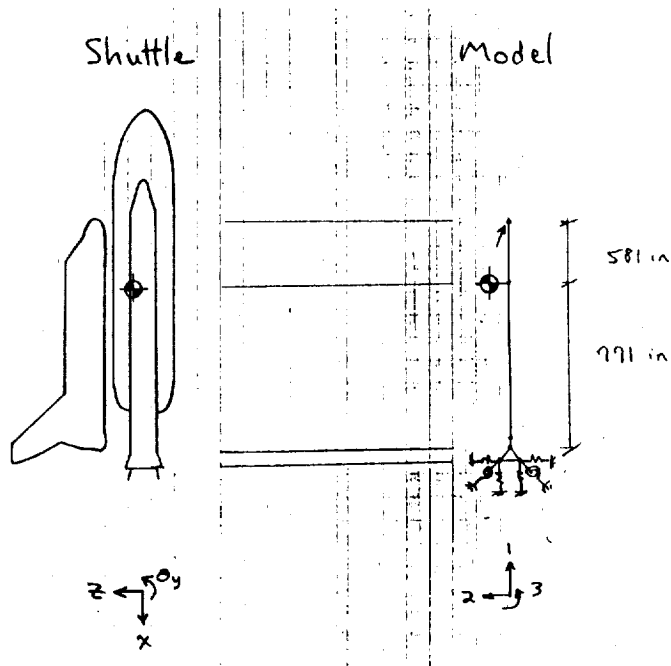
Figure 2. Simplified Model of Shuttle

1990

NASA/ASEE SUMMER FACULTY FELLOWSHIP PROGRAM

MARSHALL SPACE FLIGHT CENTER
THE UNIVERSITY OF ALABAMA

CHARACTERIZATION OF SPACE STATION MULTILAYER INSULATION DAMAGE DUE TO HYPERVELOCITY SPACE DEBRIS IMPACT

Prepared By:	William Keith Rule
Academic Rank:	Assistant Professor
University and Department:	University of Alabama - Tuscaloosa Engineering Mechanics
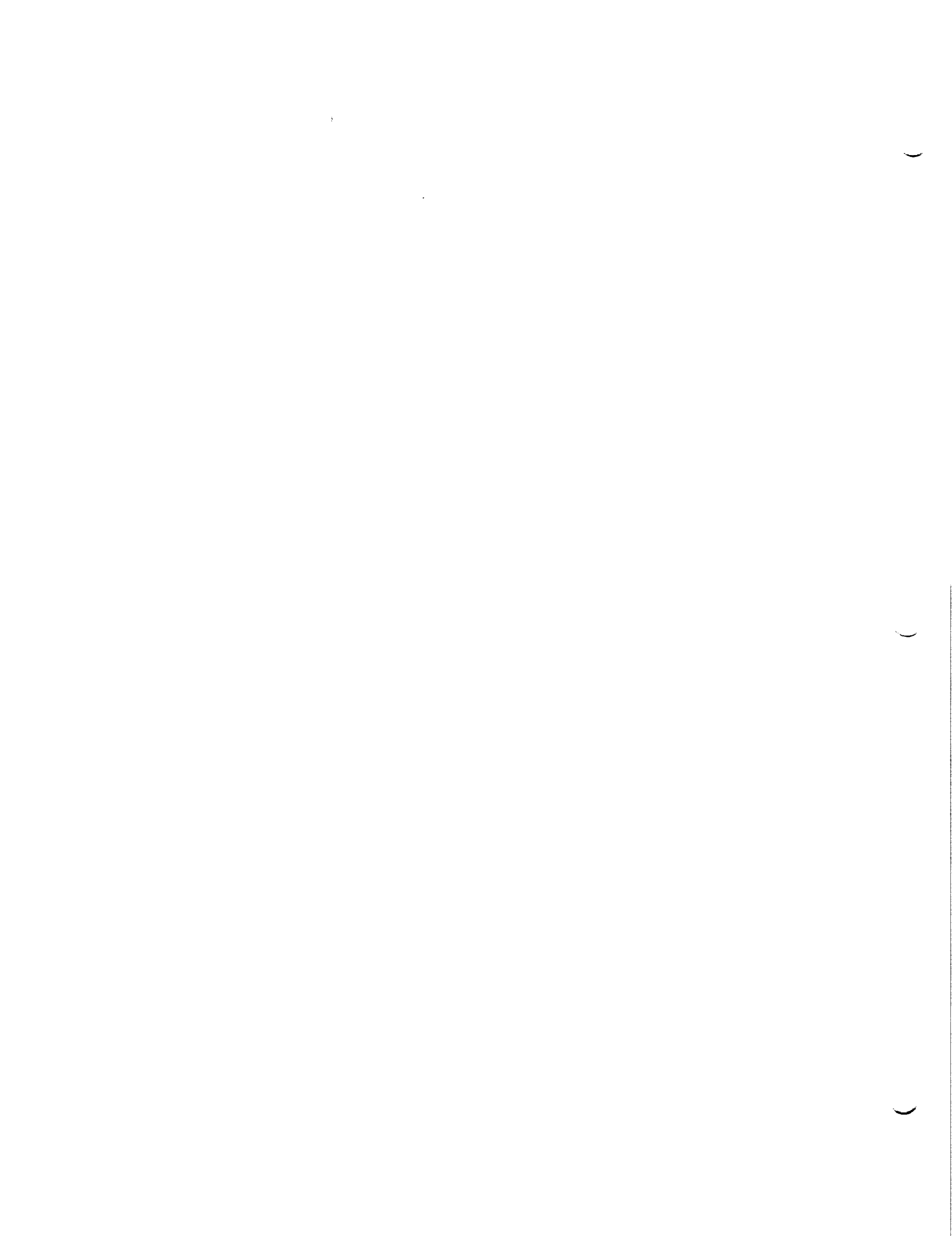
During the course of work this summer four main tasks were accomplished which are discussed in the following sections. The first three tasks were related to the goal of measuring the degradation of the insulating capabilities of Space Station multilayer insulation (MLI) due to simulated space debris impacts at hypervelocities. The last task was associated with critically reviewing a Boeing document on the fracture characteristics of the Space Station pressure wall when subjected to a simulated hypervelocity space debris impact.

TASK 1 - Write Thermal Test Procedure for Impact Damaged MLI Specimens

To determine the effects of impact damage to MLI, damaged samples of MLI will be attached (starting 8/20/90) to a test fixture built by Boeing and tested in the MSFC Sunspot 1 Thermal Vacuum Chamber. The Boeing fixture, which is similar to the Space Station wall configuration, was built to test undamaged MLI specimens. Before any damaged MLI testing could be performed, a test procedure had to be written by the author and approved.

Writing the test procedure involved three steps: first the fabrication and use of the Boeing fixture had to be studied, then the Boeing test procedure documents had to be comprehended, and finally the operating characteristics of the Sunspot Chamber had to be understood. It was decided to write the damaged MLI test procedure in a form as close as possible to that of the Boeing undamaged MLI test plan. This allowed the test plan to be written and reviewed quickly.

The related Boeing documents and test fixture drawings, the damaged MLI test plan, and all other information related to these MLI tests have been gathered together by the author in the form of a data book for future reference.

TASK 2 - Damaged MLI Specimen Preparation

Prior to thermal testing, the MLI samples were impacted with hypervelocity particles using the MSFC light gas gun to simulate a space debris impact. It had to be determined how to prepare these samples for attachment to the Boeing fixture and insertion in the Sunspot facility. Straight from the gas gun the impacted samples consisted 12" by 12" blankets of damaged MLI covered with gun soot. The damage typically takes the form of an approximately centrally located, 2" to 4" diameter, roughly circular hole.

Firstly, it was decided to trim the specimen to the form of a circular disk to preserve radial symmetry. It was also decided to make the disks as large as possible to maximize the distance between the MLI damage and the interface between the specimen and the test fixture and thereby minimize edge effects. Thus, the final form selected for the specimens is a 12" diameter disk. The MLI specimens will be taped over a 10" diameter hole cut in the MLI blanket of the Boeing test fixture during thermal testing.

Gun soot had to be removed from the specimens for two reasons. The pump-down vacuum system of Sunspot requires reasonably clean specimens in order to function properly. Also, the gun soot may significantly affect the thermal performance of the specimens. Impacted MLI in space would of course not be contaminated with gun soot. EH52 Branch developed a cleaning procedure where the MLI was placed between two stainless steel screens (for protection) and then carefully cleaned with a soft brush using freon as a solvent.

TASK 3 - Develop Computer Program to Simulate MLI Thermal Tests

The temperature measurements obtained during the thermal testing will have to be reduced down to the form of some effective measure of MLI damage such as an equivalent hole diameter. Development of a microcomputer program

by the author for this purpose was initiated this summer. The computer program mathematically models the thermal test set up. Parameters in the model (such as the size of the hole in the MLI) can be varied until the calculated results agree with those measured. Having characterized the MLI damage, then heat transfer predictions can be made with respect to the Space Station configuration on orbit.

The computer program contains a radially-symmetric finite difference model of the pressure wall, the bumper, and all MLI layers. The program iterates until the *net* heat flux into each layer is zero (steady state) and the heat flux across the plane between each layer is equal to the heat flux supplied by the test fixture (conservation of energy). Currently, the program can accurately reproduce the experimental results obtained by Boeing for the undamaged MLI case. Work is continuing to prepare for treating the damaged MLI thermal test data.

TASK 4 - Review Boeing Document on Stressed Plate Hypervelocity Impact Testing

A significant amount of time was spent this summer by the author to review a Boeing document describing hypervelocity impact testing performed by Boeing on biaxially stressed plates. For simplicity and to control costs, most hypervelocity impact testing that has been done as part of the Space Station program has been done using unstressed plates. However, the Space Station pressure wall will be subjected to relatively high biaxial stresses, and so Boeing has done some biaxially stressed plate tests using the MSFC light gas gun.
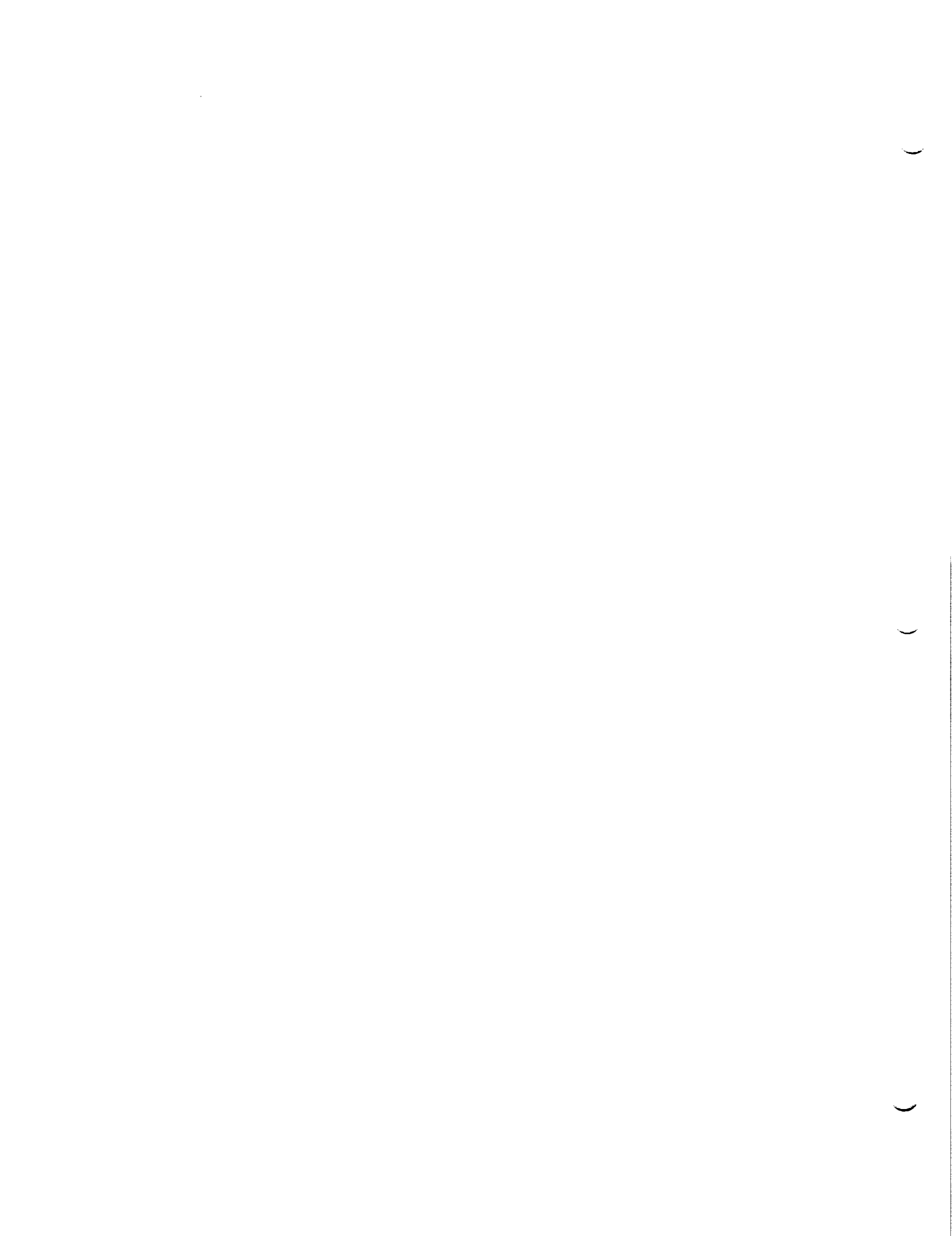
N91-19008

NASA/ASEE SUMMER FACULTY FELLOWSHIP PROGRAM

MARSHALL SPACE FLIGHT CENTER
THE UNIVERSITY OF ALABAMA

VALIDATION OF THE SPACE SHUTTLE MAIN ENGINE

STEADY STATE PERFORMANCE MODEL

Prepared By: L. Michael Santi

Academic Rank: Associate Professor

University and   Christian Brothers University
Department: Mechanical Engineering

NASA/MSFC

        Laboratory: Propulsion
        Division: Propulsion Systems
        Branch: Performance Analysis

MSFC Colleague: Mr. John Butas
                           Dr. Charles Schafer

Contract No: NGT-01-002-099
                           The University of Alabama
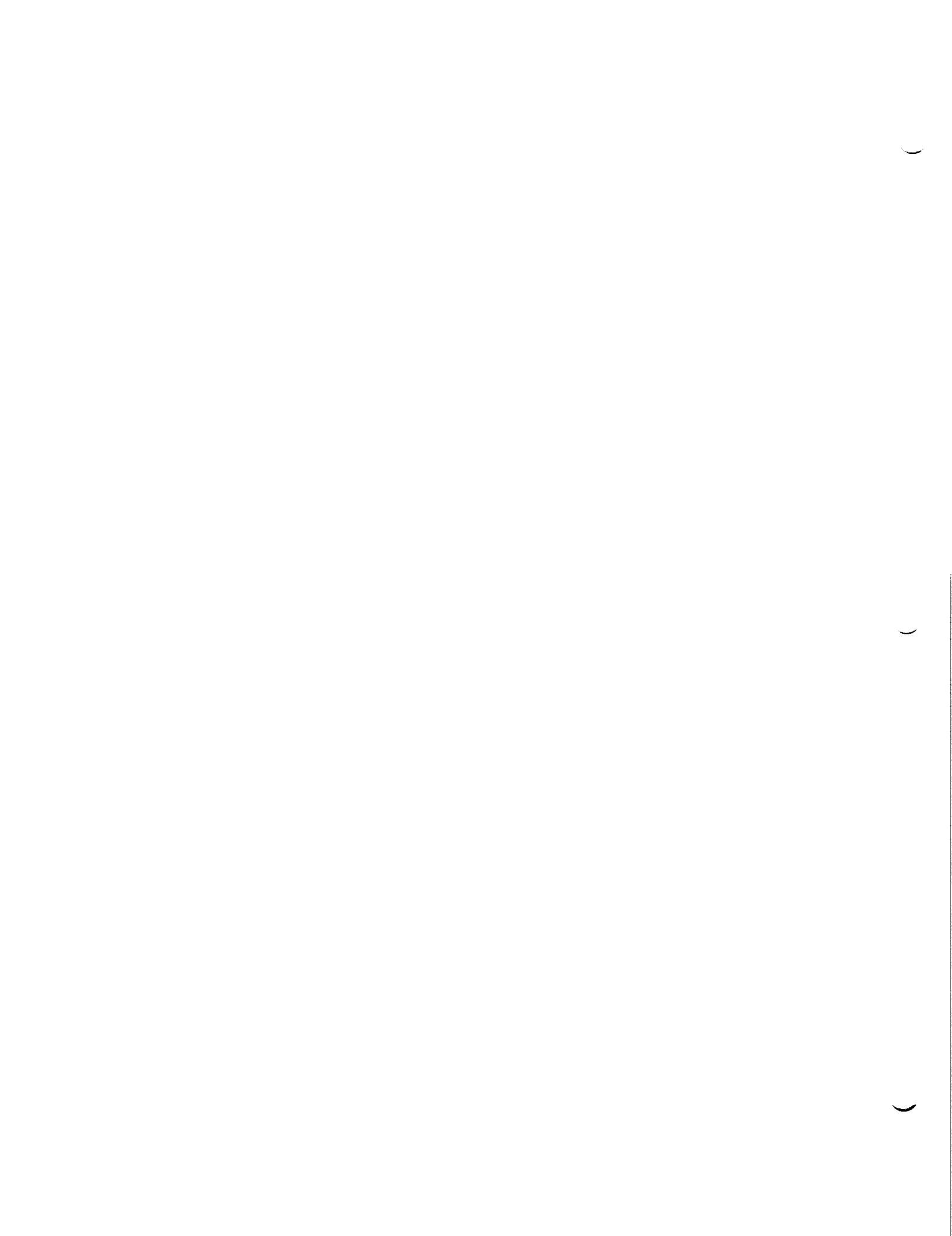
OBJECTIVES

The primary objective of this study was to present methods for validating predictions of Rocketdyne's most current version of the Space Shuttle Main Engine (SSME) Power Balance Model (PBM) with respect to physical relations governing flow systems. This required the development and implementation of postprocessors to check results of PBM computations for satisfaction of conservation relations. A cursory uncertainty analysis of PBM predictions with respect to mass and energy balances was performed. In addition, an effort to identify the empirical relations and physical assumptions within PBM which impact the ability of the model to attain rigorous balance was begun.

BACKGROUND

The SSME Power Balance Model simulates the main stage averaged operating conditions of the space shuttle main engine. It integrates test stand data and flight experience with theoretical flow simulation to predict SSME performance characteristics during ground test and flight operations. The model is composed of four basic subprograms. The power balance subprogram provides quasi-theoretical prediction of nominal and/or off-nominal engine performance characteristics. The data reduction subprogram integrates test data with theoretical simulation to refine efficiencies and other hardware performance parameters used in the prediction of engine operational characteristics. The base balance subprogram calibrates data reduction predictions by adjusting nine performance variables in order to accurately simulate engine operation during a specific time slice. The rated portion of the program uses adjusted engine performance characteristics at a specific time slice as a basis for predicting performance at other operating conditions.

Examination of PBM source code reveals a large number of "hard coded" empiricisms involving flow rates, pressures, and temperatures as a function of overall system performance parameters such as thrust level. These empiricisms do not have a clear physical basis in a flow network analysis. In addition, there are computational inconsistencies between model subprograms. Combined with complex logical sequencing and inadequate documentation, these conditions reduce the level of confidence in the integrity of performance predictions returned by PBM. The object of this effort was to perform fundamental physical analyses on various engine subsystems in order to quantify flow and energy imbalances associated with PBM calculations. The method used to determine subsystem imbalances is described in the next section.

PROCEDURE

In order to check for adherence to fundamental mass and energy conservation principles, the SSME was divided into four subsystems for purposes of analysis. These subsystems are described below.

1. LPFTP - low pressure fuel turbopump system composed of
   LPFT - low pressure fuel turbine
   LPFP - low pressure fuel pump

2. LPOTP - low pressure oxygen turbopump system composed of
   LPOT - low pressure oxygen turbine
   LPOP - low pressure oxygen pump

3. HPFTP+FPB+HGM - high pressure fuel system composed of
   HPFT - high pressure fuel turbine
   HPFP - high pressure fuel pump
   FPB - fuel preburner
   HGM - fuel side hot gas manifold

4. HPOTP+OPB+HGM - high pressure oxygen system composed of
   HPOT - high pressure oxygen turbine
   HPOP - high pressure oxygen pump
   OPB - oxygen preburner
   HGM - oxygen side hot gas manifold
   HE   - heat exchanger
   POGO - POGO accumulator

For each subsystem, the type material, mass flow rate, pressure, and temperature of each inflow/outflow was identified by position in the PBM output array. A postprocessor named VOLUME was developed to read this information and conduct standard control volume analyses on each subsystem to determine both mass and energy imbalances. VOLUME was constructed to be generic in nature so that the user could easily redefine the subsystem for analysis. This is accomplished by changing the PBM output array locations which are accessed by the VOLUME input file. These locations contain the flow rates, pressures, and temperatures for the subsystem inflows and outflows.

To guarantee the validity of VOLUME computed imbalances, it was necessary to incorporate accurate thermodynamic property relations to establish the specific energy level of each subsystem inflow/outflow. By special permission, the proprietary PROP05 property package developed by Pratt & Whitney was used to provide accurate relations between pressure, temperature, and the other thermodynamic properties for hydrogen, oxygen, steam, and hot gas mixtures. Calls to appropriate PROP05 routines were included within the VOLUME code. Results of mass and energy balance analyses conducted using the VOLUME program are presented in the next section.

RESULTS

Results of flow and energy balance analyses, conducted on the above described subsystems, are summarized in Table 1 for each of seven power level excursions ranging from 65% of engine rated power level (RPL) to 109% RPL. Subsystem imbalances in mass flow rate (DW) and energy flow rate (DE) are displayed. Energy flow rate imbalances are reported in both heat rate units (Btu/s) and power units (hp). A negative sign indicates that more of the flow exited the subsystem than entered, while a positive entry indicates the reverse. A number other than zero reflects a conservation law imbalance which requires reconciliation.

The data in Table 1 indicates a high degree of mass flow balance at all power levels. The worst case mass imbalance, which occurred in the high pressure oxygen subsystem at low RPL, was only a tiny fraction of the overall subsystem flow. Predicted power imbalances were, however, disturbingly large for both high pressure subsystems. Predicted high pressure fuel subsystem imbalances were exceptionally large at all thrust levels as displayed in Table 1. In all cases, the high pressure subsystem imbalances were negative, indicating that more energy exited the system than entered. This is of course a classical First Law violation.

A better indication of the relative magnitudes of the power imbalances is displayed in Figure 1. Each subsystem power imbalance was normalized by the required subsystem pump power. Both high pressure subsystems displayed significant proportional imbalances which decreased with increasing RPL operation and range from over 0.40 at 65% RPL to over 0.25 at 109% RPL.

In order to better determine the sources of power imbalance imposed by PBM predictions within the high pressure subsystems, component energy studies were performed with results displayed in Figures 2 through 4. As shown in Figure 2, significant discrepancy between pump power requirement and turbine delivery was observed at all power levels in the high pressure fuel subsystem. In addition, both preburners were significantly imbalanced as exhibited in Figure 3, with the fuel side imbalance again larger. The combined fuel side turbopump subsystem also displayed a larger proportional imbalance than the oxygen turbopump subsystem as displayed in Figure 4.

Because of the magnitudes of the imbalances on the fuel side, and to better understand the limitations of the study due to property and and modeling restrictions, an uncertainty analysis was performed on both the HPFP and HPFT power predictions. Error bands of approximately +/-3% for the pump and +/-10% for the turbine were estimated. The turbine side uncertainty estimate was larger due to combustion model and real gas mixture uncertainties. Fuel side power levels with uncertainty bands are plotted in Figure 5. The error banded power curves do not overlap which indicates substantial PBM computational bias as opposed to physical data and

modeling limitations.

A comparison of PBM subprogram predictions for the high pressure fuel and oxygen subsystems is exhibited in Figure 6. Predictions with significant proportional imbalance were returned by each of the data reduction, base balance, and power balance subprograms as displayed in Figure 6. The theoretical power balance subprogram returned the most imbalanced subsystem predictions in each case, although only marginally larger than data reduction and base balance predictions. In comparing fuel and oxygen side predictions, the turbopump proportional imbalances indicated by the cross-hatched columns were significantly larger on the fuel side than on the oxygen side. This is particularly disturbing since it suggests multiple sources causing the predicted imbalances.

CONCLUSIONS AND RECOMMENDATIONS

Power Balance Model predictions do not satisfy energy conservation requirements adequately. Because of failure to satisfy this fundamental physical requirement, the accuracy of mass flow rate, temperature, and pressure predictions are suspect throughout the engine system.

The following recommendations are made.

1.
Upgrade PBM to adequately account for the flow physics in addition to integrating test and flight data.

2.
Develop an independent data reconciliation model to access the integrity of test data in relation to fundamental flow physics and to reconcile differences prior to PBM data integration.

3.
In order to reduce the uncertainty due to physical property limitations within the model, implement the best available property data into PBM.

4.
Establish benchmark states for hot gas mixture properties in order to reduce prediction uncertainty in high pressure turbopumps and preburners.

5.
Perform an energy sensitivity analysis for all subsystems to estimate the consequences of First Law violation.

Table 1. Power Level Excursions

POWER BALANCE # 1   109% RPL

THRUST - 109.000% RPL

SUBSYSTEM	DW(LB/S)	DE(BTU/S)	DE(HP)
LPFTP	0.002	192.431	272.258
LPOTP	0.000	55.949	79.159
HPFTP+FPB+HGM	-0.002	-13635.504	-19292.000
HPOTP+OPB+HE+POGO+HGM	0.002	-5349.570	-7568.762

POWER BALANCE # 2   104% RPL

THRUST - 104.000% RPL

SUBSYSTEM	DW(LB/S)	DE(BTU/S)	DE(HP)
LPFTP	0.004	231.743	327.878
LPOTP	0.000	68.043	96.270
HPFTP+FPB+HGM	-0.002	-12790.664	-18108.012
HPOTP+OPB+HE+POGO+HGM	0.002	-5009.715	-7087.922

POWER BALANCE # 3   100% RPL

THRUST - 100.000% RPL

SUBSYSTEM	DW(LB/S)	DE(BTU/S)	DE(HP)
LPFTP	0.003	199.509	282.272
LPOTP	0.000	62.402	88.289
HPFTP+FPB+HGM	-0.002	-12121.488	-17149.918
HPOTP+OPB+HE+POGO+HGM	0.014	-4694.590	-6642.074

POWER BALANCE # 4   90% RPL

THRUST - 90.000% RPL

SUBSYSTEM	DW(LB/S)	DE(BTU/S)	DE(HP)
LPFTP	0.002	146.214	206.869
LPOTP	0.000	53.746	76.042
HPFTP+FPB+HGM	-0.001	-10727.629	-15177.836
HPOTP+OPB+HE+POGO+HGM	0.035	-4092.676	-5790.465

POWER BALANCE # 5   80% RPL

THRUST - 80.000% RPL

SUBSYSTEM	DW(LB/S)	DE(BTU/S)	DE(HP)
LPFTP	0.002	83.443	118.058
LPOTP	0.000	42.848	60.622
HPFTP+FPB+HGM	0.000	-9450.035	-13370.250
HPOTP+OPB+HE+POGO+HGM	0.053	-3517.473	-4976.645

POWER BALANCE # 6   70% RPL

THRUST - 70.000% RPL

SUBSYSTEM	DW(LB/S)	DE(BTU/S)	DE(HP)
LPFTP	0.002	49.171	69.569
LPOTP	0.000	25.512	36.095
HPFTP+FPB+HGM	-0.001	-8352.645	-11817.621
HPOTP+OPB+HE+POGO+HGM	0.070	-2941.273	-4161.418

POWER BALANCE # 7   65% RPL

THRUST - 65.000% RPL

SUBSYSTEM	DW(LB/S)	DE(BTU/S)	DE(HP)
LPFTP	0.001	33.004	46.696
LPOTP	0.000	20.258	28.661
HPFTP+FPB+HGM	0.000	-7815.320	-11057.395
HPOTP+OPB+HE+POGO+HGM	0.082	-2680.719	-3792.776
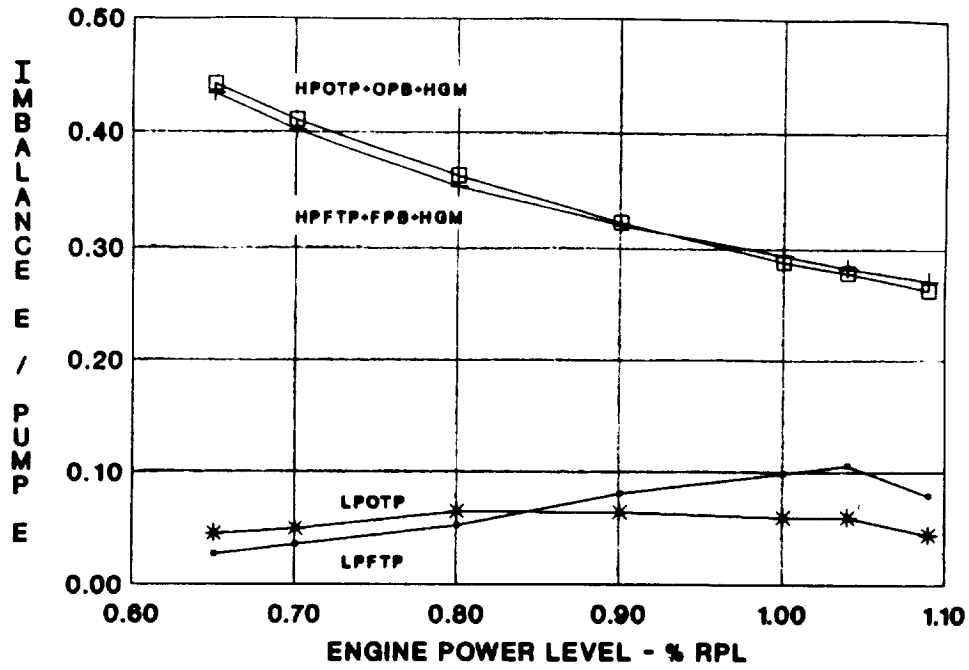
FIGURE 1. SYSTEM PROPORTIONAL IMBALANCE
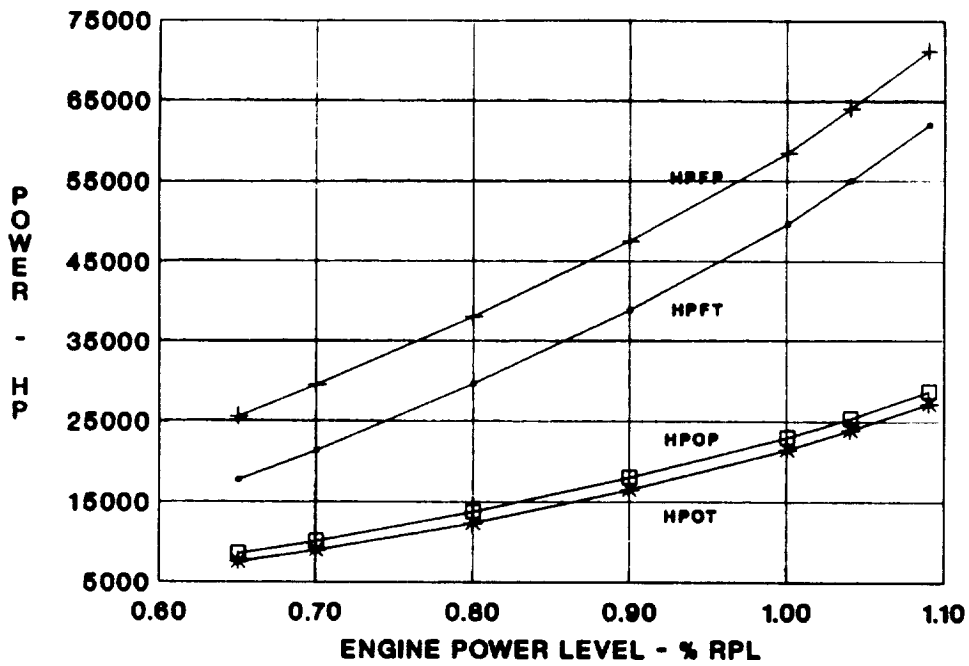
FIGURE 2. HIGH PRESSURE SYSTEM POWER

XLI-6
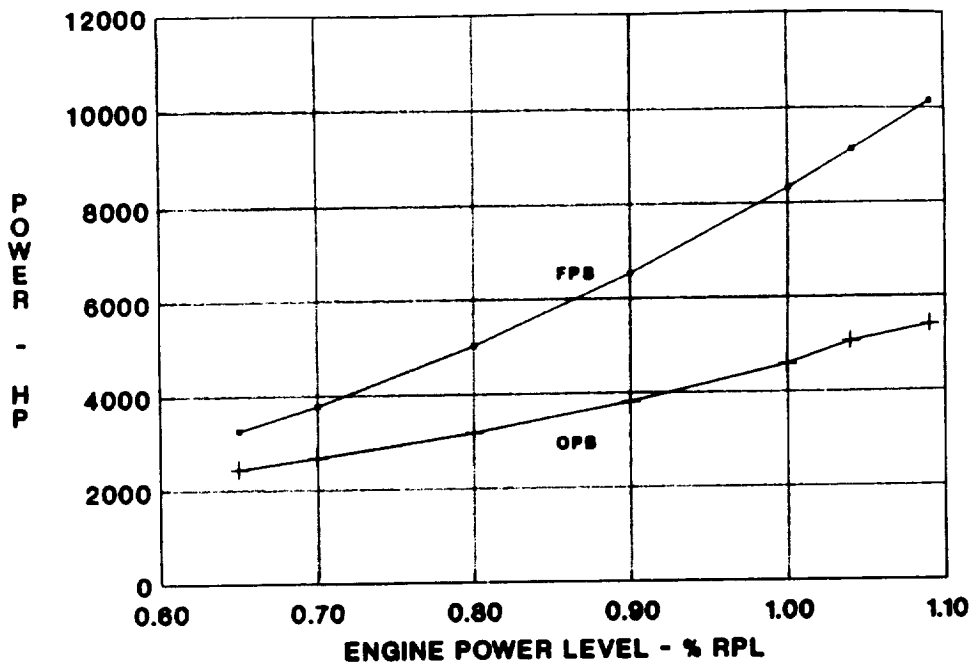
FIGURE 3. PREBURNER POWER IMBALANCE
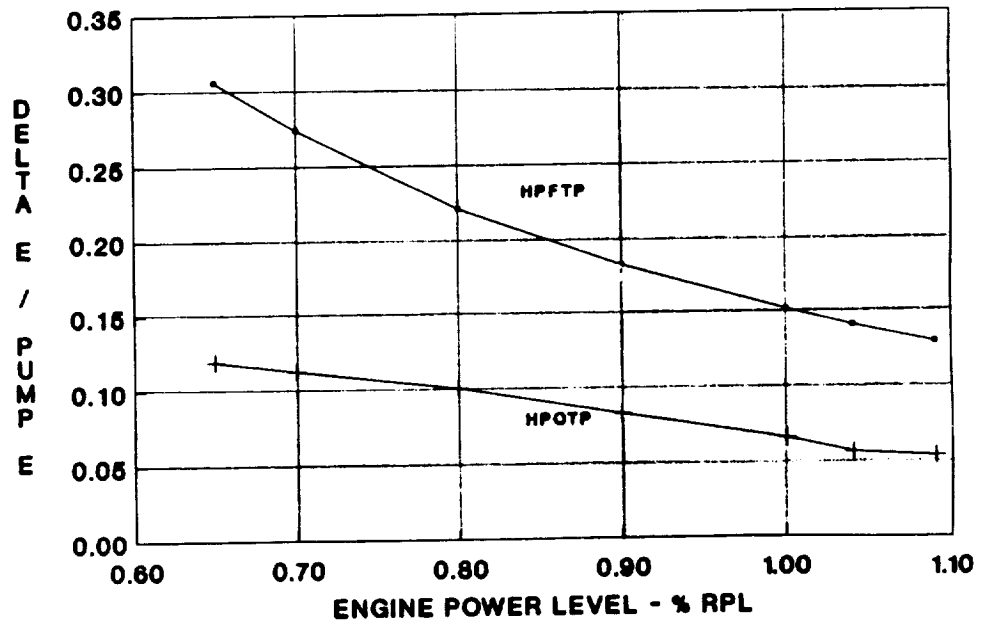
FIGURE 4. TURBOPUMP PROPORTIONAL IMBALANCE

XLI-7
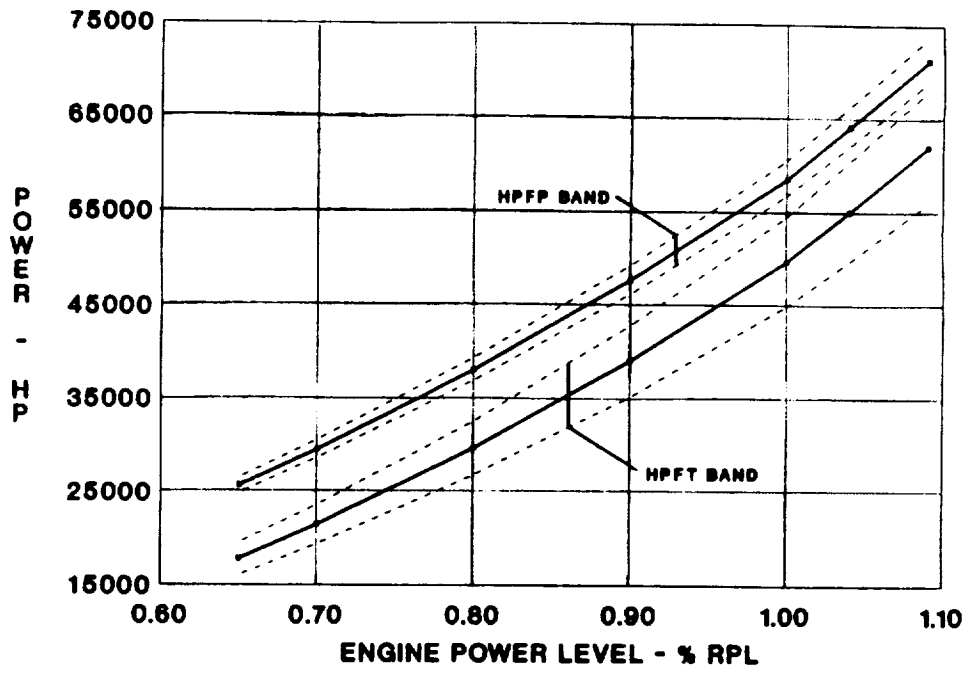
FIGURE 5. HPFTP SYSTEM UNCERTAINTY
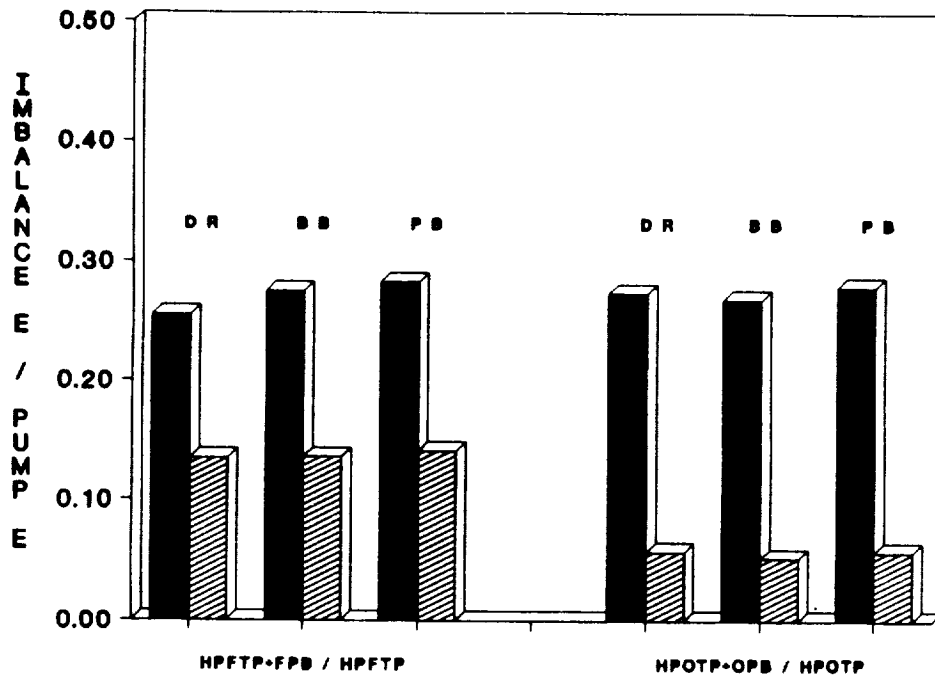
FIGURE 6. PBM90A EVALUATION AT 104% RPL

1990
NASA/ASEE SUMMER FACULTY FELLOWSHIP PROGRAM

MARSHALL SPACE FLIGHT CENTER
THE UNIVERSITY OF ALABAMA

HIGH VOLTAGE PLASMA SHEATH ANALYSIS
RELATED TO TSS-1

Prepared By: John W. Sheldon

Academic Rank: Professor

University and   Florida International University
Department: Physics Department

NASA/MSFC:

     Laboratory: Space Science Laboratory
     Division: Solar-Terrestrial Physics Division
     Branch: Magnetospheric Physics Branch

MSFC Colleague: Dr. Nobie H. Stone

Contract No: NGT-01-002-099
                      The University of Alabama
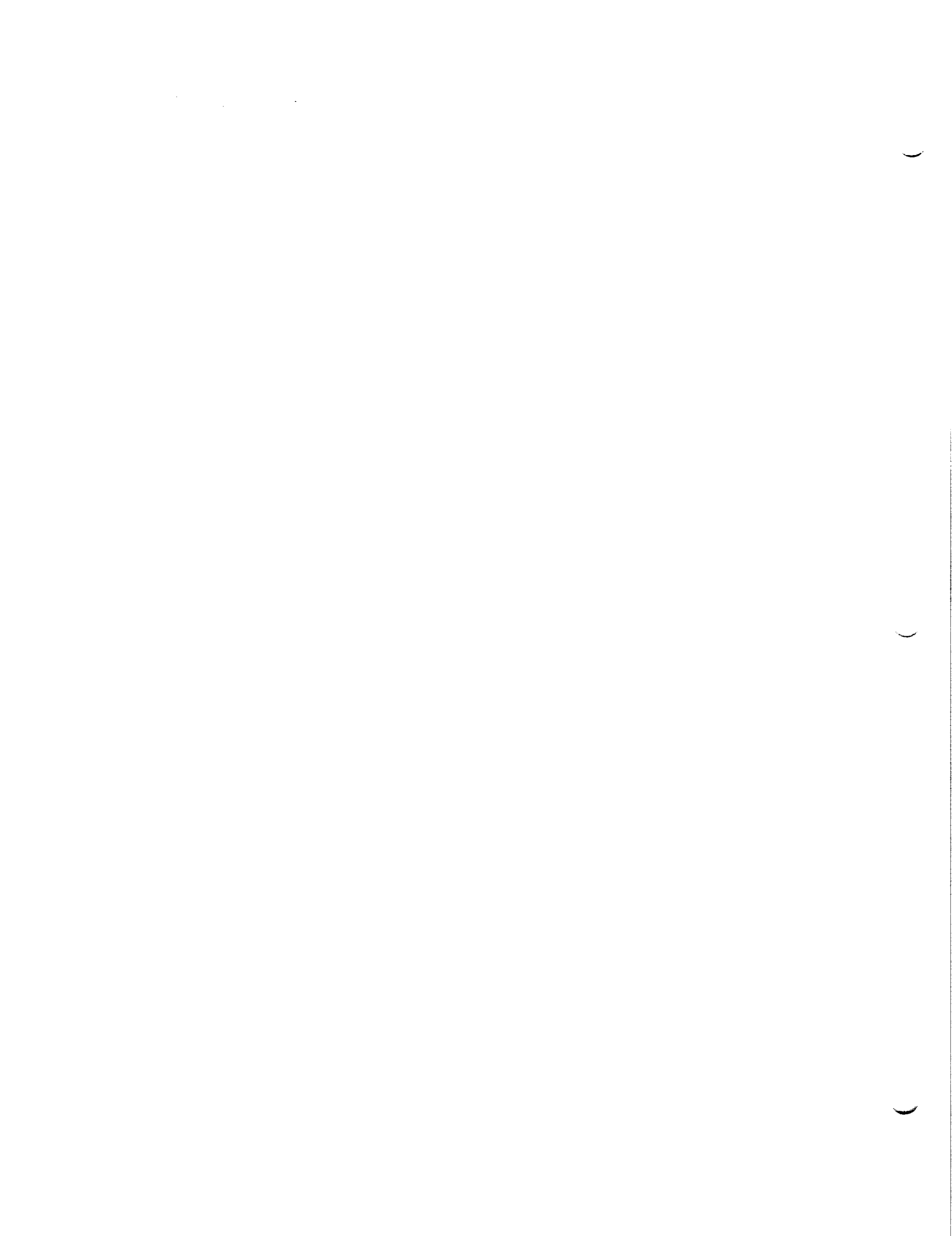
Introduction

On the first mission of the Tethered Satellite System (TSS-1), a 1.8m diameter spherical satellite will be deployed a distance of 20 km above the space shuttle Orbiter on an insulated conducting tether. The satellite will be held at electric potentials up to 5000 volts positive with respect to the ambient plasma. Due to the passage of the conducting tether through the earth's magnetic field, an emf will be created, driving electrons down the tether to the orbiter, out through an electron gun into the ionosphere and back into the positive-biased satellite. The main problem addressed herein is the current-voltage characteristics of the ionospheric interaction with the satellite.

Instrumentation on the satellite will be capable of measuring charged particle flow to the surface at several locations, but these detectors have a limited range of acceptance angle. The second problem addressed herein is the angle of incidence the incoming electrons will have relative to the local normal. This will be important in order to predict the magnitude of the detectable current at each detector location so the detector gain can be pre-set to the correct range.

The Mathematical Model

In the ionosphere at the altitude of the planned orbit, the average thermal velocity of electrons 1.9×10^5 m/s, the average thermal velocity of the ions is 1.1×10^3 m/s and the velocity of the satellite is 8×10^3 m/s. Furthermore, the electrons spiral about the earth's magnetic field lines with a radius of 3 cm, while the ions spiral with a radius of 5m.

In the present calculation, it is assumed that there will be a sheath region around the satellite devold of ions due to the high positive potential and that electrons approach this sheath along the magnetic field lines neglecting their initial velocity due to the ambient spirals. The governing equations in this sheath are taken to be (1) the Taylor-Vlasov equations which relate the components of the electron

velocity to the local electric potential, (2) the continuity equation for electrons which relates their velocity components to the electron density and, (3) the Poisson equation which relates the electron density to the electric potential. The boundary conditions at the outer edge of the sheath are that the electron velocity is equal to the ambient electron drift velocity, the electron density is the ambient value, and the electron electric potential energy is equal to the ion kinetic energy relative to the satellite. The problem is solved in the steady state so the electron current entering the sheath is equal to the current collected by the satellite.

The Solution

Finite difference equations have been written for equations (1)-(3). Equation (1) is solved numerically by applying Newton linearization and an iterative procedure. Equation (2) is solved by a direct stepwise numerical calculation. Equation (3) is solved by the successive over-relaxation method using Chebyshev acceleration. The computer program begins by using a guessed potential distribution and solving Eq. (1) to obtain the electron velocity components and from Eq. (2) the electron density. From the radial electron velocity and electron density at the satellite surface, the current to the satellite is calculated and compared to the incoming ambient current to the sheath. The sheath radius is then adjusted to make these currents equal. Using this new sheath radius and the electron density, a new potential distribution is obtained from Eq. (3). Using this new potential, the above process is repeated until potential, electron density, and electron velocity spacial distributions have converged. Then the angles of incidence of the current to the detector locations can be obtained from the electron velocity components at the satellite surface.

Status

As of this writing, the subroutines solving Eqs. (1)-(3) have been written and tested. The assembly of the overall program is underway.

Acknowledgment

The author is grateful to Dr. Nobie Stone for his hospitality, his suggestion of this problem and for many helpful and stimulating discussions concerning the work.

1990

NASA/ASEE SUMMER FACULTY FELLOWSHIP PROGRAM

MARSHALL SPACE FLIGHT CENTER
THE UNIVERSITY OF ALABAMA

A STUDY OF THE CURRENT GROUP EVAPORATION/COMBUSTION THEORIES

Prepared By: Hayley H. Shen

Academic Rank: Associate Professor

University and   Clarkson University
Department: Department of Civil and
                                Environmental Engineering

NASA/MSFC:

        Laboratory: Propulsion
        Division: Propulsion Systems
        Branch: Performance Analysis

MSFC Colleague: Dr. Charles F. Schafer

Contract No: NGT-01-002-099
                                The University of Alabama

I. INTRODUCTION

Liquid fuel combustion can be greatly enhanced by disintegrating the liquid fuel into droplets, achieved by various injector configurations. Although this fact has been known for more than a century, a scientific understanding of liquid fuel spray combustion started only but forty years ago. For most part of this time, effort has been focused on single droplet combustion. A number of experiments carried out in the seventies have shown that combustion of droplet arrays and sprays do not form individual flames. Moreover, the rate of burning in spray combustion greatly deviates from that of the single droplet combustion rate. Such observations naturally challenge its applicability to spray combustion.

A number of mathematical models have been developed to evaluate the "group combustion" and the related "group evaporation" phenomena. This study investigates the similarity and difference of these models, and their applicability to spray combustion. Future work that should be carried out in this area is indicated.

II. Group Evaporation

Evaporation precedes and maintains combustion after ignition. Understanding this process is a natural first step towards understanding combustion. Two major approaches in modeling group evaporation are represented by the works of Bellan and co-workers, and Chiu and co-workers. The physical pictures that are mathematically described in these two approaches are not the same. Bellan's model is a field of uniformly distributed identical droplets with unlimited extent. The initial conditions of the droplets and the surrounding gas are given. Chiu's model is an arbitrary cloud of uniform droplets, the conditions far away from the cloud are known.

In either case, the total evaporation of the group, that being a uniform cluster or an arbitrary cloud of droplets, is the integral of the evaporation of each droplet enclosed. Therefore, the question comes back to what is the evaporation rate of each droplet, except that the "environment" in which each droplet evaporates must now be influenced by the neighboring droplets. This "environment" includes the detailed temperature, pressure, and species concentration surrounding each droplets. Given an environment, the evaporation rate of each droplet depends on its surface temperature, which is influenced by the fluid dynamic and thermodynamic processes inside the droplet.

Because the fluid/thermo-dynamic processes have been studied for a single droplet in an infinite field of gas, Bellan's work concentrates on incorporating realistic boundary conditions located at the edge of a "bubble" surrounding each droplet. The bubbles subdivide the whole space occupied by the mixture of droplets and

the gas. Spatial variations of any variables inside each bubble and the droplet are carefully studied. The possible variation of any variable from one bubble to the other is not incorporated. This work has later been extended to a moving spherical cluster, and to finite kinetics of evaporation. Among many important results, several major finding are:

1. D^2-t law for droplet size reduction does not apply at a surprisingly lean condition.

2. Evaporation time can be an order of magnitude higher than that predicted from the single droplet case.

3. Saturation occurs at a much leaner condition than that predicted from the single droplet theory.

4. The above effects are significant even for very dilute clusters, provided that the gas phase is fuel rich.

Chiu's work, on the other hand, puts more emphasis on the thermodynamic interaction between the inside and outside of the cloud. Spatial gradient of all variables in the gas phase is modeled. But the droplets are considered as point sources of vapor. The fluid/thermo-dynamics within the droplets are ignored. The evaporation rate of each droplet is considered to be influenced by the "bubble" size, the near neighbors, and the far neighbors that constitute the "ambient" conditions. The bubble size, the extend and distribution of near neighbors are both functions of the droplet volume concentration. An important concept defined by the "group number" is used in the analysis. This number G (=evaporation time/diffusion time) controls the deviation of the group evaporation from single droplet evaporation. Important results are:

1. D^2-t law does not apply. Which agrees qualitatively with Bellan's result.

2. The spatial gradients of all variables from any given droplet outward depend strongly on the group number. For a transient process, this gradient is important even for very small group numbers.

III. GROUP COMBUSTION

Mathematical studies of group combustion began with Suzuki and Chiu. The physical picture is a spherical cloud surrounded by the oxidizer gas with given condition far away from the cloud. This picture is the same as that in Bellan's evaporation model, except that the internal gradient of variables are modeled inside the cloud. However, the droplet's own fluid/thermo-dynamics are again neglected. All droplets are treated as fuel vapor sources only. Important results include:

1. High group number condition dominates most practical operation

C. 4.

conditions in a combustor.

2. As the group number increases, only a thin layer of droplets in the cloud participates in burning. This fact may complicate the picture of incomplete burning.

Labowsky and Rosner also studied the group combustion phenomenon. They assumed a cubic lattice of point droplets. Although the analysis is different, they obtained essentially the identical group number as Chiu. The analysis of Labowsky and Rosner however covers the entire range from incipient group combustion (droplets at the center of a cloud start to share flame) to total group combustion. An interesting result of their work is that a small difference of group number can trigger the jump from individual combustion to group combustion. This may be important to the stability of combustion process.

IV. CONCLUSIONS

It is clear from the above modeling effort that group evaporation/combustion impacts combustor performance. This phenomenon can be rigorously analyzed. For group evaporation, each of the two current approaches has its strong and weak points. They are summarized below.

Bellan

Strong Points- Detailed fluid/thermo-dynamics of droplet/ environment interaction. Easy to incorporate aero-dynamic, thermal and chemical effects rigorously.

Weak Points- No spatial gradient in the cluster of droplets. Analysis is restricted to a single cluster. No indication of how to extend it to a spray.

Chiu

Strong Points- Spatial gradient inside a cloud of droplets is included. In the later work, spray evaporation is modeled based on the earlier single cluster concepts.

Weak Points- Droplet's own fluid/thermo-dynamics are ignored. Extension to spray combustion from the group evaporation is not clear.
Furthermore, neither of the two have experimental data for validation.

Based on their strong and weak points, it is clear that Bellan's analysis is applicable to larger droplets (compared with the local spray size), colder droplet temperature, hence the region closer to the spray injector. Chiu's analysis, on the other hand, applies to fine droplets, larger spray size, nearly boiling droplet

temperature, hence the region further downstream from the injector.

At this point, a group combustion theory only exists for the ideal case of a single cluster. There is no model for a true spray.

V. RECOMMENDATIONS

Recommended future analyses are summarized below.

1. Improve the existing models by combining the strong points of both approaches.

2. Relax the assumptions made in current models, such as constant mass and heat diffusion, negligible aerodynamic effects, infinite evaporation kinetics, infinite reaction rate, single step reaction, negligible radiation. Prioritizing the above should precede the analysis if possible.

3. Begin spray combustion analysis based on the single cluster idea. The group evaporation idea has been applied to spray evaporation by Chiu. However, extension from single cluster combustion to spray combustion has not been done. Combustion adds not only heat, but also changes the distribution of oxidizer and fuel concentrations in the spray. The picture obtained from pure evaporation cannot be translated to spray combustion easily.

4. Need more experimental work. First, mathematical modelers need experimental observations to assist creating a correct physical picture. Second, data obtained from experiments are necessary for model verification. Carefully designed basic experiments should go side by side with true spray combustion experiments, because in a true spray, the simultaneous heat, mass, momentum and chemical processes all interact together. The data obtained represents the bulk effect. It is impossible to use it for differentiating the degree of importance of each individual mechanism. Prototype experiments should be done primarily for observation. Only at the final stage, when modeling is "completed", can prototype results be used for model verification. Basic experiments designed for studying a few number of mechanisms at a time will have to be done to assist and verify the modeling at the building stage.

VI. ACKNOWLEDGEMENTS

1990

NASA/ASEE SUMMER FACULTY FELLOWSHIP PROGRAM

MARSHALL SPACE FLIGHT CENTER

THE UNIVERSITY OF ALABAMA

DEVELOPMENT OF NICKEL HYDROGEN BATTERY EXPERT SYSTEM

Prepared By: Sajjan G. Shiva

Academic Rank: Professor

University and   University of Alabama in Huntsville
Department   Computer Science

NASA/MSFC:

     Laboratory: Information and Electronic Systems
     Division: Electrical
     Branch: Electrical Power

MSFC Colleague: Yvette Johnson

Contract No: NGT-01-002-099
                 The University of Alabama
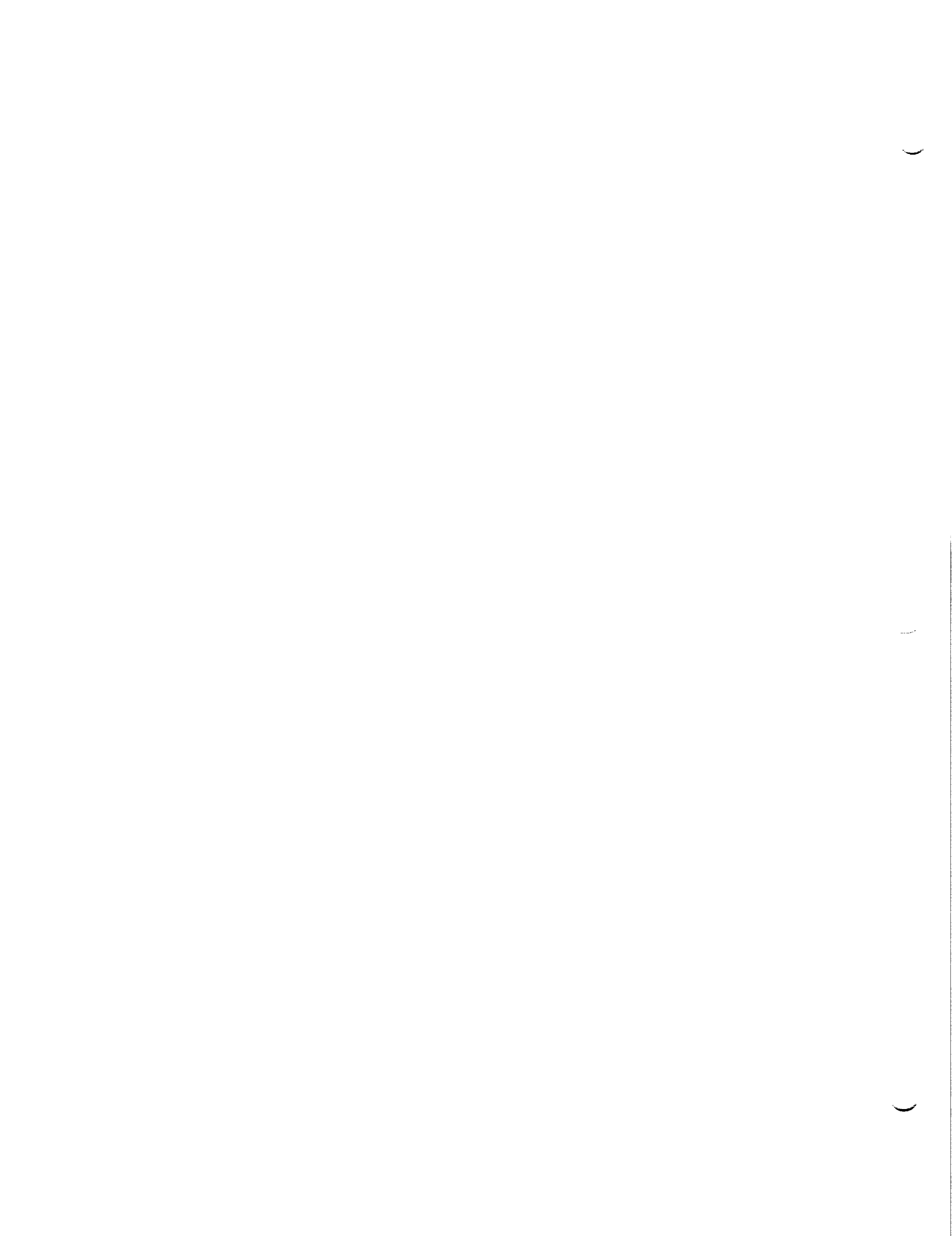
INTRODUCTION

The Hubble Telescope Battery Testbed at MSFC employes the Nickel Cadmium (NiCad) Battery Expert system (NICBES-2) which supports the evaluation of performance of Hubble Telescope space-craft batteries and provides alarm diagnosis and action advice. NICBES-2 provides a reasoning system along with a battery domain knowledge base to achieve this battery health management function. This report summarizes an effort to modify NICBES-2 to accomodate Nickel Hydrogen battery environment now in MSFC testbed.

The prototype version of NICBES (NICBES-1) was developed by Martin Marietta Corporation. It was implemented in Intel 8086 assembly language, C and Prolog and runs on an IBM PC/AT under the DOS. The current version of NICBES (NICBES-2) is implemented on a Sun Microsystem's 386i running SunOS4.0 (UNIX) and is written in SunOS C and Quintus Prolog. The system now operates in a multitasking environment along with a mouse and window based user interface.

Figure 1 shows the structure of NICBES-2. A DEC LSI-11 based system sends the battery data to the Sun 386i via an RS-232 connection running at 9600 baud using XON/XOFF control. One telemetry burst is received every 30 seconds. NICBES-2 spawns three child processes: serialport process (SPP), data handler process (DHP) and the expert system process (ESP).

When data appears on the serial port, SPP collects it character by character and feeds it into a data pipe. The DHP reads the data pipe and converts the character data into numeric

values and reduces the raw telemetry data (by calculating averages and means of various battery parameters) in preparation for use by ESP. ESP is awakened by the user's request for a consult/advice function. Each of the three processes is awakened only when its service is desired and they go to sleep when the function is completed. The SPP has the highest priority among the processes.

In short, NICBES-2 performs orbit data gathering, data evaluation, alarm diagnosis and action advice and status and history display functions.

MODIFICATIONS NEEDED

The adaptation of NICBES-2 to work with Nickel Hydrogen (NiH2) battery environment requires modifications to all the three component processes. Although the general format of the telemetry input is retained, the components of the telemetry data are different. As such, the data input routines of SPP need extensive changes. Because of the differances in the data collected between the NiCad and NiH2 batteries, all DHP routines require changes. The structure and the reasoning mechanism of ESP remain the same. But the rule base needs to be examined and changed to accomodate the NiH2 battery domain.

STATUS

The modifications to the SPP are now complete. The telemetry data stream contains excessive delimeter characters that can be eliminated to reduce the data gathering overhead.

Modifications to DHP are complete. Some data items in the

telemetry (such as Ampere-hour Out, Time-to-Trickle, Telemetry temperatures and Main and Redundant heater flags) are not utilized in ESP. Changes to DHP are needed to utilize these data. Several means and averages are now computed at 2 minute intervals (i.e. every 4 samples) rather than every other sample as in NiCad environment. Adequacy of these computation needs to be examined. The trickle charge computations need to be updated.

Modifications to ESP require consultations with NiH2 battery experts to collect the rules appropriate to that domain. These rules can then be incorporated through the Simple Interactive Rule Editor (SIRE) utility available in NICBES-2 system.

The data files generated by the system seem to be unnecessarily elaborate, and create disk space shortage in the current system. File structures need to be examined to reduce their size if possible. If not, some of the files may need to be archived on the tape storage.

REFERENCES

A. Bykat, "User's Manual for NICBES-2," NAG8-105, NASA/MSFC, Aug.89.

A. Bykat, "Program Maintenance Manuals for SPP, DHP and ESP'" NAG8-105, NASA/MSFC, August 89.

A. Bykat, "SIRE Manual'" NAG8-105, NASA/MSFC, August 89.
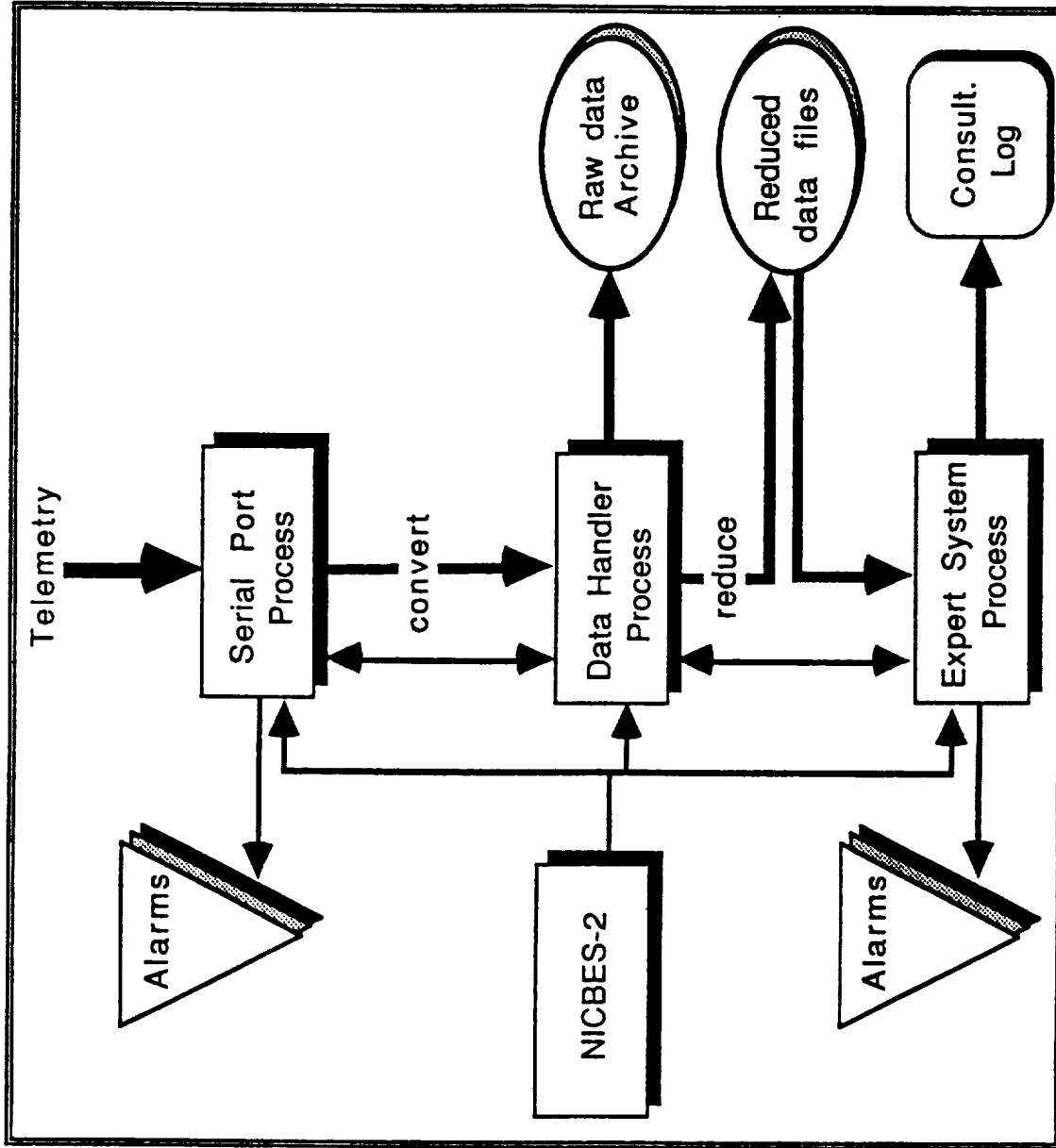
Fig.1. NICBES-2 top level structure.

1990

NASA/ASEE SUMMER FACULTY FELLOWSHIP PROGRAM

MARSHALL SPACE FLIGHT CENTER
THE UNIVERSITY OF ALABAMA

A HIGH-FIDELITY SATELLITE EPHEMERIS PROGRAM FOR EARTH

SATELLITES IN ECCENTRIC ORBITS

Prepared By: David R. Simmons

Academic Rank: Professor

University and   Louisiana College
Department: Mathematics and Computer Science

NASA/MSFC:
      Laboratory: Systems Analysis and Integration
      Division: Mission Analysis
      Branch: Flight Mechanics

MSFC Colleague: Dr. Larry Mullins

Contract Number: NGT-01-002-099
                      The University of Alabama
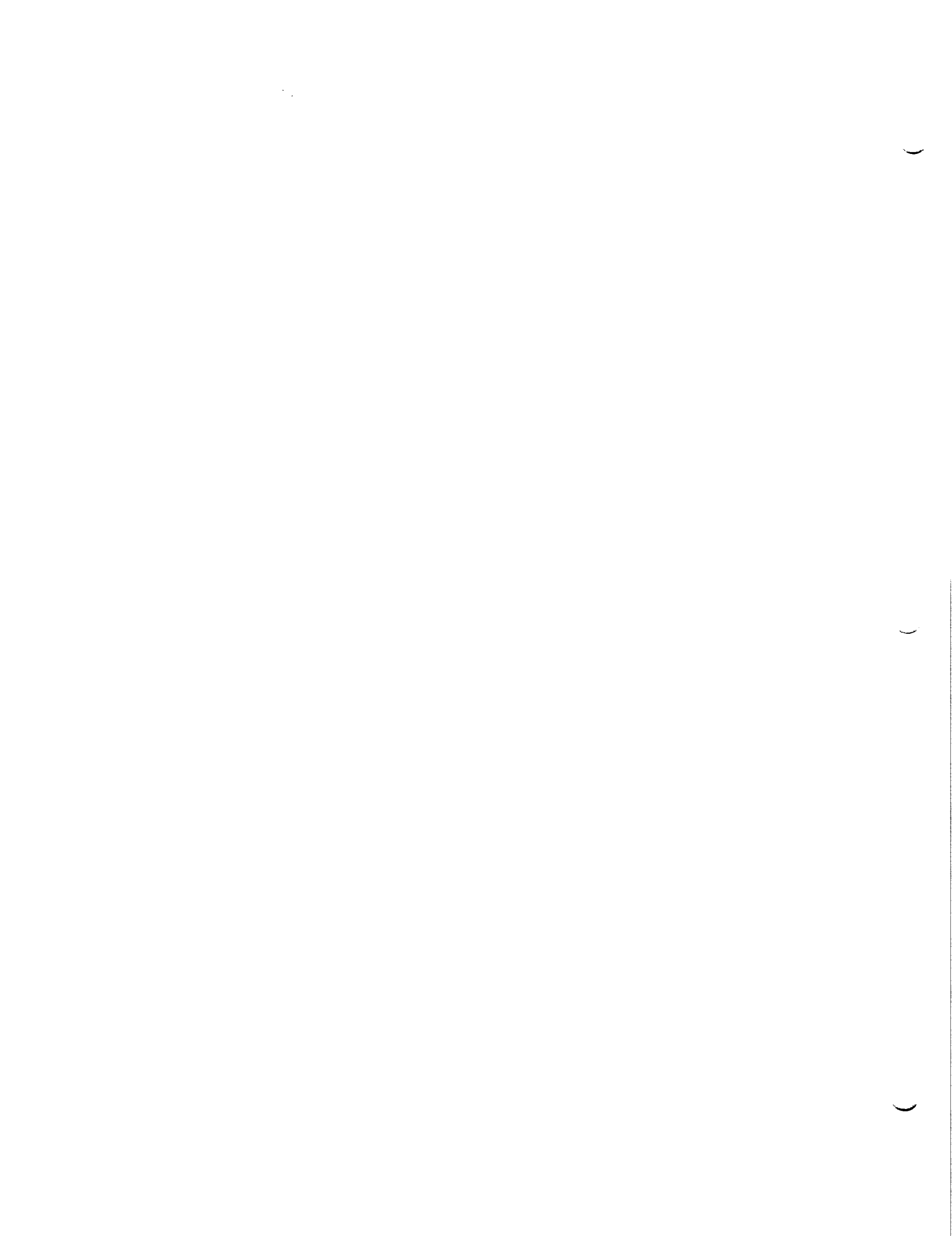
Description of the Project

The Flight Mechanics Branch is currently using a program for mission planning called the Analytic Satellite Ephemeris Program (ASEP). This program, written by Jim McCarter, produces projected data for orbits that remain fairly close to the Earth; ASEP does not take into account lunar and solar perturbations. These perturbations are accounted for in another program called GRAVE, written several years ago by Roger Burrows. This project is a revision of GRAVE which incorporates more flexible means of input for initial data, provides additional kinds of output information, and makes use of structured programming techniques to make the program more understandable and reliable.

Project Goals

Dr. Mullins and I set these goals for the project:

(1) To make the program easier to use, particularly in the initialization phase.

(2) To make the program easier to understand, and hence, easier to maintain and more reliable.

(3) To include output concerning lighting conditions.

(4) To calculate Earth shadow entry and exit times.

(5) To calculate bearings from ground stations.

Personal Goals

I had set these personal goals for the Summer Faculty Fellowship Program:

(1) To learn more about celestial mechanics.

(2) To exercise my FORTRAN programming skills and learn new features of FORTRAN.

(3) To apply modern structured programming techniques to a FORTRAN program.

(4) To get experience with a non-academic work environment.

(5) To develop a high-fidelity ephemeris program in Pascal to be used on a Personal Computer.

(6) To learn more about NASA and the space program.

(7) To have a good, intellectually refreshing summer.

(8) To get to know new people.

ORBIT

The resulting program is called ORBIT. ORBIT is written in FORTRAN; the SAIL1 VAX system was used to develop the program. In keeping with structured programming concepts, the program is divided into numerous sub-programs, each with a well-defined task to perform. The text of the source code for one sub-program can usually be printed on a page or less. Most of the variable names are whole words or short phrases which clearly identify the nature of the variable and its role in the program.

ORBIT: Initialization

ORBIT is divided into three major qhases: initialization, integration, and output. During the linking process, the block data subprogram, Load Common, gives initial values to the key variables in COMMON. Later during the initialization phase, the Get Parameter subroutine uses tree-structured menus to give users an opportunity to change the starting and ending times, output defaults and state vectors. Get Parameter can change any of the three forms of state vector (cartesian, spherical-polar, and osculating orbital elements) that are used in the program; the other forms are always re-calculated to conform to the new one. Get Parameter also provides for the selection of the kind of output to be provided.

ORBIT: Integration

The Integration phase of the program calculates new values for the elapsed time and the cartesian state vector describing the motion of the satellite. This section of the program follows the GRAVE program very closely. The Encke method is used; a subroutine called COAST calculates a position along the osculating ellipse from the current position; this position is used by the subroutine DEQG for the calculation of both gravitational and atmospheric forces. DEQG is called by RKG, a general routine for solving first-order differential equations; RKG uses Fehlberg's 13 Step version of the Runge-Kutta method. RKG is used in ORBIT with no change from its previous form. COAST has a very tangled structure; I had to split it into subroutines bases on its syntax rather than on its meaning. On the other hand, DEQG has been split into sub-programs in a natural and well-structured way.

ORBIT: Output

ORBIT produces a complete set of output data before the beginning of the integration, and after the end. The uses of the program can select an option to generate time and state-vector, which is assumed to be relative to an inertial reference system. A spherical-polar state vector and a set of osculating elements are calculated for the output phase by a set of routines organized through a master routine called UpDate Common. These subroutines also adjust various lunar, solar, and time-related variables that are maintained in COMMON. A set of routines controlled by a subroutine called Report State then display those values and calculate other values which are also displayed. Another user option is to have the displayed values stored in a file.

Pre-existing Subroutines

ORBIT makes either direct or indirect use of about a score of special-purpose routines already available in the MSFC computer systems, along with modified versions of the DEQG and COAST routines from the GRAVE program. It would not have been possible to complete this project in ten weeks if all these routines had not veen available. The use of these routines should also make it easier for MSFC personnel who are already familiar with them to understand this program.

Results: Project Goals

(1)   The menu-driven input section of ORBIT should make it easy to use; some improvements can still be made.

(2)   The structured nature of the program should make it easier to understand; it should be possible to find the section of ORBIT which performs a particular task and either change or add to it.

(3,4,5)   With formulas provided by Larry Mullins, I was able to include output concerning lighting conditions, Earth shadow entry and exit times, and bearings from ground stations.

Results: Personal Goals

(1)   I worked through MSFC Course 4181, General Description of Orbits, and was able to spend some time reading in Danby's book. I learned a lot about celestial mechanics.

(2)   I exercised my FORTRAN programming skills enough that in the last few weeks I only needed to consult a text about once a week. I learned to use BLOCK IF, BLOCK DO, and DO WHILE statements in FORTRAN.

Results: Personal Goals

(3) It is definitely possible to do structured programming in FORTRAN. the new parts of ORBIT are quite structured; some of the old parts still have GO TO statements and remnants of the old style of organization.

(4) The work environment at MSFC is surprisingly like that of a college, except for the lack of classes. The kind of conversations, the paperwork, and the intellectual atmosphere are similar in many ways.

(5) There was little time to work on a Pascal version of an ephemeris program to be used on a Personal Computer. I copied the FORTRAN files onto a floppy disk in MSDOS format and was able to get several Pascal procedures working, including RKG. This is something to work on during the next year.

(6) Frank Six and Mike Freeman organized an excellent series of seminars and tours to help us learn more about NASA and the space program.

(7) This summer has been relaxing, stimulating, and highly educational.

(8) Sharing an office with John Aberg has been an excellent way to get to know new people.

Additional work needed

A great deal of re-structuring can still be done on the program. There is a need for program output on the occurrence of specific orbital events. File output organized for conversion into graphic output would be very helpful.

References

Roger Burrows, MSFC: GRAVE.FOR (1985-1988)
J.M.A. Danby: Fundamentals of Celestial Mechanics, 2nd ed.
Larry Mullins, MSFC Course 4181: Gen. Description of Orbits

Acknowledgments

1990

NASA/ASEE SUMMER FACULTY FELLOWSHIP PROGRAM

MARSHALL SPACE FLIGHT CENTER
THE UNIVERSITY OF ALABAMA

HEAT SINK EFFECTS IN VPPA WELDING

Prepared by: Paul O. Steranka, Jr.

Academic Rank: Assistant Professor

University and   Wichita State University
Department: Mechanical Engineering

NASA/MSFC:

        Laboratory: Materials and Processes
        Division: Process Engineering
        Branch: Metals Processes

MSFC Colleague: Dr. Arthur C. Nunes, Jr.

Contract No.   NGT-01-002-099
                                    The University of Alabama
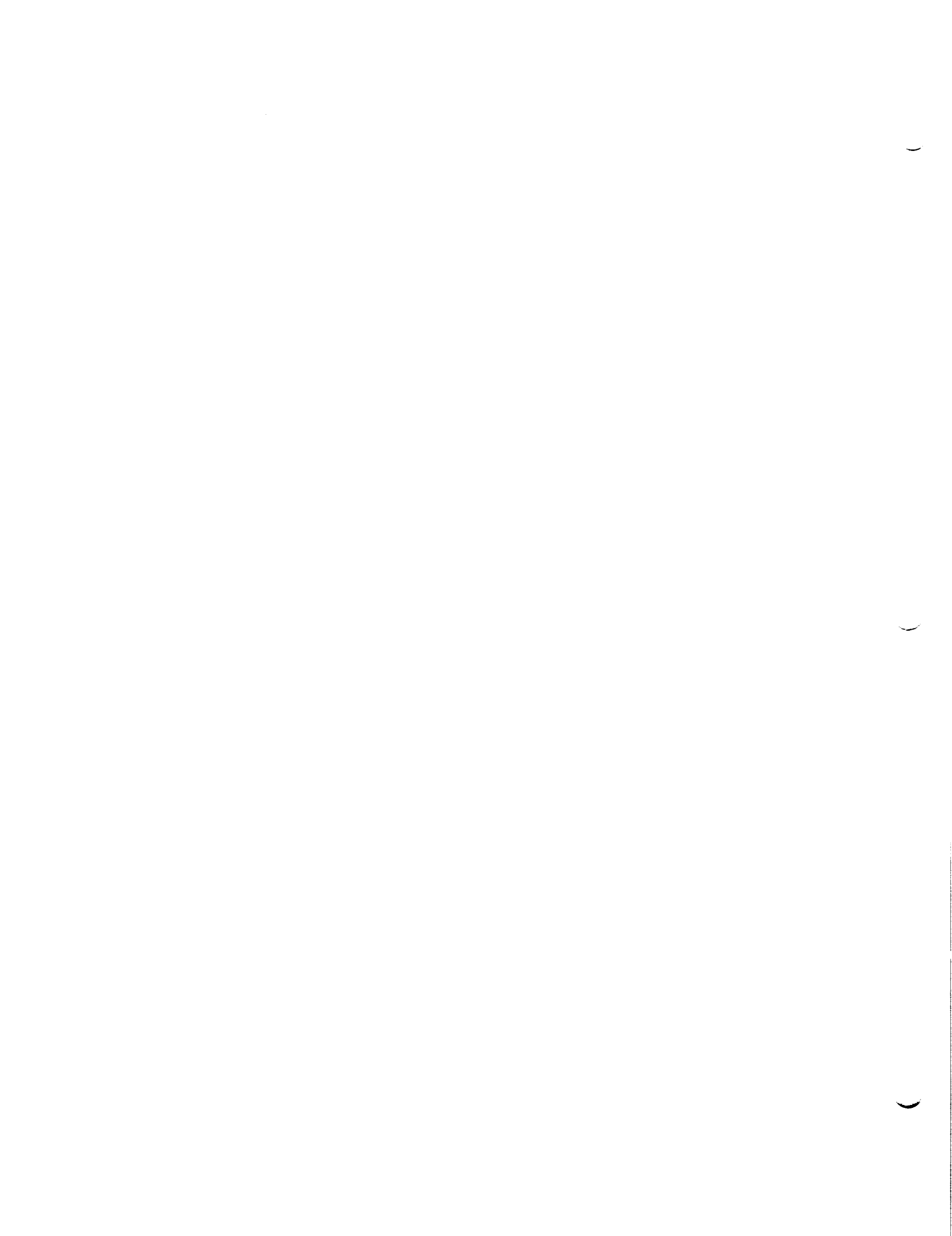
Introduction

This report is a summary of work performed toward the development of a model for prediction of heat sink effects associated with the Variable Polarity Plasma Arc (VPPA) Welding Process. The long term goal of this modeling is to provide a means for assessing potential heat sink effects and, eventually, to provide indications as to changes in the welding process that could be used to compensate for these effects and maintain the desired weld quality. Heat sink effects are created due to irregularities of the geometry of the weldment itself or by the presence of heat absorbing material in contact with the weldment. Examples of such irregularities in the weldment are reinforcing ribs or flanges in the vicinity of the weld path. Sink effects due to material in contact with the surface of the weldment may be caused by the tooling and fixtures used in the welding process. The importance of a model for such heat sink effects as part of a successful scheme for the control of welding processes has been indicated in studies such as the report prepared by the Committee on Welding Controls of the National materials Advisory Board of the National Research Council [1].

The present study began during the 1989 NASA/ASEE Summer Faculty Fellowship Program. During the 1989 program, a simple lumped capacity model for heat sink effects was developed [2]. In addition to the development of a theoretical model, a brief experimental investigation was conducted to demonstrate heat sink effects and to provide an indication of the accuracy of the model. The model successfully predicted the trends in the magnitude of the heat sink effect as a function of the welding conditions, but consistently overpredicted the size of the effect. Thus, refinement of the model was indicated.

Early work during the 1990 NASA/ASEE Summer Faculty Fellowship Program involved examination of the preceding work to identify promising areas for refinement of the model. The areas selected for improvement of the model were the modeling of the heat sink itself and the modeling of the interface between it and the weldment. The refinements of the model have led to improved predictions of the location and, in some cases, the magnitude of the maximum heat sink effect, but the predictions continue to be consistently greater than the effects observed experimentally. Therefore, further improvements in the modeling of the heat sink effects are still required.

Summary of Original Model

The model developed in 1989 is based on the consideration of the heat sink material as a lumped capacity body whose temperature follows the temperature that would be observed in the weldment at the center of contact with the heat sink, if the heat sink were to absorb no energy. The required rate of energy absorption by the heat sink material in order to follow this temperature variation is then used as the strength of an ideal line heat sink of variable strength located at the center of the contact area.

The undisturbed temperature distribution created during the welding process is approximated by use of an analytic solution for the two-dimensional quasi-steady temperature distribution created by a moving line source of constant strength per unit length published by Rosenthal in 1946 [3]. The temperature distribution is quasi-steady with respect to a translating coordinate system with heat source fixed to the z-axis and is given by

$$T - T_\infty = \frac{Q}{2\pi k} e^{-\left(\frac{Vx}{2\alpha}\right)} K_0 \left(\frac{Vr}{2\alpha}\right)$$

where Q is the power input per unit depth of weld, k is the thermal conductivity of the weldment, V is the source velocity in the x-direction, α is the thermal diffusivity of the weldment, x and r are the x distance and the radius, respectively, to the position of interest relative to the source, and K_0 is the modified Bessel function of the second kind of order 0. This two-dimensional temperature distribution is inadequate for calculation of temperatures in the vicinity of the weld pool itself, but provides a good, simple approximation for the temperatures away from the weld zone where heat sink material would typically be located. Thus, this expression was kept as a fundamental part of the revised model.

With the local temperature evolution at the heat sink provided by the above expression, the strength of the heat sink is calculated as the instantaneous change in temperature multiplied by the mass and specific heat of the heat sink. In order to evaluate the cumulative effect of this varying and moving (with respect to the translating coordinate system) heat sink, the expression provided by Carslaw and Jaeger [4] for the temperature distribution created by an instantaneous line source is multiplied by the strength of the source and integrated over time to yield the following expression for the temperature at time t

$$T - T_\infty = \int_0^t \frac{-S(\tau)}{4\pi\alpha(t-\tau)} e^{-\frac{[(x-x')^2 + (y-y')^2]}{4\alpha(t-\tau)}} d\tau$$

where $S(\tau)$ is the sink strength at time τ and (x',y') is the instantaneous location of the sink. This method of determining the net effect of a varying, moving heat sink is also used in the revised model.

Revisions to Model

The revisions to the 1989 model consist of changes in the modeling of the heat sink. The first revision deals with modeling the response of the sink to the transient temperature at the base of the sink where it is in contact with the weldment. The second revision deals with division of the heat sink into several elements when its area of contact with the weldment is large. Both revisions allow the model to more accurately predict the behavior of the heat sink if the condition at the base is known from other considerations.

The transient response of the sink to the varying temperature at the base of the sink is obviously different than the assumption used in the original model that the temperature of the whole sink is uniform and equal to the base temperature. If the evolution of the weldment temperature predicted by the Rosenthal solution is examined, it is observed that the temperature at any point in the vicinity of the weld path sees a rapid climb in temperature followed by a gradual decline as the heat source (welding torch) passes. If the height of a heat sink placed on the surface of the weldment is significant, the upper portion of the sink will not experience the same rapid increase in temperature as the lower portion. The true temperature distribution approaches that of an insulated block exposed to a specified variation in temperature on one face. Duhamel's superposition theorem may be used with the transient solution for a unit step change in temperature on one surface of the block to obtain an expression for the temperature distribution in the block as described by Özişik [5]. This expression when multiplied by the density ρ and specific heat c of the sink material and integrated over the volume v of the heat sink yields an expression for the energy contained in the heat sink as a function of time. Finally, the derivative of this expression with respect to time may be taken to obtain the equivalent strength of the sink $S(t)$ as

$$ S(t) = \frac{\partial}{\partial t} \int_0^V \int_0^t \rho c T_b(\tau) \frac{\partial \Phi(t-\tau)}{\partial t} \, d\tau \, dv $$

where T_b is the temperature of the surface and Φ is the solution for a step change in temperature. In the calculations of the revised model, the geometry of each sink element is assumed to be a rectangular prism and a series of two ramps are used to approximate the variation of the base temperature with time so that the differentiations and integrations may be performed and the sink strength may be expressed as a function of time for specified welding parameters. This sink strength is then substituted in the expression for the temperature variation due to an instantaneous heat sink discussed in the preceding section to evaluate the effect of the heat sink element on the temperature at the weld zone.

The revision to the model of dividing sinks with large areas of contact into several elements is based on consideration of the temperature field created in the weldment during the welding process. The Rosenthal solution mentioned above indicates that the temperatures attained in the weldment drop off exponentially with distance from the weld zone. Thus, the assumption in the earlier model that a sink be considered equivalent to a single line sink located at the center of the area of contact may lead to serious errors if the area of contact extends over a distance greater than the characteristic length $(2\alpha/V)$ that is seen in the Rosenthal solution. The revised model therefore divides a sink into equally-sized rectangular elements that are approximately one characteristic length on a side and treats them as separate sinks in the computations.

Results and Suggestions for Future Work

Results from the revised model have been compared to results from the original model and the brief series of experiments conducted last year. It was found that the magnitudes of the temperature effects predicted by the two models agree within 10 per cent for the input conditions corresponding to the experiments. Both models predict the overall trends in magnitude of effect, but overpredict the values observed experimentally. The revised model is clearly superior to the earlier model in that it takes into account variations in heat sink geometry, but since the geometries used in the experiments performed last year were similar, this improvement cannot be confirmed based on the experiments performed. Further refinement of the model is indicated, particularly in the modeling of the interaction of the temperature fields of the weldment and the heat sink.

In addition to further refinement of the model, other work may be suggested to advance the study of heat sink effects. Further experimentation including real-time recording of the temperatures developed in weldments with and without heat sinks would clarify the manner in which the temperature fields interact and would provide a necessary guide in the evaluation of the accuracy of modeling efforts. Another possibility is the use of comprehensive commercial computational heat transfer codes to perform "computational experiments" to obtain more insight into the problem. However, given the complexity of the heat transfer phenomena associated with the welding process, experimentation under actual welding conditions should be included in support of any such endeavor. Progress has been made in understanding heat sink effects, but more work is required to achieve the long term goal of accurate predictions of these effects.

References

1. "Control of the Welding Processes", Report of the Committee on Welding Controls, National Materials Advisory Board, National Academy Press, 1987.

2. Steranka, Jr., P.O., "Heat Sink Effects on Weld Bead - VPPA Process", Report for the NASA/ASEE Summer Faculty Research Program, The University of Alabama, Contract No. NGT-01-008-021, July 28, 1989, pp. XXVIII 1-25.

3. Rosenthal, D., "The Theory of Moving Sources of Heat and Its Application to Metal Treatments", Transactions of the A.S.M.E., Vol. 68, 1946, pp 849-866.

4. Carslaw, H.S. and Jaeger, J.C., Conduction of Heat in Solids, 2nd edition, Oxford University Press, 1959, p. 258.

5. Özişik, M.N., Heat Conduction, John Wiley & Sons, Inc., 1980, pp. 194-208.

1990

NASA/JOVE SUMMER FACULTY FELLOWSHIP PROGRAM

MARSHALL SPACE FLIGHT CENTER
THE UNIVERSITY OF ALABAMA

BIOREGENERATIVE LIFE SUPPORT

Prepared By: Bill Taylor

Academic Rank: Assistant Professor

University and   New Mexico Highlands University
Department: Engineering Technology

NASA/MSFC:

        Laboratory: Structures and Dynamics
        Division: Control Systems
        Branch: Mechanical Systems Control

MSFC Colleague: Steve Ryan

Contract No: NGT-01-002-099
                       The University of Alabama
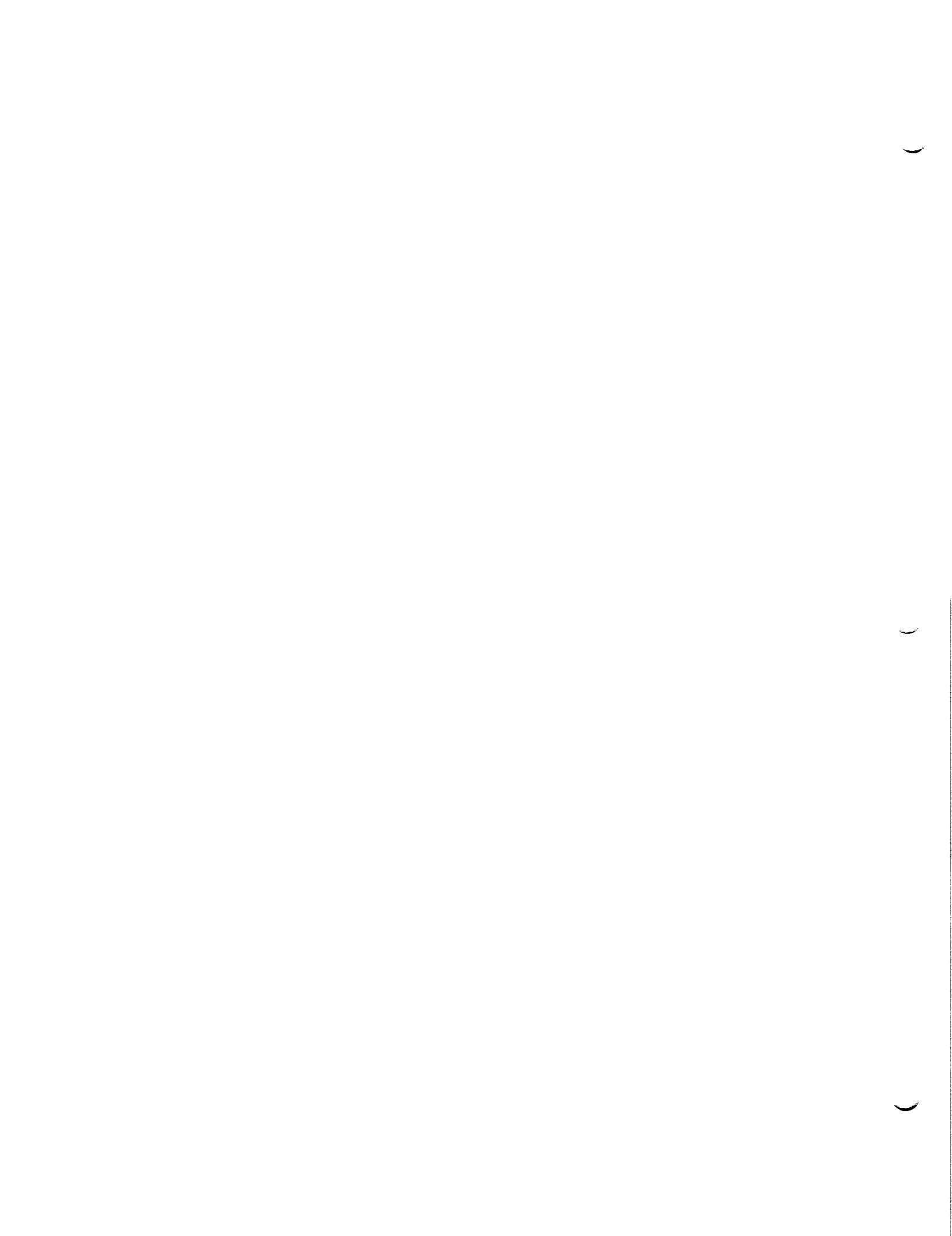
Bioregenerative Life Support

Abstract

Bioregenerative life support systems utilize plant growth for food, water, and atmospheric revitalization. Simulation studies of a simplified model suggest survivability in the face of partial plant growth chamber failure.

Introduction

The degree of closure for a life support system has been recognized to be mission dependent [Doll, 1990]. Each spaceflight mission may be characterized by four sets of parameters: available resources, resupply capability, crew size and mission duration. Resources such as energy and material are location dependent: is the mission near a body with a surface or atmosphere which may be mined for necessary resources? Does the mission trajectory allow for solar energy absorption? Resupply may be relatively inexpensive for low earth orbit missions and much more expensive, say, for a mars colony.

For a given set of parameters which would characterize a particular mission, finding the optimum degree of closure involves minimizing a specific combination of total power consumption, mass and volume. The weights of the minimized variables depended on the mission parameters. At the same time, the life support system must be optimized for maximum reliability and probability of survival.

Elements of a life support system include subsystems for the continuous supply of food, air and water as well as a waste management subsystem. A bioregenerative life support system would integrate biological materials within each subsystem, and may also operate in conjunction with an environmental control and life support system (ECLSS) such as that planned for Space Station Freedom. Alternatively, ECLSS may be seen as a back-up safety resource.

Simplifying Assumptions

Considered here are those missions which would necessitate an on-board capacity for the complete regeneration of the crew's food supply. The effect on the air and water supplies will be examined also. This analysis involves a series of simplifications in an attempt to discover the fundamental or primary dynamics of a closed biological life support system.

The growth of plant matter includes both inedible and edible fractions. The crew, of course, consumes the edible matter as well as a portion of the inedible fraction. Waste material from the crew and the inedible plant matter fraction extracted at harvest are oxidized together, yielding carbon dioxide and fertilizing

plant nutrients.   The crew produces also carbon dioxide and metabolic water.

The first simplification here limits the discussion of food stuffs to edible plant matter.   The overall empirical reaction [Volk, 1987] may be expressed as,

$$31.29 \ CO_2 + 27.81 \ H_2O + 1.74 \ HNO_3 \longrightarrow \qquad (1)$$
$$1.74 \ C_4H_5ON + 3.82 \ C_6H_{12}O_6 + 0.09 \ C_{16}H_{32}O_2 + 35.39 \ O_2$$
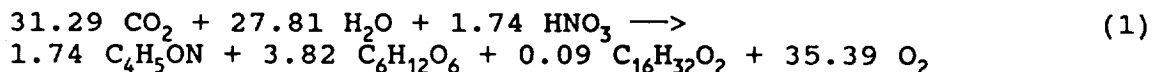
Since carbohydrate is the dominant foodstuff, limiting discussion to carbohydrate $(CH_2O)_x$ only, provides a key simplifying assumption. Were this the case, oxygen and carbon dioxide each would be produced and consumed on an equal molar basis.   This is equivalent to assuming a unity respiratory quotient (RQ), whereas, the nominal crew RQ is usually taken to be about 0.89.   The simplified plant growth equation thus becomes,

$$CO_2 + H_2O \longrightarrow CH_2O + O_2 \qquad (2)$$

Carbohydrates are completely oxidized by the crew.   All oxidation of waste material will be assumed to happen at about the same time.   The simplified oxidation equation then becomes,

$$CH_2O + O_2 \longrightarrow CO_2 + H_2O \qquad (3)$$

Not only is there molar equivalence between oxygen and carbon dioxide, but also of carbohydrate (and metabolic water).   That is, each mole of CO_2 absorbed by plants is assumed to produce one mole of CH_2O and one mole of O_2, while each mole of CH_2O is metabolized with one mole of O_2 and produces exactly one mole of CO_2.

Since the life support system is closed the total mass of each element (carbon, hydrogen and oxygen) must remain constant under the assumption of no cabin leakage.   Therefore,

$$mCO_2 + mCH_2O = \text{constant no. of moles} \qquad (4)$$

Model Development

In order to investigate the dynamics of the simplified model of a bioregenerative life support system, the following design parameters apply: The metabolic demand of a crew of eight is δQ_{crew} = 209 moles per day of carbohydrate consumed (or oxygen consumed, or carbon dioxide produced).   The nominal food storage will be 6 kmol, approximately a four week's supply of 22.5 kg per man.   On the other hand, the cabin atmosphere will be assumed to contain, nominally, 528 kg (18 kmol) carbon dioxide.

Plant growth is assumed to take 80 days to harvest.   No CO_2 uptake will be assumed to occur during a 10 day germination stage. During the next thirty days there would be a linear increase in the growth rate followed by 20 days of constant growth and 20 days of maturation having a linear decrease in the plant growth rate, or

CH_2O production. The daily increase in food is proportional to the number of plants, N_i, at each stage of growth, or,

$$\delta Q_{plant} = r \ \{\Sigma_{i=1:30} iN_{i+10} + 30\Sigma_{j=1:20}N_{j+40} + \Sigma_{k=1:20}(30-k)N_{k+60} \} \qquad (5)$$

where, $r = 0.0001436$ mole/plant-day^2.

Some authors have proposed multiple growth chambers [Babcock and Auslander, 1984] while others have proposed a system of continuous (daily) planting in a single plant growth chamber [Rummel and Volk, 1987]. The chaotic behavior observed under some conditions for the multiple chambered model may be due to the necessary multiplicity of state variables, whereas a single chamber non-linear model may be described by a single state variable.

An arbitrary, nominal planting rate of 1000 plants/day was chosen for a series of simulation studies. A maximum planting rate of 1500 and a minimum rate of 0 was set, with the planting rate adjusted by negative feedback with daily sampling of the total food storage. The system is simplified greatly by the view that CO_2 uptake by the plants results in foodstuff $(CH_2O)_x$ produced which immediately becomes part of the available food storage. This approach will not be valid, of course, in the event of the total depletion of the food supply and the immature plants are consumed. The model system is shown in Figure 1.
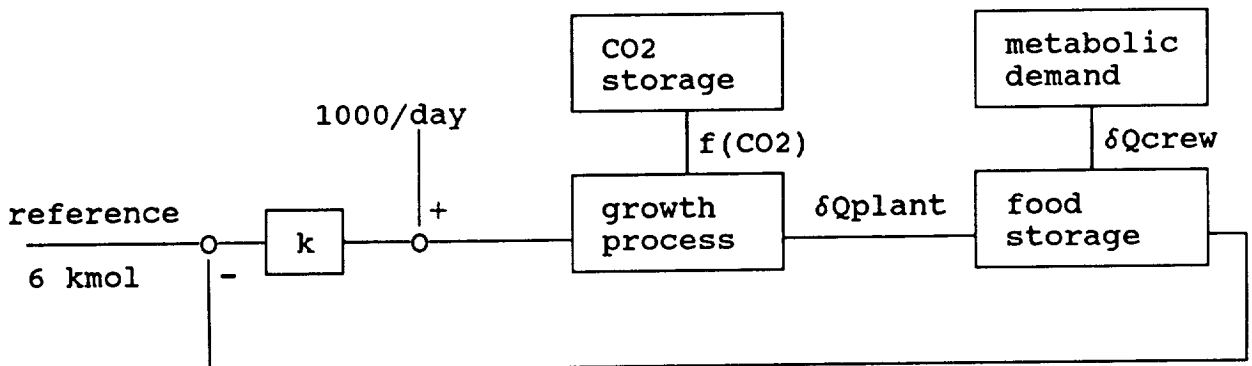
Figure 1. A block diagram of the planting control system.

Simulation Studies

A gain of 90 plants/kmol was found to provide good system response to a 30 day planting hiatus ($\approx$1.0 yr settling time) and survivability of a 50% crop loss. The growth-inducing effects of carbon dioxide in the atmosphere can be studied by assuming a linear CO_2 activation function, $f(CO_2)$. Under this assumption and a gain of 90 plants/kmol, the model predicted survival in the face of a 75% crop loss. In order to survive a 100% crop loss the food

stores would have to be increased in order to insure the food supply during the entire 80 day plant growth phase.

These simulation studies demonstrate the potential for a bioregenerative life support system on an extended mission. In addition to robustness and survivability in terms of the food supply, the plant growth chamber produces exactly the right amount of oxygen for the crew's metabolic needs. The amount of water taken up by the plants during food production is balanced by the crew's metabolic water production. However, this water would be overshadowed by the transpiration water in the plant growth chamber which is expected surpass the crew's demand several fold [MacElroy, 1989]. The excess water could be used for bathing and hygiene. There may be realized important psychological benefits which would result from passing purified waste water through the plant's transpiration system before introducing it into the crew's potable water supply.

References

Babcock, P. S., D. M. Auslander and R. C. Spear, "Dynamic considerations for control of closed life support systems," Advances in Space Research, vol. 4, pp. 263-270, 1984.

Doll, Susan C. and C. M. Case, "Life support function and technology analysis for future missions," SAE Technical Paper Series: 20th Intersociety Conference on Environmental Systems, Paper No. 901216, 1990.

Robert D. MacElroy and D. Wang, "Waste recycling issues in bioregenerative life support", in Controlled Ecological Life Support Systems: Natural and Artificial Ecosystems, NASA Conference Publication 10040, pp. 71-79, 1989.

Volk, Tyler and J. D. Rummel, "Mass balances for a biological life support system simulation model," in Controlled Ecological Life Support System: Regenerative Life Support Systems in Space, NASA Conference Publication 2480, pp. 139-146, 1987.

Rummel, John D. and T. Volk, "A modular BLSS simulation model," ibid. pp. 57-65, 1987.

1990

NASA/ASEE SUMMER FACULTY FELLOWSHIP PROGRAM

MARSHALL SPACE FLIGHT CENTER
THE UNIVERSITY OF ALABAMA

FREQUENCY RESPONSE OF ELECTROCHEMICAL CELLS

Prepared By: Daniel L. Thomas

Academic Rank: Assistant Professor

University and   The University of Alabama
Department: in Huntsville
                        Chemical Engineering Program
                        Mechanical Engineering Department

NASA/MSFC:
    Laboratory: Electronics and Information Systems
    Division: Electrical
    Branch: Electrical/Electronics Parts

MSFC Colleague: Teddy M. Edge

Contract Number: NGT-01-002-099
                        The University of Alabama
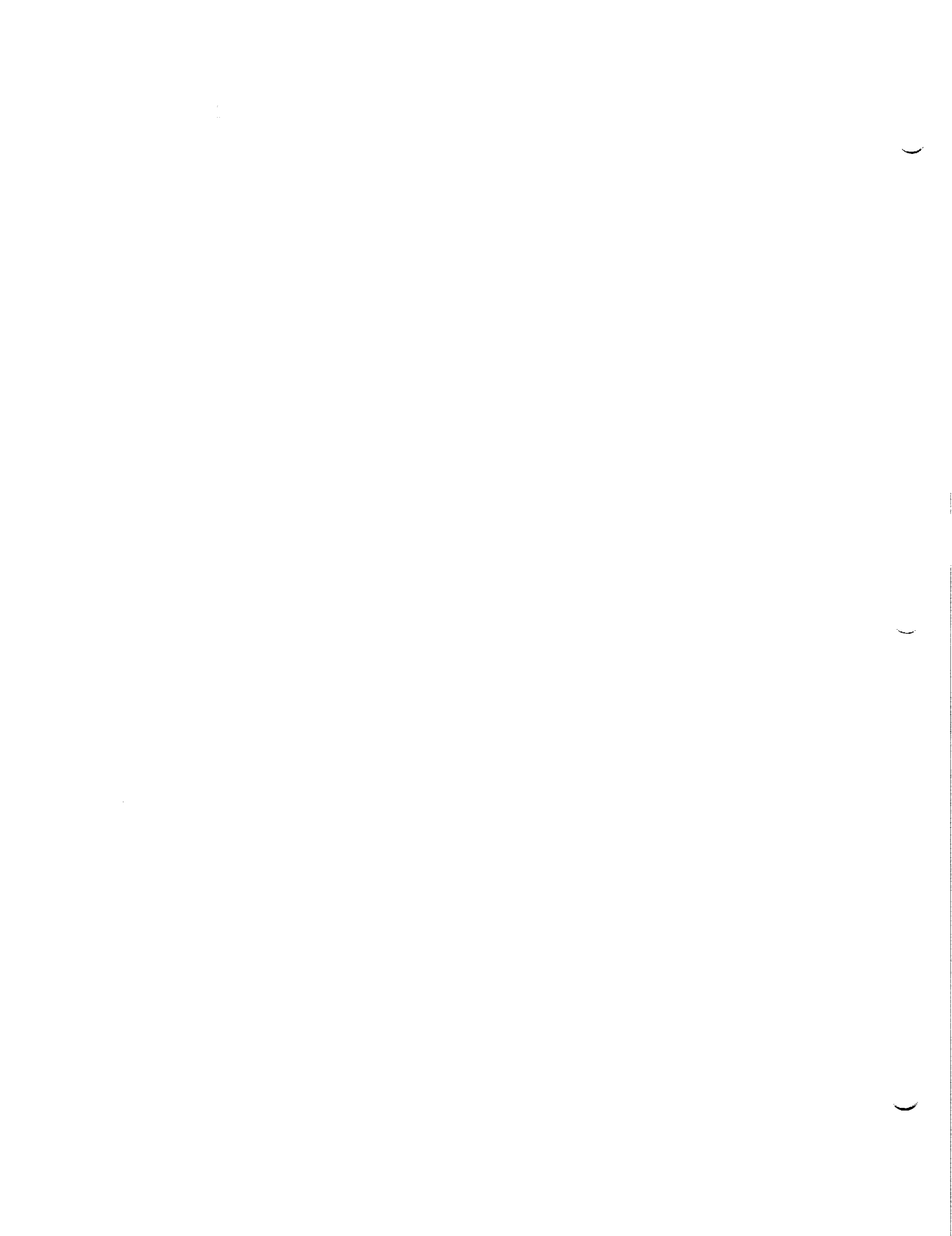
INTRODUCTION

Electrochemical processes may and have been studied using frequency response techniques and modeled using impedance concepts. Processes that occur at electrodes may be modeled as resistance, capacitance or complex impedance. More information may be gained using dynamic techniques than by using steady-state D.C. techniques. For example, one could study an electrode by measuring steady D.C. current and potential, or the same system could be studied using A.C. over a range of frequencies with an increase in the amount of information learned. Dynamic techniques have been used to estimate the specific area of porous lead-acid battery electrodes (Newman and Tiedemann, 1976), the kinetics and mechanisms of electrode reactions and a the rate of mass-transport processes such as diffusion (Bard and Faulkner, 1980). Attempts have been made to correlate cell state of charge with A.C. impedance spectra (Brodd and DeWane, 1963; Sathyanarayana et al., 1979). Zimmerman et al. (1982) studied the very low frequency impedance (as low as 0.1 Hz) of NiCd cells.

OBJECTIVES

The objective of this work was to examine the feasibility of using frequency response techniques 1) as a tool in destructive physical analysis of batteries, particularly for estimating electrode structural parameters such as specific area, porosity and tortuosity and 2) as a non-destructive testing technique for obtaining information such as state of charge and acceptability for space flight. It would be desireable to have a non-destructive battery test that can be run rapidly and as close to launch of spacecraft as possible. The battery frequency response may be such a test.

THEORY

The phenomena that contribute to the frequency response of an electrode include 1) double layer capacitance, 2) Faradaic reaction resistance, 3) mass transfer or Warburg impedance and 4) ohmic solution resistance. The double layer is a thin (about 20 Angstrom) layer of electric charge that exists at the boundary between two phases, such as an electrode/solution interface, and can be formed by preferential absorption of an ion on the surface or by orientation of polar solvent molecules. Double layers are also formed when a potential difference is placed across a cell. For example, if the applied potential is less than the decomposition potentials of the electrolyte or solvent then no steady state current can flow in the cell and there is no ohmic potential gradient. The applied potential difference occurs across the double layer. The double layer can be considered as an electric capacitor since it acts to store charge. The concept of the double layer was experimentally verified with mercury which has the advantage of a reproducible liquid surface and of inhibiting hydrogen evolution (Newman, 1973). The double layer capacitance is on the order of 10 $\mu F/cm^2$, which corresponds to a parallel plate capacitor with a plate separation of about 20 A, the double layer thickness. The double layer capacitance is potential dependent, but can be treated as constant over small (7 mV) potential range.

The Faradaic reaction resistance models chemical reaction rate at the electrode surface (current density) as a function of potential difference across the double layer. This resistance is highly non-linear, but can be linearized for potential perturbations of about 5 mV. Most electrodes used in practical energy systems exhibit combined chemicalreaction and double

layer charging. For a bare metal electrode in contact with solution this can be modeled as a parallel RC circuit.

Slow diffusion of reactants to the electrode surface or of reaction products away from the surface also causes the potential to lag the current. This impedance component is called Warburg impedance. For a planar electrode in a large excess of electrolyte solution a pure Warburg impedance causes a phase shift of 45 degrees that is independent of frequency. The Warburg impedance is usually manifested at frequencies less than 1 Hz. Measurments at frequencies as low as 0.0001 Hz have been reported. The period of such a measurement is about as long as a battery cycle, however the state of charge would probably not be altered significantly since the voltage and current amplitudes are small.

Finally, the ohmic resistance of the bulk electrolyte solution needs to be considered. Figure 1 shows a simple equivalent circuit for a planar electrode that includes all of the phenmomena discussed.

Most actual battery electrodes are high surface area porous electrodes, with the electrode processes are distributed throughout the electrode volume instead of at a single surface. One porous electrode model is the idealized cylindrical pore. The pore walls are the solid surface where the electrode reaction and double layer charging occurs. At the electrode grid all of the current is in the solid phase while at the electrode/separator boundary all of the current is in the liquid phase. The current is transferred from the liquid to the solid along the pore wall.

Figure 2 shows a model circuit for the pore, which is often called a transmission line model. The impedance Z can include reaction, double layer capacitance and Warburg impedance. The impedance of the electrode, assuming a very large solid conductivity, is

$$Z_{pore} = \frac{a}{km^2} \; \frac{\sinh(mL) + \frac{a}{m}\cosh(mL)}{\left[\frac{1}{\epsilon}\left(\frac{a}{m}\right)^2 + (1-\epsilon)\right]\sinh(mL) + \frac{a}{m}\cosh(mL)}$$

where

$$m^2 = R_f^{-1} + j\omega C \quad \text{Warburg impedance neglected}$$
$$L = \text{electrode thickness}$$

This is a rather complicated expression that includes hyperbolic functions of complex numbers. The method of non-linear least squares (Boukamp, 1986) can be used to fit experimental data to the expression and find the best values of the specific surface area a, the porosity ϵ , and the double layer capacitance and reaction resistance.

EXPERIMENTAL

Nickel-cadmium cells were constructed using electrdes from unused Eagle-Picher 50 A-Hr cells that had undergone destructive physical analysis. A negative and positive electode were placed in a plexiglass container. No separator was used, but an electrode spacing of 1 cm was maintained using plexiglass ribs. Nitrogen flowed continuously in the cell to prevent contamination by carbon dioxide. A Ag/AgO reference electrode was placed in a separate compartment with electrolyte. The two compartments were connected by a 1 mm Teflon tube filled with electrolyte. Electrolyte concentrations tested were 1% and 31% KOH.

A EG&G/PAR model 363 potentiostat was used to control the potential between the Cd and reference electrode. A Wavetek signal generator supplied the voltage perturbations that were added to the D.C. offset voltage of the potentiostat. The potential and current monitors of the potentiostat were connected to a Tektronics storage oscilloscope, from which the peak current, peak voltage and phase angles were obtained.

ACCOMPLISHMENTS

A significant amount of data for Ni and Cd electrodes in 31% and 1% KOH has been acquired. Quantitative data analysis will be performed during the coming months. Some initial observations are : 1) use of the 1% KOH seems useful for DPA since it results in phase lag at lower frequencies than for the 31% KOH. 2) Phase lags of greater than 90 degrees were observed at high frequency. One possible explanation for this is that dielectric polarization of one of the electrode materials becomes significant at high frequency.

A paper has been accepted for presentation at the Fall 1990 Electrochemical Society Meeting, and a second paper is being prepared for the Spring 1991 meeting.

FUTURE WORK

This summers effort has been concentrated on data acquisition. Quantitative data analysis, using the software developed this summer, will be performed in the coming months.

This effort will continue for at least one more year with the support of the Center Directors Discretionary Fund. State of the art equipment is being procured under that support that will enable data to be acquired with increased accuracy and rapidity. Future efforts will include 1) application of these techniques to nickel-hydrogen and silver-zinc batteries and 2) study of failed cells and development of non-destructive testing techniques. At least one graduate student will be involved in future research work.

REFERENCES

R.D. Armstrong and K. Edmondson, Electroanal. Chem. and Interfac. Electrochem, vol 53, pp 371-387, 1974.

R.D. Armstrong, K. Edmondson and J.A. Lee, J. Electroanal. Chem., vol 63, pp. 287-302, 1975.

A.J. Bard and L.R. Faulkner, Electrochemical Methods, J. Wiley and Sons, New York, 1980.

B.A. Boukamp, Solid State Ionics, vol 20, pp. 31-44 (1986).

R.J. Brodd and H.J. DeWane, J. Electrochem. Soc., vol 110, p. 1091, 1963.

R. Haak, C. Ogden and D. Tench, J. Power Sources, vol 12, pp 289-303, 1984.

R.J. Latham and N.A. Hampson, in Encyclopedia of Electrochemistry of the Elements, vol 1, A.J. Bard, ed., Marcel Dekker, New York, 1973.

J. Newman, Electrochemical Systems, Prentice Hall, Englewood Cliffs, NJ, 1973.

D.F. Pickett, Air Force Aero. Propulsion Lab., Report No. AFL-TR-75-34, 1975.

S. Sathyanarayana, S. Venugopalan and M.L. Gopikanth, J. Appl. Electrochem., vol 9, pp. 125-139, 1979.

W. Tiedemann and J. Newman, J. Electrochem. Soc., vol 122, pp 70-74 1975.

A.H. Zimmerman, M.R. Martinelli, M.C. Janecki and C.C. Badcock, ibid, pp. 289-298, 1982.

ACKNOWLEDGEMENTS
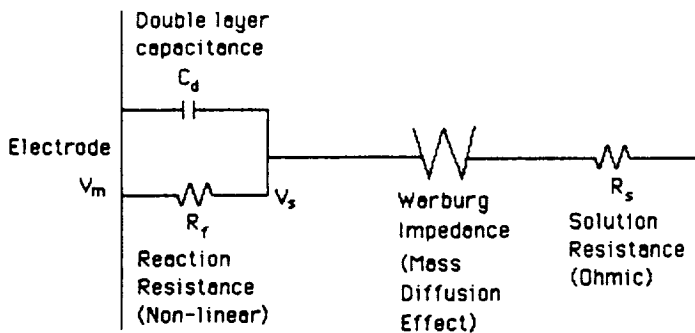
FIGURES

Figure 1. Equivalent circuit representing processes at a planar electrode.
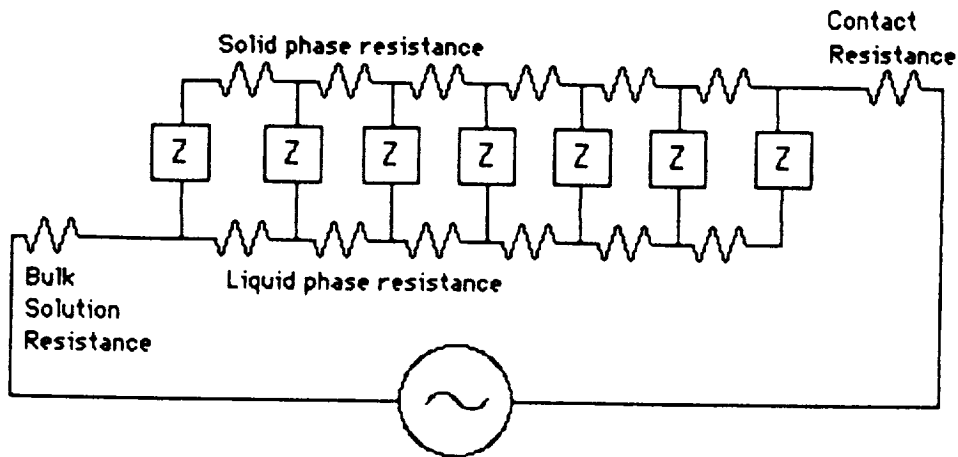
Figure 2. Equivalent circuit representing processes in an idealized pore.

1990
NASA/ASEE SUMMER FACULTY FELLOWSHIP PROGRAM

MARSHALL SPACE FLIGHT CENTER
THE UNIVERSITY OF ALABAMA

"DESIGN AND IMPLEMENTATION OF A GROUND CONTROL
CONSOLE PROTOTYPE FOR OMV"

Prepared by: Bruce L. Walcott
Academic Rank: Assistant Professor
University and   University of Kentucky
Department: Electrical Engineering

NASA/MSFC:

    Laboratory: Information and Electronics System
    Division: Guidance, Control and Opt. Sys. Div.
    Branch: Control Electronics

MSFC Colleague: Tom Bryan

Contract No.:   NGT-01-002-099
                          The University of Alabama
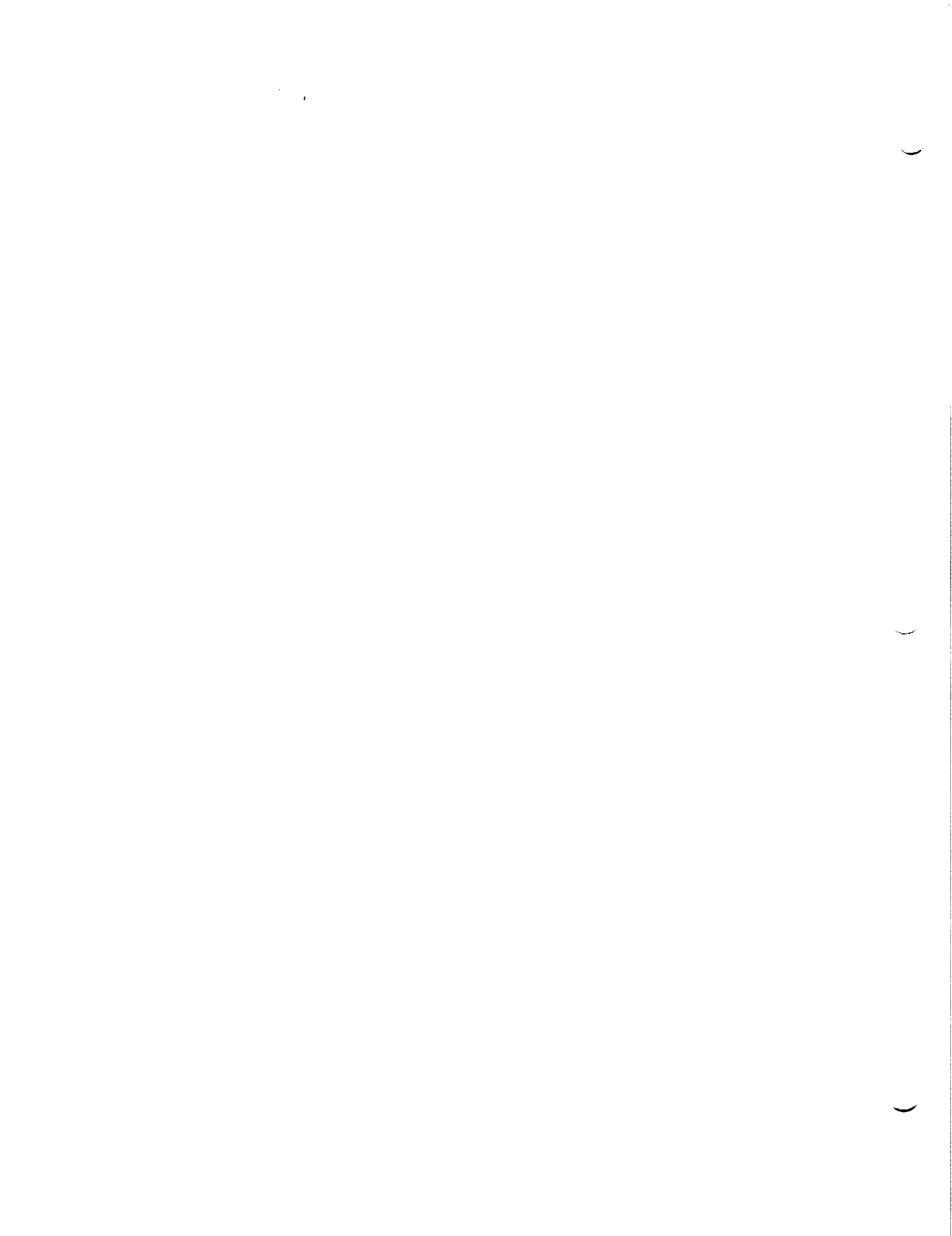
1 Introduction

The Marshall Space Flight Center in Huntsville, Alabama is home to the largest precision flat floor facility in the world. This 4200 square foot floor is constructed of self-leveling black epoxy and is flat to with 1/1000 of an inch over any given square yard and to within 3/1000 of an inch from corner to corner. Two vehicles are used to perform satellite capture and rendez-vous and docking simulations. The first of these is a 2 ton air-bearing vehicle which has a total of 6 degrees of freedom (DOF). The second vehicle is the 8 DOF dynamic overhead target simulator (DOTS). One of the primary uses of the floor is to perform autonomous and teleoperated docking of vehicles similar to NASA's Orbital Manuevering Vehicle (OMV). Using both the air-bearing vehicle and the DOTS in tandem, even the most difficult OMV docking problems can be simulated. It is important to note at this juncture that even though the OMV project was cancelled mid-way through this project, a next generation OMV is slated to return sometime in 1996.

In the past, prestigious high-tech corporations such as General Electric, TRW, and Martin Marietta have utilized the flat floor and the DOTS to develop and validate docking and rendezvous strategies as well as to investigate contact dynamic problems. Recently, Grummond has developed and shipped a Tumbling Satellite Retrieval System to the Flat Floor which has been installed on the front of the 8 DOF Dynamic Overhead Simulator. These companies have future commitments to the flat floor facility thereby making continual operation and functionality enhancement a high priorities of NASA.

New developments in the evolution of the Flat Floor Facility includ refurbishing of the Dynamic Overhead Target Simulator, a 70 x 30 flat concrete extension yielding a total of 125 feet of length, and the installation of a high fidelity lighting system, which is currently in progress. These improvements further add to the capability of the Flat Floor to recreate a realistic environment for autonomous and tele-operated vehicle operation.

2 Task Description

The OMV was planned to be flown from the ground by a pilot via tele-operation. TRW, the primary contracters on the OMV, have developed specifications for a prototype Ground Control Console (GCC) from where the vehicle will be flown. In order for testing of the OMV to occur at the Flat Floor facility, this Ground Control Con-

sole must be replicated. The project for the 10 week duration of the NASA/ASEE Summer Faculty Fellowship is to perform system design and development on a prototypical Ground Control Console to be used in conjunction with the 8 DOF Dynamic Overhead Target Simulator. Unfortunately, funds at Marshall Space Flight Center are limited thus the equipment available for the project is very limited in capability.

The equipment on hand for the project includes

Hardware

- 1 IBM AT (80286) Clone running at 12 MHz.

- 1 640 x 512 RGB monitor

- 1 Matrox PIP 640 frame grabber and processor

- 8 Micro Switch Programmable Display Pushbutton Switches

- 1 IBM Personal Computer Data Acquisition and Control Adapter

- 2 3 DOF Handcontrollers

Software

- Matrox PIP EZ

- Microsoft C 5.1

- Microsoft Assembler 5.1

The project was divided into three primary tasks: The design and development of the Video Display using the RGB monitor and the Matrox PIP 640 frame grabber; the design and development of the switch panel using the Micro Switch Programmable Display Pushbutton Switches; and finally the design and development of the hand controllers using the 3 DOF hand controllers and the IBM control adapter. Of course, a final task is to perform system integration on the results of these three primary tasks.

3 Project Summary

Due to the limited space available for this final report (4 pages maximum), only the highlights of the project will be outlined.

The first task – design and implementation of the Video Display – began the last few days of last Summmer's Fellowship Program (circa, August 1989). The engineering challenges presented by this task included learning the PIP-EZ library routines and their functions. Also, a scheme had to be devised in which graphic overlays could be placed over live incoming video. This was accomplished by using scaling and keying. First, all incoming video was scaled to the upper 64 pixels values out of a possible 256. Next, the remaining 192 pixels were used as a pallette from which colorful graphics could be created by means of scaling and a look-up table. These graphics were preserved by utilizing the keying function in the PIP-EZ library. The last challenge in constructing the Video Display was to perform real-time metering using the graphic overlays. To accomplish this feat, the current meter values had to be rewritten in the background color (i.e., erased), then new values written in the correct meter color. Due to the primitive and slow graphics capabilities of the PIP 640, all meter updates had to be performed using standard text commands.

The second task – utilizing the programmable switches to implement the GCC swtich panel – presented major engineering challenges. Most prevalent among these was the development of an RS-232 interrupt driven interface for the switch controllers. After spending most of the 10 weeks trying to debug such an interface, it is recommended that in future the RS-422 parallel interface be used when communicating to the switches.

The last task of interfacing the two 3 DOF hand controllers was relatively straight forward. The IBM control adapter had been used in last years project and NASA engineer, Charles Oliver, had developed a number of routines which proved to be invaluable. The GCC specifications required that the analog handcontrollers be used in pulse mode. This was easily accomplished via use of a quad comparator and the digital inputs on the IBM control adapter.

The completed prototype can be viewed at the Flat Floor Facility of EB24 in building 4619.

4   Future Work

Future work on the GCC includes the incorporation of a new, inexpensive high resolution Matrox imaging board called the Illuminator 16. The Illuminator 16 has real-time video insert capabilities built-in as well as hardware pan and zoom. Furthermore, the Illuminator 16 will support a high resolution (1024 x 1024) monitor.

Next, the GCC must be interfaced to the Dynamic Overhead Target Simulator driver program written by Control Dynamics Corporation which currently resides on the VAX 3602 at the Flat Floor facility.

5   Acknowledgements

1990

NASA/ASEE SUMMER FACULTY FELLOWSHIP PROGRAM

MARSHALL SPACE FLIGHT CENTER
THE UNIVERSITY OF ALABAMA

CHARACTERIZATION OF THE CORROSION RESISTANCE OF SEVERAL ALLOYS TO DILUTE BIOLOGICALLY ACTIVE SOLUTIONS

Prepared By: Daniel W. Walsh, Ph.D.

Academic Rank: Professor

University and   Cal Poly State University, SLO
Department: Materials Engineering

NASA/MSFC:

    Laboratory: Materials and Processes
    Division: Metallic Materials
    Branch: Corrosion

MSFC Colleague: Merlin D. Danford, Ph.D.

Contract No: NGT-01-002-099
                                The University of Alabama

L

ABSTRACT

Sulfate reducing bacteria (SRB) and acid producing bacteria/fungi detected in hygiene waters increased the corrosion rate (measured by resistance polarization) in Al 2219-T87. Furthermore, biologically active media enhanced the formation of pits on metal coupons. Direct observation of gas evolved at the corrosion sample, coupled with scanning electron microscopy and energy dispersive x-ray analysis of the corrosion products indicates that the corrosion rate is increased because the presence of bacteria favor the reduction of hydrogen as the cathodic reaction, instead of the production of (OH) - through the reaction of oxygen and water. SEM verifies the presence of microbes in a biofilm on the surface of corroding samples. The bacterial consortia are associated with anodic sites on the metal surface, aggressive pitting occurs adjacent to biofilms. Many pits are associated with triple points and inclusions in the aluminum alloy microstructure. Similar bacterial colonization was found on the stainless steel samples. Fourier Transform Infrared Spectroscopy (FTIR) confirmed the presence of carbonyl groups in pitted areas of samples exposed to biologically active waters.

OBJECTIVE

The objective of this project was to examine the corrosion resistance of several alloys (Aluminum 2219-T87 & AISI 316L Stainless Steel) to biologically active agents found in Environmental Control and Life Support System (ECLSS) waters. An attempt was made to correlate corrosive attack to the microstructure and compositions of the alloys examined, to the electrochemistry of the fluid media and to the microbial population of the ECLSS waters.

INTRODUCTION

The study of microbiologically influenced corrosion (MIC) is an interdisciplinary effort. An understanding of metallurgy, microbiology and electrochemistry is crucial to the resolution of MIC problems.

MIC is recognized as a major problem in many industries. The MIC problem is ubiquitous; most alloys, with the possible exception of titanium based alloys, are affected by MIC. The problem is particularly insidious because MIC can occur during system construction, during operation, or during shutdown periods. In fact, extended periods of shutdown can be particularly damaging. The stagnant water and other opportunity for the proliferation of micro-organisms. Researchers have developed an understanding of environments that promote MIC, materials susceptible to MIC, methods to detect damaging organism and

empirical approaches to the treatment and prevention of MIC. However, little understanding of the metallurgical bases for these processes has developed. Microbes attach to a variety of areas on the metal surface and form discrete deposits. In some cases these have been observed to form preferentially near weldments. Many researchers have examined the characteristics of micro-organisms as they relate to MIC. Few however, as a result of forming, welding or heat treating, has on their susceptibility to MIC. Microbes are living agents of corrosion. Their size (0.2u to 100u long, .2u to 5 u wide) provides them access to structural chemical and toward food, microbes often have specific receptors for target chemicals in their environment. Nutrients that may be scarce in flowing water are concentrated at metallic surfaces - Darwinism dictates that those microbes able to attach and establish themselves on metal surfaces will be at an advantage in such environmoents. Microbes can withstand wide temperature variation (-10 to 99 deg C), prolific and can exist in large colonies. Most microbes are able to form extra-cellular slime layers. This slime layer can also be involved in the formation of oxygen depletion cells, it can act as a sequestering agent for corrosion products and accelerate corrosion, and it can act as a barrier to biocide.

Many species of microbes produce a variety of organic acids, and enzymes that may influence the rate of corrosion. Hydrogenase, and metallic sulfides (product of SRB) have been reported to depolarize cathodic sites and accelerate corrosion. Some bacteria directly oxidize or reduce metallic ions. Carbon dioxide produced can become carbonic acid. The accretion of low solubility reaction products can lead to concentration cells. Microbes can form synergistic communities with other microbes or with higher life forms. These consortia can accomplish complex chemical reactions and can create aggressive environments. Organisms that produce organic acids under biofilms can lower local pH drastically. Any bacteria that contributes to the oxidation of metal ions will, at minimum, cause a passive co-accumulation of negative ions (e.g. Cl-). This may lead to the formation of acidic ferric chloride, cuprous chloride, magnesium chloride etc..solutions at crack tips, producing an in-vivo stress corrosion cracking environment more severe than many in-vitro tests. Slime layers produce a crevice like anaerobic environment in which passive films damaged by abrasion or by halide ion attack go unrepaired. The biofilm can consume oxygen, and prevents oxygen in the external environment from reaching the surface and restoring passive films; this work has shown that it may also promote cathodic reactions that do not involve oxygen.

SRBs can flourish in the anaerobic environment at the film metal interface, rendering the environment more chemically aggressive and providing several mechanisms to depolarize the rate limiting cathodic reaction. A catalogue

of microbes implicated in MIC of various alloy systems is provided in the literature.

Metal surfaces are extremely heterogeneous. Regional differences are so well defined that local anodes and cathodes form and corrosion can take place on individual pieces of metal. Surface condition, stress state, microstructure, chemistry and inclusion size and distribution affect local electrochemistry and MIC susceptibility. In many cases, welding seems to favor MIC. Welding changes the surface texture in the vicinity of the weld, produces local stress fields and causes other chemical, microstructural and mechanical changes that will affect the way microbes interact with the weld region.

Corrosion implies the existance of an anode, where oxidation of metallic atoms to soluble metallic ions takes place. Cathodic regions, where reduction takes place, balance the reaction. In systems where external current is not supplied, anodic and cathodic currents must be equal. Reactions at the anode and the cathode can be described as "half reactions", whose sum is the total corrosion reaction. Corrosion potentials are thermodynamic quantities, measured at equilibrium, and as such indicate what is possible. Corrosion currents are kinetic values, and reflect dynamic, nonequilibrium processes at electrodes. Typically there is one anodic reaction, however there may be several cathodic reactions; which is favored depends on the chemistry of the environment. In the system studied, pH was near neutral, and two cathodic reactions are probable:

$$O_2 + 2H_2O + 4e- = 4OH-$$
$$2H_2O + 2e- = H_2 + 2OH-$$
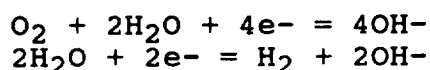
In biologically active media other reactions are possible, including the reduction of metal ions themselves, or the reduction of sulfate.

When current flows in a corroding system, the potential difference between cathode and anode diminishes, this decrease is termed polarization. Polarization decreases the corrosion rate, and can occur at either anode or cathode. The phenomena can be caused by concentration effects - a necessary reactant is depleted at an interface, by activation effects - a crucial reaction step requires large activation energy (Tafel kinetics), or by ohmic effects - resistance at the interface slows the corrosion process. Many researchers ascribe MIC to depolarization accomplished by microbial agents. Some evidence for depolarization was found in this study.

MATERIALS AND PROCEDURES

Disks of Al 2219 and 316L stainless steel, 5/8" in diameter were degreased in trichloroethylene, and washed with ethanol to remove surface films. Disks were used for

polarization resistance studies in an EG&G 350A laboratory apparatus. These studies were extended over a three week period. The program POLCUR, as modified by Danford, was used to estimate Tafel Constants and calculate corrosion rates. A polarization resistance measurement is performed by scanning through a potential range very close to Ecorr, large potential swings that damage the coupon surface are avoided. The corrosion current is related to the slope of the E-Ecorr/ current plot at E-Ecorr equal to zero through the Stern-Geary relationship:

$$Icorr = B_a B_c / [2.3(B_a + B_c) R_p]$$
B_a, B_c are anodic and cathodic Tafel Slopes

Cells employed mild corrosive water, sterile corrosive water, and corrosive water with a 10,000 to 1 dilution of ECLSS waters as electrolytes. Disks were also exposed to the same media in erlenmeyer flasks, and examined by optical and scanning electron microscopy after fixing in formaldehyde. Optical microscopy for biological agents was accomplished by staining with acridine orange, and photographed using an epiflourescence microscope. Specimens for SEM were prepared by drying in absolute ethanol and freon, then sputtercoated with Au. Regions of these disks were examined with FTIR and EDAX.

RESULTS AND DISCUSSION

Figures 1 and 2 show Icorr over a three week period. Note that initial measurement are not enough to define the relationship that develops over longer periods. The 2219 exposed to sterile corrosive water corrodes at much lower rates than either the laboratory corrosive water or the ECLSS added media. In addition, few pits (2) were found on the sterile coupon when examined at 50X, limited localized buildup of hydroxide was noted, and limited gas evolution was observed. In contrast, the coupons exposed to biologically active media exhibited numerous pits, were covered with hydroxide mounds, and produced copious amounts of gas. Many pits formed adjacent to bacterial buildups. Bright, reduced surfaces were present under the buildup, as were additional pits. The corrosion rates of stainless steel in these same media are several orders of magnitude lower. Further, the stainless coupon exposed to sterile water corrodes most rapidly. MIC kits from BioIndustrial Technologies Inc. indicated the presence of SRB's and acid producers in ECLSS waters diluted 10,000 to 1 and used as test media in the EG&G 350A for five days. Minitek analysis of similar media strongly indicated the presence of several Pseudomonas bacteris (paucimobilis and pickettii) in the ECLSS added solutions. One species, Moraxella was found in sterile waters that had been used as a test media for five days. Biofilm development was evident on Al 2219 exposed to

ECLSS waters for one day, similar films were found on the stainless steel samples. Notice the relation between the nascent pit and the biomass. EDAX of similar pitted areas on samples exposed for a five day period showed high concentrations of sulfur, and $CuAl_2$ particles in relief. Reflectance FTIR spectra of samples exposed to ECLSS waters for five days was contrasted with samples exposed to sterile waters for the same period. Carboxyl groups were evident in the bioactive sample, indicating the presence of organic acids on the surface.

CONCLUSIONS

1) SRBs and acid producing bacteria are present in ECLSS waters.
2) MIC of Al 2219 was evident in the media studied.
3) Colonization of the 316L samples was evident.
4) Enhanced corrosion of Al 2219 is caused by promotion of the more rapid hydrogen evolution reaction at the cathode. This occurs because the bacteria metabolize oxygen near the interface and produce a film that fosters anaerobic conditions. In addition, the action of SRBs serves to favor this reaction.
5) The formation of sulfides and/or the presence of hydrogenase may serve to depolarize the cathodic reaction.
6) The presence of acid producing bacteria, in conjunction with the identification of carboxyl groups in FTIR of sample surfaces indicates that organic acids may aggravate corrosion in this system.
7) Microbes act as "catalysts" for corrosion, in a literal and in a figurative sense. They are adaptable, rapidly locate susceptible areas, locally fix anodes, accumulate corrosive chemical agents from their environment and produce corrosive metabolic end-products.

ACKNOWLEDGEMENTS

The list of people who deserve thanks reads like roll call at the M&P lab. Proceeding east to west, special thanks are due Dr. Merlin Danford, who had the unenviable task of "teaching teachers" this summer, but was always there with guidance, support, interest and Red Diamond. Thanks to Joe Montano who got me here, Barry "softball mogul" Moody, Carla Hooper, Wendell Deweese, Fred Gluszek, Jim Coston, Jeff Sanders and the rest of the Corrosion and Failure groups. The microbiology group in the western wing went out of their way to help and advise at every juncture. Special thanks are due to Dr. Elizabeth Rodgers, Gwinneth Smithers, Tim Huff and Don Ovenjuber. I hope that I have not "bugged" people too much this summer. Thanks to Mike

Freeman and Frank Six, without whom the program would not exist.

Figure 1
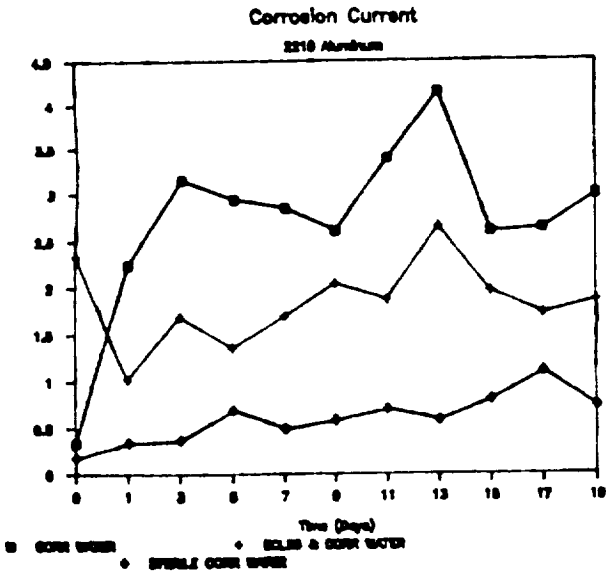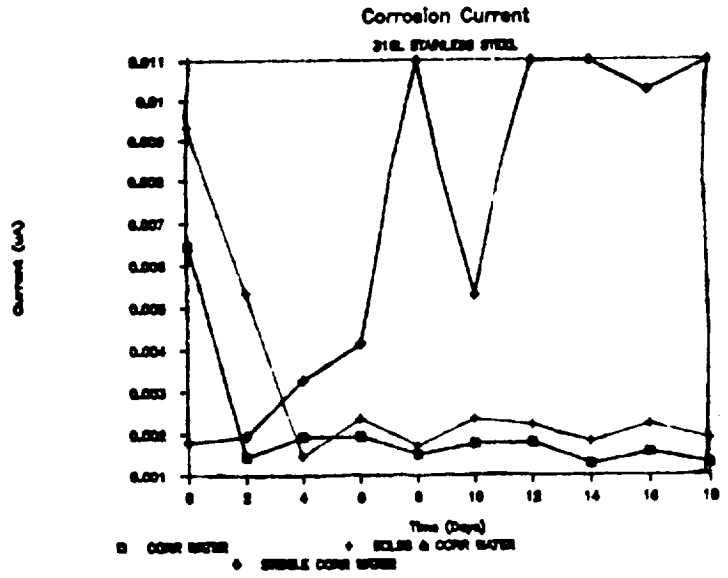
Corrosion Current

2219 Aluminum

Figure 2

Corrosion Current

316L STAINLESS STEEL

1990

NASA/ASEE SUMMER FACULTY FELLOWSHIP PROGRAM

MARSHALL SPACE FLIGHT CENTER
THE UNIVERSITY OF ALABAMA

GRAPHICS MODELLING OF NON-CONTACT THICKNESS MEASURING ROBOTICS WORK CELL

Prepared by: Charles W. Warren

Academic Rank: Assistant Professor

University and   The University of Alabama
Department: Mechanical Engineering

NASA/MSFC:

    Laboratory: Materials and Processes
    Division: Process Engineering
    Branch: Chemical and Non-Metals Processes

MSFC Colleague: Eutiquio Martinez

Contract No.:   NGT-01-002-099
                            The University of Alabama
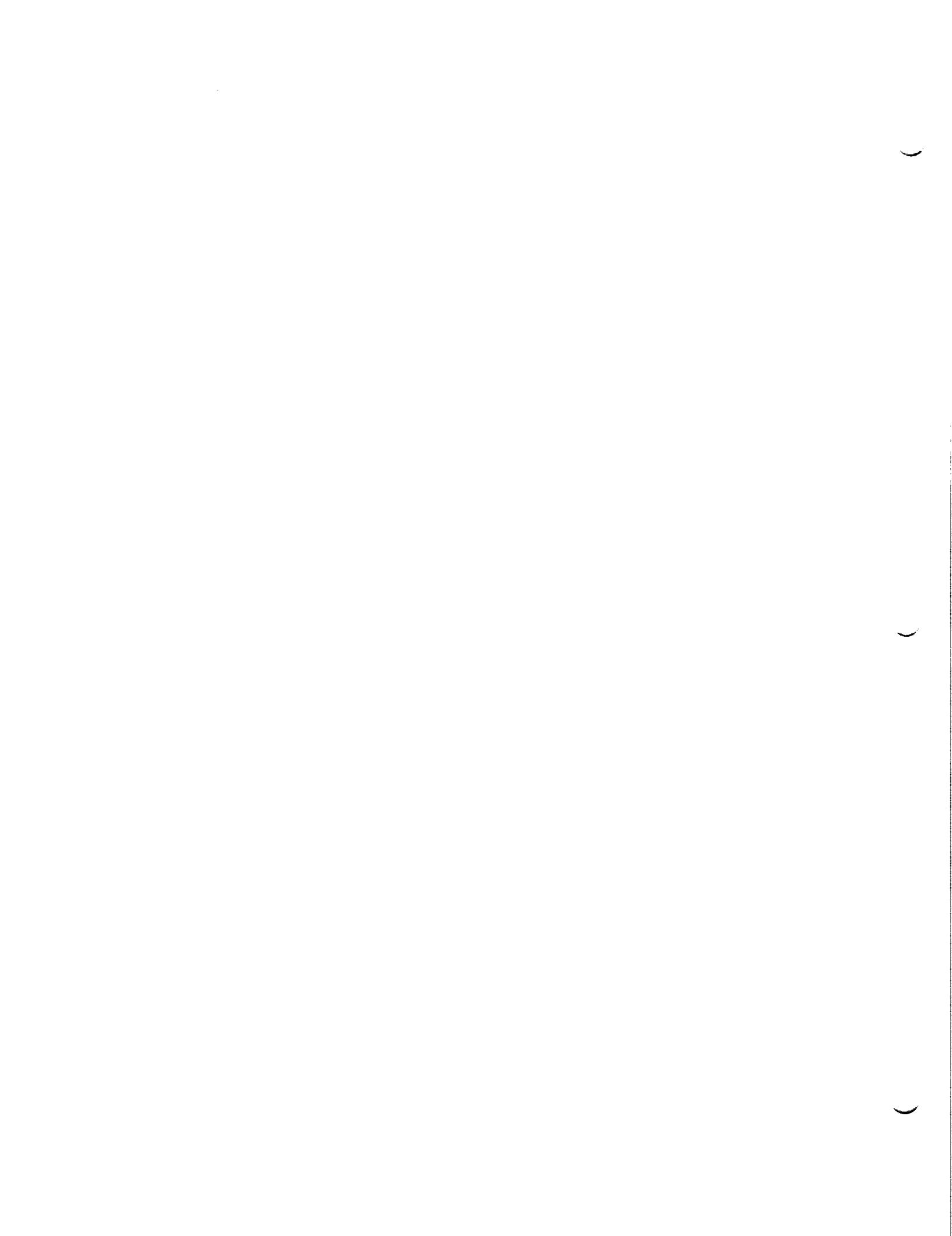
1 Introduction

The goal of this research task is to develop a system for measuring, in real time, the thickness of a sprayable insulation during its application. Two types of insulation are to be considered: MSA (Marshall Sprayable Ablator) and SOFI (Spray On Foam Insulation). By measuring the thickness of the coating during the spray process (on-line), more precise control of the process can be achieved.

An additional requirement on the system is that it must use non-contact measurement devices. The surface of the coating will be wet during the spray process and must be undisturbed during measurement.

The short term, (10 week summer), goal of this project was to graphically model the system, off-line, using a state-of-the-art graphics workstation and associated software. This model was to contain a three dimensional color model of a workcell containing a Cincinnati Milacron T3-776 robot and an air bearing turntable. The second phase of the 10 week project was to establish a communication link between the graphics workstation and the robot's controller. Sequences of robot motion generated by the computer simulation are transmitted to the robot for execution. The sections that follow describe these items as well as some additional hardware work that was performed.

2 Graphic Simulation

The graphic simulation was performed on a Silicon Graphics Iris 3120 workstation using the Igrip software from Deneb Robotics, Inc. This software allows coordinated motion between various devices in the workcell. In this case it will be the robot carrying the non-contact sensing device and a large cylinder mounted on the air bearing turntable.

The Igrip software gives an operator the ability to design new devices and experiment with the motion of its parts without actually fabricating hardware. This is ideal for the design and testing of robot systems. Deneb Robotics also markets accurate robot models that can

be retrieved to become part of the workcell. For this project, the Cincinnati Milacron T3-776 robot was to be used. This robot model is available as part of robot library from Deneb. It is then the duty of the operator to position the base of the robot in the workcell and to verify that the desired motion can be achieved from this location. Also, any end effectors to be used must be attached by the operator.

The second part of the workcell model was the air bearing turntable. This model is not available from the robot library and was developed. The model used consists of a stationary base that will be rigidly mounted to the floor. A right cylinder was used to model this fixed base. Air bearing turntables come in a variety of styles, so a cylinder was used as a generic model in lieu of a specific style. The rotating part of the turntable was placed atop the fixed base cylinder.

Once the parts of the turntable were completed, kinematics were assigned for the device. For a kinematic simulation, the motion of the parts in a device relative to one another must be known. The turntable model is relatively simple: The upper part of the turntable rotates about the axis of symmetry of the fixed base. Once this is assigned, the maximum angular velocity and the angular acceleration profiles of the turntable are assigned.

The thickness measurement system was to be generic, for the most part, so that it could be used with various coating systems. MSA is sprayed on segments of the SRB's, (Solid Rocket Booster). A right circular cylinder was used to depict one of these segments, although measurement will not be restricted to this. This cylinder is then attached to the turntable model and is fixed to the rotational part of the turntable.

The measurement hardware has not been selected for the system yet. A small package containing two cylinders and an air jacket surrounding them was used to depict the non-contact measuring device. This device will be updated when measurement hardware is selected. The graphic model is attached to the robot model at the last link and is assigned the kinematics of that link. The robot's tool point is then moved to the end of the measurement device.

The total system is now completed by placing the various devices at their appropriate location in the workcell. The base of the robot became the origin for the wokcell and the location of the turntable was determined so that most of the sprayed cylinder would be within the reach of the measurement device mounted on the robot. Following this, the motion of the turntable was coordinated with the robot so that the measurement device could be positioned at any desired location on the cylinder. Coordinated motion is achieved by establishing I/O, (input–output), connections between the robot model and the turntable model. Simulation runs were then developed to show a typical sequence of moves of the robot and the turntable.

3 Communication

The goal of this phase of the project was to establish a communication link between the graphic simulation and the robot's controller. Software is available from Cincinnati Milacron, called ROPS (Remote Off-line Programming Software), for communicating between a host VAX computer and the robot's controller. In theory, sequences of robot moves are determined on the graphic workstation, the files that contain these are transferred to the VAX host computer, and finally are translated into the robot's machine code and downloaded from the VAX computer to the robot.

In practice, however, there is a problem. The Deneb software does not properly output coordinate data to the ROPS program. The Igrip software uses Z–Y–X Euler angles to define the rotations of rigid bodies, while the ROPS software uses Z–Y–Z Euler angles. A program was written to convert the data files from the Igrip software into data files compatible with the ROPS software. The procedure is to rebuild the transformation matrix using the data from Igrip and then extract the Z–Y–Z Euler angles from this matrix. Once the conversion software was completed, several sequences of robot moves were downloaded without error.

4 Hardware

The original ten week goals were accomplished ahead of schedule. This allowed time to begin on the hardware aspects of the project. The first step was to determine what types of sensors are available, (off the shelf), for measuring the thickness of coatings. The sensors fall into three major categories: optical, acoustic, and inductive and capacitive. After discussion with several vendors of these devices, it appears as though the ultrasonic (acoustic) and the laser (optical) sensors are best suited for this task. Two sensors have been sent by vendors for evaluation and two others were demonstrated by other vendors.

5 Future Work

There is quite a bit of work left to do on this project in the areas of sensor evaluation, measurement system design, and final hardware designs. To fully evaluate the various sensors that are available, several need to be acquired and tested in a controlled environment as well as in the spray environment in which the sensors will ultimately be used.

Once the appropriate sensors have been selected, a complete measurement system needs to be developed. Questions to be answered include the placement of the sensors and any additional actuators that will be needed to move the sensors to various places within the workspace. Finally, an engineering design and analysis needs to be completed for any hardware to be constructed for use with the measurement system.

1990

NASA/ASEE SUMMER FACULTY FELLOWSHIP PROGRAM

MARSHALL SPACE FLIGHT CENTER
THE UNIVERSITY OF ALABAMA

IMPLEMENTATION STRATEGIES
for
LOAD CENTER AUTOMATION
on the
SPACE STATION MODULE/POWER MANAGEMENT AND DISTRIBUTION TESTBED

Prepared By: Karan Watson

Academic Rank: Associate Professor

University and   Texas A&M University
Department: Electrical Engineering

NASA/MSFC:

        Laboratory: Information and Electronic Systems
        Division: Electrical
        Branch: Electrical Power

MSFC Colleague: Louis Lollar

Contract No: NGT-01-002-099
                                The University of Alabama
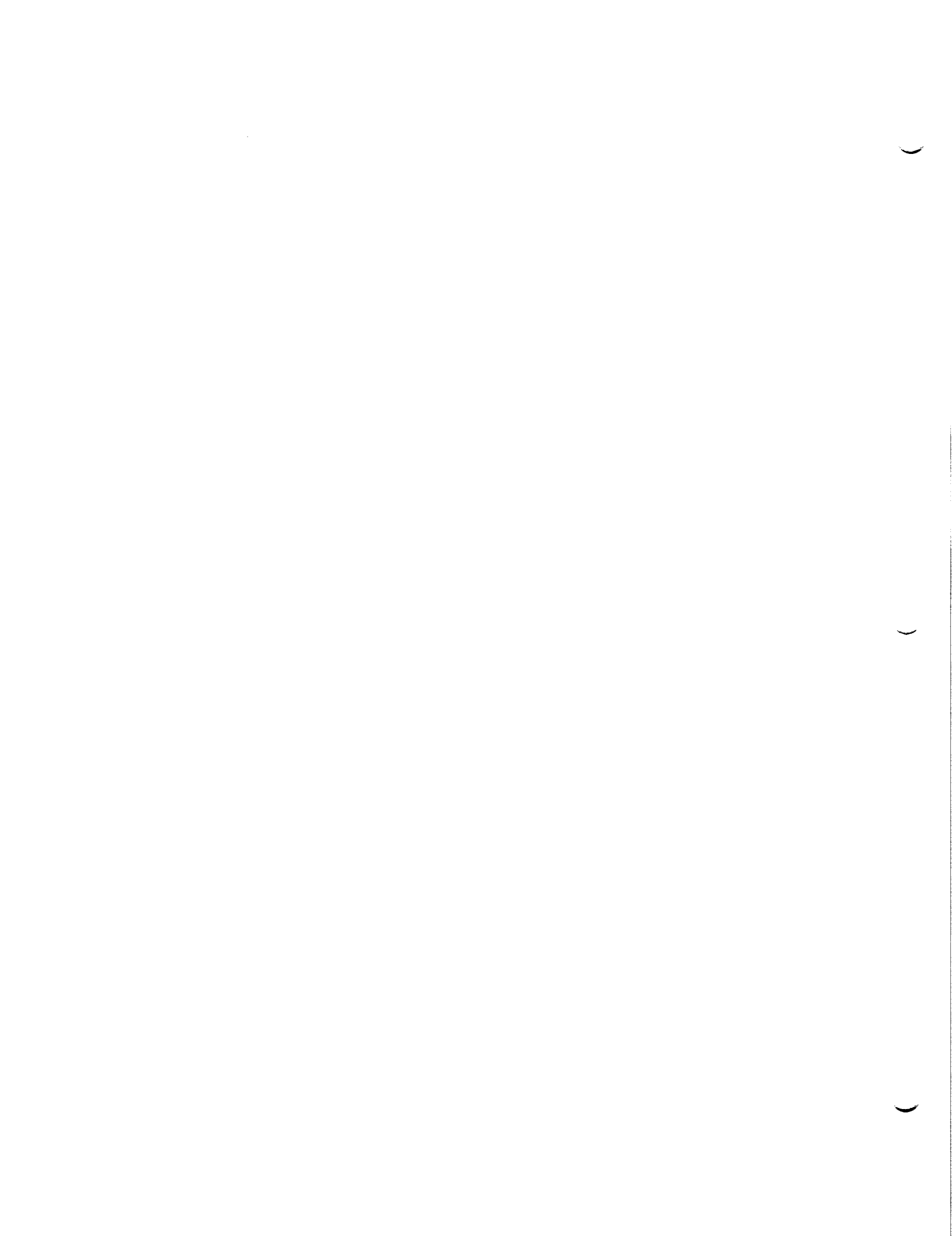
THE LOAD CENTER AUTOMATIOM ON THE SSM/PMAD

The Space Station Module/Power Management and Distribution, SSM/PMAD, testbed has been developed at the NASA-Marshall Space Flight Center in order to study the tertiary power management on modules in large spacecraft. This testbed has been developed to be flexible (as an example of this it was changed from a 20Khz to a DC system in 1989). The goal has been to study automation techniques, not necessarily develop flight ready systems. Because of the confidence gained in many of the automation strategies investigated, it is appropriate at this time to study, in more detail, implementation strategies in order to find better trade-offs for nearer to flight ready systems. These trade-offs particularly concern the weight, volume, power consumption and performance of the automation system. With this in mind the Load Center automation systems were studied. These systems, in their present implementation are described in sections I-IV. In section V a recommendation for a new implementation strategy is made.

I. THE RPC

The purpose of the Power Controller, RPC, is to provide the actual switch which will control power to a load. The current switching activity is accomplished by FET's. The Generic Controller, GC commands the switch on or off. In addition to the GC commanding the switch on or off, there is surge current conditioning and detection which can independently trip the switch off in the event of a large overcurrent. In this circuitry an inductor has been sized to control the slope (V/L) of the surge current. If a significant surge current occurs the gate control circuitry for the FETs switches these FETs from the on mode to the linear mode. In this mode the FETs absorb the excess power generated by the faulty current and limit the current. Also during this time a capacitor begins charging, and if the current does not drop within rated values then the charged capacitor will cause the gate control circuitry to turn the FETs off. This sequence is referred to as the FAST trip.

The RPC can provide five sensor signals to the GC. One signal **SWITCH 2**, indicates if the FETs are conducting or not. The magnitude of the current, **I1**. The signal **VDC+**, is a digital bit which is low if the line voltage is $\leq$ 60Vdc and is high if the line voltage is $\geq$ 60Vdc. A thermal resistor, **LM335**, is used to detect temperature readings on the RPC. Signal leads for a second current detection, **I2**, are on the board, but there is no sensor for this signal at this time (this should be the sensor for ground fault detection).

II. THE GC

The purpose of the Generic Controller, GC, is to accept sensor readings from the Remote Power Controller, RPC, and commands from the Switchgear Interface Card, SIC, in order to generate appropriate signals to the switch located on the RPC. The GC will pass status information and current, I, data to the SIC, when enabled to do so. The GCs are in the same card cage as the SICs for a given load center. Communication between these cards is accomplished over a wire-wrapped back-plane bus (Specialized- non-commercial nor standard bus).

The heart of the GC logic is programmed in the Altera 1800J chip. The main functions contained in this logic are: The Trip logic, the data sending logic, and the state machine. There are a few logic functions off chip: an A/D converter to generate **ADDATA** (which is **I1** in 8 bit digitized data in serial form); a timer; and powerup logic to assure we start in the correct state.

The state machine is a bit, six state encoder. The purpose of the state machine is to remember which state (On, Off, or Tripped) we are in, and move us from state to state as the inputs deem appropriate. Outputs to the RPC are determined by the state.

In the trip logic the digital signals from analog comparators for **SRGEI**, **I2TRIP**, **GNDTRP**, **UNDVLT**, **TMPTRP** are latched until a **RESET** command is given. The signal for a **FAST** trip is generated if we are in the on state and the RPC says the switch goes off. Any of these indicators can cause the **TRIP** signal to latch which will send us to the tripped state, if we were in the on state, and turns the switch off.

There is a 4 bit binary counter in the logic which synchronized with the SIC clock to generate the serial DATA response to the SIC inquiries and commands.

III. THE SIC

The purpose of the Switchgear Interface Card, SIC, is to control the communication flow between the Lowest Level Processor, LLP, and up to 14 Generic Controllers, GCs, as well as one A/D card as via the special, wire wrapped, backplane in the testbed (not a commercial or standard backplane). The interface to the LLP is accomplished via an RS-422 connection.

The hardware on the SIC include hardware for serial reception and transmission of data from the LLP and the GCs. The heart of the SIC is a Motorola 6800 microprocessor, with associated clock generators, reset circuitry, bus drivers, memory, parity generation and checking device, and address decoding circuitry. Thememory consists of 8 KBytes of EPROM for the firmware, and 8 KBytes of RAM. There are Mux's and FETs for selecting and driving control signals to the GCs and A/D card.

The firmware for the SIC is written in 6800 assembly language. Basically the code initializes the system, executes data in the continuous buffer, watches for the trigger for the once buffer, checks the input buffer for incoming commands, and puts data and status responses in the output buffer. Execution proceeds according to the continuous buffer commands or an incoming command.

IV. THE LLP

The purpose of the Lowest Level Processor, LLP, is to provide the Load Centers with an interface between the functions occurring in the Load Center and the higher level computing systems, which will interface with operators and crew members. Thus, the LLP serves as the data gatherer and formatter for the Fault Recovery And Management Expert System, FRAMES, which runs of a Solborn workstation. The link between the LLPs and the FRAMES is accomplished by TCP/IP on an ETHERNET. The current LLP configuration is a 20 MHz 386 microcomputer with 1.2 MByte of RAM, a floppy disk drive, a 422 communication card, and an ETHERNET card. The operating system is DOS 3.3, and the software is coded in TURBO PASCAL.

V. RECOMMENDATIONS FOR NEW IMPLEMENTATION

After this review of the functions and the implementation of the Load Center automation systems the primary recommendation, at this time, is to incorporate the use of commercially available microcontrollers in the automation system. To illustrate the advantage of these devices, several microcontrollers were reviewed (Motorola 68HC11, TI 37010, Intel 87196) and one was chosen to illustrate the advantages of microcontrollers. For this report the Intel 87196 was chosen. This initial choice was based primarily upon the fact that the 87196 has: A CMOS implementation and a power save mode to minimize power consumption, a serial I/O port, timers, 8-channel-10-bit A/D conversion, multiple output ports, on chip EPROM for the program, and is more compatible with the Intel 386 systems already in the LLPs.

The strategy for new Load Center automation is illustrated in figure 1. This strategy calls for the replacement of the GC card with a 68-pin 87196, reset circuitry, a crystal, and possibly bus drivers. All of this new GC implementation should reside on the RPC card, thus eliminating the GC card. The gains in the new implementation are clear in volume and weight, and should be substantial in power consumption. We also gain in functionality and performance.

In a similar manner, a small board involving an 87196 can be used to replace the SIC and the A/D card. In this

strategy we need the 68-pin 87196, the reset circuitry, a crystal, bus drivers to send signals to the GCs, and, if the exact programming strategy as used in the current SIC were used, one RAM chip is needed. In this case we gain some functionality and performance while reducing weight, power consumption and volume. We can relieve the LLP of many of its communication formatting and status checking functions.

The LLP functions should remain in the 386 based computer. This system should now be able to absorb some of the FRAMES processing done in the SOLBORNE. (At a minumum it will provide more refined information to FRAMES.) The possibility of combining present LLP functions into fewer 386 processors is possible. Currently it appears that if no new functions were added to the LLP level then one machine might handle all 5 load centers envisioned in the testbed. However, before this tradeoff was made a careful study of the distribution and faulty tolerance effects should be made.

VI.   CONCLUSIONS

The functions and implementations in the Load Center Automation systems (RPC, GC, SIC, LLP) have been reviewed. The general conclusion is: now that automation strategies have been studied, a more integrated implementation is possible, which saves weight, volume, and power consumption, while costing no reduction in functional performance or flexibility. This new strategy should incorportae the use of commercially available microcontrollers, as discussed above. The use of microcontrollers, and other highly integrated automation systems should be actively pursued and demonstrated on the SSM/PMAD testbed.

1b) Recommended Load Center Automation

RPC
Switch
2 Current Sensor and conditioning
Voltage Sensor and conditioning
Temperature sensor
Fast trip detection and control
Power conditioning for signal cond.
A/D 10 bit conversion of currents, voltage, and temperature
Serial communication with 1 of 2 SICs
Switch control
Soft faults- out of current range
9"x12"
X up to 14

SIC
Distribute LLP commands to RPCs
A/D 10 bit conversion of 8 sensors
Serial communications with LLP
Periodic data gathering and schedule execution
Load center Fault diagnosis (part of FRAMES)
Power conditioning for SIC, maybe RPC
9"x9"
X 2

LLP
Receive schedule and commands via eternet from FRAMES
Send scheduled, immediate, or manual commands to SIC
Gather data from SIC and format for ethernet
Check soft fault (current out of specified limit) and other diagnostics done by FRAMES
19"x7"x23"
X 1/5

1a) Present Load Center Automation

RPC
Switch
1 Current Sensor and conditioning
Voltage Sensor and conditioning
Temperature sensor
Fast trip detection and control
Power conditioning for signal cond.
9"x6"
X up to 14

GC
Signal Conditioning
A/D 8 bit conv. of switch current
Serial Communication with 1 of 2 SICs
Switch Control
5"x16"
half of the 9"x16"
X up to 14

A/D Card
A/D 8 bit conversion of 16 sensors
A/D 8 bit conversion of 16 temperature sensors
9"x16"
X 1

SIC
Distribute LLP commands to GCs
Interface to A/D Card
Serial communications with LLP
Periodic data gathering and schedule execution
Power conditioning for SIC,GC A/D and RPC
9"x16"
X 2

LLP
Receive schedule and commands via ethernet from FRAMES
Send scheduled, immediate, or manual commands to SIC
Gather data from SIC and format for ethernet
Check soft fault (current out of specified limit)
19"x7"x23"
X 1

Figure 1 Present versus Recommended Load Center Automation Implementation

1990

NASA/ASEE SUMMER FACULTY FELLOWSHIP PROGRAM

MARSHALL SPACE FLIGHT CENTER
THE UNIVERSITY OF ALABAMA

CHARACTERIZATION OF WELDED HP 9-4-30 STEEL

FOR THE ADVANCED SOLID ROCKET MOTOR

Prepared By:	George William Watt
Academic Rank:	Assistant Professor
University and Department	Utah State University Industrial Technology
NASA/MSFC:	
Laboratory:	Materials and Processes
Division:	Metallic Materials
Branch:	Metallurgy Research
MSFC Colleague:	Tina W. Malone
Contract No.:	NGT-01-002-099 The University of Alabama
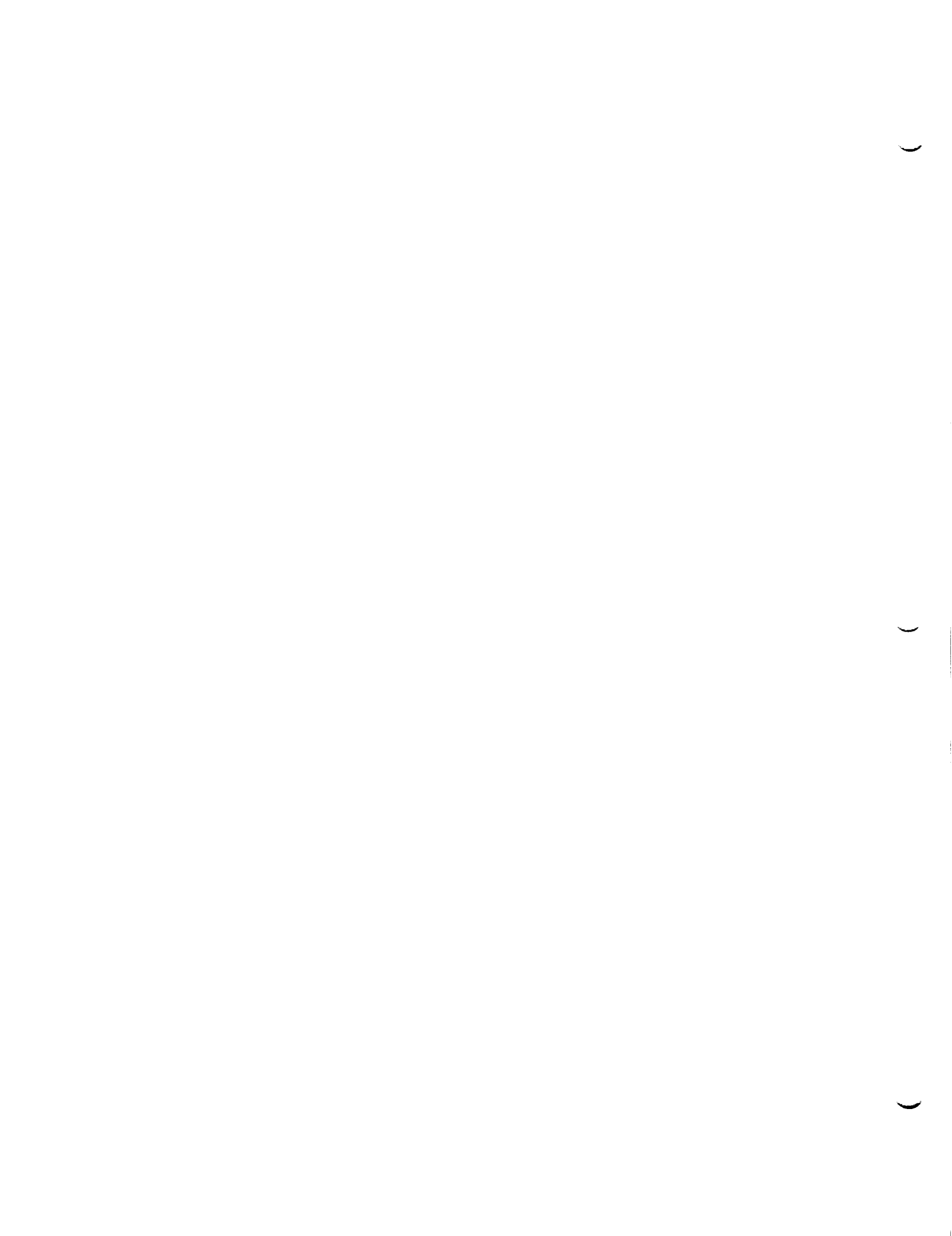
INTRODUCTION

Solid rocket motor case materials must be high-strength, high-toughness, weldable alloys. The Advanced Solid Rocket Motor (ASRM) cases currently being developed will be made from a 9Ni-4Co quench and temper steel called HP 9-4-30. These ultra high-strength steels must be carefully processed to give a very clean material and a fine grained microstructure upon treat treatment. This insures excellent ductility and toughness. The HP 9-4-30 steels are vacuum arc remelted and carbon deoxidized to give the cleanliness required. The typical heat treatment consists of: (1) normalizing at 1650 °F, (2) austenitizing at 1550 °F for 1 hour and quenching in oil followed by cooling to -100 °F for 2 hours, and (3) double tempering at 900-1000 °F for 2 hours. Typical properties are shown in Table I with some ASRM tentative requirements.

Table I

	HP 9-4-30	ASRM
UTS (ksi)	227	200
YS (ksi)	206	225
Elongation (%)	23	17
RA (%)	54	-
K_{IC} (ksi (in.)$^{1/2}$)	120	-

The ASRM case material will be formed into rings of the required thickness and diameter, and then welded together to form the case segments. Welding is the desired joining technique because it results in a lower weight than other joining techniques. Consequently, weldability of the HP 9-4-30 is very important and, as in most cases, the joint becomes the critical link in the structure. For this reason the mechanical and corrosion properties of the weld region material must be studied fully.

This research effort, carried out at the Metallurgy Research Branch (EH23) at the Marshall Space Flight Center, consisted of studying the microstructure of the fusion zone (FZ) and heat affected zone (HAZ) of welded HP 9-4-30. The microstructures were then related to the mechanical properties of the weld metal where possible. In addition, the relationship of certain weld joint design and weld process parameters was examined and related to the mechanical properties.

DISCUSSION

The mechanical properties of a metal are closely related to the microstructure. A study of the microstructure and related mechanical properties often identifies failure mechanisms and the means to modify the microstructure and achieve the desired properties. The welding process produces significant microstructural changes in the weld FZ and HAZ which then influence the properties. Upon welding, quench and temper steels like HP 9-4-30 may undergo significant changes such as: (1) a distinctive solidification substructure in the FZ, (2) grain growth and/or refinement in the FZ and HAZ, (3) micro and macrosegregation, and (4) retained austenite. The techniques used to study the microstructural/property relationships were tensile testing, light microscopy, microhardness, and Rockwell C hardness measurements, SEM, and microprobe analysis. Tests are also planned to determine the weld fracture toughness and crack growth rate.

In addition to the microstructural/property relationships, interaction between properties and additional factors such as: (1) filler metal composition, (2) linear heat input, (3) weld joint design, (4) base metal composition, and (5) weld reinforcement were examined. A mass balance approach, neglecting losses of base metal and filler metal alloying elements, resulted in a rule of mixtures equation in terms of the base metal amount of alloying element (X_{BM}), filler metal composition (C) given as the ratio of the amount of alloying element X in the filler metal (X_{FM}) to the amount in the base metal (X_{BM}), and the dilution ration (f_{FM}) which is the ratio of the amount of filler metal to the total amount of fused metal. The equation is

$$X_{WM} = X_{BM} [1 + f_{FM} (C-1)] \qquad (1)$$

where X_{WM} is the amount of element X in the weld metal. Since the mechanical properties of the weld metal depend on composition (X_{WM}), it becomes important to know how the composition varies. Equation (1) shows that X_{WM} depends strongly on f_{FM} and C, the filler metal composition

parameter. f_{FM} depends on several base metal thermal properties and the weld parameters heat input (Q) and travel speed (U). A possible relationship for f_{FM} is

$$f_{FM} = \frac{A_j + A_R}{B \, (Q/U)^M} \qquad (2)$$

where: A_j = joint cross-sectional area
         A_R = weld reinforcement cross-sectional area
         M, B = constants depending on materials and
                 welding process (M is of order 1.)

From Equations (1) and (2), it is clear that when Q/U increases f_{FM} will decrease and, since $0 \leq C \leq 1$, X_{WM} will increase for a given X_{BM}. Such changes can significantly change the weld mechanical properties.

RESULTS

Light microscopy and microhardness measurements of the HP 9-4-30 welded with a straight polarity plasma arc (SPPA) process in two passes showed several characteristic microstructures. The solidification substructure was cellular dendritic with an average cell size of about 0.030 mm. Strong microsegregation was evident in the interdendritic regions. The HAZ showed large prior austenite grains (about 0.12 mm grain diameter) near the fusion line with very small grains nearer the base metal. The hardness of the FZ and HAZ without any post weld heat treatment (PWHT) was 54-55 hardness Rockwell C (HRC) while the base metal hardness was about 48 HRC. Because of grain size variation and carbide dissolution the hardness varied within the HAZ. Subsequent passes tended to preserve aspects of the solidification substructure from the prior pass, but did result in tempering parts of the prior pass FZ and HAZ. This tempering reduced the hardness to near base metal values. However, the region in the base metal adjacent to the HAZ underwent overtempering and resulted in a narrow softened region of about 44 HRC. This region was only 2 mm wide. The hardness readings also indicated a distinct pass-to-pass hardness difference in the fusion zones. This occurred because the filler metal was very close in composition to HP 9-4-20 with 0.20 percent C, while the base metal had about 0.30 percent C. The mixing of filler metal and base metal gives a second

pass weld metal composition close to that of the filler metal. This reduced carbon content caused a significant reduction in hardness of the second pass FZ. Equation (1) quite accurately predicted the second pass FZ carbon content and confirmed the possible problem associated with pass-to-pass composition differences.

The microstructural/property analysis completed to this point indicates three areas of possible concern: (1) the microsegregation in the FZ solidification substructure which will tend to reduce ductility and toughness from base metal values, (2) the narrow overtempered zone in the base metal adjacent to the HAZ, and (3) the compositional variations from pass-to-pass due to dilution and filler metal composition. Careful control of joint design, filler metal composition, and welding parameters will be required to reduce this pass-to-pass variation. Solidification substructure can also be influenced by weld parameters. For example, as Q/U is decreased the cooling rate will increase and result in a finer solidification substructure which should give a tougher, more ductile material. However, note that a reduced Q/U will increase f_{FM} and thus reduce X_{WM} and consequently strength, while perhaps enhancing toughness and ductility. Thus, trade-offs among weld parameters, filler metal composition, and joint design will be required to optimize the final weld metal properties.

RECOMMENDATIONS

The following recommendations are offered:

(1)   The currently planned subsize tensile, K_{IC}, da/dN tests should be very important in understanding the fracture process. Fractures surfaces should be examined and related to FZ microstructure.

(2)   Babcock and Wilcox is planning to vary joint design, filler metal composition, and number of passes. This should be monitored carefully to determine dilution and pass-to-pass compositional variations.

(3)   The overtempered zone should be examined in more detail as it relates to the actual state of stress in the joint.

Overall the HP 9-4-30 appears to be very weldable.

1990

NASA/ASEE SUMMER FACULTY FELLOWSHIP PROGRAM

MARSHALL SPACE FLIGHT CENTER
THE UNIVERSITY OF ALABAMA

VERIFICATION OF COMPONENT MODE TECHNIQUES

FOR FLEXIBLE MULTIBODY SYSTEMS

Prepared By: Gloria J. Wiens

Academic Rank: Assistant Professor

University and   Auburn University
Department: Mechanical Engineering

NASA/MSFC:

    Laboratory: Structures and Dynamics
    Division: Control Systems Division
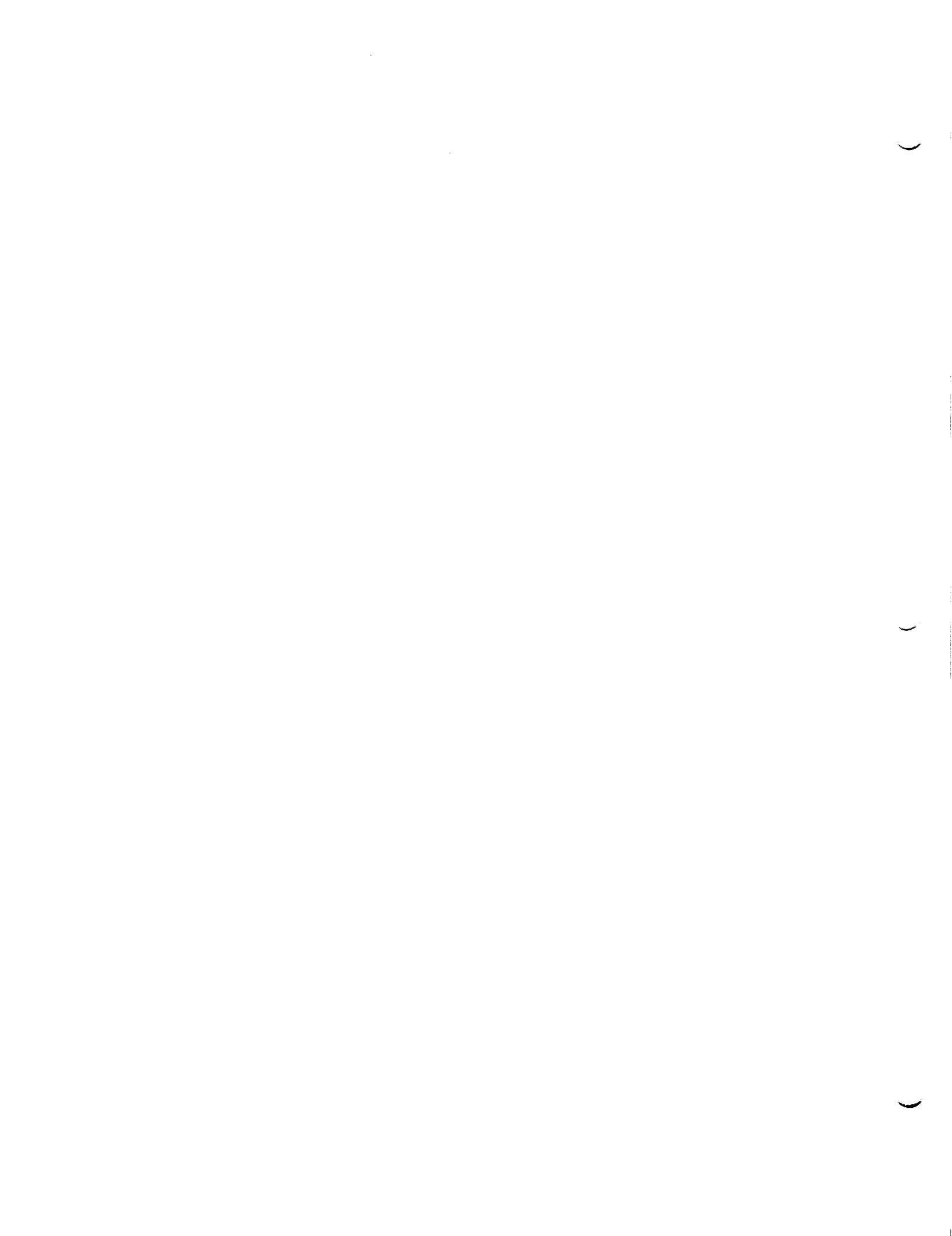   Branch: Pointing Control Systems

MSFC Colleague: Dr. Henry B. Waites

Contract No: NGT-01-002-099
                                The University of Alabama

INTRODUCTION

Since the 1960's, a significant amount of theoretical work has been undertaken in the area of modeling and simulation of multibody systems. However, for systems having flexible components, there still seems to be no well defined method for selecting component modes for systems, in which due to large displacements, the boundary conditions of the original assumed modes varies. Furthermore, there has been very limited experimental verification of the existing modeling and simulation techniques. Hence, over the past fifteen months, research has been initiated with NASA/MSFC and Auburn University in the flexible multibody modeling and verification area [1-3]. The emphasis of the work is focused on the lack of experimental verification of current modeling and simulation techniques. In particular, analytical and experimental data is to be used in addressing the question of which boundary conditions and corresponding component modes should one use in describing the dynamics of flexible multibody systems. Other issues of interest are the gravity loading effects on geometric stiffing and the effects of configuration changes on assumed inertia values used in mode selection.

PROJECT DESCRIPTION

The proposed summer research activities were a continuation of last summer's project with NASA/MSFC. One of the selected tasks was to conduct further investigations in the modeling aspects of flexible multibodies undergoing large angular displacements. Models were to be generated and analyzed through application of computer simulation packages employing the 'component mode synthesis' techniques. The primary task set forth was the implementation of Phase I of the Multibody Modeling, Verification and Control Laboratory (MMVC) plan [1]. This was to include running experimental tests on flexible multibody test articles. From these tests, data was to be collected for later correlation and verification of the theoretical results predicted by the modeling and simulation process. The theoretical and numerical modeling techniques are being used in deriving a functional relationship and/or trends for as many of the issues stated above as possible.

MODELING ASPECTS

In addressing the modeling task, the work concentrated on the design of the first test article for Phase I of the MMVC experiments. This involved extensive NASTRAN analyses. In addition, ADAMS and TREETOPS numerical models were used to determine some preliminary estimates. Various materials,

configurations and dimensions were considered in the design process. After exhaustive study, a test article exhibiting low frequency characteristics, high modal density, a degree of dynamic coupling, and small static deflections due to gravitational loading was designed (see Figures 1-2 and Table 1). The resulting test article, currently under fabrication by NASA/MSFC, has the following material and dimension specifications.

Material of all members: Aluminum$_{6061}$
Young's Modulus, $E=68.95e9$ N/m^2
Density = 2,768 kg/m^3

Dimensions:
Link 1:   Length = 2.440m
Box Beam: Width, b = 0.0762m
Height, h = 0.0254m
Wall Thickness, t = 0.0032m

Link 2:   Lengths (Two Branches) L_a = 1.500m, L_b = 1.450m
Solid Beam: Width, b = 0.0335m
Height, h = 0.0090m

Links 3, 4, 5, 6:
Lengths: L_3 = 0.8200m, L_4 = 0.8000m
L_5 = 0.7800m, L_6 = 0.7600m
Solid Beam: Width, b = 0.0050m
Height, h = 0.0020m

With the addition of motor, joints and sensors, the first seven frequencies dropped approximately 1 Hz in value. In addition, there was approximately a 52 per cent reduction in modal density range of these frequencies. The cost for the fabrication of two test articles is under $5,000.

The first generation of the test article's joints were designed to be light-weight and rigid. They were also designed using a pipe clamp approach to allow ease in changing body configurations. Since the initial testing will be for different static configurations of the test article, the joints will be fixed in each given configuration using a frictionless locking approach. Future improvements will be needed for the next phase of dynamic testing.

PHASE I IMPLEMENTATION

The implementation of Phase I of the MMVC Laboratory plan was not completed. However, important progress was made. Preliminary details and arrangements have been outlined for implementation once the test article is received (late September). The sensor and instrumentation specifications have been given. The base support which is to cantilevered off a platform in the west high bay area of building 4619 has been located and awaits mounting. In addition, the Base Excitation Table is in the process of being designed and fabricated between now and early November 1990. The joints will be fabricated once the test article has been received.

The above items will be carried out by NASA employees. According to their schedules, our first experimental testing is expected to be conducted between November and December.

REFERENCES

1. Wiens, G. J., "Multibody Modeling and Verification", Final Report, NASA/ASEE 1989 Summer Faculty Fellowship Program, Contract No. NGT-10-008-021, Marshall Space Flight Center, Huntsville, AL.

2. Tsai, H.-D., "Normal Modes and Static Analysis of MMV Design 1: Part I", edited by G. J. Wiens, NASA/MSFC Report, May 29, 1990.

3. Wiens, G. J., "Flexible Multibody Modeling and Mode Selection Dependencies", Six Months Technical Progress Report, Contract No. NASA/NAG8-123, August 27, 1990.
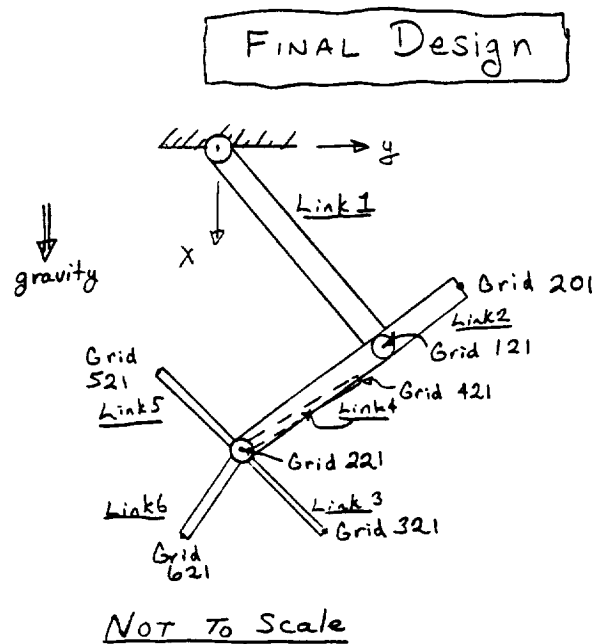
Figure 1.

Final Design

TABLE 1.

NORMAL MODE ANALYSIS FOR MMV DESIGN 12-NATURAL FREQUENCY

TEST ARTICLE 1: $\theta_1=0$ AND $\theta_2=0$

LINK1: A1(HOLLOW-R, AL) LINK4: A3(SOLID-R, AL)
LINK2: A2(SOLID-R, AL)   LINK5: A3(SOLID-R, AL)
LINK3: A3(SOLID-R, AL)   LINK6: A3(SOLID-R, AL)

MODE NO.	SYSTEM MODE	COMPONENT MODE: LINK1	LINK2	LINK3
1	1.379	1.672	2.578	2.397
2	2.250	21.801	3.452	15.021
3	2.416	69.198	17.251	42.060
4	2.539	143.586	21.637	82.425
5	2.591	223.398	50.042	136.269
6	3.100	245.037	60.598	203.604
7	3.458	373.588	100.456	284.471
8	14.202	529.314	118.830	378.940
9	15.160	(Hz)	(Hz)	(Hz)
10	15.896			
11	15.972	LINK4	LINK5	LINK6
12	17.372	2.518	2.649	2.790
13	20.658	15.782	16.601	17.486
14	23.057	44.190	46.485	48.963
15	40.295	86.598	91.096	95.953
16	42.420	143.168	150.604	158.635
	(Hz)	213.912	225.022	237.021
		298.873	314.396	331.162
		398.124	418.802	441.135
		(Hz)	(Hz)	(Hz)

| 1 (0.962) 1.379 Hz | 2 (0.447) 2.250 Hz | 3 (0.411) 2.416 Hz | 4 (0.435) 2.539 Hz | 5 (0.430) 2.591 Hz | 6 (0.892) 3.100 Hz | 7 (0.345) 3.458 | 8 (0.125) 14.202 Hz |

| 9 (0.119) 15.160 Hz | 10 (0.120) 15.896 Hz | 11 0.128) 15.972 Hz | 12 (0.121) 17.372 Hz | 13 (0.207) 20.658 Hz | 14 (0.133) 23.057 Hz | 15 (0.076) 40.295 Hz | 16 (0.072) 42.421 Hz |
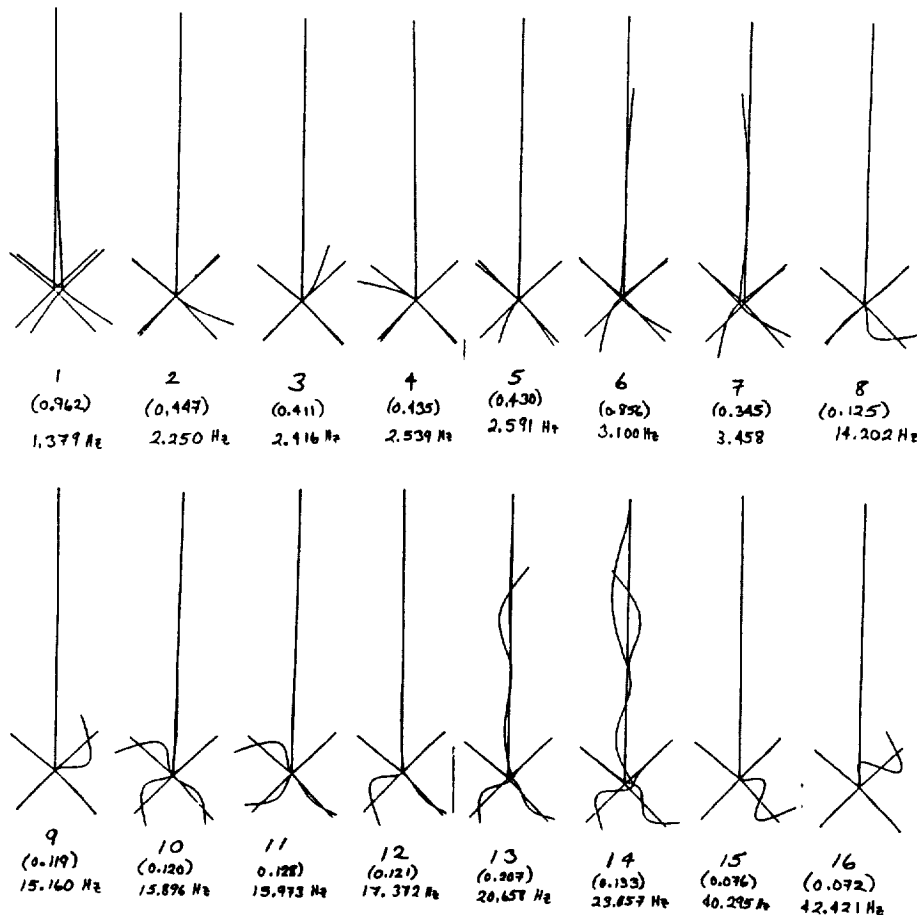
Figure 2. Mode Shapes

LIV-4